Nanoparticles

Building Blocks for Nanotechnology

Edited by
Vincent Rotello

Nanoparticles
Building Blocks for Nanotechnology

Nanostructure Science and Technology

Series Editor: David J. Lockwood, FRSC
National Research Council of Canada
Ottawa, Ontario, Canada

Current volumes in this series:

Alternative Lithography: Unleashing the Potentials of Nanotechnology
Edited by Clivia M. Sotomayor Torres

Nanoparticles: Building Blocks for Nanotechnology
Edited by Vincent Rotello

Nanostructured Catalysts
Edited by Susannah L. Scott, Cathleen M. Crudden, and Christopher W. Jones

Nanotechnology in Catalysis, Volumes 1 and 2
Edited by Bing Zhou, Sophie Hermans, and Gabor A. Somorjai

Polyoxometalate Chemistry for Nano-Composite Design
Edited by Toshihiro Yamase and Michael T. Pope

Self-Assembled Nanostructures
Jin Z. Zhang, Zhong-lin Wang, Jun Liu, Shaowei Chen, and Gang-yu Liu

Semiconductor Nanocrystals: From Basic Principles to Applications
Edited by Alexander L. Efros, David J. Lockwood, and Leonid Tsybeskov

Nanoparticles

Building Blocks for Nanotechnology

Edited by

Vincent Rotello

University of Massachusetts
Amherst, Massachusetts

9 8 7 6 5 4 3 2

springeronline.com

Preface

The integration of top-down lithographic techniques with synthetic organic and inorganic technologies is a key challenge for the development of effective nanoscale devices. In terms of assembly, nanoparticles provide an excellent tool for bridging the gap between the resolution of electron beam lithography (~60 nm) and the molecular level. Nanoparticles possess an array of unique properties associated with their core materials, including distinctive magnetic, photonic and electronic behavior. This behavior can be controlled and applied through monolayer functionalization and assembly strategies, making nanoparticles both scaffolds and building blocks for nanotechnology.

The diverse structures and properties of nanoparticles makes them useful tools for both fundamental studies and pragmatic applications in a range of disciplines. This volume is intended to provide an integrated overview of the synthesis and assembly of nanoparticles, and their applications in chemistry, biology, and materials science.

The first three chapters focus on the creation and intrinsic properties of nanoparticles, covering some of the myriad core materials and shapes that have been created. The remaining chapters of the book discuss the assembly of nanoparticles, and applications of both discrete particles and particle assemblies in a wide range of fields, including device and sensor fabrication, catalysis, biology, and nanoscale electronic and magnetic systems.

Of course, no single book can hope to cover the diverse array of research encompassed by researchers making and applying nanoparticles. I hope, however, that this book will prove useful for whetting the imagination of researchers currently pursuing nanotechnology, as well as those contemplating joining this uniquely multidisciplinary field.

Vincent M. Rotello

Department of Chemistry
University of Massachusetts, Amherst MA 01003

Contents

1

Synthesis and Applications of Magnetic Nanoparticles

Andrew K. Boal

Sandia National Labratories, Albuquerque, NM, USA

1.1. INTRODUCTION

Magnetic nanoparticles (MNPs) have been the focus of an increasing amount of the recent literature, which has chronicled research into both the fabrication and applications of MNPs. The explosion of research in this area is driven by the extensive technological applications of MNPs which includes single-bit elements in high-density magnetic data storage arrays, magneto-optical switches, and novel photoluminescent materials. In biomedicine, MNPs serve as contrast enhancement agents for Magnetic Resonance Imaging, selective probes for bimolecular interactions, and cell sorters. Nanoparticles of magnetic metals are also finding applications as catalysts, nucleators for the growth of high-aspect-ratio nanomaterials, and toxic waste remediation. Methodologies for the synthesis of MNPs are being developed by scientists working in fields spanning Biology, Chemistry, and Materials Science. In the last decade, these efforts have provided access to nanoscale magnetic materials ranging from inorganic metal clusters to custom-built Single Molecule Magnets. The goal of this chapter is to provide broad overviews of both the applications of MNPs and the synthetic methodologies used in their production.[1,2]

1.2.   APPLICATIONS OF MAGNETIC NANOPARTICLES

High-density magnetic data storage arrays provide a major technological driving force for the exploration of MNPs. If a reliable data storage system based on a single 5 nm MNP acting as an individual bit of information could be created, storage densities of 10 Gbit/cm^2 would be possible.[3] MNPs have also been demonstrated to be functional elements in magneto-optical switches,[4] sensors based on Giant Magnetoresistance,[5] and magnetically controllable Single Electron Transistor devices[6] or photonic crystals.[7] One of the first stages in the development these MNP-based materials is the creation of ordered 2- and 3-dimensional arrays of MNPs.[8] Two dimensional arrays are typically fabricated by the slow evaporation of highly monodisperse MNP solutions onto a substrate.[9] Structural control can be achieved by the application of a magnetic field[10] or patterning using dip-pen nanolithography.[11] Three dimensional nanoparticle assemblies with complex structures can also be fabricated by the slow evaporation technique in the presence of an applied magnetic field.[12] These technological applications are all in addition to the numerous known and developed applications of aqueous suspensions of MNPs (ferrofluids).[13]

Doping magnetic ions into semiconductors to produce Dilute Magnetic Semiconductors (DMS) has long been used to alter the electronic and optical properties of the parent materials.[14] Similarly, DMS nanoparticles can be produced by including metal ions in reactions used to prepare semiconductor nanoparticles.[15] DMS nanoparticles have applications in the fabrication of novel optical materials. For example, both Ni:ZnS and Co:ZnS DMS nanoparticles display strong photoluminescent emission of green light.[16] Additionally, the electronic properties of DMS materials are responsive to both light and magnetic fields, making them useful in the fabrication of magneto-optical switches.[17]

MNPs are also finding a multitude of biomedical applications, the most prevalent of which is Magnetic Resonance Imaging (MRI) contrast agents.[18] Recent work has involved the development of bioconjugated MNPs,[19] which facilitate specific targeting of these MRI probes to brain tumors[20] and enabled real-time monitoring of both gene expression[21] and T-cell[22] or progenitor cell[23] migration. Bioconjugate MNPs are also useful as probes for *in vitro* detection of bimolecular interactions using a variety of techniques, including the detection of DNA hybridization by NMR.[24] Antigen-antibody interactions can be detected using either Superconducting Quantum Interference Device (SQUID)[25] or magnetically induced birefringence[26] based immunoassays. MNPs have also been utilized in the purification of both cells[27] and biomacromolecules[28] from complex mixtures. In purification applications, the MNP is modified so as to specifically bind the target cell or molecule of interest and the complex is then magnetically purified from undesired components.

MNPs are also used as highly active catalysts which has long been demonstrated by the use of finely divided metals in several reactions.[29] Recent synthetic advances have resulted in the preparation of catalysts based on smaller particles or matrix supported nanoparticle catalysts. Smaller particles increase the

surface-to-area ratio and therefore the catalytic activity while supported nanoparticle catalyst materials show enhanced stability and broader scope of applications.[30] Electro-oxidation of methanol for fuel cells applications can be catalyzed by NiPt, PtRuNi,[31] and CoPt[32] nanoparticles. Similarly, $LiCoO_2$[33] and $Li_xCu_{1-y}Fe_yO_z$[34] nanoparticles have been evaluated as potential components of lithium-ion batteries. Finally, recent reports have described the application of Co nanoparticles in the Pauson-Khand reaction.[35]

MNPs can nucleate and control the growth of high aspect ratio nanomaterials such as carbon nanotubes (CNTs). Here, a substrate is coated with nanoparticles and CNTs are then grown using a variety of chemical vapor deposition (CVD) processes. Nanoparticles of Fe, Ni, Co,[36] FeMo,[37] and iron carbides[38] have all been shown to be active in this process. In the case of Fe nanoparticles, the diameter of the nucleating nanoparticle has been shown to control the diameter of the resulting CNT over the range of 3-13 nm.[39] Iron nanoparticles have also been used to nucleate the growth of iron nanorods.[40]

Finally, iron nanoparticles have also been used as toxic waste remediators. Bulk iron is an established waste remediator as, in aqueous solutions, it acts as a reducing agent capable of decomposing a variety of toxic chemicals in groundwater including halogenated alkanes[41] and nitroaromatics.[42] Owing to their higher surface-to-area ratio, nanoparticles are more efficient at waste remediation, as demonstrated for FePd nanoparticles used to decompose halogenated alkanes[43] and Fe nanoparticles acting to remove Cr^{4+} and Pb^{2+} from aqueous solutions.[44]

1.3. SYNTHESIS OF SINGLE METAL MNPS

Solution phase synthesis of transition metal nanoparticles is accomplished via two generic pathways: the reduction of a metal salt or decomposition of an organometallic complex. Two of the largest concerns regarding MNP synthesis are the ability to both tune the size of the nanoparticle and control particle size dispersity. These concerns are addressed in a number of ways and are dependent on the synthetic methodology employed. In the case of metal ion reduction, successful strategies include conducting the reaction in a confined environment or in the presence of a suitable capping ligand. For the case of organometallic decomposition, size control and dispersity is usually attained by conducting the reactions at high temperature, which ensures a high rate of nanoparticle nucleation and growth. Capping ligands, which form a self-assembled monolayer of the nanoparticle, can also be used to mediate particle growth.

Water-in-oil microemulsions (w/o microemulsions) and inverse micelles are often employed as nanoconfined reactors in the synthesis of many varieties of nanoparticles.[45] For both, the size of the confined space can be defined by varying the amounts of both surfactant and solvent, which allows for direct control over the size of the resulting MNPs. Typically, MNP preparation in w/o

microemulsions is achieved by mixing an emulsion containing metal salts with an emulsion containing a suitable reducing agent (*e.g.* NaBH$_4$ or N$_2$H$_4$). This produces surfactant capped metal nanoparticles with diameters of less than 10 nm (Scheme 1.1). Similarly, aqueous solutions of reducing agents can be added to inverse micellar solutions of metal salts in nonpolar solvents. Using these methodologies, MNPs of Fe,[46] Co,[47] and Ni[48] have been prepared.
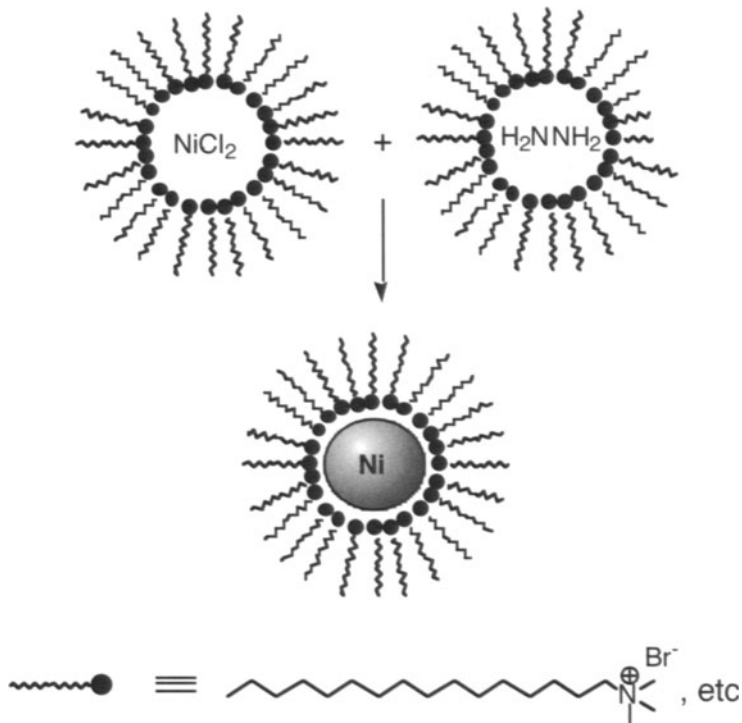
SCHEME 1.1. Example of the production of Ni MNPs by H$_2$NNH$_2$ reduction of NiCl$_2$ in a w/o microemulsion system.

Co MNPs have also been produced by the reducing CoCl$_2$ with LiBEt$_3$H in dioctyl ether containing oleic acid and trialkyl phosphines. In this reaction, ε-Co MNPs are produced and the size is controlled by varying the alkyl groups on the trialkyl phosphine.[49] Gd MNPs, the only present example of a lanthanide metal nanoparticle produced by a solution route, can be produced by alkalide reduction of GdCl$_3$ under strictly anaerobic and anhydrous conditions.[50]

Thermal decomposition of organometallic complexes is of great interest as many of the synthetic procedures produce highly monodisperse nanoparticles. Metal carbonyl complexes represent the most common organometallic precursor for this reaction Fe MNPs, for example, are produced by the thermal decomposition of Fe(CO)$_5$ in trioctylphosphine oxide (TOPO) solutions containing oleic acid, which acts to passivate the product nanoparticle (Scheme 1.2a).[40] Polymer-coated Fe MNPs have also been prepared by thermal decomposition of Fe(CO)$_5$ in the presence of poly(styrene) functionalized with

tetraethylenepentamine.[51] Thermal decomposition of $Co_2(CO)_8$ in hot toluene solutions containing TOPO produces ε-Co MNPs.[52] Similar reactions carried out in o-dichlorobenzene in the presence of various ligands allows for MNP morphological control (Scheme 1.2b).[53] Co MNPs embedded in polymers have been prepared both by H_2 promoted decomposition of $Co(\eta^3\text{-}C_8H_{13})(COD)$ in poly(vinylpyrrolidone) (PVP)[54] or by charging either crosslinked poly(styrene)[55] or poly(dimethylsiloxane)-*block*-poly((3-cyannopropyl)methylsiloxane)-*block*-poly(dimethylsiloxane)[56] with $Co_2(CO)_8$ followed by heating. Ni MNPs can be fabricated by H_2 induced decomposition of $Ni(COD)_2$. By varying the ligands present in the decomposition reaction, the morphology of the resulting Ni MNPs can be varied.[57] Ni MNPs can also be prepared in PVP matrices either by the direct decomposition of $Ni(COD)_2$ at room temperature by PVP[58] or by H_2 promoted decomposition.[59]
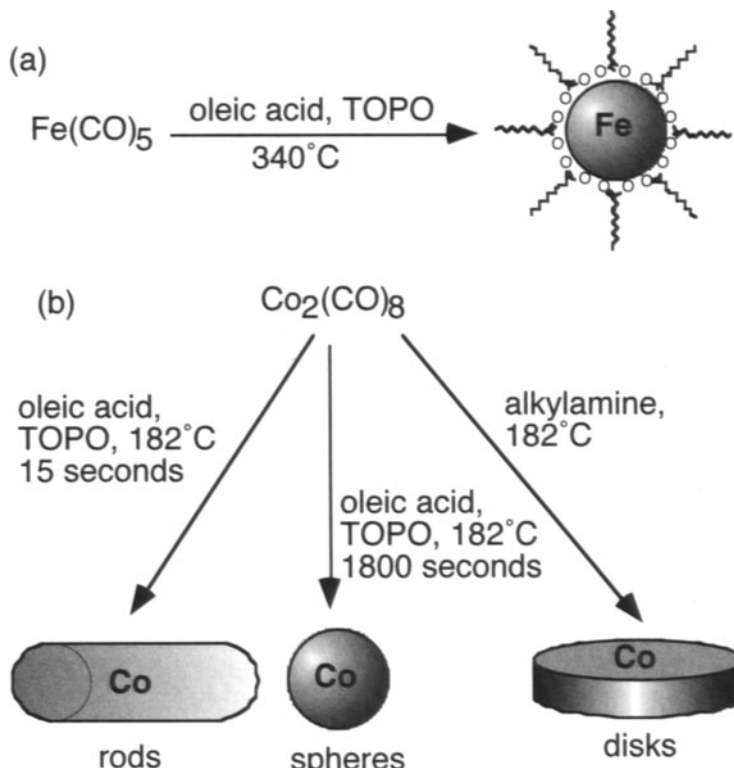
SCHEME 1.2. (a) Thermal decomposition of $Fe(CO)_5$ in the presence of oleic acid and TOPO to produce Fe MNPs and (b) use of varying ligands to produce Co MNPs with spherical, rod, and disk morphologies from $Co_2(CO)_8$

Sonochemical decomposition of organometallic complexes has also been used to produce MNPs. Sonication of $Fe(CO)_5$ either as a neat liquid or in a noncoordinating, high boiling solvent such as decilin leads to the formation of agglomerates of polydisperse Fe MNPs.[60] Coordinating ligands or polymers that can attach to the MNP surface prevents agglomeration and allow for better

control over particle size dispersity.[61] Sonication has also be used to produce Ni MNPs by the decomposition of Ni(COD)$_2$.[62]

1.4.   SYNTHESIS OF ALLOYED METAL NANOPARTICLES

MNPs of alloyed transition metals can be prepared by reactions in which two metal precursors are decomposed in tandem, producing solid solution nanoparticles, or sequentially to give core-shell nanoparticles.[63] The most heavily studied alloy MNPs are FePt and CoPt, both of which are of high interest for applications in data storage. FePt MNPs are prepared by the simultaneous thermal decomposition of Fe(CO)$_5$ to Fe and the polyol reduction of Pt(acac)$_2$ by 1,2-dodecanediol to Pt at 250°C in solutions containing oleic acid and oleyl amine (Scheme 1.3).[64] This process yields monodisperse, solid solution FePt MNPs coated by a monolayer of oleyl amine and oleic acid that can be exchanged for shorter or longer acids or amines after synthesis. The composition of the MNP core can be controlled by varying the relative concentrations of the iron and platinum precursors. Further, the diameter of these MNPs can be adjusted between 3-10 nm.
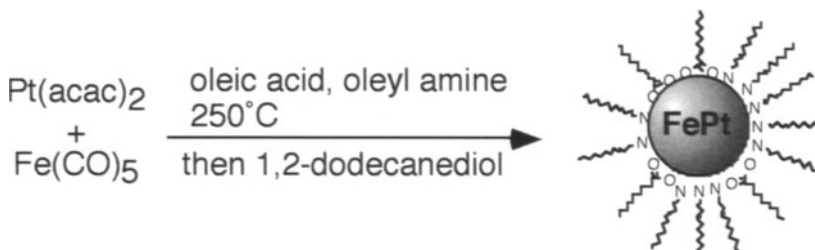
SCHEME 1.3. Synthesis of solid solution FePt MNPs.

Variations on the tandem organometallic decomposition/polyol reduction method allows for the synthesis of MNPs of other alloys of iron. Including either AgAc or Co(acac)$_2$ in the reaction produces [Fe$_{49}$Pt$_{51}$]$_{88}$Ag$_{12}$[65] or Fe$_x$Co$_y$Pt$_{100-x-y}$[66] nanoparticles, respectively. Pd(acac)$_2$ can be used instead of Pt(acac)$_2$ to produce MNPs of FePd.[67] The simultaneous decomposition of Fe(CO)$_5$ and Mo(CO)$_6$ in the presence of bis-2-ethylhexylamine and octanoic acid in refluxing dioctyl ether produces FeMo MNPs whose size can be varied between 3-11 nm by changing the amount of acid in the reaction.[37] FeAu MNPs can be prepared by reducing w/o micelles of FeSO$_4$ and HAuCl$_4$ with NaBH$_4$. This procedure has been used to prepare both Fe$_{core}$Au$_{shell}$[68] and Au$_{core}$Fe$_{shell}$Au$_{shell}$[69] MNPs by a stepwise reduction process where each successive step uses larger diameter water droplets to yield the alloyed particle (Scheme 1.4). Similarly, FeCu nanoparticles can be prepared by the simultaneous reduction of Fe^{2+} and Cu^{2+} in inverse micelles producing MNPs of various FeCu ratios.[70]
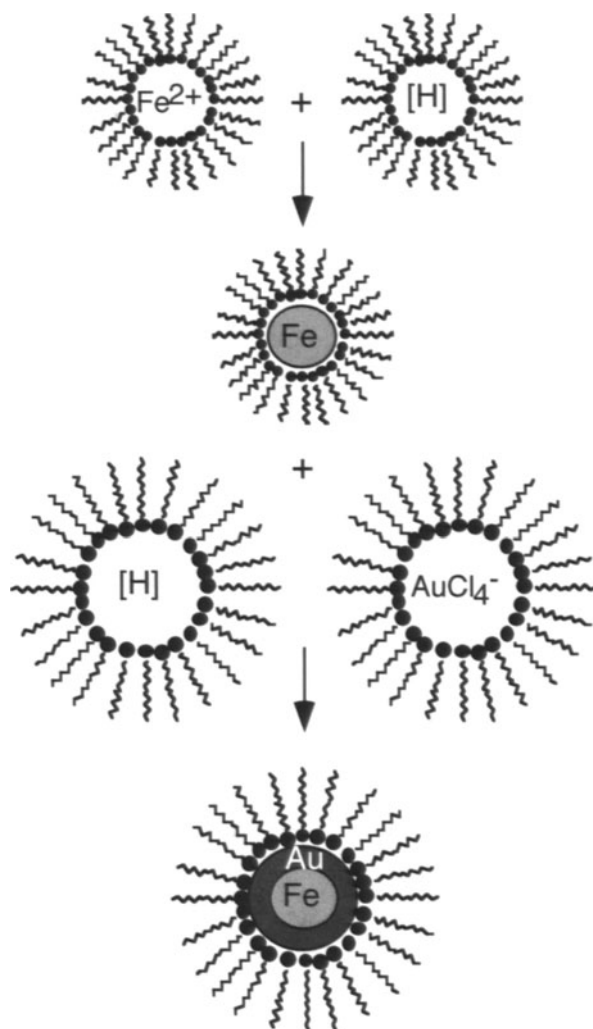
SCHEME 1.4. Synthesis of $Fe_{core}Au_{shell}$ MNPs.

CoPt MNPs can be fabricated by several different routes. Simultaneous reaction of $Co(\eta^3\text{-}C_8H_{18})(\eta^4\text{-}C_8H_{12})$ and $Pt_2(dba)_3$ with H_2 in the presence of PVP leads to the production of 1-1.5 nm diameter, polymer coated MNPs.[71] The composition of these nanoparticles can be varied between Co_3Pt_1, Co_1Pt_1, and Co_1Pt_3 by changing the ratio of the inorganic precursors subjected to the reaction. Simultaneous decomposition of $Co_2(CO)_8$ and reduction of $Pt(acac)_2$ in the presence of 1-adamantanecarboxylic acid and various coordinating solvents allows for the synthesis of $CoPt_3$ MNPs with diameters controllable between 1.5-7.2 nm.[72] Likewise, simultaneous decomposition of $Co_2(CO)_8$ and either $Rh(acac)(COD)$ or $Sm(acac)_3$ in hot surfactants produces solid solution $RhCo$[73] or $SmCo$[74] MNPs. The simultaneous reduction of $PtCl_6^{2-}$ and Co^{2+} ions by hydrazine in w/o microemulsions leads to the formation of 3-4 nm diameter CoPt

nanoparticles.[32] $Co_{core}Pt_{shell}$ MNPs can be prepared by using Co MNPs to reduce $Pt(hfac)_2$, giving the desired nanoparticle via a transmetalation process (Scheme 1.5).[75] Co nanoparticles have also been used to reduce $AgClO_4$, producing $Co_{core}Ag_{shell}$ MNPs.[76]
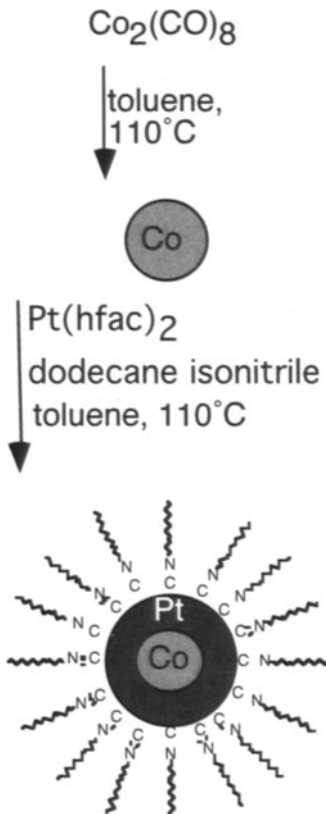
SCHEME 1.5. Synthesis of $Co_{core}Pt_{shell}$ MNPs where a Co nanoparticle is used to reduce $Pt(hfac)_2$

Several nickel alloy MNPs have also been described. Simultaneous reduction of $NiSO_4$ and $Pd(Ac)_2$ by glycerol in the presence of PVP leads to the formation of solid solution NiPd MNPs whose composition can be controlled by varying the ratios of metal salts in the reaction.[77] A stepwise variation of this process, where H_2PdCl_4 is first reduced in the presence of PVP followed by the reduction of $Ni(Ac)_2$ leads to the formation of $Pd_{core}Ni_{shell}$ MNPs. Here, shell thickness is varied by changing the amount of $Ni(Ac)_2$ added to the Pd nanoparticles.[78] Simultaneous reduction of mixtures of either $NiCl_2$ and H_2PtCl_6 or $NiCl_2$, H_2PtCl_6, and $RuCl_3$ in water with $NaBH_4$ leads to the formation of either NiPt or NiPtRu MNPs, respectivley.[31]

MNPs can also be prepared by alloying magnetic metals with nonmetals such as boron, nitrogen, and carbon. For example, Ni_2B MNPs can be prepared by the mixture of w/o microemulsion solutions of $Ni(AOT)_2$ and $NaBH_4$.[79] FeCuB MNPs are likewise produced when micelle solutions of Fe^{2+} and Cu^{2+} are reduced

with $NaBH_4$.[80] Both iron carbide (Fe_3C) and iron nitride (Fe_xN, x = 2-4) MNPs have been prepared via sonochemical methods. In the case of Fe_3C, $Fe(CO)_5$ is sonicated in the presence of diphenylmethane followed by annealing at 700°C, which yielded 20-100 nm diameter nanoparticles.[81] Similarly, Fe_xN nanoparticles are prepared either by the sonication of $Fe(CO)_5$ in decane while being exposed to a 3.5:1 mixture of NH_3 and H_2 gases, which produced $Fe_{2-3}N$, or by treatment of amorphous Fe nanoparticles at 400°C with the same mixture of gases to produce Fe_4N nanoparticles.[82]

1.5. SYNTHESIS OF METAL OXIDE NANOPARTICLES

Ferrofluids, aqueous suspensions of iron oxide nanoparticles, are well known members of this class of MNPs.[13] The iron oxide nanoparticles that comprise ferrofluids, typically Fe_3O_4, are prepared by either coprecipitation of mixtures of Fe^{2+} and Fe^{3+} ions in the presence of base or the precipitation/oxidation of Fe^{2+} ions by the action of base and an oxidant (Scheme 1.6). Recent advances in these techniques include the use of iron precursors which form micelles[83] or synthesis within w/o microemulsions.[84] These reactions produce MNPs resistant to agglomeration and allow for the synthesis of small (<10 nm diameter) nanoparticles with controllable size. Further, when the reaction is carried out in the presence of and appropriate surfactant, the *in situ* fabrication of three-dimensional MNP assemblies occurs.[85] The polyol method used to produce metal and alloy nanoparticles can also be adapted, by the addition of water to the reaction mixture, for the preparation of metal oxide MNPs.[86]

SCHEME 1.6. Aqueous preparative methods for the synthesis of iron oxide MNPs.

Iron oxide MNPs can also be prepared using coprecipitation routes in the presence of a variety of polymers leading to processable nanocomposites.[87] Recent advances include the use of triblock copolymers as nanoreactors which allow for particle size control by varying the polymer block composition.[88] Further, the preparation of dendrimer coated iron oxide MNPs has also been reported.[89] Precipitation techniques can also be used to produce iron oxide MNPs in solid matrices such as alumina,[90] silica,[91] and crosslinked copolymers.[92]

Nonhydrolytic procedures for the preparation of iron oxide nanoparticles typically involve the thermal decomposition of an appropriate iron containing precursor in hot surfactants. Injecting octylamine solutions of iron cupferon ($Fe(Cup)_3$) into hot trioctylamine leads to the formation of γ-Fe_2O_3 nanoparticles coated with an amine monolayer (Scheme 1.7a).[93] The diameter of these

nanoparticles can be varied between 5 and 10 nm by either changing the reaction temperature or by performing multiple injections of Fe(Cup)$_3$. Refluxing Fe(CO)$_5$ in octyl ether containing oleic acid and trimethylamine oxide (TMO) leads to the formation of oleate coated γ-Fe$_2$O$_3$ MNPs (Scheme 1.7b), which can also be prepared by TMO oxidation of iron MNPs.[94] The size of these highly monodisperse particles is controlled between 4 to 16 nm by varying the ratio of Fe(CO)$_5$ and oleic acid. The reaction of Fe(CO)$_5$ in DMF in the presence of poly(vinylidene difluoride) leads either to spherical or pyramidal Fe$_2$O$_3$ nanoparticles, depending on the reaction temperature.[95] Fe$_3$O$_4$ nanoparticles can be prepared by the reaction of Fe(acac)$_3$ in phenyl ether solution with oleic acid, oleylamine, and 1,2-dexadecanediol at reflux, which produces oleyl-capped nanoparticles 4 nm in diameter.[96] Iron oxide MNPs can also be prepared in an electrochemical route, which utilizes a sacrificial iron anode. The size of the resulting nanoparticles can be controlled between 3 and 8 nm by varying the current density.[97]
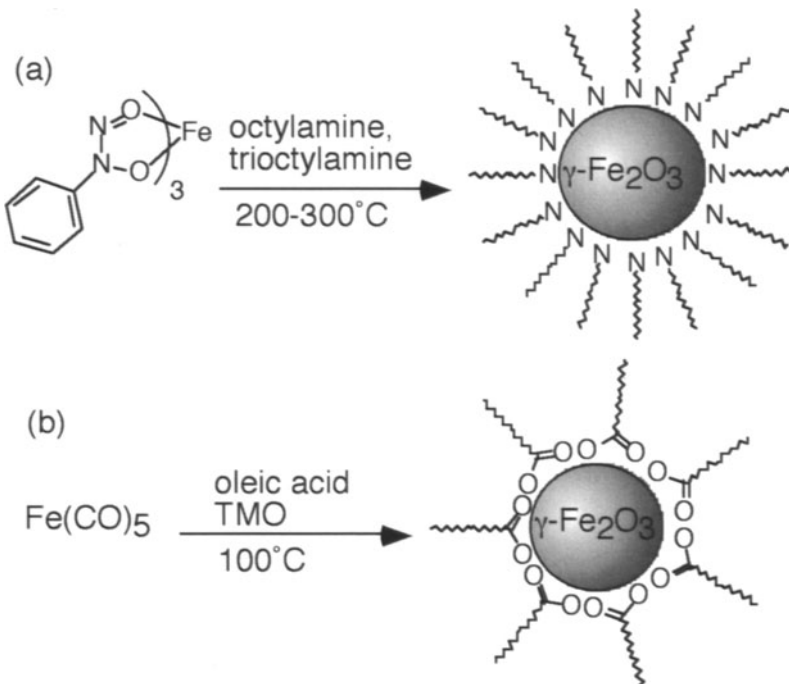
SCHEME 1.7. Nonhydrolytic synthetic routes to iron oxide MNPs. (a) Thermal decomposition of Fe(Cup)$_3$ in hot surfactants producing amine coated γ-Fe$_2$O$_3$ and (b) γ-Fe$_2$O$_3$ MNPs prepared by the decomposition and oxidation of Fe(CO)$_5$.

Many of the procedures used in the synthesis of iron oxide MNPs can be applied to the preparation of nanoparticles of other metal oxides. Cobalt oxide (CoO and Co$_3$O$_4$) MNPs have been prepared by the aerial oxidation of polymer-protected Co nanoparticles.[98] MNPs of α-Ni(OH)$_2$ can be prepared by sonication of Ni(NO$_3$)$_2$.[99] The production of Ni(OH)$_2$ from NiCl$_2$ followed by heating to

250°C produces NiO MNPs.[100] Finally, MnO nanoparticles have been prepared by thermal decomposition of $Mn_2(CO)_8$ at 400-450°C.[101]

Metal ferrite (MFe_2O_3) and ferrite derivative MNPs are typically prepared by variations of the coprecipitation methods used in the production of iron oxide nanoparticles. Typically, aqueous solutions of the desired metal salts are combined in the desired ratios, often in inverse micelles or in the presence of polymers, and base is then added to promote the formation of the nanoparticle. From such routes, MNPs of $BaFe_{12}O_{19}$,[102] $CoFe_2O_3$,[103] $CoCrFeO_4$,[104] $CoLn_{0.12}Fe_{1.88}O_4$ (Ln = Ce, Sm, Eu, Gd, Dy, Er),[105] GdFeO$_3$,106 $MnFe_2O_3$,[107] $NiFe_2O_3$,[108] $Ni_{0.5}Zn_{0.5}Fe_2O_3$,[109] $SrFe_{12}O_{19}$,[110] and $ZnFe_2O_3$[111] have been prepared.

Other mixed metal oxide MNPs have also been described. Magnetically doped aluminum oxide nanoparticles, either MAl_2O_3 (M=Co, Cu, Ni)[112] or Fe_2O_3/Al_2O_3 composite MNPs[113] have been prepared by the cohydrolysis of precursor metal salts or complexes. MNPs of both $La_{0.75}Ca_{0.2}MnO_3$ and $LaCo_xMn_{1-x}O_3$ have been prepared by hydrolysis of precursors metal salts with NaOH, followed by calcination at ~500°C.[114] Finally, yttrium iron garnet ($Y_3Fe_5O_{12}$) MNPs have been prepared by a gellation/calcination methodology[115] or the basic hydrolysis of $Fe(NO_3)_3$ and $Y(NO_3)_3$ in a microemulsion system.[116]

1.6. SELF-ASSEMBLED MONOLAYERS ON IRON AND IRON OXIDE MNPS

Iron and iron oxide MNPs prepared by sonication of $Fe(CO)_5$ represent the best-studied MNP-monolayer system. After sonication, these MNPs are nanoparticle agglomerates which lack monolayer functionality. Reacting these nanoparticles with a variety of functionalized alkanes, including alcohols,[117] carboxylic acids,[118] thiols,[119] phosphonic or sulfonic acids,[120] or silanes,[121] produces monolayer coated MNPs (Scheme 1.8). Monolayer coated iron oxide MNPs can be formed directly by sonicating $Fe(CO)_5$ in the presence of various organic acids.[122]

Monolayer exchange chemistry allows for the integration of diverse molecular functionality into magnetic nanoparticles and has been described for both γ-Fe_2O_3 and Fe_3O_4 MNPs. When long chain alkane alcohols or carboxylic acids are used to modify the amine monolayer of γ-Fe_2O_3 nanoparticles prepared by the thermal decomposition of $Fe(Cup)_3$, the resulting nanoparticle-monolayer system rapidly and irreversibly produces insoluble agglomerates. Stable MNP-monolayer systems are produced by using 2,2-dialkyl-1,3-propane diol ligands, which have both a bulky tail and multivalent bonding capabilities (Scheme 1.9a).[123] Another MNP-monolayer system where the monolayer can be modified after nanoparticle syntheses is that of oleate coated γ-Fe_2O_3 nanoparticles. Exposure of these nanoparticles to pyrene butyric acid incorporated the pyrene functionality into the monolayer (Scheme 1.9b). The acid functionality is required, as pyrenes bearing either alcohol or ester groups cannot not be inserted into the monolayer.[124]
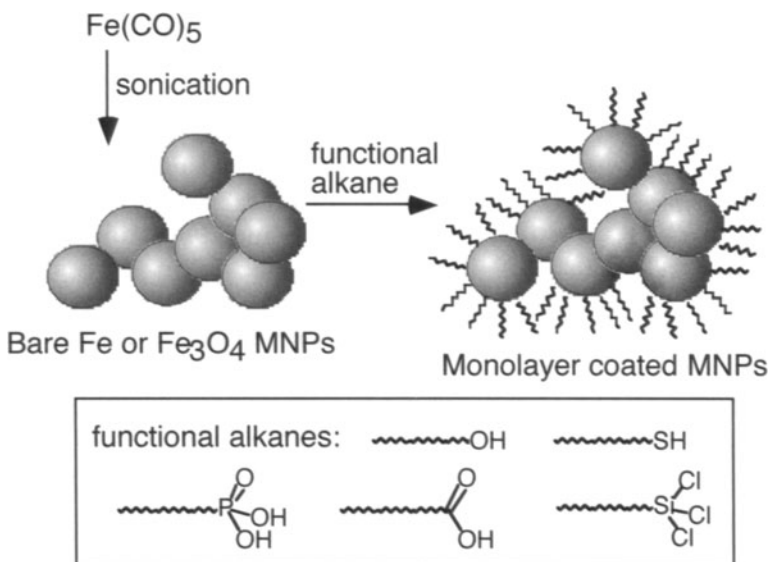
SCHEME 1.8. Route to monolayer protected iron or iron oxide nanoparticle produced by sonication of Fe(CO)$_5$.
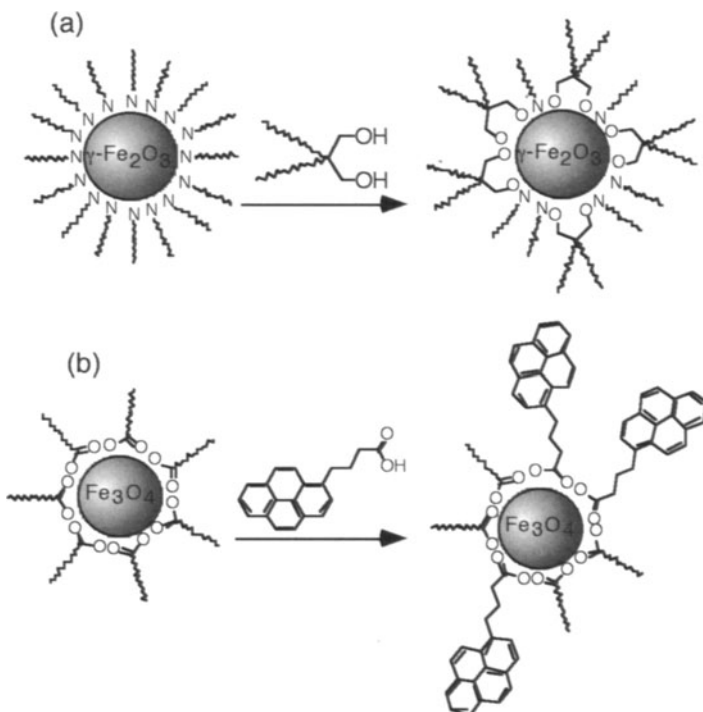
SCHEME 1.9. Monolayer exchange chemistry on (a) amine coated γ-Fe$_2$O$_3$ and (b) oleate coated Fe$_3$O$_4$ MNPs.

1.7.   PREPARATION OF BIOCONJUGATE MNPS

Many biomedical applications involve the conjugation of biomacromolecules to iron oxide MNPs. Amino crosslinked iron oxide (CLIO-NH$_2$) nanoparticles, iron oxide MNPs coated with crosslinked dextran and functionalized with amine groups, are the most common starting material for the production of bioconjugated MNPs.[125] The amine functionality is reacted with heterobifunctional crosslinking agents such as succinimidyl iodoacetate (Scheme 1.10a) or N-succinimidyl 3-(pyridyldithiol)propionate (Scheme 1.10b), which then allows for the attachment of biomacromolecules. Amine functionality can also be introduced by sol-gel coating of MNPs with 3-aminopropyltrimethoxysilane, which can then be similarly derivitized.[126] Other methods for the production of bioconjugated or biocompatible MNPs include magnetoliposomes bearing functional groups in the lipid layer,[28] direct adsorption of proteins onto the nanoparticle surface,[127] and coating the MNPs with nonionic surfactants.[128]
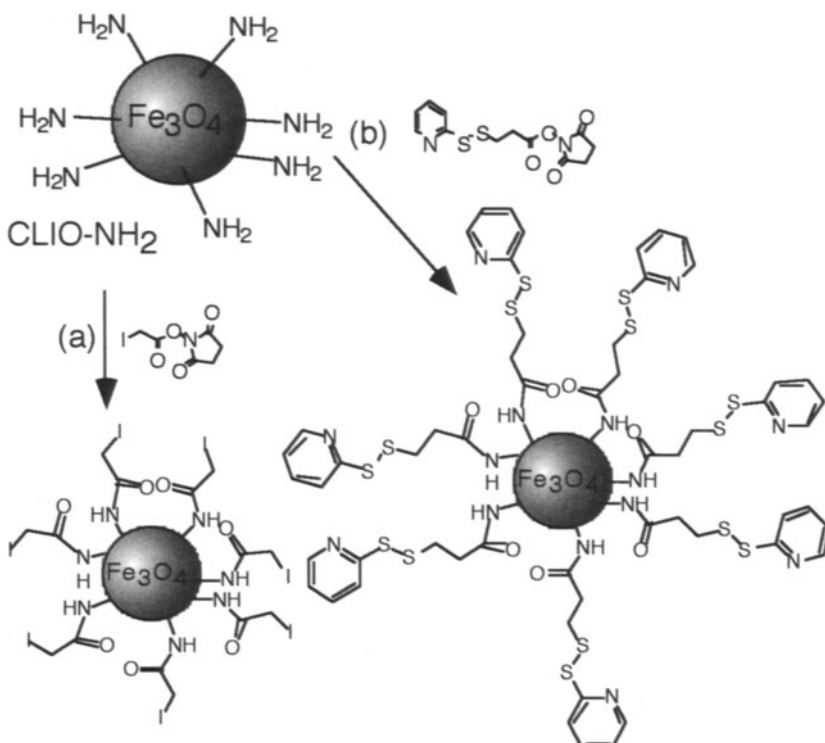
SCHEME 1.10. Reaction of CLIO-NH$_2$ with heterobifunctional crosslinkers, producing nanoparticles that are starting points for the creation of bioconjugated MNPs.

1.8. BIOSYNTHETIC ROUTES TO MNPS

MNPs, typically iron oxide, are also common products of Nature's synthetic laboratories.[129] For example, several bacteria are known to produce Fe_3O_4 nanoparticles encapsulated in a phospholipid bilayer (magnetoliposomes).[130,131] Synthetic magnetoliposomes can be formed by coating iron oxide nanoparticles with lipid bilayers after synthesis of the nanoparticle core. Here, Fe^{2+} and Fe^{3+} are first coprecipitated with base and stabilized by lauric acid. These particles are then coated with dimyristoylphosphatidylcholine (DMPC), producing the magnetoliposome (Scheme 1.11a).[132] Alternatively, preformed liposomes can be employed as microreactors in which Fe^{2+} is first sequestered inside of the liposome followed by the addition of base to produce iron oxide MNPs (Scheme 1.11b).[133] Similar methodologies have allowed for the preparation of Gd_2O_3[134] magnetoliposomes.
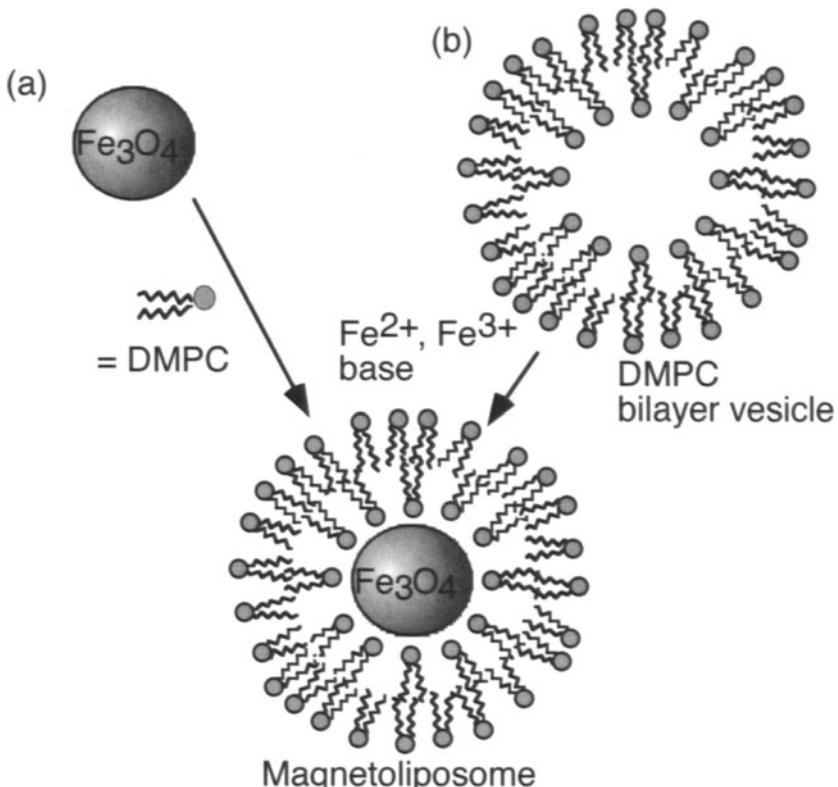
SCHEME 1.11. Synthesis of magnetoliposomes (a) by employing a lipid bilayer as a reactor and (b) lipid coating of Fe_3O_4 MNPs.

Ferritin, an iron storage protein,[135] provides a template which has been used in the production of iron oxide and other nanoparticles. Native ferritin forms a

shell with a 12 nm outer diameter and 8 nm inner diameter that surrounds a 6 nm γ-FeOOH nanoparticle core. Removal of the naturally occurring core yields the empty shell, called apoferritin. Sequential exposure of apoferritin to aqueous Fe^{2+} solutions and air yields a 6 nm Fe_3O_4 MNP within the ferritin shell (Scheme 12a).[136] Apoferritin has also been utilized in the production of both CoPt[137] and CoOOH[138] MNPs by acting as a reactor for the simultaneous $NaBH_4$ reduction of Co^{2+} and Pt^{3+} ions or H_2O_2 mediated oxidation of Co^{2+} in slightly basic solutions, respectively. Viral capsids, such as that of the tobacco mosaic virus (TMV) or cowpea chlorotic mottle virus (CCMV), are protein cages similar to ferritin and can be used in the fabrication of nanoscale materials.[139] In the case of the TMV capsid, which has a cylindrical shape 18 nm in diameter and 300 nm long, the anionically charged exterior of the capsid provides a platform for the nucleation of mineralization processes.[140] For example, iron oxide shells on the capsid have been formed by exposing a solution of TMV to a mixture of Fe^{2+} and Fe^{3+} ions, followed by the addition of a base to produce a Fe_3O_4 shell (Scheme 1.13b). The CCMV capsid, which has an inner diameter of 18-24 nm, is genetically engineered to create an anionic interior similar to ferritin. Upon exposure to Fe^{2+} and air, the formation of γ-FeOOH nanoparticles up to 24 nm in diameter within the capsid is observed.[141]
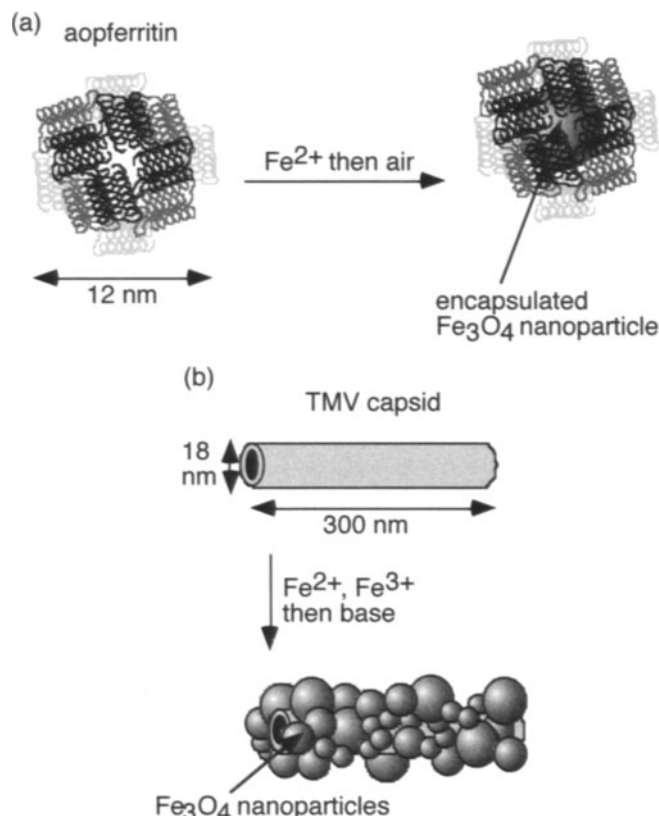
SCHEME 1.12. (a) Formation of Fe_3O_4 a nanoparticle within the confines of an apoferritin template and (b) biomineralization on the surface of the TMV.

1.9. SYNTHESIS OF DILUTED MAGNETIC SEMICONDUCTOR NANOPARTICLES

Magnetic nanoparticles can be prepared by doping CdS, ZnS, or CdSe nanoparticles with either Mn^{2+} or Co^{2+} ions. Like metallic MNPs, Dilute Magnetic Semiconductor (DMS) nanoparticles are mainly produced by either coprecipitation of ions in reverse micellar solutions or the decomposition of organometallic precursors in hot surfactant solutions. Both methods provide control over both size and dopant concentration, and therefore the magnetic properties, of the resulting DMS nanoparticles. Careful purification of DMS nanoparticles is critical as some reactions can yield nanoparticles where some of the magnetic ions are weakly bound to the surface and are not true DMS nanoparticles.[142]

Manganese doped CdS, CdSe, and ZnS nanoparticles are among the best-characterized systems of this class of magnetic nanoparticles. Mn:CdS DMS nanoparticles are typically prepared in a reverse micelle system where Na_2S is used to simultaneously precipitate $Cd(AOT)_2$ and $Mn(AOT)_2$.[143] The solid solution nature of these nanoparticles has been confirmed using X-ray absorbtion fine-structure (EXAFS) spectroscopy (Scheme 1.13a).[144] In the case of Mn:ZnS, preparative routes include coprecipitation of $MnCl_2$ and $Zn(S_2CNEt_2)$ in hot TOP/TOPO mixes, yielding TOPO capped nanoparticles with an average size of 5.4 nm.[145] An alternative route involves the precipitation of $ZnAc_2$ and $MnCl_2$ in the presence of thioacetamide at 80°C in acidic aqueous solution.[146] Mn:CdSe MNPs have been prepared using an organometallic decomposition methodology. Here, the reaction of several organometallic Mn precursors ($Mn(CO_5)Me$, TCPMn, $MnMe_2$, and $Mn_2(u$-$SeMe)_2(CO)_8$) with $CdMe_2$ and tiroctylphosphine selenide (TOPSe) in hot TOP/TOPO were explored. After careful purification and characterization of the nanoparticles, it was found that only the $Mn_2(u$-$SeMe)_2(CO)_8$ precursor gave true DMS nanoparticles (Scheme 1.13b), the other Mn precursors lead to the formation of CdSe nanoparticles with Mn^{2+} adsorbed onto the surface.[147] For all of these nanoparticles, the initial surfactant monolayer can be displaced with either alkane thiols or pyridine, allowing for the purification and further functionalization of the nanoparticles.

DMS nanoparticles can also be prepared by doping CdS, CdSe, and ZnS with Co^{2+} ions. Both Co:CdS and Co:ZnS nanoparticles have been prepared using reverse micelle/co-precipitation methodologies.[148] Co:CdSe nanoparticles have been prepared by heating two cluster compounds, $[Cd_{10}Se_4(SC_5H_6)_{16}](NMe_4)_4$ and $[Co_4(SC_5H_6)_{10}](NMe_4)_2$, in hexadecylamine at 170-210°C to give amine capped nanoparticles whose size and doping level can be controlled.[149]
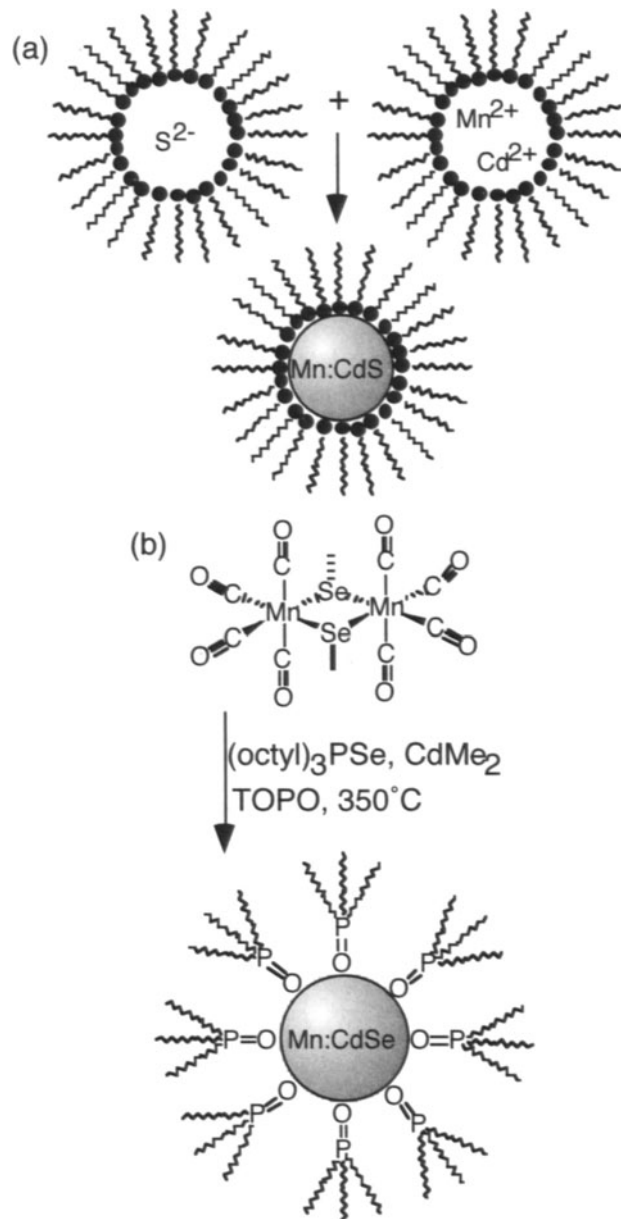
SCHEME 1.13. Synthetic routes to (a) Mn:CdS and (b) Mn:CdSe DMS nanoparticles.

1.10.   SYNTHESIS OF TRANSITION METAL COORDINATION POLYMER NANOPARTICLES

Magnetic nanoparticles have been prepared from transition metal coordination polymers such as Prussian Blue analogs, including $Cu_2[Fe(CN)_6]$,[150] $NH_4Fe[Fe(CN)_6]$,[151] $Co_3[Fe(CN)_6]_2$, $Co[Fe(CN)NO]$, and $Cr_3[Cr(CN)_6]_2$.[152] These materials are generally prepared by the mixture of two reactants in a reverse micelle solution, which then allows for control over the size of the nanoparticles. For example, in the case of $Cu_2[Fe(CN)_6]$, particles are prepared from AOT reverse micelles of $CuSO_4$ and $K_4[Fe(CN)_6]$. The preparation of $NH_4Fe[Fe(CN)_6]$ is accomplished by exposing solutions containing both ammonium iron(III) oxalate and ammonium ferricyanide AOT solutions to light (Scheme 1.14). This reaction produces surfactant coated cubic nanoparticles with an average size of 16 nm. Nanoparticles of $Co_3[Fe(CN)_6]_2$, $Co[Fe(CN)NO]$, and $Cr_3[Cr(CN)_6]_2$ were prepared by mixing w/o microemulsions of the appropriate components, yielding nanoparticles coated with a monolayer of surfactant. By attenuating the reaction conditions, particles of varying morphologies (cubes to spheres), sizes (10-200 nm) and low polydispersity can be formed.

$(NH_4)_3[Fe(CN)_6]$
$(NH_4)_3[Fe(C_2O_4)_3]$
$h\nu$
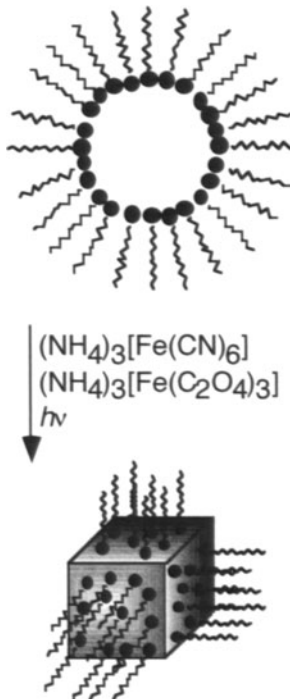
SCHEME 1.14. Preparation of cubic $NH_4Fe[Fe(CN)_6]$ Prussian Blue nanoparticles.

Nanoparticles of the anti-ferromagnetic materials NH_4MnF_3[153] and $KMnF_3$[154] have been prepared by microemulsion techniques. NH_4MnF_3 nanoparticles are made by first mixing micellar solutions of $MnAc_2$ and NH_4F,

followed by the addition of acetone to cause nanoparticle coagulation. Purification of the resulting material lead to nanoparticles free of both reaction byproducts as well as surface bound monolayer. $KMnF_3$ nanoparticles were produced by combining inverse micellar solutions of $MnCl_2$ and KF, resulting in the formation of ~68 nm cubes which could be coated with either pyridine or thiols.

1.11. THE LIMITS OF NANO: SINGLE MOLECULE MAGNETS

While materials scientists are continually trying to make bulk materials smaller to prepare nanosized materials, chemists are working in the opposite direction to build magnetic materials from molecular components.[155] A recent development of this field is the discovery of transition metal clusters which, due to a high degree of magnetic anisotropy, behave as Single Molecule Magnets (SMMs) at cryogenic temperatures.[156] SMMs have a key advantage over "traditional" MNPs in that the magnetic nature of the material is synthetically controlled at the molecular level. Like MNPs, the "size" of the SMM can be altered by changing the number of metal ions in the cluster, and the composition can also be altered by preparing clusters from multiple metal components. Unlike MNPs, however, the magnetic interaction *between* the metal ions can be adjusted by changing the nature of the chemical linkage between them. This unique aspect of SMMs allows for a much higher degree of control over magnetic properties than can be achieved with MNPs.

The first example of a SMM was $[Mn_{12}O_{12}Ac_{16}(H_2O)_4] \cdot 4H_2O \cdot AcOH$ (Scheme 1.15), which contains a central $Mn_{12}O_{12}$ core capped with acetate ligands. This cluster exhibits magnetic ordering and hysteresis at cryogenic temperatures.[157] Since then, a large number of other SMM compounds have been discovered,[158] including many expansions of the $Mn_{12}O_{12}$ family,[159] Mn_4O_3X (X=Cl⁻, F⁻, N_3^-, NCO⁻, or Ac) clusters,[160] molecular Prussian Blue compounds[161] containing as few as seven transition metal ions,[162] and Fe_4O_4 cubic clusters.[163] Typically, these clusters are prepared by reacting transition metal ions with a combination of ligands that act to bridge metal centers and ligands that act to "cap" transition metal centers.

1.12 SUMMARY AND OUTLOOK

In summary, a substantial amount of work in the last decade has been devoted to the development of novel solution-phase MNP synthetic methodologies. Combined, this work provides access to MNPs of a large variety of materials including single metals, metal alloys, metal oxides, Dilute Magnetic Semiconductors, and transition metal coordination polymers. Further, these

synthetic techniques enable a high degree of control over MNP characteristics such as particle size and size dispersity. The chemistry of self-assembled monolayers on MNPs, primarily iron oxide nanoparticles, has also been explored and allows for the preparation of bioconjugated MNP materials. Knowledge of both monolayer structure and exchange chemistry is, however, much less than what is known for noble metal nanoparticles, and represents an area of MNP chemistry ripe for further study. The current frontier in the synthesis of nanoscale magnetic materials, SMMs, is still in the early stages of development and will ultimately provide access to tailor-made nanomagnetic materials. The further elaboration of synthetic techniques for the preparation of MNPs, SMMs, and self-assembled monolayers on MNPs will further defining the role of broadening MNPs in nanotechnological applications.

$$[Mn_3O(Ac)_6(py)_3](ClO_4)$$

$$\downarrow \begin{array}{l} KMnO_4 \\ AcOH/H_2O \\ 60°C \end{array}$$

$Mn_{12}O_{12}$ core of
$$[Mn_{12}O_{12}Ac_{16}(H_2O)_4] \cdot 4H_2O \cdot AcOH$$
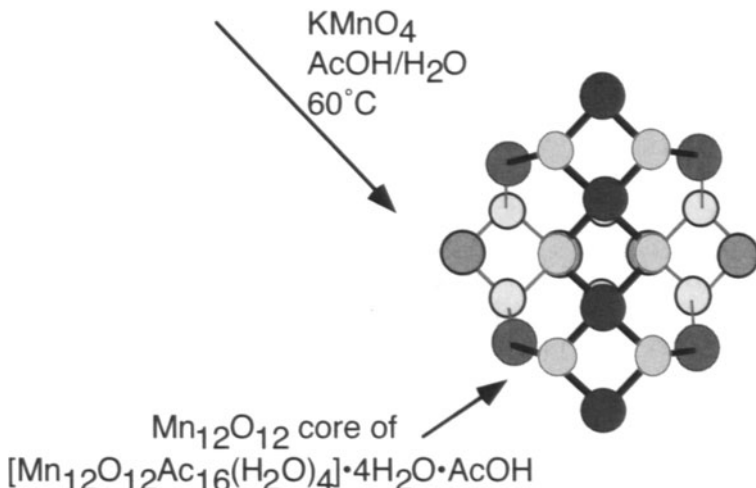
SCHEME 1.15. Preparation of the SMM $[Mn_{12}O_{12}Ac_{16}(H_2O)_4] \cdot 4H_2O \cdot AcOH$, drawing of the product shows the $Mn_{12}O_{12}$ (Mn is dark, O is light) core arrangement and is based on crystal structures in reference 159(a).

ACKNOWLEDGEMENTS

REFERENCES

1. This review will focus entirely on solution phase routes to MNPs. For reviews of ball-milling and gas-phase routes, see: (a) Murty, B. S.; Ranganathan, S. *Int. Mater. Rev.* **1998**, *43*, 101-141, (b) Kruis, F. E.; Fissan, H.; Peled, A. *J. Aerosol. Sci.* **1998**, *29*, 511-535.
2. For information on the magnetic properties of MNPs, see: (a) *Nanomagnetism*; Hernando, A., Ed.; Kluwer Academic Publishers: New York, 1993. (b) Majetich, S. A.; Scot, J. H.; Mirkpatrick, E. M.; Chowdary, K.; Gallagher, K.; McHenry, M. E. *NanoStr. Mater.* **1997**, *9*, 291-300. (c) Perez, A.; Melinon, P.; Dupuis, V.; Jensen, P.; Prevel, B.; Tuaillon, J.; Bardotti, L.; Martet, C.; Treilleux, M.; Broyer, M.; Pellarin, M.; Vaille, J. L.; Lerme, J. *J. Phys. D* **1997**, *30*, 709-721. (d) Himpsel, F. J.; Ortega, J. E.; Mankey, G. J.; Willis, R. F. *Adv. Phys.* **1998**, *47*, 511-597. (e) Cowburn, R. P. *J. Phys. D* **2000**, *33*, R1-R16. (f) Binns, C.; Baker, S. H.; Maher, M. J.; Louch, S.; Thornton, S. C.; Edmonds, K. W.; Dhesi, S. S.; Brookes, N. B. *Phys. Stat. Sol.* **2002**, *189*, 339-350.
3. Frolov, G. I. *Tech. Phys.* **2001**, *46*, 1537-1544.
4. (a) Hasmonay, E.; Dubois, E.; Bacri, J.-C.; Perzynski, R.; Raikher, Yu. L.; Stepanov, V. I. *Eur. Phys. J. B* **1998**, *5*, 859-867. (b) Giri, A. K.; Pellerin, K.; Pongsaksawad, W.; Sorescu, M.; Majetich, S. A. *IEEE Trans. Magn.* **2000**, *36*, 3029-3031. (b) Menéndez, J. L.; Bescós, B. Armelles, G.; Cebollada, A.; Quintana, C.; Navarro, E.; Serna, R.; Gonzalo, J.; Afonso, C. N.; Doole, R.; Petford-Long, A. K.; Hole, D. *IEE Trans. Magn.* **2001**, *37*, 1416-1418. (c) Menéndez, J. L.; Bescós, B. Armelles, G.; Serna, R.; Gonzalo, J.; Doole, R.; Petford-Long, A. K.; Alonso, M. I. *Phys. Rev. B* **2002**, *65*, 205413. (d) Aktsipetrov, O. A. *Coll. Surf. A* **2002**, *202*, 165-173. (e) Shemer, G.; Markovich, G. *J. Phys. Chem. B* **2002**, *106*, 9195-9197.
5. (a) Kechrakos, D.; Trohidou, K. N.; Blackman, J. A. *Phys. Rev. B* **2001**, *63*, 134422. (b) Xu, C.; Li. Z.-Y.; Dikshtein, I. E.; Hui, P. M. *Phys. Lett. A* **2001**, *291*, 325-332. (c) Ram, S.; Frankwicz, P. S. *Physica. Status. Solidi. A* **2001**, *188*, 1129-1140. (d) Kechrakos, D.; Trohidou, K. N. *Physica B* **2002**, *318*, 360-364.
6. (a) Yakushiji, K.; Mitani, S.; Takanashi, K.; Takahashi, S.; Maekawa, S.; Imamura, H.; Fujimori, H. *Appl. Phys. Lett.* **2001**, *78*, 515-517. (b) Graf, H.; Vancea, J.; Hoffmann, H. *Appl. Phys. Lett.* **2002**, *80*, 1264-1266. (c) Fiete, G. A.; Zarand, G.; Halperin, B. I.; Oreg, Y. *Phys. Rev. B* **2002**, *66*, 024431.
7. Xu, X.; Friedman, G.; Humfeld, K. D.; Majetich, S. A.; Asher, S. A. *Chem Mater.* **2002**, *14*, 1249-1256.
8. (a) Kirk, K. J. *Contemp. Phys.* **2000**, *41*, 61-78. (b) Warne, B.; Kasyutich, O. I.; Mayes, E. L.; Wiggins, J. A. L.; Wong, K. K. W. *IEEE Trans. Magn.* **2000**, *36*, 3009-3011. (c) Giersig, M.; Hilgendorff, M. *Coll. Surf. A* **2002**, *202*, 207-213.
9. Murray, C. B.; Sun, S.; Doyle, H.; Betley, T. *MRS. Bull.* **2001**, 985-991.
10. Giersig, M.; Hilgendorff, M. *Coll. Surf. A* **2002**, *202*, 207-213.
11. Liu, X.; Fu, L.; Hong, S.; Dravid, V. P.; Mirkin, C. A. *Adv. Mater.* **2002**, *14*, 231-234.
12. (a) Pileni, M. P. *Adv. Mater.* **1998**, *10*, 259-261. (b) Pileni, M. P. *Adv. Funct. Mater.* **2001**, *11*, 323-336. (c) Pileni, M. P. *J. Phys. Chem. B* **2001**, *105*, 3358-3371.
13. Berkovskii, B. M.; Medvedev, V. F.; Krakov, M. S. *Magnetic Fluids: Engineering Applications*; Oxford University Press: Oxford, 1993.
14. Furdyna, J. K.; Kossut, J. *Semiconductors and Semimetals*; Academic Press: New York, 1988; Vol. 25.
15. (a) Feltin, N.; Levy, L.; Ingert, D.; Pileni, M. P. *Adv. Mater.* **1999**, *11*, 398-402. (b) Feltin, N.; Levy, L.; Ingert, D.; Pileni, M. P. *J. Phys. Chem. B* **1999**, *103*, 4-10.
16. (a) Yang, P.; Lü, M.; Zhou, G.; Yuan, R.; Xü, D. *Inorg. Chem. Comm.* **2001**, *4*, 734-737. (b) Yang, P.; Lü, M.; Xü, D.; Yuan, D.; Chang, J.; Zhou, G.; Pan, M. *Appl. Phys. A* **2002**, *74*, 257-259.

17. (a) Furdyna, J. K. *J. Appl. Phys.* **1988**, *64*, R29-R64. (b) Wolf, S. A.; Awschalom, D. D.; Burhrman, R. A.; Daughton, J. M.; von Molnar, S.; Roukes, M. L.; Chtchelkanova, A. Y.; Treger, D. M. *Science* **2001**, *294*, 1488-1495.

18. See, for example: (a) Chouly, C.; Pouliquen, D.; Lucet, I.; Jeune, J. J.; Jallet, P. *J. Microencapsulation* **1996**, *13*, 245-255. (b) Tiefenauer, L. X.; Tschirky, A.; Kuhne, G.; Anders, R. Y. *Mag. Res. Imag.* **1996**, *14*, 391-402. (c) Jung, C. W.; Rogers, J. M.; Groman, E. V. *J. Magn. Magn. Mater.* **1999**, *194*, 210-216. (d) Bonnemain, B. *J. Drug. Target.* **1998**, *6*, 167-174. (e) Bjørnerud, A.; Johansson, L. O.; Ahlström, H. K. *Mag. Res. Med.* **2002**, *47*, 298-304.

19. Högemann, D.; Ntziachristos, V.; Josephson, L.; Weissleder, R. *Bioconjugate Chem.* **2002**, *13*, 116-121.

20. Mykhaylyk, O.; Cherchenko, A.; Ilkin, A.; Dudchenko, N.; Ruditsa, Novoseletz, M.; Zozulya, Y. *J. Magn. Magn. Mater.* **2001**, *225*, 241-247.

21. Högemann, D.; Josephson, L.; Weissleder, R.; Basilion, J. P. *Bioconjugate Chem.* **2000**, *11*, 941-946.

22. Dodd, C. H.; Hsu, H.-C.; Chu, W.-J.; Yang, P.; Zhang, H.-G.; Mountz, J. D. Jr.; Zimm, K.; Forder, J.; Josephson, L.; Weissleder, R.; Mountz, J. M.; Mountz, J. D. *J. Immun. Meth.* **2001**, *256*, 89-105.

23. Lewin, M.; Carlesso, N.; Tung, C. H.; Tang, X. W.; Cory, D.; Scadden, D. T.; Weissleder, R. *Nature Biotech.* **2000**, *18*, 410-414.

24. Josephson, L.; Perez, J. M.; Weissleder, R. *Angew. Chem. Int. Ed. Engl.* **2001**, *40*, 3204-3206.

25. Chemla, Y. R.; Grossman, H. L.; Poon, Y.; McDermott, R.; Stevens, R.; Apler, M. D.; Clarke, J. *PNAS* **2000**, *97*, 14268-14272.

26. Wilhelm, C.; Gazeau, F.; Roger, J.; Pons, J. N.; Salis, M. F.; Perzynski, R.; Bacri, J. C. *Phys. Rev. E* **2002**, *65*, 031404.

27. (a) Roger, J.; Pons, J. N.; Massart, R.; Halbreich, A.; Bacri, J. C. *Eur. J. Phys. AP* **1999**, *5*, 321-325. (b) Chatterjee, J.; Haik, Y.; Chen, C. J. *J. Magn. Magn. Mater.* **2001**, *225*, 21-26.

28. Dumitrascu, G.; Kumbhar, A.; Zhou, W.; Rosenzweig, Z. *IEEE Trans. Magn.* **2001**, *37*, 2932-2934.

29. (a) Raney, M.; *Ind. Eng. Chem.* **1921**, *32*, 1199-1203. (b) Rieke, R. D. *Acc. Chem. Res.* **1977**, *10*, 301-306.

30. (a) Teunissen, W.; Geus, J. W. *Stud. Surf. Sci. Catl.* **1999**, *121*, 185-190. (b) Gelman, F.; Avnir, D.; Schumann, H.; Blum, J. *J. Mol. Cat. A* **2001**, *171*, 191-194. (c) Leite, E. R.; Carreno, N. L. V.; Longo, E.; Valentini, A.; Probst, L. F. D. *J. Nanosci. Tech.* **2002**, *2*, 89-94. (d) Richards, R.; Geibel, G.; Hofstadt, W.; Bonnemann, H. *Adv. Orgnmet. Chem.* **2002**, *16*, 377-383. (e) Puntes, V. F.; Krishnan, K.; Alivisatos, A. P. *Top. Catl.* **2002**, *19*, 145-148.

31. Park, K.-W.; Choi, J.-H.; Kwon, B.-K.; Lee, S.-A.; Sung, Y.-E.; Ha, H.-Y.; Hong, S.-A.; Kim, H.; Wieckowski, A. *J. Phys. Chem. B* **2002**, *106*, 1869-1877.

32. Zhang, X.; Chan, K.-W. *J. Mater. Chem.* **2002**, *12*, 1203-1206.

33. Chen, H.; Qiu, X.; Zhu, W.; Hagenmuller, P. *Electrochem. Comm.* **2002**, *4*, 488-491.

34. Choi, S.; Manthiram, A. *J. Electrochem. Soc.* **2002**, *149*, A570-A573.

35. (a) Kim, S.-W.; Son, S. U.; Lee, S. S.; Hyeon, T.; Chung, Y. K. *Chem. Commun.* **2001**, 2212-2213. (b) Son, S. U.; Lee, S. I.; Chung, Y. K.; Kim, S.-W.; Hyeon, T. *Nano. Lett.* **2002**, *2*, 277-279. (c) Son, S. U.; Park, K. H.; Chung, Y. K. *Nano. Lett.* **2002**, *2*, 3983-3986.

36. (a) Lee, Y. T.; Park, J.; Choi, Y. S.; Ryu, H.; Lee, H. J. *J. Phys. Chem. B* **2002**, *106*, 7614-7618. (b) Kim, N. S.; Lee, Y. T.; Park, J.; Ryu, H.; Lee, H. J.; Choi, S. Y.; Choo, J. *J. Phys. Chem. B* **2002**, *106*, 9286-9290.

37. Li, Y.; Liu, J.; Wang, Y.; Wang, Z. L. *Chem. Mater.* **2001**, *13*, 1008-1014.

38. Peigney, A.; Coquay, P.; Flahaut, E.; Vandenberghe, R. E.; De Grave, E.; Laurent, C. *J. Phys. Chem.* **2001**, *105*, 9699-9710.

39. Cheung, C. L.; Kurtz, A.; Park, H.; Liber, C. M. *J. Phys. Chem. B* **2002**, *106*, 2429-2433.

40. Park, S.-J.; Kim, S.; Lee, S.; Khim, Z. G.; Char, K. Hyeon, T. *J. Am. Chem. Soc.* **2000**, *122*, 8581-8582.

41. (a) Matheson, L. J.; Tratnyek, P. G. *Environ. Sci. Technol.* **1994**, *28*, 2045-2053. (b) Orth, W. S.; Gillham, R. W. *Environ. Sci. Technol.* **1996**, *30*, 66-71. (c) Johnson, T. L.; Scherer, M. M.; Tratnyek, P. G. *Environ. Sci. Technol.* **1996**, *30*, 2634-2640.

42. (a) Devlin, J. F.; Klausen, J.; Schwarzenbach, R. P. *Environ. Sci.. Technol.* **1998**, *32*, 1941-1947. (b) Singh, J.; Comfort, S. D.; Shea, P. J. *Environ. Sci. Technol.* **1999**, *33*, 1488-1494. (c) Hofstetter, T. B.; Heijman, C. G.; Haderlein, S. B.; Holliger, C.; Schwarzenbach, R. P. *Environ. Sci.. Technol.* **1999**, *33*, 1479-1487.

43. Elliott, D. W.; Zhang, W.-X. *Environ. Sci. Technol.* **2001**, *35*, 4922-4926.

44. Ponder, S. M.; Darab, J. G.; Mallouk, T. E. *Environ. Sci. Technol.* **2000**, *34*, 2564-2569

45. Pillai, V.; Kumar, P.; Hou, N. J.; Ayyub, P.; Shah, D. O. *Adv. Coll. Inter. Sci.* **1995**, *55*, 241-269.

46. (a) Klabunde, K. J.; Zhang, D.; Glavee, G. N.; Sorensen, C. M. *Chem. Mater.* **1994**, *6*, 784-787. (b) O'Connor, C. J.; Seip, C.; Sangregorio, C.; Carpenter, E.; Li, S. C.; Irvin, G.; John, V. T. *Mol. Cryst. Liq. Cryst. Sci. Tech. A* **1999**, *334*, 1135-1154.

47. (a) Lin, X. M.; Sorensen, C. M.; Klabunde, K. J.; Hadjipanayis, G. C. *Langmuir* **1998**, *14*, 7140-7146. (b) Lin, X. M.; Sorensen, C. M.; Klabunde, K. J.; Hadjipanayis, G. C. *J. Mater. Res.* **1999**, *14*, 1542-1547.

48. (a) Chen, D.-H.; Wu, S.-H. *Chem. Mater.* **2000**, *12*, 1354-1360. (b) Chen, D.-H.; Hsieh, C.-H. *J. Mater. Chem.* **2002**, *12*, 2412-2415.

49. Sun, S.; Murray, C. B. *J. Appl. Phys.* **1999**, *85*, 4325-4330.

50. Nelson, J. A.; Bennett, L. H.; Wagner, M. J. *J. Am. Chem. Soc.* **2002**, *124*, 2979-2983

51. Burke, N. A. D.; Stöver, H. D. H.; Dawson, F. P.; Lavers, J. D.; Jain, P. K.; Oka, H. *IEEE Trans. Magn.* **2001**, *37*, 2660-2662.

52. Dinega, D. P.; Bawendi, M. G. *Angew. Chem. Int. Ed. Engl.* **1999**, *38*, 1788-1791

53. (a) Puntes, V. F.; Krishnan, K. M.; Alivisatos, A. P. *Science* **2001**, *291*, 2115-2117. (b) Ountes, V. F.; Zanchet, D.; Erdonmez, C. K.; Alivisatos, A. P. *J. Am. Chem. Soc.* **2002** *In Press.*

54. Osuna, J.; de Caro, D.; Amiens, C.; Chaudret, B.; Snoeck, E.; Respaud, M.; Broto, J.-M.; Fert, A. *J. Phys. Chem.* **1996**, *100*, 14571-14575.

55. Sidorov, S. N.; Bronstein, L. M.; Davankov, V. A.; Tsyurupa, M. P.; Solodovnikov, S. P.; Valetsky, P. M.; Wilder, E. A.; Spontak, R. J. *Chem. Mater.* **1999**, *11*, 3210-3215.

56. Rutnakornpituk, M.; Thompson, M. S.; Harris, L. A.; Farmer, K. E.; Esker, A. R.; Riffle, J. S.; Connoly, J.; St. Pierre, T. G. *Polymer* **2002**, *43*, 2337-2348.

57. (a) Bradley, J. S.; Tesche, B.; Busser, W.; Maase, M.; Reetz, M. T. *J. Am. Chem. Soc.* **2000**, *122*, 4631-4636. (b) Cordente, N.; Respaud, M.; Senocq, F.; Casanove, M.-J.; Aminens, C.; Chaudret, B. *Nano. Lett.* **2001**, *1*, 565-568.

58. de Caro, D.; Bradley, J. S. *Langmuir* **1997**, *13*, 3067-3069.

59. Ely, T. O.; Amiens, C.; Chaudret, B.; Snoeck, E.; Verelst, M.; Respaud, M.; Broto, J.-M. *Chem. Mater.* **1999**, *11*, 526-529.

60. (a) Suslick, K. S.; Choe, S. B.; Cichowlas, A.; Grinstaff, M. W.; *Nature* **1991**, *353*, 414-416. (b) Suslick, K. S.; Price, G. J. *Ann. Rev. Mater. Sci.* **1999**, *29*, 295-326.

61. (a) Suslick, K. S.; Fang, M.; Hyeon, T. *J. Am. Chem. Soc.* **1996**, *118*, 11960-11961. (b) de Caro, D.; Ely, T. O.; Mari, A.; Chaudret, B.; Snoeck, E.; respaud, M.; Broto, J.-M.; Fert, A. *Chem. Mater.* **1996**, *8*, 1987-1991.

62. Koltypin, Y.; Fernandez, A.; Rojas, T. C.; Campora, J.; Palma, P.; Prozorov, R.; Gedanken, A. *Chem. Mater.* **1999**, *11*, 1331-1335.

63. Schneider, J. J. *Adv. Mater.* **2001**, *13*, 529-533.

64. (a) Sun, S.; Murray, C. B.; Weller, D.; Folks, L.; Moser, A. *Science* **2000**, *287*, 1989-1992. (b) Sun, S.; Fullerton, E. E.; Weller, D.; Murray, C. B. *IEEE Trans. Mag.* **2001**, *37*, 1239-1243.

(c) Stahl, B.; Gajbhiye, N. S.; Wilde, G.; Kramer, D.; Ellrich, J.; Ghafari, M.; Hahn, H.; Gleiter, H.; Weißmüller, J.; Würschum, R.; Schlossmacher, P. *Adv. Mater.* **2002**, *14*, 24-27.

65. Kang, S.; Harrell, J. W.; Nikles, D. E. *Nano. Lett.* **2002** *In Press*

66. Chen, M.; Nikles, D. E. *Nano. Lett.* **2002**, *2*, 211-214.

67. Chen, M.; Nikles, D. E. *J. Appl. Phys.* **2002**, *91*, 8477-8479.

68. Lin, J.; Zhou, W.; Kumbhar, A.; Wiemann, J.; Fang, J.; Carpenter, E. E.; O'Connor, C. J. *J. Sol. Stat. Chem.* **2001**, *159*, 26-31.

69. Carpenter, E. E.; Kumbhar, A.; Wiemann, J. A.; Srikanth, H.; Wiggins, J.; Zhou, W.; O'Connor, C. J. *Mater. Sci. Eng.* **2000**, *A286*, 81-86.

70. Tanori, J.; Cuxin, N.; Petit, C.; Lisiecki, I.; Veillet, P.; Pileni, M. P. *Coll. Pol. Sci.* **1995**, *273*, 886-892.

71. Ely, T. O.; Pan, C.; Amiens, C.; Chaudret, B.; Dassenoy, F.; Lecante, P.; Casanove, M.-J.; Mosset, A.; Respaud, M.; Broto, J.-M. *J. Phys. Chem. B* **2000**, *104*, 695-702.

72. Shevchenko, E. V.; Talapin, D. V.; Rogach, A. L.; Mornowski, A.; Haase, M.; Weller, H. *J. Am. Chem. Soc.* **2002**, *124*, 11480-11485.

73. Fromen, M. C.; Serres, A.; Zitoun, D.; Respaud, M.; Amiens, C.; Chaudret, B.; Lecante, P.; Casanove, M. J. *J. Magn. Magn. Mater.* **2002**, *242-245*, 610-612.

74. Ono, K.; Kakefuda, Y.; Okuda, R.; Ishii, Y.; Kamimura, S.; Kitamura, A.; Oshima, M. *J. Appl. Phys.* **2002**, *91*, 8480-8482.

75. Park, J.-I.; Cheon, J. *J. Am. Chem. Soc.* **2001**, *123*, 5743-5746.

76. Sobal, N. S.; Hilgendorff, M.; Möhwald, H.; Giersig, M.; Spasova, M.; Radetic, T.; Farle, M. *Nano. Lett.* **2002**, *2*, 621-624.

77. Lu, P.; Teranishi, T.; Asakura, K.; Miyake, M.; Toshima, N. *J. Phys. Chem. B* **1999**, *103*, 9673-9682.

78. (a) Nunomura, T.; Teranishi, T.; Miyake, M.; Oki, A.; Yamada, S.; Toshima, N.; Hori, H. *J. Magn. Magn. Mater.* **1998**, *177*, 947-948. (b) Teranishi, T.; Miyake, M. *Chem. Mater.* **1999**, *11*, 3414-3416.

79. Legrand, J.; Taleb, A.; Gota, S.; Guittet, M.-J.; Petit, C. *Langmuir* **2002**, *18*, 4131-4137.

80. Duxin, N.; Brun, N.; Bonville, P.; Colliex, C.; Pileni, M. P. *J. Phys. Chem. B* **1997**, *101*, 8907-8913.

81. Nikitenko, S. I.; Koltypin, Y.; Palchik, O.; Felner, I.; Xu, X. N.; Gedanken, A. *Angew. Chem. Int. Ed. Engl.* **2001**, *40*, 4447-4449.

82. Koltypin, Y.; Cao, X.; Balogu, J.; Kaptas, D.; Gedanken, A. *J. Mater. Chem.* **1997**, *7*, 2453-2456.

83. Feltin, N.; Pileni, M. P. *Langmuir* **1997**, *13*, 3927-3933.

84. (a) López-Pérez, J. A.; López-Quintela, M. A.; Mira, J.; Rivas, J.; Charles, S. W. *J. Phys. Chem. B* **1997**, *101*, 8045-8047. (b) Zhou, Z. H.; Wang, J.; Liu, X.; Chan, H. S. O. *J. Mater. Chem.* **2001**, *11*, 1704-1709.

85. Jin, J.; Iyoda, T.; Cao, C.; Song, Y.; Jiang, L.; Li, T. J.; Zhu, D. B. *Angew. Chem. Int. Ed. Engl.* **2000**, *40*, 2135-2138.

86. (a) Merikhi, J.; Jungk, H.-O.; Feldmann, C. *J. Mater. Chem.* **2000**, *10*, 1311-1314. (b) Jungk, H.-O.; Feldmann, C. *J. Mater. Res.* **2000**, *15*, 2244-2248. (c) Feldmann, C.; Jungk, H.-O. *Angew. Chem. Int. Ed. Engl.* **2001**, *40*, 359-3362. (d) Pardoe, H.; Chua-anusorn, W.; St. Pierre, T. G.; Dobson, J. *J. Mag. Mag. Mater.* **2001**, *225*, 41-46.

87. (a) Nguyen, M. T.; Diaz, A. F. *Adv. Mater.* **1994**, *6*, 858-860. (b) Dante, S.; Hou, Z.; Risbud, S.; Stroeve, P. *Langmuir* **1999**, *15*, 2176-2182. (c) Dutta, A. K.; Jarero, G.; Zhang, L.; Stroeve, P. *Chem. Mater.* **2000**, *12*, 176-181.

88. Underhill, R. S.; Liu, G. *Chem. Mater.* **2000**, *12*, 2082-2091.

89. Strable, E.; Bulte, J. W. M.; Moskowitz, B.; Vivekanandan, K.; Allen, M.; Douglas, T. *Chem. Mater.* **2001**, *13*, 2201-2209.

90. Schneider, J. J.; Czap, N.; Hagen, J.; Engstler, J.; Ensling, J.; Gutlich, P.; Reinoehl, U.; Bertagnolli, H.; Luis, F.; deJongh, J. J.; Wark, M.; Grubert, G.; Hornyak, G. L.; Zanoni, R. *Chem. Eur. J.* **2000**, *6*, 4305-4321.

91. (a) del Monte, F.; Morales, M. P.; Levy, D.; Fernandez, A.; Ocaña, M.; Roig, A.; Molins, E.; O'Gradey, K.; Serna, C. J. *Langmuir* **1997**, *13*, 3627-3634. (b) Cannas, C.; Gatteschi, D. Musinu, A.; Piccaluga, G.; Sangregorio, C. *J. Phys. Chem. B* **1998**, *102*, 7721-7726. (c) Fröba, M.; Köhn, R.; Bouffaud, G.; Richard, O.; van Tendeloo, G. *Chem. Mater.* **1999**, *11*, 2858-2865. (d) Moreno, E. M.; Zayat, M.; Morales, M. P.; Serna, C. J.; Roig, A.; Levy, D. *Langmuir* **2002**, *18*, 4972-4978.

92. Rabelo, D.; Lima, E. C. D.; Reis, A. C.; Nunes, W. C.; Novak, M. A.; Grag, V. K.; Oliveira, A. C.; Morais, P. C. *Nano. Lett.* **2001**, *1*, 105-108.

93. Rockenberger, J.; Scher, E. C.; Alivisatos, A. P. *J. Am. Chem. Soc.* **1999**, *121*, 11595-11596.

94. Hyeon, T.; Lee, S. S.; Park, J.; Chung, Y.; Na, H. B. *J. Am. Chem. Soc.* **2001**, *123*, 12798-12801.

95. Tannenbaum, R.; Reich, S.; Flenniken, C. L.; Goldberg, E. P. *Adv. Mater.* **2002**, *14*, 1402-1405.

96. Sun, S.; Zeng, H. *J. Am. Chem. Soc.* **2002**, *124*, 8204-8205.

97. Pascal, C.; Pascal, J. L. ;Favier, F.; Moubtassim, M. L. E.; Payen, C. *Chem. Mater.* **1999**, *11*, 141-147.

98. Verelst, M.; Ely, T. O.; Aminens, C.; Snoeck, E.; Lecante, P.; Mosset, A.; Respaud, M.; Broto, J. M.; Chaudret, B. *Chem. Mater.* **1999**, *11*, 2702-2708.

99. Jeevanandam, P.; Koltypin, Yu.; Gedanken, A. *Nano. Lett.* **2001**, *1*, 263-266.

100. Carnes, C. L.; Stipp, J.; Klabunde, K. J.; Bonevich, J. *Langmuir* **2002**, *18*, 1352-1359.

101. Lee, G. H.; Huh, S. H.; Jeong, J. W.; Choi, B. J.; Kim, S. H.; Ri, H.-C. *J. Am. Chem. Soc.* **2002**, *In Press.*

102. Zhong, W.; Ding, W. P.; Jiang, Y. M.; Zhang, N.; Zhang, J. R.; Du, Y. W.; Yan, Q. J. *J. Am. Cer. Soc.* **1997**, *80*, 3258-3262.

103. (a) Pillai, V.; Shah, D. O. *J. Mag. Mag. Mater.* **1996**, *163*, 243-248. (b) Moumen, N.; Pileni, M. P. *Chem. Mater.* **1996**, *8*, 1128-1134. (c) Rondinone, A. J.; Samia, A. C. S.; Zhang, Z. J. *J. Phys. Chem. B* **2000**, *104*, 7919-7922. (d) Ammar, S.; Helfen, A.; Jouini, N.; Fiévet, F.; Rosenman, I.; Villain, F.; Molinié, P.; Danot, M. *J. Mater. Chem.* **2001**, *11*, 186-192. (e) Li, S.; Liu, L.; John, V. T.; O'Connor, C. J.; Harris, V. G. *IEEE Trans. Magn.* **2001**, *37*, 2350-2352. (f) Ahmed, S. R.; Kofinas, P. *Macromolecules* **2002**, *35*, 3338-3341.

104. (a) Xiong, G.; Mai, Z.; Xu, M.; Cui, S. Ni, Y.; Zhao, Z.; Wang, X.; Lu, L. *Chem. Mater.* **2001**, *13*, 1943-1945. (b) Vestal, C. R.; Zhang, Z. J. *Chem. Mater.* **2002**, *14*, 3817-3822.

105. Kahn, M. L.; Zhang, Z. J. *App. Phys. Lett.* **2001**, *78*, 3651-3653.

106. Mathur, S.; Shen, H.; Leceref, N.; Kjekshus, A.; Fjellvåg, H.; Goya, G. F. *Adv. Mater.* **2002**, *14*, 1405-1409.

107. (a) Zhang, Z. J.; Wang, Z. L.; Chakoumakos, B. C.; Yin, J. S. *J. Am. Chem. Soc.* **1998**, *120*, 1800-1804. (b) Liu, C.; Zou, B.; Rondinone, A. J.; Zhang, Z. J. *J. Phys. Chem. B* **2000**, *104*, 1141-1145. (c) Rondinone, A. J.; Liu, C.; Zhang, Z. J. *J.Phys. Chem. B* **2001**, *105*, 7967-7971. (d) Liu, C.; Zhang, Z. J. *Chem. Mater.* **2001**, *13*, 2092-2096.

108. (a) Li, L.; Li, G.; Smith, R. L. Jr.; Inomata, H. *Chem. Mater.* **2000**, *12*, 3705-3714. (b) Chen, D.-H.; He, X.-R. *Mat. Res. Bull.* **2001**, *36*, 1369-1377.

109. Albuquerque, A. S.; Ardisson, J. D.; Macedo, W. A. A.; Alves, M. C. M. *J. Appl. Phys.* **2000**, *87*, 4352-4357.

110. Chen, D.-H.; Chen, Y.-Y. *Mater. Res. Bull.* **2002**, *37*, 801-810.

111. Hochepied, J. F.; Bonville, P.; Pileni, M. P. *J. Phys. Chem. B* **2000**, *104*, 905-912.

112. Meyer, F.; Hempelmann, R.; Mathur, S.; Veith, M. *J. Mater. Chem.* **1999**, *9*, 1755-1763.

113. Tartaj, P.; Tartaj, J. *Chem. Mater.* **2002**, *14*, 536-541.

114. (a) Yi, T.; Gao, S.; Qi, X.; Zhu, Y.; Cheng, F.; Ma, B.; Huang, Y.; Liao, C.; Yan, C. *J. Phys. Chem. Sol.* **2000**, *61*, 1407-1413. (b) Tan, R.; Zhu, Y.; Feng, J.; Ji, S.; Cao, L. *J. All. Comp.* **2002**, *337*, 282-288.

115. Vaqueiro, P.; Crosnier-Lopez, M. P.; López-Quintela, M. A. *J. Solid State Chem.* **1996**, *126*, 161-168.

116. Vaqueiro, P.; López-Quintela, M. A.; Rivas, J. *J. Mater. Chem.* **1997**, *7*, 501-504.

117. Kataby, G.; Prozorov, T.; Koltypin, Y.; Cohen, H.; Sukenik, C. N.; Ulman, A.; Gedanken, A. *Langmuir* **1997**, *13*, 6151-6158.

118. (a) Liu, A.; Xu, Z. *Langmuir* **1995**, *11*, 4167-4622. (b) Kataby, G.; Ulman, A.; Cojocaru, M.; Gedanken, A. *J. Mater. Chem.* **1999**, *9*, 1501-1506. (c) Kataby, G.; Cojocaru, M.; Prozorov, R.; Gedanken, A. *Langmuir* **1999**, *15*, 1703-1708.

119. Kataby, G.; Ulman, A.; Prozorov, R.; Gedanken, A. *Langmuir* **1998**, *14*, 1512-1515.

120. Yee, C.; Kataby, G.; Ulman, A.; Prozorov, T.; White, H.; King, A. Rafailovich, M.; Sokolov, J.; Gedanken, A. *Langmuir* **1999**, *15*, 7111-7115.

121. Shafi, K. V. P. M.; Ulman, A.; Dayl, A.; Yan, X.; Yang, N.-L.; Estournès, C.; Fournès, L.; Wattiaux, A.; White, H.; Rafailovich, M. *Chem. Mater.* **2002**, *14*, 1778-1787.

122. Shafi, K. V. P. M.; Ulman, A.; Yan, X.; Yang, N.-L.; Estournès, C.; White, H.; Rafailovich, M. *Langmuir* **2001**, *17*, 5093-5097.

123. Boal, A. K.; Das, K.; Gray, M.; Rotello, V. M. *Chem. Mater.* **2002**, *14*, 2628-2636.

124. Turro, N. J.; Lakshminarasimhan, P. H.; Jockusch, S.; O'Brien, S. P.; Grancharov, S. G.; Redl, F. X. *Nano. Lett.* **2002**, *2*, 325-328.

125. Moore, A.; Marecos, E.; Bogdanov, A.; Weissleder, R. *Radiology* **2000**, *214*, 568-574

126. Grasset, F.; Mornet, S.; Demourgues, A.; Portier, J.; Bonnet, J.; Vekris, A.; Duguet, E. *J. Magn. Magn. Mater.* **2001**, *234*, 409-418.

127. (a) Chatterjee, J.; Haik, Y.; Chan, C.-J. *Colloid. Polym. Sci.* **2001**, *279*, 1073-1081. (b) Lind, K.; Kresse, M.; Muller, R. H. *Electrophoresis* **2001**, *22*, 3514-3521.

128. Kim, D. K.; Zhang, Y.; Voit, W.; Rao, K. V.; Kehr, J.; Bjelke, B.; Muhammed, M. *Scripta Mater.* **2001**, *44*, 1713-1717.

129. Dickson, D. P. E. *J. Magn. Magn. Mater.* **1999**, *203*, 46-49.

130. Blakemore, R. *Science* **1975**, *190*, 377-379.

131. Matsunaga, T.; Takeyama, H. *Supramolecular Sci.* **1998**, *5*, 391-394.

132. (a) De Cuyper, M.; Joniau, M. *Eur. Biophys. J.* **1988**, *15*, 311-319. (b) De Cuyper, M.; Joniau, M. *Langmuir* **1991**, *7*, 647-652.

133. Sangregorio, C.; Wiemann, J. K.; O'Connor, C. J.; Rosenzweig, Z. *J. Appl. Phys.* **1999**, *85*, 5699-5701.

134. Roberts, D.; Zhu, W. L.; Frommen, C. M.; Rosenzweig, Z. *J. Appl. Phys.* **2000**, *87*, 6208-6210.

135. Chasteen, N. D.; Harrison, P. M. *J. Str. Bio.* **1999**, *126*, 182-194.

136. (a) Meldrum, F. C.; Heywood, B. R.; Mann, S. *Science* **1992**, *257*, 522-523. (b) Dickson, D. P. E.; Walton, S. A.; Mann, S.; Wong, K. *Nanostr. Mater.* **1997**, *9*, 595-598.

137. Warne, B.; Kasyutich, O. I.; Mayes, E. L.; Wiggins, J. A. L.; Wong, K. K. W. *IEEE Trans. Magn.* **2000**, *36*, 3009-3011.

138. Douglas, T.; Stark, V. T. *Inorg. Chem.* **2000**, *39*, 1828-1830.

139. (a) Douglas, T.; Young, M. *Nature* **1998**, *393*, 152-155. (b) Douglas, T.; Young, M. *Adv. Mater.* **1999**, *11*, 679-681.

140. Shenton, W.; Douglas, T.; Young, M.; Stubbs, G.; Mann, S. *Adv. Mater.* **1999**, *11*, 253-256.

141. Douglas, T.; Strable, E.; Willits, D.; Aitouchen, A.; Libera, M.; Young, M. *Adv. Mater.* **2002**, *14*, 415-418.

142. (a) Ladizhansky, V.; Hodes, G.; Vega, S. *J. Phys. Chem. B* **1998**, *102*, 8505-8509. (b) Counio, G.; Gacoin, T.; Boilot, J. P. *J. Phys. Chem. B* **1998**, *102*, 5257-5260.

143. Levy, L.; Hochepied, J. F.; Pileni, M. P. *J. Phys. Chem.* **1996**, *100*, 18322-18326.

144. Levy, L.; Ingert, D.; Feltin, N.; Briois, V.; Pileni, M. P. *Langmuir* **2002**, *18*, 1490-1493

145. Malik, M. A.; O'Brien, P.; Revaprasadu, N. *J. Mater. Chem.* **2001**, *11*, 2382-2386.

146. Ynag, P.; Lü, M.; Xü, D.; Yuan, D.; Zhou, G. *App. Phys. A* **2001**, *73*, 455-458.

147. Mikulec, F. V.; Kuno, M.; Bennati, M.; Hall, D. A.; Griffin, R. G.; Bawendi, M. G. *J. Am. Chem. Soc.* **2000**, *122*, 2532-2540.

148. Radovanovic, P. V.; Gamelin, D. R. *J. Am. Chem. Soc.* **2001**, *132*, 12207-12214.

149. Hanif, K. M.; Meulenberg, R. W.; Strouse, G. F. *J. Am. Chem. Soc.* **2002**, *124*, 11495-11502.

150. Moulik, S. P.; De, G. C.; Panda, A. K.; Bhowmik, B. B.; Das, A. R. *Langmuir* **1999**, *15*, 8361-8367.

151. Vaucher, S.; Li, M.; Mann, S. *Angew. Chem. Int. Ed. Engl.* **2000**, *39*, 1793-1796.

152. Vaucher, S.; Fielden, J.; Li, M.; Dujardin, E.; Mann, S. *Nano. Lett.* **2002**, *2*, 225-229.

153. Roth, M.; Hempelmann, R. *Chem. Mater.* **1998**, *10*, 78-82.

154. Agnoli, F.; Zhou, W. L.; O'Connor, C. J. *Adv. Mater.* **2001**, *13*, 1697-1699.

155. Kahn, O. *Molecular Magnetism*, VCH Publishers, Inc.: New York, 1993.

156. (a) Christou, G.; Gatteschi, D.; Hendrickson, D. N.; Sessoli, R. *MRS Bulletin* **2000**, *25*, 66-71. (b) Gatteschi, D.; *J. Alloy. Comp.* **2001**, *317-318*, 8-12.

157. Sessoli, R.; Gatteschi, D.; Caneschi, A.; Novak, M. A. *Nature* **1993**, *365*, 141-143.

158. It should be noted that, while an enormous varity of transition metal clusters are known and many are thought to be likely to SMM candidates, this papers describes the *first observation* of SMM behavior.

159. (a) Caneschi, A.; Gatteschi, D.; Sessoli, R.; Barra, A. L.; Brunel, L. C..; Guillot, M. *J. Am. Chem. Soc.* **1991**, *113*, 5873-5874. (b) Sessoli, R.; Tsai, H.-L.; Schake, A. R.; Wang, S.; Vincent, J. B.; Folting, K.; Gatteschi, D.; Christou, G.; Hendrickson, D. N. *J. Am. Chem. Soc.* **1993**, *115*, 1804-1816. (c) Barra, A. L.; Caneschi, A.; Gatteschi, D.; Sessoli, R. *J. Am. Chem. Soc.* **1995**, *117*, 8855-8856. (d) Kuroda-Sowa, T.; Lam, M.; Rheingold, A. L.; Frommen, C.; Reiff, W. M.; Nakano, M.; Yoo, J.; Maniero, A. L.; Brunel, L.-C.; Christou, G.; Hendrickson, D. N. *Inorg. Chem.* **2001**, *40*, 6469-6480. (e) Boskovic, C.; Brechin, E. K.; Streib, W. E.; Folting, K.; Bollinger, J. C.; Hendrickson, D. N.; Christou, G. *J. Am. Chem. Soc.* **2002**, *124*, 3725-3736.

160. Aubin, S. M. J.; Wemple, M. W.; Adams, D. M.; Tsai, H.-L.; Christou, G.; Hendrickson, D. N. *J. Am. Chem. Soc.* **1996**, *118*, 7746-7754.

161. Berseth, P. A.; Sokol, J. J.; Shores, M. P.; Heinrich, J. J.; Long, J. R. *J. Am. Chem. Soc.* **2000**, *122*, 9655-9662.

162. Rogez, G.; Parsons, S.; Paulsen, C.; Villar, V.; Mallah, T. *Inorg. Chem.* **2001**, *40*, 3836-3837.

163. Oshio, H.; Hoshino, N.; Ito, T. *J. Am. Chem. Soc.* **2000**, *122*, 12602-12603.

2

Semiconductor Nanoparticles

Synthesis, properties, and integration into polymers for the generation of novel composite materials

Habib Skaff and Todd Emrick
Department of Polymer Science & Engineering, University of Massachusetts, Conte Center for Polymer Research, 120 Governors Drive, Amherst, MA 01003

2.1.   INTRODUCTION

Semiconductors are key components of devices used everyday, including computers, light emitting diodes, sensors, etc. Semiconductors are a unique class of materials in that they can assume characteristic properties of both metals and insulators, depending on conditions that determine the electronic nature of the valence and conduction bands. In the ground state, the valence band is completely filled and separated from the conduction band by a narrow band gap (E_g). When sufficient energy is applied to a semiconductor, it becomes conducting by excitation of electrons from the valence band into the conduction band. This excitation process leaves holes in the valence band, and thus creates "electron-hole pairs" (EHPs). When these EHPs are in intimate contact (i.e., the electrons and holes have not dissociated) they are termed "excitons." In the presence of an external electric field, the electron and the hole will migrate (in opposite directions) in the conduction and valence bands, respectively (Figure 2.1).[1,2]
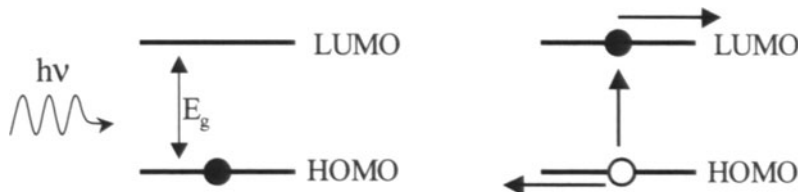
FIGURE 2.1. Formation of "electron-hole pair" induced by an excitation from an external energy source.

Studies focused on reducing the size of semiconductors to the nanometer regime have led to a fascinating class of novel materials that possess characteristics between the classic bulk and molecular descriptions, and that exhibit properties of quantum confinement. These materials are referred to as nanoparticles (or nanocrystals), or "quantum dots." Quantum confinement is observed in nanoparticles with radii smaller than the average distance between the electron and the hole, known as the bulk exciton Bohr radius (e.g., approximately 11 nm in the case of CdSe nanocrystals). The electronic states of spherical nanocrystals can be modeled by considering a particle in a sphere, where the electron and the hole are confined to a relatively small area. In this model, the charge carrying electrons and holes are confined by a potential that is infinite at the nanocrystal surface. As a result, semiconductors of nanoscopic dimensions show larger band gaps relative to the bulk material and have discrete excitable states (Figure 2.2).[3-14]
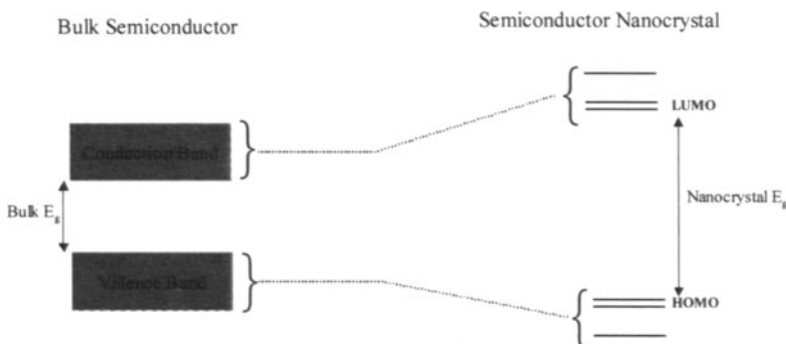
FIGURE 2.2. Comparison of the electronic states in a bulk semiconductor *vs.* a nanoparticle-based semiconductor (for a description in greater detail, see for example reference 16).

Band gap energies of nanoscopic semiconductors are strongly size-dependent, such that as the radius of the nanocrystal decreases, the band gap increases (Figure 2.3). This is a very exciting feature of semiconductor nanoparticles, as it allows one to tune the emission wavelength of the nanoparticle by adjusting its size within the quantum-confined regime.[7,15-22] This dramatic size dependent property affords a technological significance to semiconductor nanocrystals that will be discussed herein.
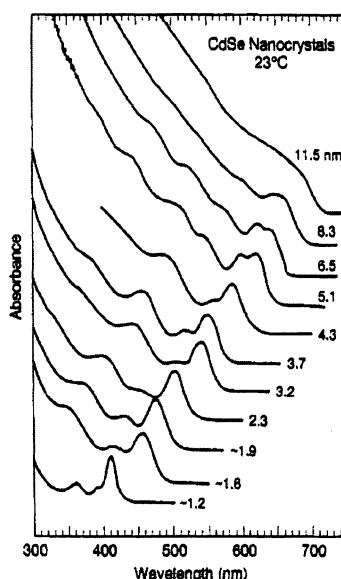
FIGURE 2.3. Size dependence of CdSe nanocrystals due to quantum confinement. As the nanocrystal diameter increases the bandgap decreases. Reprinted figure with permission from Brust, L. *J. Phys. Chem. Solids* **1998**, *59*, 459-465. Copyright 1998.

Semiconductor nanocrystals, or quantum dots, have been reported from a variety of compositions, including CdSe, CdS, Si, GaAs, PbSe, and InP. Excitation of an electron from the highest occupied molecular orbital (HOMO) to the lowest unoccupied molecular orbital (LUMO) results in rapidly moving charge carriers. These sp^3 hybridized systems experience little lattice distortion upon exciton formation (i.e., the Frank-Condon factors are small),[16] and the small lattice distortions preclude the formation of defects and allow the charge carriers to move fluidly through the nanocrystal. In addition, radiationless internal conversion, or the conversion of electronic energy into heat, is slow. The efficiency of these factors, coupled with the quantum confinement, affords the observed luminescence in nanoparticles that is not found in bulk semiconductors. In practice, however, semiconductor nanoparticles are far from ideal materials, as their luminescence intensity is reduced by internal and surface defects that emanate from the synthetic preparations. These defects act as electron and hole traps, leading to non-radiative emission and reduced luminescence. Typical solution quantum yields for high quality, organically passivated semiconductor nanoparticles prepared by methods discussed below are in the range of 5-15%.

This review will focus on the synthesis of semiconductor nanoparticles, especially cadmium selenide, from early procedures to currently used techniques. The integration of these nanoparticles into polymers will be described, evolving from simple techniques such as blending the two

components, to the more sophisticated approaches of chain-end attachment, radial growth, and directed assembly. The use of polymers offers great potential in manipulating the spatial arrangement and properties of nanoparticles, where the interplay between the polymeric and nanoparticle components, in terms of surface and interfacial interaction, is key.

2.2.   NANOPARTICLE SYNTHESIS

The preparation of nanoscale structures and devices can be accomplished through "bottom-up" or "top-down" methods. In the bottom-up approach, small building blocks are assembled into larger structures; examples of this approach include chemical synthesis,[23,24] laser-induced assembly (i.e., laser-trapping),[25,26] self-assembly,[27] colloidal aggregation,[28] and 2-photon confocal processing.[29,30] In the top-down approach, large objects are modified to give smaller features, for example by lithographic techniques[31] (e.g.., UV, electron or ion-beam, scanning probe, optical near field), film deposition and growth,[32] laser-beam processing,[26,33] and mechanical techniques (e.g., machining, grinding, and polishing).[34] While bottom-up techniques can provide access to extremely fine features and state-of-the-art structures, the complexities associated with these techniques still limit large-scale production. Ultimate physical limits may also be encountered, such as perturbations (e.g., molecular vibrations) that disrupt the smallest of nanoscopic structures. Many top-down techniques have been developed on the industrial scale, and optimization of these processes has produced well-defined structures on scales previously thought unreachable. However, these techniques have an inherent size limit that is larger than that of bottom-up techniques. Thus, to produce devices with extraordinarily fine detail on the molecular level, self-assembly and directed assembly approaches must become integrated into the industrial process. It is expected that nanoparticles prepared by chemical synthesis and manipulated by polymeric materials and self-assembly will play a critical role in this effort.

2.2.1. ROOM TEMPERATURE SYNTHETIC METHODS

Synthetic procedures for nanoparticle preparations have been performed by both bottom-up and top-down approaches, but the bottom-up approach has become favored, as steady improvement in synthetic protocols over the past 20 years have resulted in particle syntheses that are highly controllable. CdSe nanocrystal chemistry has been especially active due to the extraordinary properties of the particles that have become better understood and refined through enhanced syntheses.

Seminal nanoparticle synthetic work by Brus and coworkers at Bell Laboratories focused on room temperature nanocrystal preparations using inverse micellar solutions, with an organic solvent (e.g., heptane) as the major phase, and water as the minor phase. Typical procedures involved rapid stirring of surfactants, such as bis(2-ethylhexyl) sulfosuccinate, at room temperature in heptane/water to afford optically clear microemulsions, followed by introduction of an aqueous $Cd(ClO_4)_2$ solution, then rapid injection of a solution of $(TMS)_2Se$ in heptane. These solutions develop distinctive colors that depend on the size of the nanocrystals formed. Reports on this inverse micellar approach indicate that nanoparticle size could be controlled over the range of ca. 1.7 nm to 4.5 nm by simply adjusting the micelle size, dictated by the water-to-surfactant ratio.[35,36]

This demonstrated size control represented a major advance in the field, due to the critically size-dependent properties of nanoparticles. However, these were difficult materials to isolate, as they aggregated upon drying, and could not be dissolved subsequently. Henglein and coworkers addressed this problem by precipitating the CdSe nanoparticles in the presence of polymeric hexametaphosphate.[37] Brus and coworkers used an *in situ* modification of the nanocrystal surface, where the micellar-based nanocrystal synthesis was followed by a second addition of $Cd(ClO_4)_2$, and finally Ph(TMS)Se. This monofunctional selenium reagent acts as an end-capper, and provides the nanocrystal with a phenyl periphery. The phenyl periphery effectively functions to prevent aggregation during isolation, and provides longer-term solubility of the nanocrystals. Methods that give isolable, soluble, and stable nanoparticles are critical for advancing nanoparticle-based technologies, and have thus been the subject of much subsequent work.

2.2.2. HIGH TEMPERATURE ORGANOMETALLIC SYNTHESES

A critical target in nanoparticle research has centered on the development of preparative methods that afford highly crystalline nanoparticles with very low size dispersity. The early synthetic procedures suffered from relatively broad size distributions due to unfavorable kinetics and distribution in the micelle size. While the use of fractional precipitation techniques can significantly lower the size dispersity, this also reduces the overall yield, and does not address the problems of low crystallinity due to structural defects.

Recent synthetic advances based on the reactions of organometallic precursors at high temperatures have given CdSe, CdS, and CdTe nanocrystals with narrow size distributions.[38] Key to these syntheses is the separation of the nucleation and growth steps. By using a hot coordinating

solvent/surfactant, i.e. tri-*n*-octylphosphine oxide (TOPO), and reactive organometallic precursors, nanocrystal nucleation occurs in a fast burst. The uniform growth rate of the formed nuclei leads to a fairly narrow size distribution in the product (ca. 5 - 10%). This nucleation and growth process can be likened conceptually to "living" polymerization methods, in that all the propagating species (in this case the CdSe nuclei) form at nearly the same time, then grow at the same rate. The role of TOPO is similar to that of the surfactants in the earlier synthetic approaches; TOPO forms an inverse micellar environment by virtue of its polar phosphine oxide head and nonpolar alkyl tails. In addition, TOPO stabilizes the nanocrystals by coordination to surface cadmium atoms, concomitantly preventing aggregation and providing solubility in organic media.

CdSe nanocrystal preparations that remain in common use today consist of rapidly injecting a tri-*n*-octyl phosphine (TOP) solution of $Cd(CH_3)_2$ and $(TMS)_2Se$ (or Se(0) powder) at 300 °C in an inert atmosphere (Scheme 2.1). This injection results in rapid nucleation, followed by particle growth, the rate of which can be controlled by adjusting temperature. Growth is terminated at the desired nanocrystal size by simply removing the reaction vessel from the heat. The high temperature synthesis not only allows for a narrow size distribution but also anneals the nanocrystals, affording fewer defects and thus high crystallinity. Repeated precipitation and washing of the nanocrystals (e.g., with methanol) removes the excess TOPO to afford stable, soluble, highly crystalline quantum dots with low size distribution. Similar preparative methods are used for CdS and CdTe nanocrystals, by substitution of the appropriate organometallic precursor for $(TMS)_2Se$.
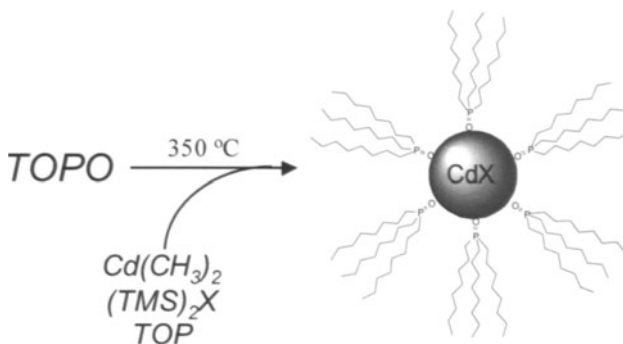
SCHEME 2.1. High temperature organometallic preparative methods are used for the growth of high quality CdX (X = S, Se, Te) nanocrystals.

By these high temperature methods, nanocrystals can be made with low polydispersity, high crystallinity, and a low number of internal defects. These nanocrystals, while being highly luminescent, have relatively low

quantum yields, typically in the range of 5 to 15%. The low quantum yield is attributed to surface defects, or "dangling bonds", that act as charge carrier traps and ultimately non-radiative recombination of the electron and hole. The groups of Alivisatos and Bawendi have addressed this surface defect problem by developing inorganic passivation procedures.[39,40] This works best by growth of a larger bandgap semiconductor material, such as ZnS or CdS, to overcoat the CdSe nanocrystal surface (Figure 2.4). The commensurate nature (i.e., low lattice mismatch) of both ZnS and CdS with CdSe is important in this overcoating process, as significant mismatch would lead to lattice stress at the interface. This core/shell architecture eliminates the surface "dangling bonds" and protects the nanocrystal from oxidation. It is important to note that the core is almost wholly responsible for the absorption and emission characteristics of these systems, and the shell acts only to passivate the surface.
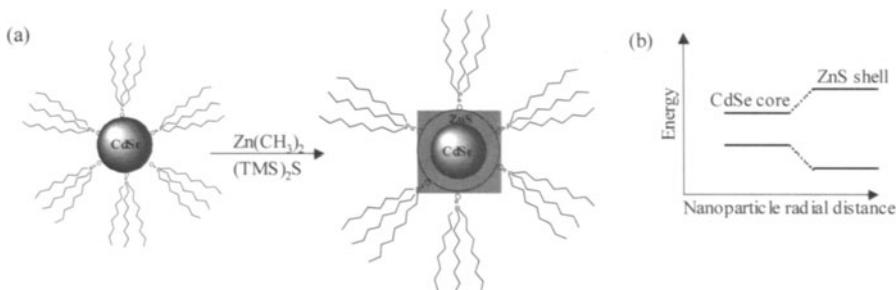
FIGURE 2.4. (a) Synthesis of CdSe/ZnS core/shell nanocrystals; (b) schematic band diagram of core/shell nanocrystals showing the larger bandgap ZnS shell overcoating the CdSe core.

In an early and still often-used procedure for preparing core-shell CdSe-ZnS nanoparticles, the quantum dot core is prepared as described earlier, followed by slow addition of the zinc or cadmium sources (e.g., $Zn(CH_3)_2$ or $Cd(CH_3)_2$) and $(TMS)_2S$ with TOP between 100-150 °C. Relatively low temperatures must maintained to avoid nucleation of new nanocrystals, which would increase the size distribution of the sample. In essence, the cores act as seeds onto which the shell material nucleates. This process affords materials with quantum yields in the range of 50 to 80%, a massive increase over the TOPO-CdSe materials.

These core-shell systems can be further functionalized with a siloxane shell that provides the ability to subsequently alter the encapsulating environment around the nanoparticle. Attachment of charged moieties to the nanoparticle periphery provides sufficient hydrophilicity for biological studies.[41] Nanoparticles that are water-soluble and well-passivated in this core-shell structure are under investigation as luminescent tags for identification of biologically active molecules and diseases (e.g., cancer cells). Other methods to achieve water-soluble CdSe nanoparticles also give

nanoparticles relevant to biological applications. For example, Thompson and coworkers functionalized CdSe/ZnS core/shell nanocrystals with dithiothreitol (DTT), and subsequently attached oligonucleotides to the nanoparticle periphery.[42] Two oligonucleotide sequences were used for the fluorescence *in situ* hybridization (FISH) studies that followed. One sequence was "Y-specific" (i.e., complimentary sequence is present on the human Y chromosome), and the other sequence was random. The FISH experiments showed that nanocrystals functionalized with the "Y-specific" sequence attached exclusively to the complimentary base sequence of the Y chromosome derived oligonucleotide, while the random sequence functionalized nanocrystals showed no such attachment. Further advances in the area of stable, water-soluble, functionalizable nanoparticles will be very useful in extending these studies towards multiple biological targets.

While the organometallic preparations described above produce high quality nanocrystals with high quantum yields, the pyrophoric and toxic nature of the precursors has to some extent limited their accessibility. Recent reports that employ less toxic and more stable cadmium precursors, such as CdO, $CdCO_3$, and $Cd(OAc)_2$ are still able to provide high quality CdSe nanocrystals. While the use of these precursors does require high temperatures, the chemicals are much easier to handle, and in some cases these new procedures afford nanocrystals with quantum yields greater than 50%, without an inorganic shell. The authors attribute the high nanocrystal quantum yields that result from these procedures to a combination of factors including the passivation of the nanocrystal surface by aliphatic amines used in the process, and control over the cadmium to selenium ratios in either direction (the emission bright point increased as the Cd:Se ratio deviated from 1:1).[43-46]

Nanocrystals of III-V semiconductors such as GaAs and InP have also attracted a great deal of interest. These materials differ from the II-VI semiconductors in that they have less ionic lattices, larger dielectric constants, larger bulk exciton diameters, smaller effective masses, and weaker phonon coupling. The larger bulk exciton diameter and dielectric constant allows for greater electron-hole delocalization, because the Coulombic attraction between the electron and the hole is more completely shielded. As with II-VI nanocrystals, high temperature organometallic methods has thus far proven most successful for the preparation of high quality III-V semiconductor nanocrystals.[47]

Alivisatos and coworkers reported high temperature syntheses of InP and GaAs nanocrystals. For the synthesis of InP nanocrystals, $InCl_3$ and TOPO are heated in an inert atmosphere at 100 °C for 12 hours. Neat $P(Si(CH_3)_3)_3$ is then added, and the mixture heated to 265 °C for 6 days in order to fully anneal the nanocrystals, then cooled and quenched with dodecylamine as the

surface capping agent. The nanocrystals can be precipitated into non-solvents such as methanol, and readily redissolved in organic solvents. Nanocrystals prepared by this method are highly crystalline with have tunable bandgaps and diameters of 2–5 nm.[48]

The synthesis of GaAs nanocrystals follows a similar synthetic procedure.[49] Here, a quinoline solution containing $As(Si(CH_3)_3)_3$ is added to $GaCl_3$, also dissolved in quinoline, and this mixture is heated to 240 °C for three days. These GaAs nanocrystal powders could be annealed at 450 °C under vacuum in order to improve the crystallinity of the sample, but this annealing leads to insoluble particles. Similar to the InP case, the GaAs nanocrystal size distribution is relatively broad due to unfavorable kinetics. Nevertheless, these are highly crystalline materials, and future synthetic improvements will drive these materials towards their full potential in device applications.

2.3. SEMICONDUCTOR NANOPARTICLE/POLYMER COMPOSITES

It is clear that the organic ligand environment used to encapsulate and passivate semiconductor nanoparticles is for future developments in the field, as the ligands establish the solution properties of the nanoparticles, aid in their luminescence by quenching surface defects, and maintain their nanoscopic integrity by preventing aggregation.[20,48,50,51] One of the most promising topics in organic-inorganic hybrid materials is found in attempts to integrate semiconductor nanocrystals and polymers. The unique properties of polymers, including their thermal behavior, processability, and ability to assemble into ordered structures, offer the potential for compatibilizing nanocrystals, directing their assembly, and providing a mechanism for charge transport. Confirmation of theoretical predictions of the spatial distribution of nanoparticles within polymer hosts[52] will to some extent depend on the interactions between the ligand periphery and the polymer environment. Indeed, polymer-nanocrystal composite materials are already finding applications ranging from electronically active materials to the biological sciences.[41,42,53-60] In the following sections, we provide a non-exhaustive review of some recent advances in this area.

Four major approaches designed to integrate semiconductor nanoparticles into polymer matrices have been established, including 1) simple mixing of nanoparticles with functional or non-functional polymers, 2) growth of nanoparticles in polymers from organometallic precursors, 3) chain-end attachment of polymers to nanoparticle surfaces, either by mixing end-functional polymers with the nanoparticles, or by growing polymers radially

outward from the nanoparticle surface, and 4) assembling nanoparticles in polymer templates, where the structure of the template dictates the assembly of the nanoparticles. Each of these approaches carries certain advantages that best apply to the particular target.

2.3.1. POLYMER-NANOPARTICLE BLENDS

While mixing polymer materials and nanoparticles is the simplest method of composite formation, it is usually accompanied by the significant nanoparticle aggregation problems. The disparate nature of polymers and nanoparticles generally precludes homogenous particle dispersion, as the entropic gain associated with random dispersion is overwhelmed by the enthalpic penalty. Phase separation in these materials destroys the nanoscopic integrity of the nanoparticle, and leads to a reduction in properties of the polymer material due to severe interruption of chain-entanglement. Several methods have been considered to overcome, or at least control to some degree, the phase separation that occurs during this polymer-nanoparticle mixing process.

Alivisatos and coworkers have explored mixtures of CdSe nanoparticles and poly(3-hexylthiophene) (P3HT), a p-type conducting polymer, for photovoltaic applications.[57,58,61] In order to avoid gross aggregation, P3HT and CdSe were dissolved in a mixture of chloroform and pyridine, good solvents for the polymer and the nanoparticle, respectively. Composite films were obtained by spin-casting these solutions to afford CdSe-based composites with particle-particle contacts that are surmised to function as a percolating network for charge transport (Figure 2.5). Photovoltaic cells generated from these materials exhibited an external quantum efficiency of 54%, and a monochromatic power conversion efficiency of 6.9%. While these efficiencies are lower than those of pure inorganic solar cells (e.g., silicon, CdSe, etc.) they offer significantly easier processing. For example, conventional solar cell fabrication involves high temperatures (400 to 1400 °C), ultrahigh vacuum, and many lithographic steps, but polymer/semiconductor nanocrystal solar cells offer a lower cost alternative, as fabrication is performed at room temperature in significantly fewer steps.

The polymer structure can be tuned to better match the structure of conventional, aliphatic chain covered CdSe nanoparticles. For example, Bawendi and coworkers blended poly(laurylmethacrylate) with (CdSe)ZnS core-shell nanocrystals encapsulated with TOP.[59] The aliphatic nature of the lauryl (dodecyl ester) side chains of this polymer serve to solubilize the nanoparticles by interaction with their aliphatic (TOP) organic corona. The benefit of this compatibilization is manifest in the optical clarity of the composites obtained upon blending, which suggests the likelihood of

unaggregated nanocrystals in the composite material. Solid-state quantum yields of these composites ranged from 22% to 44 %.
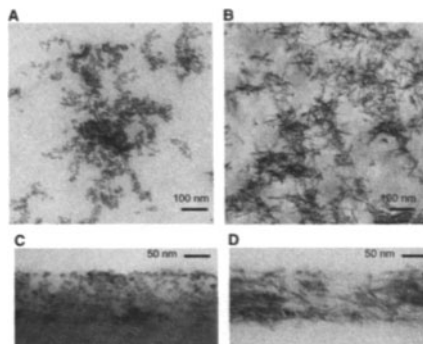
FIGURE 2.5. TEM image of CdSe-polythiophene composite material cast form a binary solvent system. Images A and B are thin films of 7 nm spheres and 7 x 60 nm rods, respectively, in poly-3-hexylthiophene; images C and D are cross-sections of 10 nm spheres and 7 x 60 nm rods, respectively, in poly-3-hexylthiophene. Reprinted figure with permission from Huynh, W. U.; Dittmer, J. J.; Alivisatos, A. P. *Science* **2002**, *295*, 2425-2427. Copyright 2002 American Association for the Advancement of Science.

Schrock and coworkers reported a different approach, where functional polymers were prepared with pendant coordination sites capable of nanocrystal passivation. [62] Specifically, monomeric norbornene derivatives were prepared with pendant phosphines or phosphine oxides, and these were copolymerized with methyltetracyclododecane by ring opening metathesis polymerization (ROMP) using molybdenum alkylidene catalyst to form a diblock copolymer with pendant coordination sites (Scheme 2.2). This polymer was then dissolved in THF with CdSe nanocrystals to give optically clear solutions as the polymer coordinates to the nanocrystals. These coordinating monomers were also used as precursors to block copolymers (i.e., with one functional and one non-functional block), in which case the block copolymer can self-assemble upon annealing. When this self-assembly is performed in the presence of nanocrystals, the resulting TEM images show complete segregation of the nanocrystals into the coordinating block. This was a very significant paper in that block copolymers were shown to provide control over nanocrystal patterning through phase-separation and self-assembly to generate a periodic array of nanocrystals. This was one of the early contributions that helped set the stage for future efforts focused on directing nanocrystals into higher order structures through the use of polymeric materials and self-assembly.

R'= -CH$_2$P(O)(octyl)$_2$, -CH$_2$O(CH$_2$)P(octyl)$_2$, -CH$_2$O(CH$_2$)$_5$P(O)(octyl)$_2$
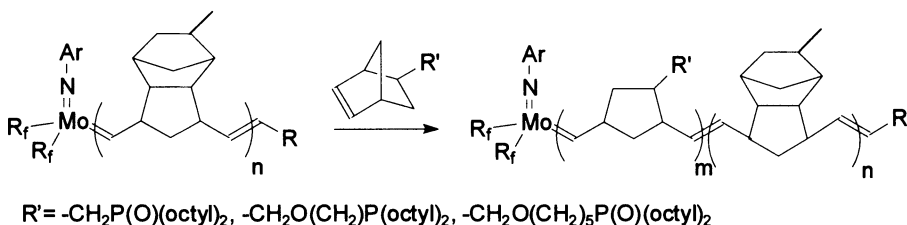
SCHEME 2.2. Diblock copolymers with one block that contains nanoparticle-coordinating phosphine or phosphine oxide moieties.

2.3.2. NANOPARTICLE GROWTH IN POLYMERS

Significant efforts have been applied to the development of procedures whereby nanoparticles are grown in polymers to afford novel hybrid materials. This approach allows for the placement of nanoparticles within particular polymeric domains, through preferential growth in one of the domains. Recent reports show that this methodology can be used to 1) imbed nanoparticles in a polymer matrix in an unaggregated fashion, 2) grow nanoparticles in specific regions of host materials, and 3) fabricate nanocrystal gradients throughout a polymer matrix.

Homopolymer mixtures or block copolymers can be used in these procedures. For example, Godovsky and coworkers demonstrated the growth of CdS and Cu$_2$S nanoparticles in poly(vinyl alcohol) (PVA)/ poly(acrylic acid) (PAA) mixtures, where PVA serves as the matrix material and PAA serves as the ionogenic agent. These two polymers were blended and swollen in water. The matrix was crosslinked to make it insoluble in water then treated with the nanoparticle precursors, for example Cd(NO$_3$)$_2$ and Na$_2$S to afford CdS nanoparticles. As the nanocrystal precursors accumulated in the ionic phase, the growth and subsequent location of the nanocrystals was in the PAA phase.

One of the interesting observations from this approach is that two different species with different conductivities (i.e., one p-type the other n-type) can be grown in the same matrix. Here, the first nanocrystal is grown by introduction of reagents from one side of a swollen matrix. This asymmetric growth provides a concentration profile of the first type of nanocrystal. In the next step, a second nanocrystal is grown from the opposite side to give a material where a particular type of nanocrystal is present at either edge of the matrix, with a mixed region in between. This interpenetrating network of both p- and n-type semiconducting nanocrystals (e.g., Cu$_2$S and CdS) provides improved device performance in solar cells and photodiodes due to increased charge separation of the electron and hole (Figure 2.6).[55]

FIGURE 2.6. Asymmetric growth of n-type and p-type semiconducting nanocrystals.

Godovsky and coworkers have also shown that gradient assemblies of semiconductor nanocrystals in polymers can be formed by spin-casting a solution of nanocrystals on top of a swollen polymer matrix. The nanocrystals diffuse through the polymer forming a gradient of nanocrystals throughout the polymer, with the highest concentration of particles at the surface. In this process, swelling the polymer layer enlarges voids within the polymer and allows for easier nanoparticle penetration. The gradient can be altered simply by increasing the temperature or choosing a different solvent. Higher temperatures serve to increase the diffusion rate, and the use of solvents that induce significant swelling provide voids of substantial size that allow for faster diffusion of nanoparticulate material.[55]

The growth of semiconductor nanoparticles in copolymers has attracted much attention, as copolymers provide potential for sequestration of nanoparticles into phase-separated polymer domains. Schrock and coworkers used a poly(norbornene)-based diblock copolymer for this purpose, where one block was composed of unsubstituted poly(norbornene), and the other contained a pendant lead metallocene poly(norbornene).[63] Thin films of the copolymer shown in Figure 2.7 undergo microphase separation into microdomains that act as nanoreactors. The polymer films were treated with H_2S, which reacts with $PbCp_2$ to give PbS nanoparticles in the microdomains that originally contained the lead metallocene.

FIGURE 2.7 Synthesis of poly(norbornene) diblock copolymer with a lead metallocene moiety in one block. The lead metallocene acts as a precursor for nanoparticle formation by reaction with H_2S that is introduced to the system.

Moffitt and coworkers used poly(styrene) random ionomers with either aromatic or aliphatic carboxylic acids to incorporate CdS into a polymer matrix.[64] These random copolymers were cast as thin films in their deprotonated form, then neutralized by soaking in a solution of cadmium acetate dihydrate. The soaking step allows for penetration of Cd^{2+} ions into the polymer, after which the films are washed with a toluene/methanol

mixture to remove excess salt. The films can then be treated with H_2S to afford CdS nanocrystals embedded in the random copolymer.

Douglas and coworkers developed an approach to prepare CdS nanoparticles in salt-induced block copolymer micelles.[65] In this work, cadmium acetate was added to a THF solution of poly(styrene-*b*-2-vinylpyridine). The cadmium ions aggregated in the poly(2-vinylpyridine) block due to a complexation of the ions with the pyridine units to give a salt induced micelle. The micelle, in essence, has a Cd^{2+}/poly(2-vinylpyridine) core and a poly(styrene) corona, which upon addition of H_2S forms CdS in the micelles.

"Double hydrophilic" block copolymers have also been explored as nanoparticle scaffolds by Antonietti and coworkers for the synthesis of CdS nanoparticles.[66] In this work, poly(ethylene glycol)-*b*-poly(ethyleneimine) (PEG-*b*-PEI) copolymers are used, where the PEI block stabilizes the nanoparticles. In these methods, the block copolymer serves to prevent aggregation and provide solubility to the particles, allowing this composite to be cast or processed as required.

While the methodologies described above are very useful for the preparation of polymer stabilized nanoparticles and higher order structures, one drawback is that the quality of the nanocrystals obtained is not as high as for samples prepared through the high temperature organometallic routes. Thus, separating the nanoparticle growth and polymer functionalization steps is an important alternate route, as described in later sections.

2.4. NANOPARTICLE-POLYMER COMPOSITES OBTAINED BY END-GROUP ATTACHMENT

The attachment of polymer end-groups to flat metal surfaces has garnered much attention in the literature, and this concept has more recently been applied to nanoparticles.[61,67-73] The general scheme for these systems can be divided into two major categories: 1) attachment of a preformed end-functional polymer to the nanocrystal surface, and 2) polymer growth from the nanocrystal surface through the use of surface bound functionality capable of initiating polymerization. Both of these approaches have been used successfully to provide nanoparticle passivation, functionalization, and solubilization.

2.4.1. CHAIN-END ATTACHMENT OF PREFORMED POLYMERS

The tethering of polymers to nanoparticles through the polymer chain-ends has been reported by several groups on various semiconductor nanoparticle substrates, using polymers of various architectures. Thiols end-groups have been used extensively for attachment to surfaces, for example by Hedrick and coworkers with thiol-terminated polyesters for CdS nanoparticle growth and stabilization.[74] Peng and coworkers have used thiol terminated dendrimers to encapsulate CdSe nanocrystals.[51] Comparative photooxidation studies were performed to compare these dendritically encapsulated nanoparticles to those functionalized with small linear molecules. Dilute samples of both types of nanocrystals were prepared and irradiated with UV light while exposed to air. Significant differences were observed in the photochemical stability of the linear versus the dendritic system, as well as a substantial difference in the photochemical stability of CdSe nanocrystals coated with dendrimers of various generations. Higher molecular weight (i.e., higher generation) dendrons gave better protective coatings. This observed photostabilty is rationalized by considering the steric crowding provided by the dendritic macromolecule that is reasoned to slow the penetration of oxygen and ions to the nanoparticle surface. This steric crowding is a function in part of the high degree of branching and relative chain-flexibility of the polyamidoamine dendritic molecules used in this study.

Dendritic encapsulation also provides many chain-ends for further chemical modifications of the CdSe nanocrystals. The dendrimer encapsulants used by Peng and coworkers contain a multifunctional hydroxy periphery that is amenable to chemical modification. Through simple functional group transformations, the hydroxy groups could be converted to ester, carboxylic acid, and amide groups using chemistry that did not disrupt the nanoparticle surface. This functional group transformation greatly alters the solution properties as well as the solid-state dispersion of the nanocrystals. For instance, the hydroxyl terminated dendrimers are water soluble, while the ester terminated dendrimers are only soluble in organic solvents. These studies reiterate the importance of the nature of the encapsulating periphery, especially the chain-end moieties as these groups tend to dictate the physical properties of the nanocrystalline species (Figure 2.8).

Attachment of linear polymer chain-ends has also proven useful for the preparation of amphiphilic and modifiable CdSe nanocrystals. Skaff and Emrick have exploited the amphiphilic nature of poly(ethylene glycol) (PEG) to afford CdSe nanocrystals that are soluble in a wide range of

organic and aqueous media (Figure 2.9).[75] Substituted pyridines were chosen for this functionalization, where pyridine functions as the surface active ligand, and the PEG chain controls the solution properties. Pyridine, used in ligand exchange chemistry on CdSe nanoparticles, is commonly used as an "intermediate" ligand in exchange chemistry. In the case of *para*-ether pyridines, the basicity of the pyridine derivative is increased by the electron donating ether group, which results in tighter binding to the nanocrystal. The PEG-pyridine ligands used in this work were prepared by a Mitsunobu coupling of 4-hydoxypyridine and poly(ethylene glycol). Attachment of PEG-pyridine ligands to CdSe nanocrystals can be accomplished in a number of ways: 1) conventional stripping with pyridine and exchange for PEG-pyridine; 2) direct exchange of TOPO-coverage for PEG-pyridine coverage in THF or water. The PEG-functionalized nanoparticles are soluble in a wide rage of organic solvents and aqueous media of various pH. The diverse range of properties from a single nanoparticle composition is promising for applications ranging from biotechnology, due to the known characteristics of PEG, to patterned surfaces.
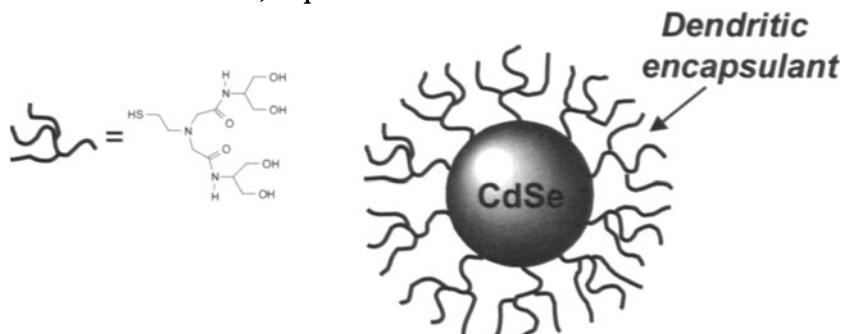
FIGURE 2.8. CdSe core with dendritic periphery show greater photostabilty compared to CdSe nanocrystals with linear small molecule encapsulants.
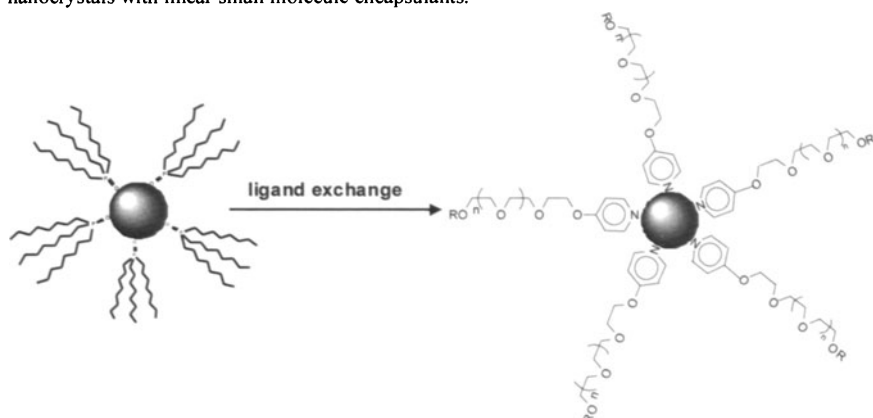
FIGURE 2.9. Pegylated pyridines can be used to displace TOPO-coverage on conventional CdSe nanoparticles.

2.4.2. RADIAL GROWTH OF POLYMERS FROM NANOPARTICLE SURFACES

The ability to perform controlled polymerizations from the surface of semiconductor nanocrystals is an appealing approach for compatibilization of nanocrystals in solution and solid-state environments. This approach begins with functionalized nanoparticles that contain moieties capable of initiating polymerization reactions. An early example reported by Patten and coworkers used atom transfer radical polymerization (ATRP) from the surface of CdS/SiO$_2$ core/shell nanoparticles.[76] These core/shell nanocrystals were resuspended in THF and 3-(2-bromopropionyloxy)-propyl dimethylethoxysilane (BIDS) was added to the dispersed nanocrystals and the reaction was heated. The functionalized CdS/SiO$_2$ nanocrystals were added to a solution of NiBr(PPh$_3$)$_2$ and methyl methacrylate (MMA) and subsequently polymerized at 100 $^\circ$C for three hours. The nature of the polymer grown in the process was studied following polymer cleavage from the nanoparticle surface using a hydrofluoric acid solution. Gel permeation chromatography was used to determine the molecular weights (ca. M$_w$=1.75 x 10^5 g/mol) and polydispersities (PDI ca. 1.3) of the cleaved chains. This showed that reasonably controlled free-radical polymerizations can be performed from the nanoparticle surface, while preserving the inherent properties of the nanoparticle, and maintaining the general features of the controlled polymerization mechanism.

Mirkin and coworkers first demonstrated ring-opening metathesis polymerization (ROMP) as an effective method for polymerization from gold nanoparticles.[77] In the case of semiconductors, Skaff, *et. al.* reported the effectiveness of functional phosphine oxide ligands to support ROMP from CdSe nanoparticles.[78] The functional phosphine oxides were synthesized by replacing the P-H of di-*n*-octyl phosphine oxide with, for example, a vinyl benzyl group. This functional ligand can be attached to CdSe nanoparticles through ligand exchange chemistry, and the ligand periphery decorated subsequently by cross-metathesis. This exchange could be monitored by ^{1}H NMR spectroscopy of the benzylidene proton on the ROMP catalyst, and the polymerization could be performed with a variety of cyclic olefins such as cyclooctene and norbornene, and substituted derivatives of the two. Upon formation of the macroinitiator, monomer is added and allowed to react for an hour at room temperature. These polymerizations are terminated by the addition of ethyl vinyl ether, which attaches to the catalyst and renders it inactive.[79] Precipitation into methanol allows for the separation of the catalyst from the polymer-nanocrystal composite (Figure 2.10).
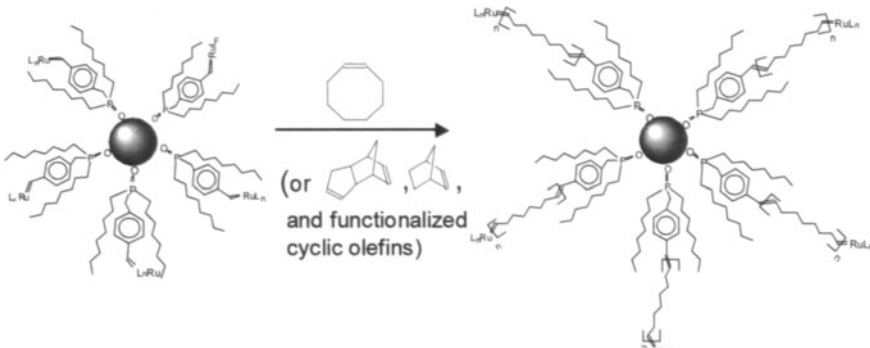
FIGURE 2.10. ROMP-active nanoparticle-based "macroinitiators" for growth of polyolefins from the nanoparticle surface.

These polymer-encapsulated nanocrystals were shown to maintain the inherent optical properties of the starting material. In addition, the particles showed excellent dispersion when the composite materials were cast from solution and probed by transmission electron microscopy. Such dispersion was not obtained by related polymerizations performed in the presence of conventional TOPO-covered CdSe. The generality of this approach is of significant interest as a methodology for obtaining well-dispersed composite materials, as specially prepared functional monomers are not required, and one may use a single macrointiator system to polymerize a wide range of monomers.

2.5. SELF- AND DIRECTED-ASSEMBLY OF SEMICONDUCTING NANOPARTICLES

A fundamentally interesting and technologically important challenge in the field of semiconductor nanocrystals is the production of ordered arrays. High-density arrays are needed for sensors, storage devices, and electro-optical devices. The preferred techniques for producing these ordered arrays are self-assembly or directed assembly. To date, ordered arrays of semiconductor nanocrystals have been obtained by careful crystallization from solution, and by the use of polymer templates. The use of two-solvent recrystallization to form colloidal crystal assemblies has been of scientific interest for over 50 years; a renewed interest in this topic on the nanometer size scale has grown out of the unique properties expected from these assemblies.

The formation of CdSe superlattices was reported by Murray *et. al.* in 1995.[80] In this procedure, CdSe nanocrystals of various size were prepared by the high temperature organometallic methods described earlier.

The nanoparticle size distribution was further narrowed by size selective precipitation such that the nanoparticle sample was almost monodisperse. The nanocrystals were dissolved in a two-solvent mixture, and through the careful regulation of temperature and pressure the quantum dot dispersion is destabilized. In one procedure described, nanocrystals were dissolved in a solvent mixture consisting of 90% octane and 10% octanol at 80 °C. Slow reduction of pressure resulted in selective evaporation of the octane and crystallization. Two types of ordered arrays were obtained through this process. In the bulk, 3-D crystals formed as homogeneous nucleation is the dominate form of nuclei formation. When thin films of nanocrystals were cast, heterogeneous nucleation dominated due to the large nanocrystal/substrate surface contact, and 2-D ordered films were observed. The nanocrystals in the ordered array are close-packed into an fcc structure as indicated by X-ray diffraction. The quantum dot superlattices show behavior commensurate with quantum confinement, but also show electronic behavior resulting from nanocrystal interactions. Absorption data of the quantum dot superlattices show a strong size-dependent exciton peak, while the photoluminescence spectra show a red-shift with respect to dots in solution, indicating the presence of interparticle interactions. The spacing between the nanocrystals was shown to be tunable and dependent on the ligands used for surface coverage. Tributylphosphine oxide, trioctylphosphine, and trihexadecylphosphate surface coverage provided interparticle spacing of 7, 11, and 17 Å respectively (Figure 2.11).
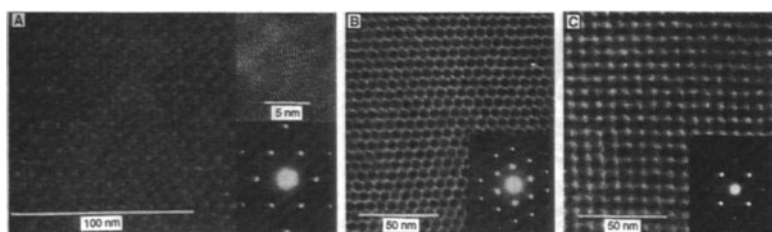
FIGURE 2.11. CdSe nanocrystal superlattices obtained by two-solvent crystallization methods. (A) (111)-oriented array of 6.4 nm CdSe nanocrystals; (B) (101)-oriented fcc array of 4.8 nm CdSe nanocrystals; (C) (100)–oriented fcc array of 4.8 nm CdSe nanocrystals. Reprinted figure with permission from Murray, C. B.; Kagan, C. R.; Bawendi, M. G. *Science* **1995**, *270*, 1335-1338. Copyright 1995 American Association for the Advancement of Science.

Polymers, especially block copolymer templates, offer an appealing alternative for nanocrystal templating because they are easily processable and have the inherent ability to self-assemble into ordered arrays. For example, Kotov and coworkers have used a layer-by layer (LBL) assembly approach to assemble CdTe nanocrystals of various sizes and emissions.[81] The CdTe nanocrystals were coated with thiogylcolic acid and a partner polyelectrolyte poly(diallyldimethylammonium chloride). The LBL

deposition of nanocrystals of various size allows for the formation of graded semiconductor films with promise as photodetectors, waveguides, and bipolar transistors.

An approach that uses block copolymer templates[82] as a means to assemble semiconductor nanoparticles was discussed by Russell, Emrick and coworkers.[83] In this work, nanoporous templates were dipped into heptane solutions of CdSe nanocrystals at various concentration and rates. As the template is withdrawn, capillary force drives the nanoparticle solution into the nanopores, and as the solution evaporates the nanoparticles are deposited into the template (Figure 2.11). The number of nanoparticles per nanopore can be controlled by two factors: 1) the relative ratio of the nanopore to the nanoparticle diameter and 2) the concentration of the nanoparticle solutions. In the case of 10 nm particles and 17 nm pores, a large fraction of the holes contain were found to contain one nanoparticle (Figure 2.12). In addition, it was found that slower withdrawal rates resulted in fewer nanocrystals settled on the template surface rather than in the pores. Such template directed assembly offers much promise for providing site-isolated nanoparticles with potential applications in catalysts, sensor materials, and other areas.
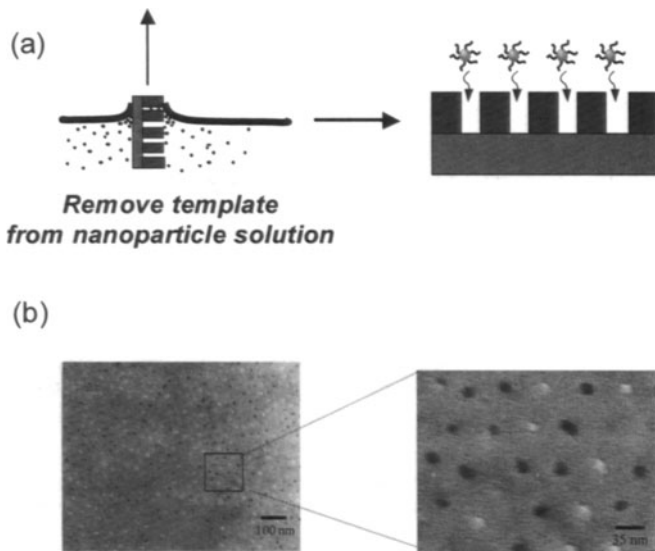
FIGURE 2.12. (a) Illustration of dip-coating process; (b) TEM image of 10 nm CdSe nanocrystals arranged in a hexagonal array as directed by the polymer template.

2.6. SUMMARY AND FUTURE OUTLOOK

This review has provided an overview of semiconductor nanoparticles, focused especially on CdSe, from some of the early synthetic work to the more recent attempts to assemble these particles into higher order structures. Over the last 20 years the field of semiconductor nanoparticles has been extraordinarily active, and remarkable advances have been made. Semiconductor nanocrystals can now be synthesized routinely with high crystallinity and quantum yields that allow one to take advantage of the unique properties associated with the nanoscale, such as tunable bandgaps, large surface-to-volume ratios, and easier processability. The incorporation of these nanoparticles into polymer matrices and ultimately devices shows great potential for photovoltaic cells, LED's, tunable lasers, and biologically active tags and diagnostic devices. Research activities in the future are expected to continue to focus on synthetic methods, assemblies, and device applications, both for materials science and biology. As synthetic methods become increasingly routine and commercialized, even greater focus will be placed on nanoparticle applications.

REFERENCES

1. Hummel, R. E. *Electronic Properties of Materials*; 2 ed.; Springer-Verlag, 1993.
2. Klabunde, K. J. *Nanoscale Materials in Chemistry*; John Wiley & Sons, 2001.
3. Bawendi, M. G.; Wilson, W. L.; Rothberg, L.; Carroll, P. J.; Jedju, T. M.; Steigerwald, M. L.; Brus, L. E. *Phys. Rev. Lett.* **1990**, *65*, 1623-1626.
4. Brus, L. *Appl. Phys. A-Mater. Sci. Process.* **1991**, *53*, 465-474.
5. Brus, L. E.; Szajowski, P. F.; Wilson, W. L.; Harris, T. D.; Schuppler, S.; Citrin, P. H. *J. Am. Chem. Soc.* **1995**, *117*, 2915-2922.
6. Chen, C. C.; Herhold, A. B.; Johnson, C. S.; Alivisatos, A. P. *Science* **1997**, *276*, 398-401.
7. Chestnoy, N.; Hull, R.; Brus, L. E. *J. Chem. Phys.* **1986**, *85*, 2237-2242.
8. Empedocles, S. A.; Bawendi, M. G. *Science* **1997**, *278*, 2114-2117.
9. Empedocles, S.; Bawendi, M. *Accounts of Chemical Research* **1999**, *32*, 389-396.
10. Nirmal, M.; Dabbousi, B. O.; Bawendi, M. G.; Macklin, J. J.; Trautman, J. K.; Harris, T. D.; Brus, L. E. *Nature* **1996**, *383*, 802-804.
11. Nirmal, M.; Brus, L. *Accounts Chem. Res.* **1999**, *32*, 407-414.
12. Shim, M.; Wang, C. J.; Guyot-Sionnest, P. *J. Phys. Chem. B* **2001**, *105*, 2369-2373.
13. Shim, M.; Guyot-Sionnest, P. *Phys. Rev. B* **2001**, *6424*, 245342.
14. Shim, M.; Wang, C. J.; Norris, D. J.; Guyot-Sionnest, P. *MRS Bull.* **2001**, *26*, 1005-1008.
15. Gaponenko, S. v. *Optical Porperties of Semiconductor Nanocrystals*; Cambridge University Press: New York, 1998.
16. Brus, L. *J. Phys. Chem. Solids* **1998**, *59*, 459-465.
17. Alivisatos, A. P.; Harris, T. D.; Brus, L. E.; Jayaraman, A. *J. Chem. Phys.* **1988**, *89*, 5979-5982.
18. De Schryver, F. C. *Pure Appl. Chem.* **1998**, *70*, 2147.

19. Li, L. S.; Hu, J. T.; Yang, W. D.; Alivisatos, A. P. *Nano Lett.* **2001**, *1*, 349-351.

20. Marcus, M. A.; Flood, W.; Stiegerwald, M.; Brus, L.; Bawendi, M. *J. Phys. Chem.* **1991**, *95*, 1572-1576.

21. Rabani, E.; Hetenyi, B.; Berne, B. J.; Brus, L. E. *J. Chem. Phys.* **1999**, *110*, 5355-5369.

22. Rossetti, R.; Ellison, J. L.; Gibson, J. M.; Brus, L. E. *J. Chem. Phys.* **1984**, *80*, 4464-4469.

23. Tully, D. C.; Wilder, K.; Frechet, J. M. J.; Trimble, A. R.; Quate, C. F. *Adv. Mater.* **1999**, *11*, 314-318.

24. Bosman, A. W.; Heumann, A.; Klaerner, G.; Benoit, D.; Frechet, J. M. J.; Hawker, C. J. *J. Am. Chem. Soc.* **2001**, *123*, 6461-6462.

25. Calander, N.; Willander, M. *Phys. Rev. Lett.* **2002**, *89*, 143603.

26. Townsend, P.; Olivares, J. *Appl. Surf. Sci.* **1997**, *110*, 275-282.

27. Boal, A. K.; Ilhan, F.; DeRouchey, J. E.; Thurn-Albrecht, T.; Russell, T. P.; Rotello, V. M. *Nature* **2000**, *404*, 746-748.

28. Haw, M. D.; Poon, W. C. K.; Pusey, P. N. *Phys. Rev. E* **1997**, *56*, 1918-1933.

29. Bunning, T. J.; Kirkpatrick, S. M.; Natarajan, L. V.; Tondiglia, V. P.; Tomlin, D. W. *Chem. Mat.* **2000**, *12*, 2842.

30. Brott, L. L.; Naik, R. R.; Pikas, D. J.; Kirkpatrick, S. M.; Tomlin, D. W.; Whitlock, P. W.; Clarson, S. J.; Stone, M. O. *Nature* **2001**, *413*, 291-293.

31. Htoo, M. S., Ed. *Microelectronic Polymers*; M. Dekker, 1989.

32. Sneh, O.; Clark-Phelps, R. B.; Londergan, A. R.; Winkler, J.; Seidel, T. E. *Thin Solid Films* **2002**, *402*, 248-261.

33. Hong, L.; Vilar, R. M.; Wang, Y. M. *J. Mater. Sci.* **1997**, *32*, 5545-5550.

34. Brown, T. L.; Swaminathan, S.; Chandrasekar, S.; Compton, W. D.; King, A. H.; Trumble, K. P. *J. Mater. Res.* **2002**, *17*, 2484-2488.

35. Steigerwald, M. L.; Alivisatos, A. P.; Gibson, J. M.; Harris, T. D.; Kortan, R.; Muller, A. J.; Thayer, A. M.; Duncan, T. M.; Douglass, D. C.; Brus, L. E. *J. Am. Chem. Soc.* **1988**, *110*, 3046-3050.

36. Steigerwald, M. L.; Brus, L. E. *Annu. Rev. Mater. Sci.* **1989**, *19*, 471-495.

37. Fojtik, A.; Weller, H.; Koch, U.; Henglein, A. *Ber. Bunsen-Ges. Phys. Chem. Chem. Phys.* **1984**, *88*, 969-977.

38. Murray, C. B.; Norris, D. J.; Bawendi, M. G. *J. Am. Chem. Soc.* **1993**, *115*, 8706-8715.

39. Peng, X. G.; Schlamp, M. C.; Kadavanich, A. V.; Alivisatos, A. P. *J. Am. Chem. Soc.* **1997**, *119*, 7019-7029.

40. Dabbousi, B. O.; RodriguezViejo, J.; Mikulec, F. V.; Heine, J. R.; Mattoussi, H.; Ober, R.; Jensen, K. F.; Bawendi, M. G. *J. Phys. Chem. B* **1997**, *101*, 9463-9475.

41. Gerion, D.; Pinaud, F.; Williams, S. C.; Parak, W. J.; Zanchet, D.; Weiss, S.; Alivisatos, A. P. *J. Phys. Chem. B* **2001**, *105*, 8861-8871.

42. Pathak, S.; Choi, S. K.; Arnheim, N.; Thompson, M. E. *J. Am. Chem. Soc.* **2001**, *123*, 4103-4104.

43. Qu, L. H.; Peng, Z. A.; Peng, X. G. *Nano Lett.* **2001**, *1*, 333-337.

44. Peng, Z. A.; Peng, X. G. *J. Am. Chem. Soc.* **2001**, *123*, 183-184.

45. Peng, Z. A.; Peng, X. G. *J. Am. Chem. Soc.* **2002**, *124*, 3343-3353.

46. Qu, L. H.; Peng, X. G. *J. Am. Chem. Soc.* **2002**, *124*, 2049-2055.

47. Battaglia, D.; Peng, X. G. *Nano Lett.* **2002**, *2*, 1027-1030.

48. Guzelian, A. A.; Katari, J. E. B.; Kadavanich, A. V.; Banin, U.; Hamad, K.; Juban, E.; Alivisatos, A. P.; Wolters, R. H.; Arnold, C. C.; Heath, J. R. *J. Phys. Chem.* **1996**, *100*, 7212-7219.

49. Olshavsky, M. A.; Goldstein, A. N.; Alivisatos, A. P. *J. Am. Chem. Soc.* **1990**, *112*, 9438-9439.

50. Becerra, L. R.; Murray, C. B.; Griffin, R. G.; Bawendi, M. G. *J. Chem. Phys.* **1994**, *100*, 3297-3300.
51. Wang, Y. A.; Li, J. J.; Chen, H.; Peng, X. G. *J. Am. Chem. Soc.* **2002**, *124*, 2293-2298.
52. Balazs, A.; Ginzburg, V. V.; Qui, F.; Peng, G.; Jasnow, D. *J. Phys. Chem. B* **2000**, *104*, 3411-3422.
53. Colvin, V. L.; Schlamp, M. C.; Alivisatos, A. P. *Nature* **1994**, *370*, 354-357.
54. Dameron, C. T.; Reese, R. N.; Mehra, R. K.; Kortan, A. R.; Carroll, P. J.; Steigerwald, M. L.; Brus, L. E.; Winge, D. R. *Nature* **1989**, *338*, 596-597.
55. Godovsky, D. Y. In *Biopolymers/Pva Hydrogels/Anionic Polymerisation Nanocomposites*, 2000; Vol. 153, pp 163-205.
56. Harrison, M. T.; Kershaw, S. V.; Burt, M. G.; Rogach, A. L.; Kornowski, A.; Eychmuller, A.; Weller, H. *Pure Appl. Chem.* **2000**, *72*, 295-307.
57. Huynh, W. U.; Peng, X. G.; Alivisatos, A. P. *Adv. Mater.* **1999**, *11*, 923.
58. Huynh, W. U.; Dittmer, J. J.; Alivisatos, A. P. *Science* **2002**, *295*, 2425-2427.
59. Lee, J.; Sundar, V. C.; Heine, J. R.; Bawendi, M. G.; Jensen, K. F. *Adv. Mater.* **2000**, *12*, 1311-1311.
60 Michalet, X.; Pinaud, F.; Lacoste, T. D.; Dahan, M.; Bruchez, M. P.; Alivisatos, A. P.; Weiss, S. *Single Mol.* **2001**, *2*, 261-276.
61. Salafsky, J. S. *Solid-State Electron.* **2001**, *45*, 53-58.
62. Fogg, D. E.; Radzilowski, L. H.; Blanski, R.; Schrock, R. R.; Thomas, E. L. *Macromolecules* **1997**, *30*, 417-426.
63. Sankaran, V.; Cummins, C. C.; Schrock, R. R.; Cohen, R. E.; Silbey, R. J. *J. Am. Chem. Soc.* **1990**, *112*, 6858-6859.
64. Moffitt, M.; McMahon, L.; Pessel, V.; Eisenberg, A. *Chem. Mat.* **1995**, *7*, 1185-1192.
65. Zhao, H. Y.; Douglas, E. P.; Harrison, B. S.; Schanze, K. S. *Langmuir* **2001**, *17*, 8428-8433.
66. Qi, L.; Colfen, H.; Antonietti, M. *Nano Lett.* **2001**, *1*, 61-65.
67. Gu, Y. D.; Nederberg, F.; Kange, R.; Shah, R. R.; Hawker, C. J.; Moller, M.; Hedrick, J. L.; Abbott, N. L. *ChemPhysChem* **2002**, *3*, 448.
68. Petrash, S.; Cregger, T.; Zhao, B.; Pokidysheva, E.; Foster, M. D.; Brittain, W. J.; Sevastianov, V.; Majkrzak, C. F. *Langmuir* **2001**, *17*, 7645-7651.
69. Moller, M.; Nederberg, F.; Lim, L. S.; Kange, R.; Hawker, C. J.; Hedrick, J. L.; Gu, Y. D.; Shah, R.; Abbott, N. L. *J. Polym. Sci. Pol. Chem.* **2001**, *39*, 3529-3538.
70. Juang, A.; Scherman, O. A.; Grubbs, R. H.; Lewis, N. S. *Langmuir* **2001**, *17*, 1321-1323.
71. Zhao, B.; Brittain, W. J. *Macromolecules* **2000**, *33*, 8813-8820.
72. Rajagopalan, P.; McCarthy, T. J. *Macromolecules* **1998**, *31*, 4791-4797.
73. Chen, W.; McCarthy, T. J. *Macromolecules* **1998**, *31*, 3648-3655.
74. Carrot, G.; Scholz, S. M.; Plummer, C. J. G.; Hilborn, J. G.; Hedrick, J. L. *Chem. Mat.* **1999**, *11*, 3571-3577.
75. Skaff, H.; Emrick, T. *Chem. Comm.* **2002**, *in press*.
76. Farmer, S. C.; Patten, T. E. *Chem. Mat.* **2001**, *13*, 3920-3926.
77. Watson, K. J.; Zhu, J.; Nguyen, S. T.; Mirkin, C. A. *J. Am. Chem. Soc.* **1999**, *121*, 462-463.
78. Skaff, H.; Ilker, M. F.; Coughlin, E. B.; Emrick, T. *J. Am. Chem. Soc.* **2002**, *124*, 5729-5733.
79. Schwab, P.; Grubbs, R. H.; Ziller, J. W. *J. Am. Chem. Soc.* **1996**, *118*, 100.
80. Murray, C. B.; Kagan, C. R.; Bawendi, M. G. *Science* **1995**, *270*, 1335-1338.
81. Mamedov, A. A.; Belov, A.; Giersig, M.; Mamedova, N. N.; Kotov, N. A. *J. Am. Chem. Soc.* **2001**, *123*, 7738-7739.
82. Russell, T. P.; Sackmann, E. *Curr. Opin. Colloid Interface Sci.* **1998**, *3*, 3-4.

83. Misner, M. J.; Skaff, H.; Emrick, T.; Russell, T. P. *Adv. Mater.* **2002**, *in press*.

3

Architecture of Nanocrystal Building Blocks

Jinwoo Cheon*, Young-wook Jun[1], and Sang-Min Lee
Department of Chemistry, Yonsei Universiy, 120-749 Seoul, Korea.
Email: jcheon@alchemy.yonsei.ac.kr

3.1.   INTRODUCTION

Crystals consist of a periodic alternation of specific repeating molecules. The individual repeating molecules have quantized electronic structures while crystals have continuous electronic band structures that result from the overlap and combination of molecular orbitals of repeating molecules. Therefore, isolated molecules exhibit quantum mechanical properties, while the chemical and physical properties of bulk crystals obey the laws of classical mechanics. However, when the crystal size decreases into the nano-scale regime (1 ~ 100 nm), the electronic band of the crystals starts to be quantized and the resulting nanocrystals behave as an intermediate between molecules and crystals.[2-5] These nanocrystals exhibit novel properties which differ from both molecular and bulk properties. For example, CdSe semiconductor crystals on the 10 nm scale, the characteristic red luminescence is no longer observed but the luminescence can be continuously tuned from red to blue by varying the crystal size. The melting temperature of nanocrystals simultaneously decreases when the nanocrystal size

is reduced.[6,7] In the nanoscopic world, crystal properties are highly dependent on the size, shape, and surface state of the crystals.

If the precise control of nanocrystal size and shape is possible, their chemical and physical properties can be manipulated as desired. Then, these nanocrystals can be used as the building blocks for assembling and patterning future nanodevices.

3.1.1   CRYSTAL SHAPE

The size and shape of nanocrystals are crucial parameters for controlling nanocrystal properties. The electronic band of the crystal is gradually quantized starting from the band edges as a function of size reduction, resulting in an increase in the band-gap energy. For example, CdSe nanocrystals luminescence red to blue as the size is decreased from 12 nm to 1.2 nm. The electrical transport properties are also highly dependent on the nanocrystal size. One example is Coulomb blockade phenomena.[8,9] The injection of an additional electric charge into a nanocrystal that is already charged by an electron is prevented by the coulombic repulsion between the two electrons.

The shape of the nanocrystals also strongly influences their properties. The density of energy states (DOS) for inorganic crystals, which is predicted by a simple particle in a box type model, simultaneously evolves from–continuous levels into discrete states as the dimensionality is decreased from three to zero dimensions (Figure 3.1).
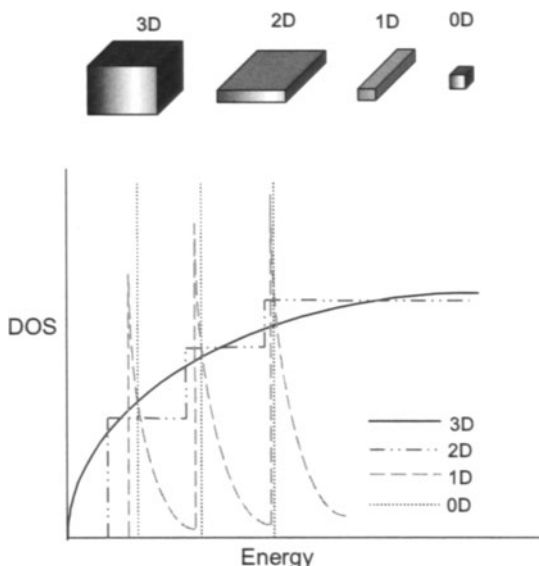
FIGURE 3.1. Energy vs. density of electronic states (DOS) for inorganic crystals of 3, 2, 1, and 0-dimensions.
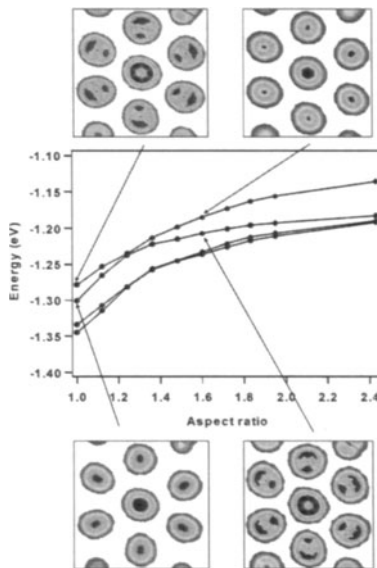
FIGURE 3.2. The four highest occupied electronic states of 3.0 nm diameter CdSe nanorods calculated with an empirical pseudopotential method with different aspect ratios. (From Alivisatos, 2001, Ref. 10.)
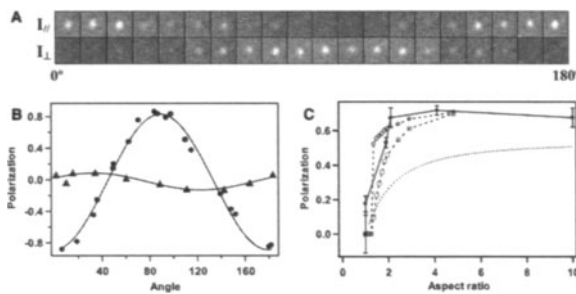
FIGURE 3.3. (a) Linearly polarized emission of single CdSe nanorod with an aspect ratio of ~ 10. (b) Polarization of a rod (aspect ratio ~ 10, circles) and a sphere (triangles). (From Alivisatos, 2001, Ref. 10.)

Varying the nanocrystal's shape also induces novel optical properties. The shape dependent optical properties of cadmium selenide (CdSe) nanocrystals are a good example.[10] The highest occupied molecular orbital arises from Se 4p orbitals that are arranged to be in phase between unit cells, while the lowest unoccupied molecular orbital is comprised of Cd 5s orbitals that are also in phase between unit cells. Therefore, optical luminescence of the direct band gap semiconductor CdSe results via a vertical transition between these two orbitals. For CdSe nanospheres (aspect ratio ~ 1), electronic states with predominantly Se $4p_z$ character are slightly more stable than that with Se $4p_x$ and $4p_y$ character. However, as the aspect ratio of CdSe nanorods with an elongated c-axis paralleling the Se p_z orbitals increases, the electronic energy levels of states with Se $4p_z$ character gradually increases and a crossover between the two highest occupied electronic states occurs (Figure 3.2). These changes induce a transition

from weakly plane-polarized emission to linearly polarized emission. Thus, CdSe nanorods with aspect ratios of ~ 10 emit with a polarization factor of 86 % (Figure 3.3).
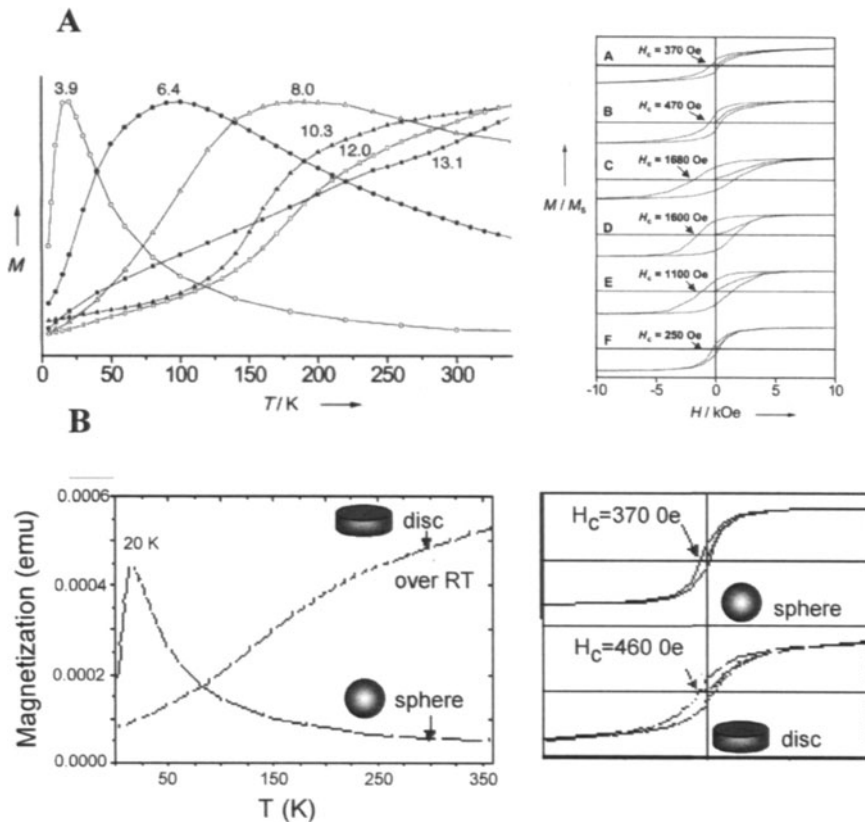
FIGURE 3.4. Size and shape dependent magnetic properties of cobalt nanocrystals. (a) Size dependent blocking temperature and magnetic coercivity of cobalt spheres. A. 3.9, B 6.4, C 8.0, D 10.3, E 12.0, F 13.1 nm. (b) Blocking temperature and magnetic coercivity of 4 nm cobalt spheres and discs. (From Cheon, 2002, Ref. 11.)

Magnetic properties of crystal are also highly dependent on the size and shape of nanocrystals.[11] The blocking temperature of cobalt nanocrystals gradually increases from 20 K to over room temperature when the nanocrystal sizes increase from ~4 to 13 nm. This is consistent with the linear relationship between crystal volume and blocking temperature as predicted from the equation $KV=25K_BT_B$. The magnetic coercivity of the cobalt nanocrystals reaches a maximum value when forming a single domain with a size of ~ 8 nm. The shape of cobalt nanocrystals also strongly influences the magnetic properties of the nanocrystals. In the case of cobalt nanospheres ~ 4 nm, the blocking temperature

of the nanospheres is 20 K. However, when nanocrystals with a disc shape (height ~ 4 nm) are formed, a huge increase in the blocking temperature is observed due to enhanced anisotropy. Similarly, the magnetic coercivity of the discs has a higher value relative to that of spheres. Even at room temperature, these discs exhibit ferromagnetic behavior with a coercivity of ~ 35 Oe. Enhanced shape anisotropy induces a preferential alignment of the magnetic spins along the long axis of the discs.[12,13]

3.1.2   BASIC NANOSCALE BUILDING BLOCKS

Atoms as basic elements do not allow for the control of its various properties, while optical, chemical, and physical properties of nanocrystals can be controlled by tuning the nanocrystal size and shape as described in the previous section. Nanocrystals that are usually regarded as "artificial atoms" are the basic units for nano-scale devices, and the design and operation of these devices will be easily accomplished by using nanocrystals with distinct sizes and shapes.[14] By assembling and patterning nano-building blocks in a manner similar to assembling "Lego" blocks, the fabrication of future devices that are extremely fast, efficient, and small will be possible. As with Lego blocks, various shapes and sizes of nano building blocks will be required for the various components of the nanostructure. Therefore, the control of nanobuilding blocks is crucial for the success of future nanodevices.

Basic nanobuilding blocks can be classified by crystal symmetry and dimensionality (Figure 3.5). Isotropic spheres, icosahedrons, and cubes can be classified as 0-dimensional building blocks. These are of the most familiar shape in the nano world. Semiconductor and metal nanospheres and C_{60} are in this group. Rods, cylinders with polygon shape, and wires are examples of 1-dimensional building blocks. These building blocks can be applicable for 2-terminal circuit devices.[15,16] Carbon nanotubes are another good example of 1-dimensional building blocks. Using cross-junctions of carbon nanotubes, nonvolatile random access memory devices are possible.[17] Discs, plates with polygon shape belong to 2-dimensional building blocks. Examples of rather complex structured building blocks are star shaped and multi pod structures such as highly symmetric crosses.

There are several approaches to preparing nanobuilding blocks including gas phase synthesis and liquid phase synthesis. In the past decade efforts for controlling nanocrystal shape using liquid phase synthesis has been extensively carried out, but has been limited to certain systems such as II-VI semiconductors. To obtain various shapes of nanobuilding blocks, the presentation of a general synthetic scheme and the unraveling of shape guiding mechanisms are necessary. In the next two sections, recent developments in shape controlled nanocrystal

synthesis using liquid phase synthesis and proposed shape guiding mechanisms will be described.
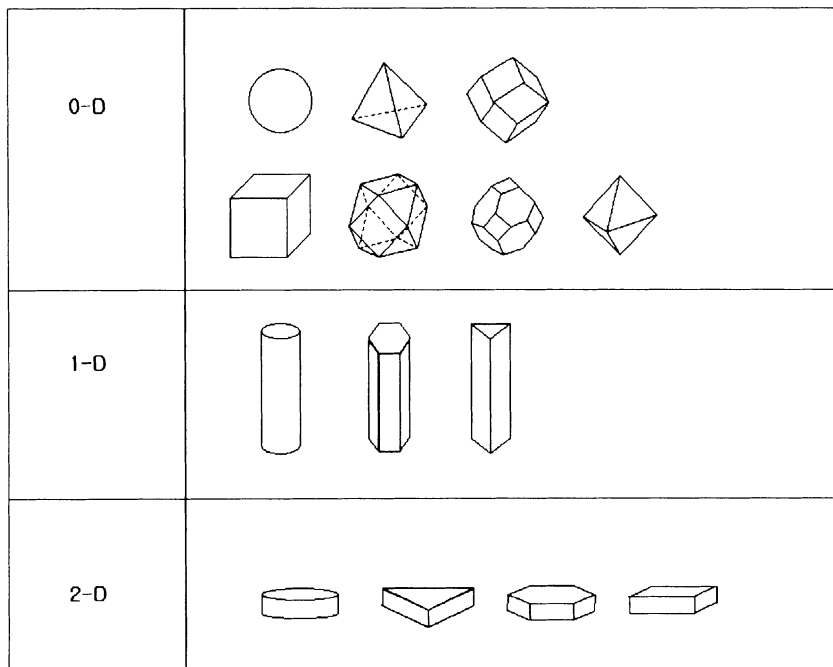
FIGURE 3.5. Geometrical shapes of basic building blocks.

3.2.   RECENT DEVELOPMENTS IN THE ARCHITECTURAL CONTROL OF NANOBUILDING BLOCKS

3.2.1   0-DIMENSIONAL SPHERES AND CUBES

During the past decade, metal and semiconductor nanospheres have been extensively studied using various methods. In the early stages of this type of work, nanocrystals were usually grown in a hydrolytic media in the presence of structured micelles.[18] Several metallic and semiconducting nanocrystals have been grown from aging processes of ionic precursors inside Na-AOT micelles. However, nanocrystals obtained using this method have relatively poor crystallinities and polydispersity in size.

To address these problems, the method of injecting precursor into organic surfactants at a high temperature was developed. Bawendi et al.[5] synthesized various sized CdSe nanocrystals via thermal decomposition of dimethyl cadmium and trioctylphosphine selenide in a hot trioctylphosphine oxide solution. The nanocrystal size varied from 1.2 to 12 nm with high monodispersity and crystallinity and the nanocrystals obtained were highly soluble in various organic solvents. (Figure 3.6) Optical spectra clearly exhibit quantum confinement effects and it also reveals that CdSe nanocrystals are formed with tunable sizes, high monodispersity, and high crystallinity. This high temperature injection method has been applied to various materials such as other semiconductors, metals, and metal oxides.
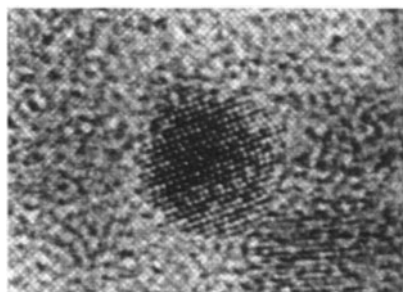
FIGURE 3.6. HRTEM image of 0-dimensional spherical CdSe nanocrystals synthesized using a high temperature injection method. (From Bawendi, 1993, Ref. 5.)

Isotropic 0-D nanocrystals with faceted faces are also obtainable by careful controlling crystal surface energy. El-Sayed et al. demonstrated the shape control of Pt nanocrystals as FCC structure.[19] The Pt precursor is reduced by hydrogen gas bubbling in a reaction solution that includes a capping polymer. By controlling the concentration of the capping polymer, the resulting shapes are changed. At high polymer concentration, nanocrystals are prevented from rapid growth and the resulting shape is a small tetrahedron with only {111} faces (Figure 3.7 a). At low polymer concentrations, the deposition rate of Pt atom on the crystal surfaces is faster on the {111} faces and the final shape becomes a more rectangular cubic shape (Figure 3.7 b).
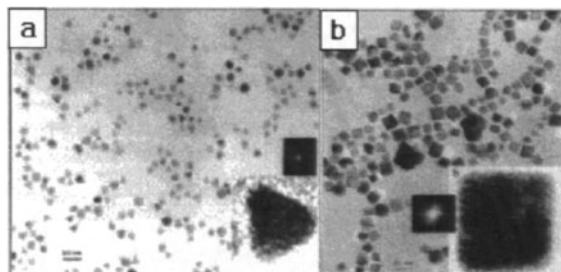
FIGURE 3.7. (a) Tetrahedral Pt nanocrystals grown in a high polymer concentration, (b) cubic shaped Pt nanocrystals grown in a low polymer concentration. (From El-Sayed, 1996, Ref. 19.)

0-dimensional polygonal shapes were also observed in semiconductor nanocrystals. Cheon et al. demonstrated shape controllable synthesis of PbS nanocrystals as an isotropic rock salt model system.[20] Due to the high surface energy of the {111} faces in a rock salt system, a cubic shape is generally obtained in the presence of weakly binding capping molecules (Figure 3.8 a). However, the presence of tightly binding capping molecules such as dodecanethiol mainly affected the shapes of the nanocrystals. Since dodecanethiol is much more strongly binding on the {111} faces, tetradecahedron shapes highly truncated on the {111} faces were obtained at high concentrations of dodecanethiol (Figure 3.8 b). Similarly, O'Brien et al. also synthesized cubic shaped PbS nanocrystals via a single source precursor.[21]
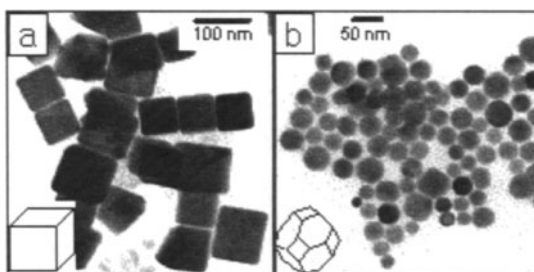
FIGURE 3.8. TEM images of PbS nanocrystals and their polygonal models. (a) Dodecylamine capping molecular system and corresponding crystal model (Inset) (b) Dodecanethiol capping molecular system and corresponding crystal model (Inset). (From Cheon, 2002, Ref. 20.)

As described above, polygonal shape control in 0-dimensions is relatively feasible by regulation of the relative surface energies.

3.2.2   1-DIMENSIONAL RODS AND WIRES

3.2.2.1 GROUP II-VI SEMICONDUCTORS

1-dimensional nanorods and wires have been extensively explored not only because they exhibit novel shape dependent properties such as linearly polarized luminescence,[10] liquid crystal phenomena,[22] and enhanced magnetic properties [11] but they can also be utilized as key components in two terminal circuits.[15,16]

The high temperature injection method can also be utilized for high quality nanorod synthesis. Alivisatos and Peng et al. first reported shape control of CdSe nanorods with high monodispersity and crystallinity via thermal decomposition of dimethylcadmium and trioctylphosphineselenide in a hot surfactant mixture of trioctylphosphine oxide (TOPO) and hexylphophonic acid (HPA).[23] In this synthesis, 1-dimensional rod shaped structures result from preferential growth along the [001] direction of wurtzite CdSe that is promoted by a selective adhesion of HPA molecules on specific faces. With increasing HPA

concentration, the nanocrystal shape evolves from spheres and short rods to long rods with high aspect ratios (Figure 3.9).

On the other hand, Cheon et al. reported a simpler synthetic method using a single source precursor instead of dual sources. For example, zinc telluride nanorods were formed when a single source precursor, $Zn(TePh)_2$-TMEDA, decomposed in a hot amine surfactant mixture (Figure 3.10).[24] Anisotropic 1-dimensional growth of metal sulfide nanocrystals including CdS, MnS, and PbS was also possible by thermal decomposition of stable single molecular precursors in a *mono-surfactant system.*[20,25,26]
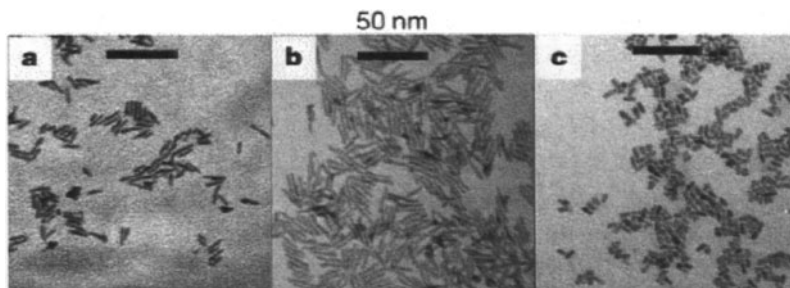
FIGURE 3.9. CdSe nanorods grown using thermal decomposition of precursors in the presence of binary surfactants. (From Alivisatos, 2000. Ref. 23.)

Hydrolytic synthesis of II-VI semiconductors also produces 1-dimensional rod-shaped nanocrystals by shape transformations involving oriented attachment processes. Weller et al. have proposed an alignment and reorganization of zinc oxide nanocrystals via oriented attachment process.[27] In this synthesis, zinc acetate produces zinc oxide nanospheres through hydrolysis and aging processes. The nanospheres are then aligned and fused together in order to remove high-energy surfaces. Finally, reconstruction processes of the fused nanocrystal surfaces result in rod shaped nanocrystals with flat surfaces (Figure 3.11).
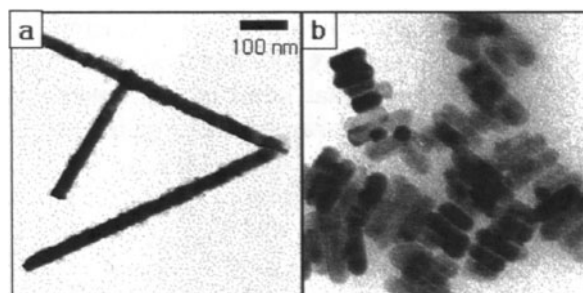
FIGURE 3.10. II-VI semiconductor nanorods. (a) ZnTe (From Cheon, 2001, ref. 8), (B) CdS (From Cheon, 2001, Ref. 25.).

Similar shape transformation processes were also observed in other II-VI semiconductor nanocrystals. Kotov et al. reported a shape transformation from sphere to rod by dipole-induced fusion of CdTe individual nanospheres.[28] Zinc blende CdTe spheres were first formed by reaction between Cd and Te precursors in aqueous solution. Then, CdTe spheres obtained were aligned through dipole interactions between nanocrystals. Finally, the nanospheres were fused together with a simultaneous crystal phase transition to wurtzite.
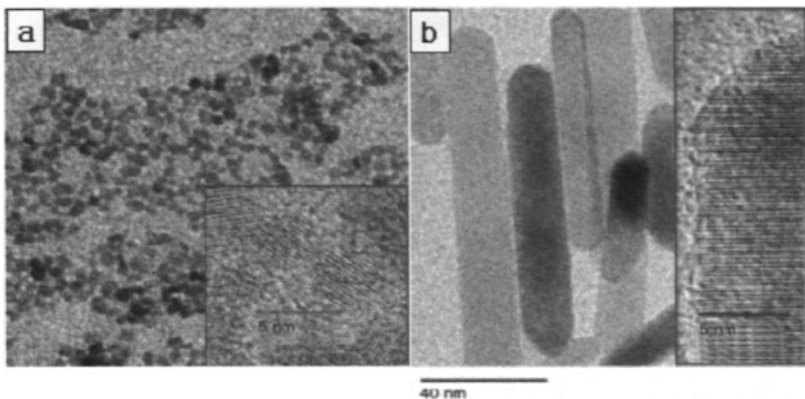
FIGURE 3.11. Shape tranformation of ZnO nanocrystals from aggregates of (a) ZnO nanospheres to (b) ZnO nanorods. Inset: high resolution TEM images of spheres and rods. (From Weller, 2002, Ref. 27.)

3.2.2.2. GROUP III-V SEMICONDUCTORS

Unlike II-VI semiconductor systems that have been thoroughly studied, anisotropic shape control of III-V semiconductor nanocrystals has been very limited. This is most likely due to a greater degree of covalent bonding and the absence of suitable precursors. Moreover, except for metal nitrides, III-V semiconductors favor isotropic zinc blende structures and thus 0-D nanocrystal growth is commonly preferred rather than rod growth.[29] Cheon et al. have shown that the crystalline phase of gallium phosphide nanocrystals can be chemically controlled by adopting suitable surfactants, and the formation of wurtzite GaP nanorods as well as zinc blende GaP nanospheres is possible.[30] When highly bulky trioctylamine (TOA) is used as a surfactant, the formation of zinc blende GaP nanospheres is favored, minimizing steric hindrance between incoming monomer complexes (GaP-TOA complex) and GaP lattices. In contrast, when sterically less hindered primary amine (hexadecylamine) is added to TOA solution, formation of GaP wurtzite rods is preferred (Figure 3.12).
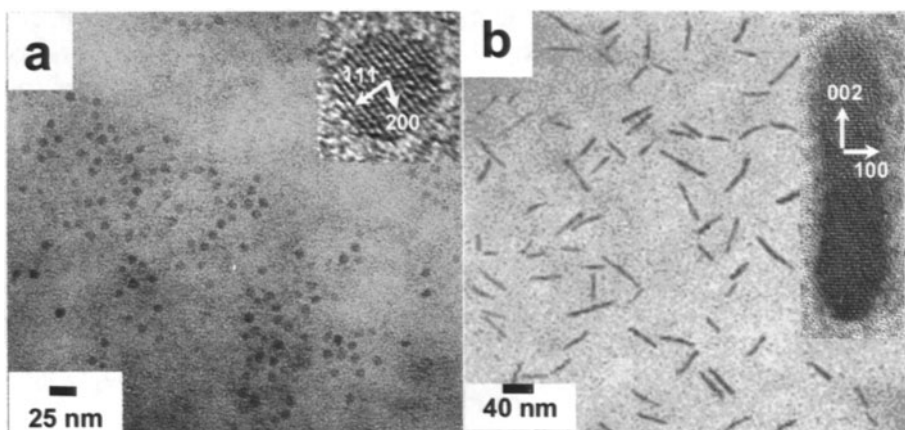
FIGURE 3.12. GaP nanocrystals (a) spheres, (b) rods. (From Cheon, 2002. Ref. 30.)

III-V semiconductor 1-dimensional nanocrystals can also be synthesized via solution-liquid-solid (SLS) processes.[31] When InP semiconductor precursors decompose, precursor molecules generate InP monomers in solution and indium metallic seeds via two cycles of In-P bond cleavage and reformation. The monomers diffuse into liquid indium seeds and eventually precipitate and crystallize along a specific direction when the liquids seeds are super-saturated, inducing the formation of wire-shaped InP nanocrystals.
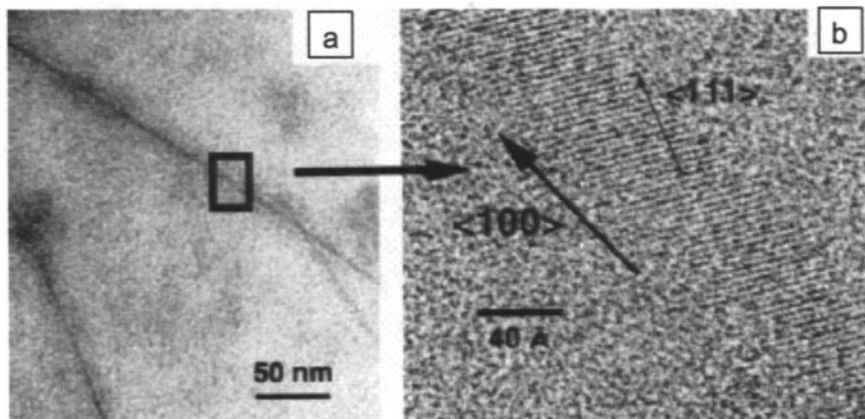
FIGURE 3.13. Silicon nanocrystals. (a) Low magnification image. (b) HRTEM image. (From Korgel, 2000, Ref. 33.)

3.2.2.3 GROUP IV SEMICONDUCTORS

In the case of group IV semiconductor systems, it is extremely difficult to obtain nanorods by typical solution based precursor injection methods due to their highly covalent character. In contrast, under gas phase based syntheses such

as chemical vapor deposition, 1-dimensional Si wires can be easily obtained on a substrate using vapor-liquid-solid (VLS) growth mechanisms.[32] In VLS growth mechanisms, monomers can form an alloy in equilibrium with their pure solid in a catalytic seed and 1-dimensional semiconductor nanowire is expelled from the seed as they reach supersaturation. Above 360°, by using gold nanocrystals as catalytic seeds, pure solid Si nanowires were obtained under a supercritical fluid environment by B. A. Korgel.[33] Size-monodispersed Au nanocrystals are necessary to achieve a narrow distribution of diameter (Figure 3.13). By changing the reaction pressure, it is also possible to control the growth direction of nanowire.

3.2.2.4 METALS

Preparation of metallic rods is also possible via a hot temperature precursor injection method. Hyeon et al. reported that iron nanorods were produced by thermal decomposition of iron pentacarbonyl in a hot surfactant solution (Figure 3.14 a).[34] Similarly, Chaudret et al. reported that rod-shaped nickel nanocrystals were formed by thermal decomposition of an organometallic precursor, $Ni(COD)_2$, (COD=cyclo-octadiene) in hot THF solution including hexadecylamine surfactants (Figure 3.14 b).[35]
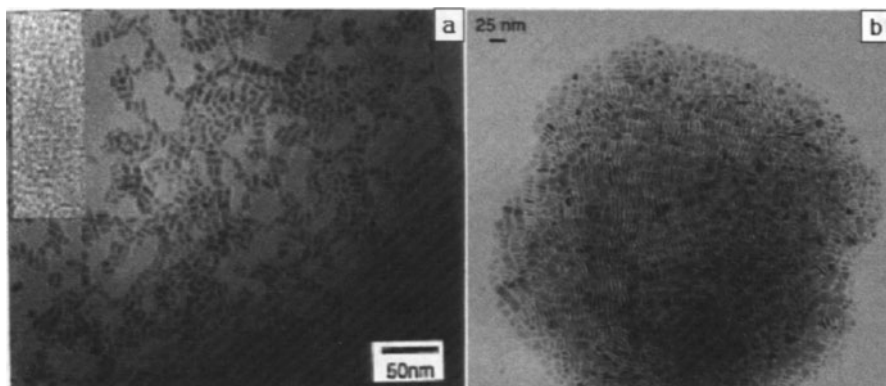
FIGURE 3.14. Various metal nanorods (a) iron nanorods (From Hyeon, 2000, Ref. 34.) (b) nickel nanorods (From Chaudret, 2001, Ref. 35.)

1-dimensional growth of gold nanorods via an electrochemical method was also possible in rod-shaped micelles reported by El-Sayed et al.[36] and Shih et al.[37] Gold ions were dissoluted from a gold anode and the shape distribution of the rods was determined by the current and the ratio of the concentration of the surfactant to that of the cosurfactant. Short Au nanorods with aspect ratios of ~3-7 mainly dominated by {100} and {110} facets with growth directions parallel to the [001] direction.

3.2.2.5 TRANSITION METAL OXIDES

Transition metal oxides are an important group of materials used in white pigment, cosmetics, supports in catalysis, and as a photocatalyst. Nanostructured titania is of particular interest with potential applications as solar cell materials. Chemseddine et al. demonstrated elongated TiO_2 nanocrystals synthesized by hydrolysis and polycondensation of titanium alkoxide $[Ti(OR)_4]$ in the presence of tetramethyl ammonium hydroxide (Me_4NOH) as a stabilizer and reaction catalyst.[38] Organic cations stabilized the anatase polyanionic core and increased monomer flux induced 1-dimensional growth of the titania nanocrystals. Banfield et al. also demonstrated naturally aligned titania nanocrystals under hydrothermal conditions,[39] by adapting an oriented attachment mechanism into the nanocrystal development (Figure 3.15).
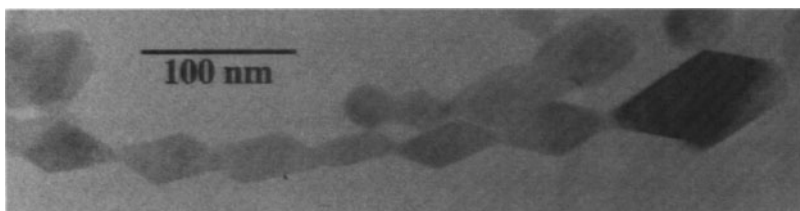
FIGURE 3.15. TEM image of naturally aligned anatase TiO_2 nanocrystals. (From Banfield, 1999, Ref. 39.)

A cubic-perovskite structured transition metal oxide is important due to its unique electronic, magnetic, and optical properties. The 1-dimensional ternary perovskite oxide was first demonstrated in solution-based synthesis by Park et al.[40] They synthesized single-crystalline cubic perovskite $BaTiO_3$ and $SrTiO_3$ by solution phase decomposition of bimetallic precursors in the presence of stabilizing ligands.

3.2.3   2-DIMENSIONAL DISCS

Unlike 1-dimensional rod systems, formation of disc-shaped nanocrystals is very rare in colloidal systems. In a kinetically driven growth regime, 1-dimensional nanorod growth is promoted when preferential growth along a specific direction is induced. Likewise, when growth along a specific axis is prevented, the formation of disc shaped nanocrystals is induced. Very recently, Alivisatos et al. reported the formation of disc shaped cobalt nanocrystals (Figure 3.16 a-b).[41] When alkylamines are added to a mixture of TOPO and oleic acid, alkylamines strongly bind to the {001} faces of hexagonally close-packed cobalt and prevent growth along the [001] directions. The nanodiscs obtained assemble into long ribbons where discs are stacked face-to-face via a magnetic interaction between individual nanodiscs (Figure 3.16 b).
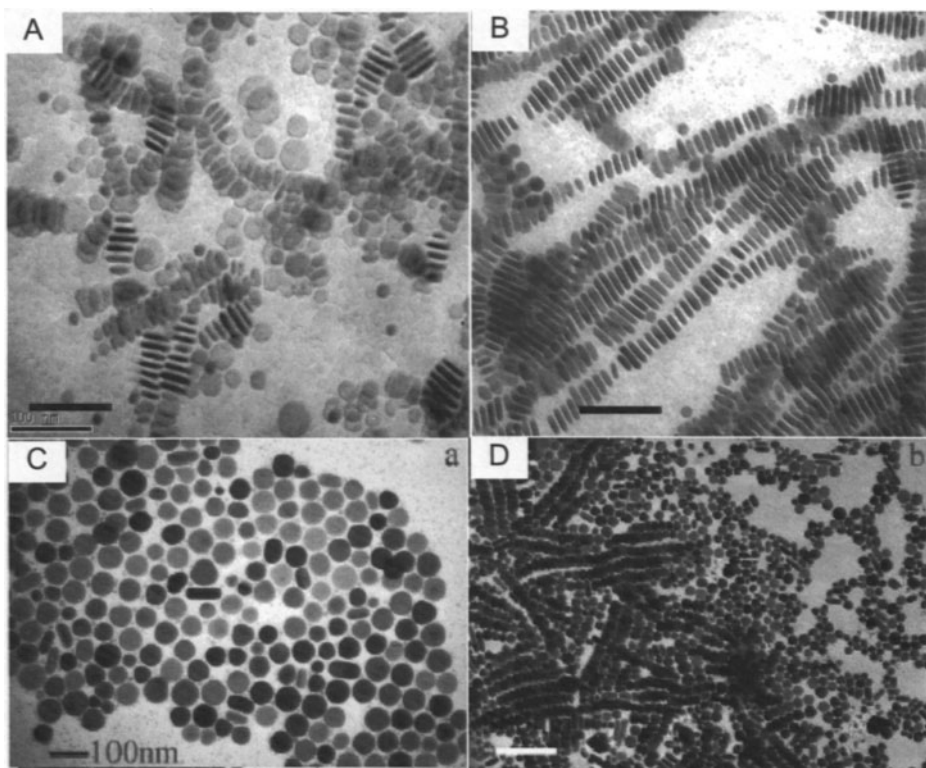
FIGURE 3.16. Various metal nanodiscs and their assemblies. (a, b) cobalt nanodiscs and their magnetic assembly. (From Puntes and Alivisatos, 2002, Ref. 41.) (c, d) silver nanodiscs and their assembly. (From Chen, 2002, Ref. 42.)

Seed mediated growth in a micelle solution also promotes disc shaped nanocrystals (Figure 3.16 c-d). Silver nanocrystals with disc shape were formed when silver nitrate solution was added to concentrated acetylammonium bromide solution containing silver seeds.[42] The disc shape of the silver nanocrystals results from plane growth from silver seeds inside the CTAB micelle structure. Silver nanocrystals obtained also assemble into necklace-like structure similar to that observed in cobalt nanodiscs. However, silver nanodiscs assembled via Van der Waals interactions between self-assembled monolayers on the basal plane of the discs (Figure 3.16 d).

In addition to the disc shapes, 2-dimensional prismatic shapes have been widely observed. These nanoprisms predominantly appear in FCC structured transition metals. Photoinduced silver nanoprisms were demonstrated by Mirkin et al.[43] (Figure 3.17). Ag nanospheres synthesized by the reduction of $AgNO_3$ were irradiated with a conventional 40-W fluorescent lamp. As the irradiation time was increased, an unexpected color change was observed from yellow (which is a characteristic surface plasmon band of the spherical particle) to green, and finally blue. Simultaneously, the shape change of nanospheres into

nanoprisms was also observed by TEM measurements. Electron energy loss spectroscopy analysis (EELS) showed that the formed triangular shaped Ag nanocrystals were actually flat-top prismatic shapes.
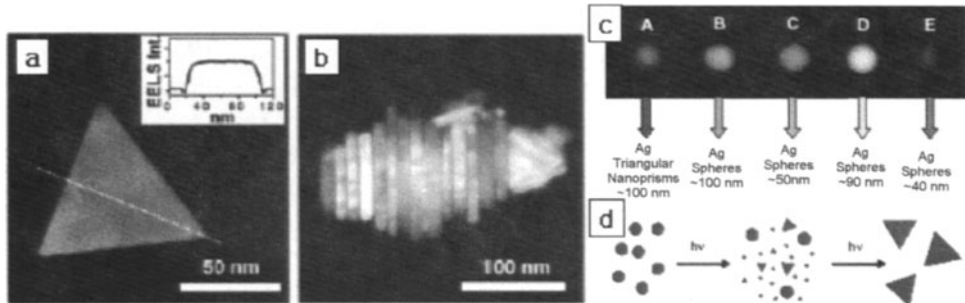
FIGURE 3.17. (a,b) TEM images of Ag nanoprisms and (c) corresponding surface plasmon color change as the shape transforms (red on the left to blue) (d) Scheme of shape transformation. (From Mirkin, 2001, Ref. 43.)

Other FCC structured transition metal nanoprisms such as Pd and Ni were also demonstrated by Reetz et al.[44] (Figure 3.18). Tetra-N-octylammonium carboxylates were used as reducing and stabilizing agents. Scanning tunneling microscopy (STM) measurements showed that the trigonal particles turned out to have an extended flat character in their shapes. Pileni et al. also observed prismatic semiconductor nanocrystals.[45] Triangular CdS nanocrystals were synthesized. The triangular nanocrystals turned out to be flat and the crystalline phase was proved as a hexagonal wurtzite structure.
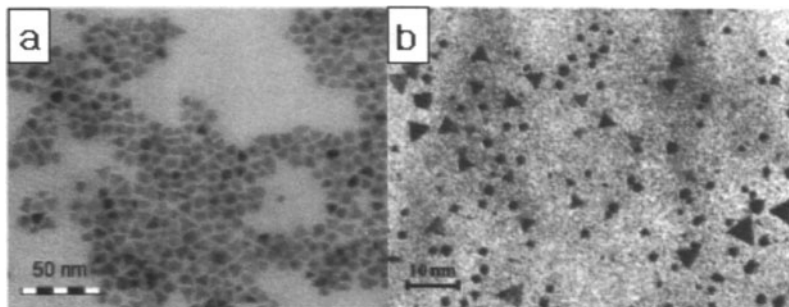
FIGURE 3.18. Various metal nanoplates with triangular shapes. (a) palladium nanoplates stabilized with glycolate (b) nickel nanoplates stabilized with tetra-N-octylammonium carboxylate (From Reetz, 2000, Ref. 44.)

3.2.4 NOVEL NANOBUILDING STRUCTURES

As described above, shape controls of nanocrystals have been widely studied between 0-dimensional spheres, icosahedrons, 1-dimensional rods, and 2-dimensional plates. These basic building blocks have unique geometry and

properties with their shapes and they can be used as components of nanobuilding structures. If the assemblies of each component with different geometries can be controlled, construction of novel nanobuilding structures may be possible. For example, L-shaped structures can be obtained using two rods and a cube and V-shaped structures can be achieved by assembling two rods and a tetrahedron. CdSe tetrapods obtained by Alivisatos and MnS tetrapods by Cheon, respectively, are a good example of such a nanosystem (Figure 3.19).[46] Under certain conditions, zinc blende tetrahedron seeds with four {111} faces and subsequent rod growth on these four surfaces resulted in tetrapod shaped nanocrystals with tetrahedral (T_d) symmetry.[25] Wire formation of MnS instead of rod-shaped nanocrystals arises from a larger surface energy difference between the {001} faces of wurtzite due to the unoccupied d orbitals of the surface manganese metals.[26]
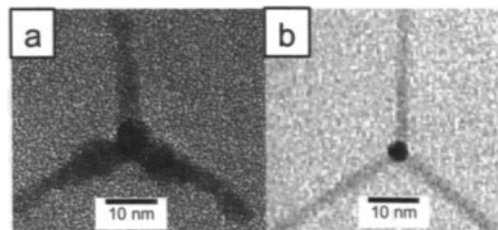
FIGURE 3.19. Various tetrapod shapes. (a) CdSe rod-based tetrapods (From Alivisatos, 2000, Ref. 46) and (b) MnS wire-based tetrapods (From Cheon, 2002, Ref. 26.)
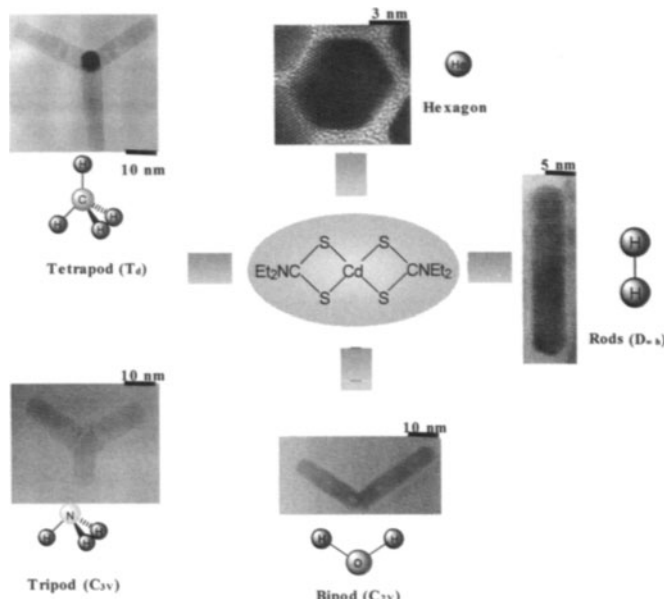
FIGURE 3.20. CdS multipods with various symmetry. The nanocrystals shape changes form isotropic sphere to rod, bipod, tripod, and tetrapod. (From Cheon, 2001, Ref. 25.)

Formation of novel multipod structures using a tetrahedron and 1-dimensional rods were thoroughly studied in the case of CdS nanocrystals. Kinetic controlled growth resulted in a systematic variation of novel structures from spheres to 1-D rod, bipod, tripod, and tetrapod with corresponding point symmetry of $D_{\infty h}$, C_{2v}, T_d, C_{3v}, respectively (Figure 3.20).

Rod-based multi pod shapes were also observed in the case of isotropic rock salt structured PbS nanocrystals.[20] Rapid injection of a PbS precursor into hot solution containing dodecanethiol as capping molecules leads to the formation of various branched nanocrystals with an angle of ~ 90° as well as cross shaped tetrapods, L-shaped bipods, T-shaped tripods, I-shaped bipods. Under kinetically fast growth along the {100} faces of the tetradecahedral seed (Figure 3.21). As the growth condition shifts into thermodynamic region (e.g. high growth temp.), the growth rate in the [111] direction accelerated and the resulting shapes were changed into rectangular cubic shapes via the star shape as a transition shape.
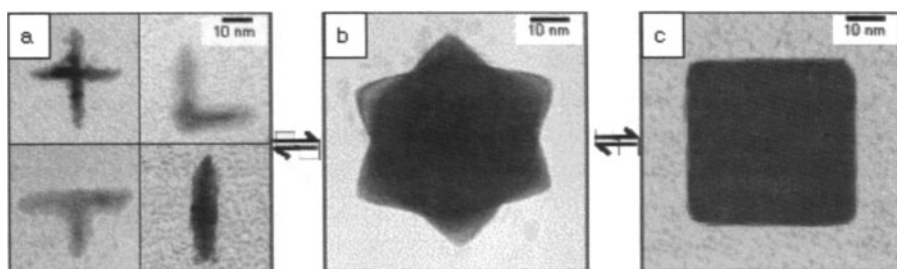
FIGURE 3.21. Shape transition of PbS nanocrystals from (a) rod-based multi-pods, through (b) nanostars as a transition shape, to (c) nanocubes. (From Cheon, 2002, Ref. 20.)

3.2.5 SUPERSTRUCUTURES: ASSEMBLIES OF NANOBUILDING BLOCKS

Superstructures that are built up with basic nanobuilding blocks can also be achieved by chemical interparticle interactions. When nanocrystals are formed with highly monodispersed size and shape, slow evaporation of solvent from nanocrsytal solution leads to highly ordered 3-dimensional close-packing of nanocrystals via Van der Waals interaction between nanocrystals coated with long chain alkane molecules. The symmetry of a close-packed array of nanocrystals can be modulated by changing parameters including particle sizes, shape, and interparticle distances.

Superlattices of CdSe nanocrystals were first reported by Bawendi et al. using selective solvent evaporation from a mixture of octane and octanol solution containing spherical CdSe nanocrystals under reduced pressures (Figure 3.22 a).[47] Superlattices obtained were in face-centered-cubic close packing of CdSe nanocrystals and exhibited novel optical characteristics that were different from

those of diluted CdSe nanospheres in solution. The emission spectra of the superlattices were red-shifted from those of individual CdSe nanocrystals through interparticle coupling, although the absorption spectra were identical.
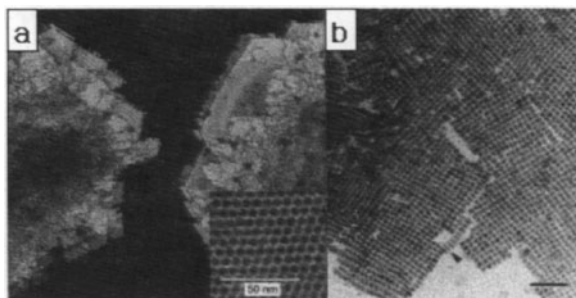
FIGURE 3.22. (a) Dark-field optical micrograph of faceted colloidal crystals. Inset : TEM image of superlattices in face-centered-cubic close packed CdSe nanocrystals. (From Bawendi, 1995, Ref. 47) (b) Rectangular superlattice of BaCrO$_4$ nanoparticles. (From Mann, 1999, Ref. 48.)

The symmetry of superlattices constructed with spheres are strongly dependent on interparticle distances. Short-chain capping groups lead to formation of cubic packed superlattices, while long chain capping groups induce hexagonal close packing of nanospheres.

Nanocrystal shape also strongly influences the symmetry of superlattices. When nanospheres were used as building blocks, superlattices with fcc or hcp symmetry were observed. However, when prismatic particles with tetragonal geometry were assembled, thin flake-like aggregates of a 2-dimensional superlattice with pseudo-rectangular symmetry were obtained (Figure 3.22 b).[48]

3.3.   SHAPE-GUIDING GROWTH MECHANISMS

Recent studies on the shape control of nanocrystals have been highly focused on 1-dimensional systems. Because 1-dimensional rod growth is the most fundamental step of anisotropic shape control, it can be possible to present general shape control strategies even for nanocrystals with highly complex structures once we understand the shape guiding mechanisms of nanorods. In this section, various proposed mechanisms and critical parameters for shape guiding processes of nanostructures will be discussed.

3.3.1   APPROACHES FOR OBTAINING 1-DIMENSIONAL NANOCRYSTALS

There have been excellent studies for the liquid phase preparation of Si and metallic rods via a 'two step seed mediated synthesis'. In the first step, spherical seed nanocrystals are synthesized and isolated. Precursors of desired 1-D structure then chemically reduced in the presence of capping molecules where seed nanocrystals serve as nucleation points. Gold nanosphere direct growth of Si nanowires by seed catalytic growth in supercritical fluid was examined by Korgel et al.,[33] and metallic rod systems including Au or Ag rods obtained by seed mediated growth in solution were presented by Murphy et al.[49] Although interface issues between the seed and growth materials have not been well resolved, this method has great potential for further advances of researches on 1-D rod structured materials. The general applicability of this method to other materials needs to be further explored.

On the other hand, researchers have also explored simpler 'one step in situ synthesis' of 1-D nanorods utilizing methods similar to those for the well-studied spherical nanocrystals. For example, the 1-D colloidal rod based system of CdSe has been successfully demonstrated by Peng and Alivisatos et al.[23,50] The use of binary capping molecules such as TOPO and HPA is effective for the generation of shape anisotropy in CdSe along with the nature of its intrinsic hexagonal structure. Recent studies on in-situ anisotropic growth of the nanocrystals propose a growth process that is referred to as "oriented attachment". Hyeon et al. reported iron nanorods that were formed by a stabilizer-induced aggregation process of iron nanospheres[34] while Kotov et al demonstrated the formation of CdTe nanowires via crystal dipole-induced self-assembly of CdTe nanospheres.[28] Although these recent studies of 'one step in situ synthesis' of 1-D nanorods show new successful avenues for a variety of novel 1-D nanorods, further efforts are required to obtain a full understanding of their growth mechanisms.

3.3.1.1   TWO STEP SEED MEDIATED GROWTH

In colloidal systems, there are two stages in nanocrystal growth – the nucleation stage and the crystal growth stage.[51] In the nucleating stage, the concentration of monomers increases rapidly and the initial seeds of the crystals are formed upon pyrolysis. During the crystal growth stage, monomers diffuse onto the seed and deposit on its surface resulting in crystal growth. A prerequisite to obtaining the monodispersed nanocrystals, is the short nucleating stage, a relatively slow growth stage, and the separation between these two stages. Otherwise, bimodal nucleation may occur and the resulting sizes and shapes of

the nanocrystals become polydispersed. One alternative is to add previously formed seeds in an effort to separate the nucleation stage from the crystal growth stage.
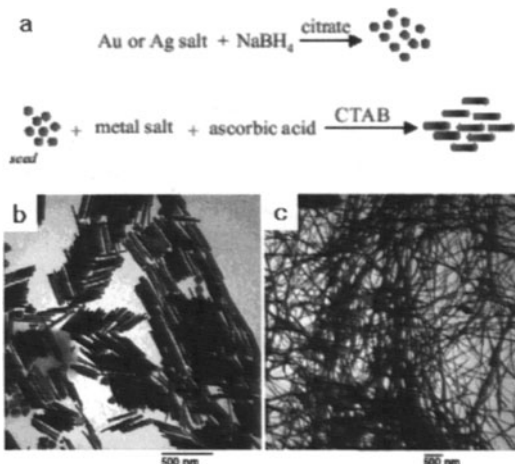
FIGURE 3.23. (a) Scheme of seed mediated Ag nanorod growth. TEM image of (b) Ag nanorod and (c) Ag nanowire. (From Murphy, 2002, Ref. 49.)

3.3.1.2 SEED MEDIATED GROWTH INSIDE A STATIC MICELLE TEMPLATE

Murphy et al. utilized nanoscale metallic seeds as nuclei for crystal growth and can obtain 1-dimensional noble metal nanorods (Figure 3.23).[49] At first, spherical metallic gold or silver seeds are made by chemical reaction of metal salt with a strong reducing agent in the presence of capping agents such as citrate. And then these seeds are added to a solution containing metal salt, a weak reducing agent and a rodlike micellar soft template. In this method, the aspect ratio is controlled by the ratio of metal seed to metal salt concentration. At lower concentrations of metal seeds, there is relatively higher monomer flux into the seed, and longer rods can be produced. Furthermore, delicate control of solution pH can make it possible to obtain aspect ratios as large as ~ 350.

3.3.1.3 SOLUTION-LIQUID-SOLID (SLS) NANOCRYSTAL GROWTH

The nanocrystal seeds can not only become the nuclei for the crystal growth but can also form the catalyst for the crystal growth. Monomers diffuse onto the catalytic seeds and form an alloy with them. As the dissolution of monomers into the seed increases, the supersaturated pure solid nanowire grows out of the catalytic seed (Figure 3.24 a).[33] Semiconductor nanowires can also be made via metallic seed catalysts. In the supercritical fluid environment, Si nanowires have been obtained via gold catalysts by B. A. Korgel (Figure 3.24 b-c). Above 360 , Si and Au can form an alloy in equilibrium with pure solid Si.

Monomers made by thermal degradation of Si precursor dissolute into Au nanocrystals until reaching a Si:Au alloy supersaturation and pure solid Si is expelled from the Au seeds. Size-monodispersed Au nanocrystals are necessary to achieve nanowire growth. By changing the reaction pressure, it is possible to control the growth direction of nanowire.
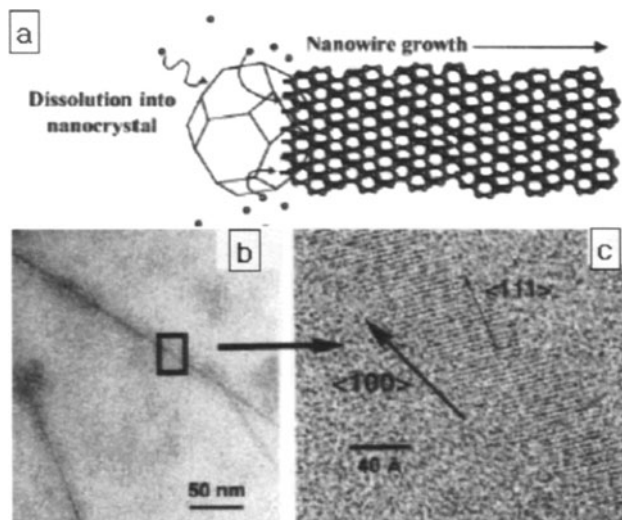
FIGURE 3.24. Seed-mediated SLS nanocrystal growth. (a) Schematic growth mechanism, (b) Low resolution TEM image, (c) high resolution TEM image of Si nanowire. (From Korgel, 2000, Ref. 33.)

3.3.1.4 ORIENTED ATTACHMENT PROCESSES

Another approach to obtain 1-dimensional nanorods is shape transformation via oriented attachment processes. Because the surface to volume ratio of nanocrystals is higher than that of bulk crystals, the surface energy significantly contributes to the total energy of nanocrystals. Therefore, when the surface area is reduced by crystal growth or aggregation processes, the total energy of the crystal decreases.

When spherical or icosahedral shaped nanocrystals are formed, the nanocrystals are terminated with several different kinds of surfaces. These surfaces have different surface energies. For example, diamond shaped anatase titanium dioxide nanocrystals that were reported by Banfield et al.[39] were truncated with three different kinds of faces: {001}, {121}, and {101} faces. Because the (001) face has the largest number of dangling bonds and the (101) face has the lowest number of dangling bonds, the surface energy of the (001) face is higher than that of the (101) face. When a sufficient thermal energy was supplied to the system, the removal of high energy surfaces was thermodynamically favorable. Thus, fusion between diamond shaped

nanocrystals along the [001] direction was preferred, resulting in a necklace shape nanocrystal.

Similar observations were made in the case of ZnO^{27} and CdTe [28] nanocrystals. In the early stages, the nanocrystals were formed with spherical shapes. However, through aging processes in aqueous solvent, the nanospheres were aligned and fused together along a specific axis in order to remove {001} faces with high surface energy. Surface reconstruction processes followed, resulting in rod-shaped nanocrystals (Scheme 3.1).
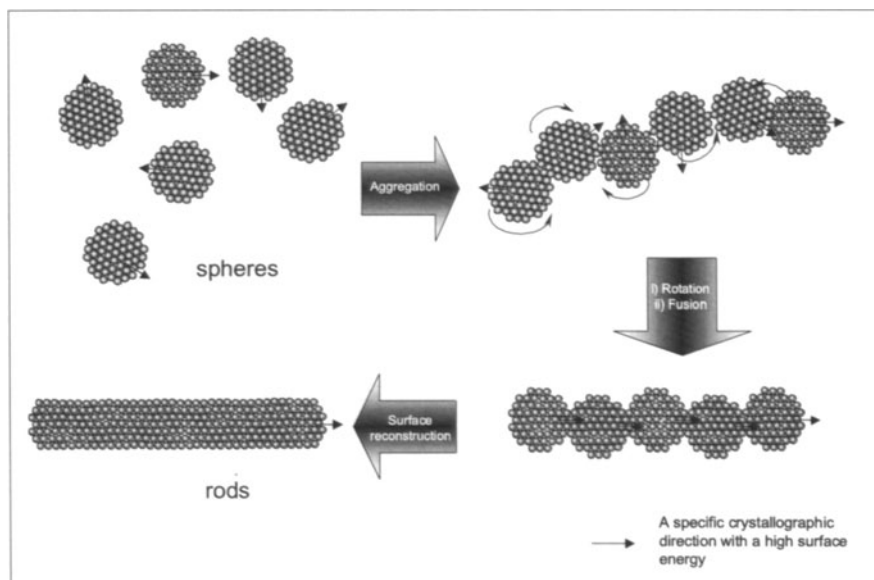
SCHEME 3.1. Illustration of oriented attachment processes.

3.3.1.5   "ONE STEP IN SITU SYNTHESIS" DRIVEN BY KINETIC AND THERMODYNAMIC PROCESSES

"One step in situ synthesis" using hot temperature injection method is another approach to obtain 1-dimensional nanocrystals. During the growth stage just following the nucleation stage that determines the preferred crystalline phase, the delicate balance between the kinetic growth and thermodynamic growth regimes strongly governs the final architecture of the nanocrystals.

3.3.1.5.1   SELECTIVE ADHESION MODEL

Surface energy of the nanocrystals can be modulated by introducing surfactants that adsorb onto surfaces of growing crystallites. Especially, when capping molecules stabilize a specific face by selective adhesion, the growth rate differences between different crystallographic directions can be accentuated.

In the CdSe growth that was reported by Alivisatos et al.,[23,46] selective adhesion of surfactants is crucial for determining the final shape. When dimethylcadmium and trioctylphosphine selenide (TOPSe) were injected into a hot surfactant mixture of trioctylphosphine oxide (TOPO) and hexylphosphonic acid (HPA), the amount of HPA that selectively binds to the specific surfaces (such as {100} and {110} faces) of the growing crystallites modulate the final shape of CdSe nanocrystals. At low HPA concentration or without HPA, only spherical shaped nanocrystals were formed. However, when the HPA concentration was increased, the HPA molecules enhanced growth along the [001] direction and blocked growth along the other directions by selective adhesion and promoted elongation of the c-axis (Figure 3.25 a).
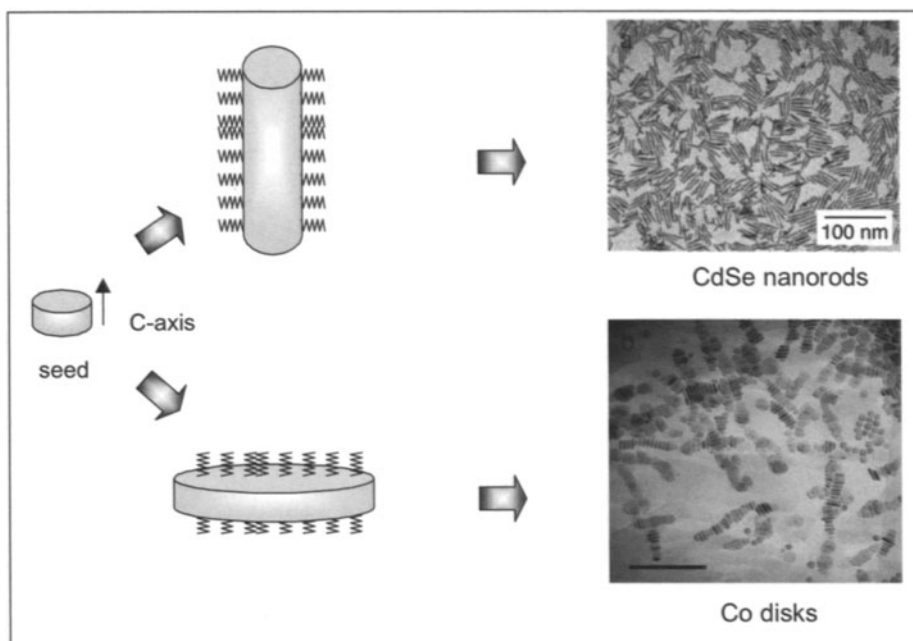
FIGURE 3.25. Growth mechanism based on surface selective adhesion model. (a) CdSe nanocrystal growth (From Alivisatos, 2000, Ref. 23. and 46.) and (b) Co nanocrystal growth (From Alivisatos, 2001, Ref. 41.)

Selective adhesion of surfactants can not only induce elongation along a specific axis but it can also induce compression along a specific axis. The formation of cobalt nanodiscs under a surface selective surfactant is a good example (Figure 3.25 b).[41] When oleic acids that bind to all surfaces of growing crystallites were used as a surfactant, only spherical shaped cobalt nanocrystals were obtained. In contrast, when small amounts of long chain alkylamine were added to the surfactant solution, alkylamine molecules that strongly adsorb to the 001 faces of hcp cobalt effectively block the growth along c-axis, resulting in disc-shaped nanocrystals.

3.3.1.5.2 DIFFUSION FLUX MODEL

Because high monomer concentration is critical for inducing the kinetic growth of nanocrystals, control of monomer concentration is also an important parameter for shape control of nanocrystals. Peng et al. proposed a CdSe nanocrystal growth model that is controlled by diffusion flux of monomers.[50] In their model, alkylphosphonic acids (APA) generate stable monomers and Cd-APA complexes, and keep the diffusion layer of growing crystallites with high monomer concentration rather than accentuating the growth rate differences by a surface selective adhesion as proposed by Alivisatos et al.. In this model, CdSe nanocrystals grow through four growth modes: 1-D growth stage, 3-D growth stage, 1-D to 2-D ripening stage, and Ostwald ripening stage. (Figure 3.26) At
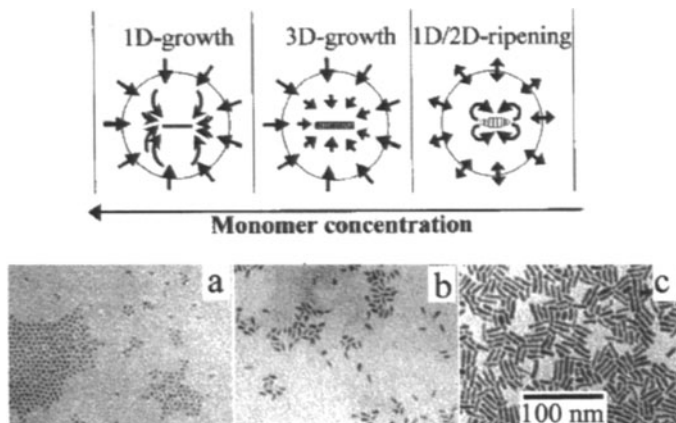
FIGURE 3.26. CdSe nanorod growth based on diffusion flux model and shape transformation from (a) spheres to (b) short rods and (c) long rods. (From Peng, 2002, Ref. 50.)

very high monomer concentrations in the bulk solution where 1-D growth is induced, the chemical potential of the monomers in bulk solution is higher than of those in the stagnant solution at all faces of the growing crystallites. This huge chemical potential difference induces a high diffusion flux into the diffusion layer and promotes 1-D growth that results from the high surface energy of the {001} faces. When the monomer concentration drops to a certain level (in the 3-D growth stage), a decrease of the chemical potential difference results in relatively low diffusion flux. In this stage, the nanocrystals grow equi-directionally. When the monomer concentration is low (in the 1-D to 2-D ripening stage), the chemical potential of the monomers in bulk solution is lower than that of the stagnant solution at the {001} faces but is still higher than that of the stagnant solution at other faces. This leads to diffusion equilibrium on the interface of the diffusion layer. Without diffusion flux, the system reaches equilibrium by dissolution and re-growth of the monomers from the {001} faces with high surface energy onto the other faces. On the other hand, at very low

monomer concentrations, the nanocrystals grow via interparticular Ostwald ripening process.

These three growth stages can be modulated by varying the growth conditions. When TOPO is used as a surfactant, Ostwald ripening process due to the instabilities of Cd-TOPO complexes govern the growth process, resulting in spherical CdSe. At low concentrations of HPA, Cd monomers form stable complexes with HPA, which leads to 1-D growth processes. High concentration of HPA promotes longer periods of 1-D growth and results in the formation of rods with higher aspect ratios.

3.3.1.5.3 DYNAMIC STERIC LIGAND MODEL

Crystallographic symmetry of the unit cells strongly influences the final shape of the nanocrystals. When crystals are in the zinc blende phase, they tend to grow isotropically along the three crystallographic axes (a, b, and c directions), resulting in 0-dimensional shapes such as spheres and cubes. However, when crystals are formed with a wurtzite structure, crystals can easily grow anisotropically, resulting in anisotropic shapes such as rods and discs. Hence, control of the key factors affecting the crystalline phases of seeds and subsequent growth is of particular interest for the shape determination.

In the case of III/V GaP semiconductor nanocrystal growth, a "dynamic steric ligand model" has been proposed by Cheon et. al.[30] In this model, the crystalline phase of the seeds and sterically induced dynamic binding of capping ligands are closely related and critical for both isotropic (O-D) and anisotropic (1-D) growth of nanocrystals. During the crystal growth, because capping molecules dynamically bind to the crystal surface, the conformation of crystal structure is highly affected by the identity of the capping molecules.

GaP semiconductors have two different crystalline phases that are in rotational isomerism- the zinc blende phase is a staggered conformation with [111] directions while the wurtzite phase is an eclipsed conformation with [001] directions (Figure 3.27 a,b).[29] Zinc blende GaP is a thermodynamically stable phase that is sterically favored. Wurtzite GaP is a kinetically stable phase that is electronically favored due to the electrostatic interaction between geminal gallium and phosphine atoms when wurtzite GaP monomers approach on to the crystal surface. When sterically bulky tertiary amines are used as capping molecules, the staggered conformation is highly favored due to the large steric hindrance between capping molecules and the crystal surface. Therefore, formation of zinc blende GaP nanospheres is favored (Figure 3.27 a). However, when sterically less hindered primary amines are present, steric energy difference between the eclipsed conformation and the staggered conformation is diminished. Steric effects on determining the binding geometry of incoming monomers are now small and electronic effects play a major role under a kinetically driven

growth regime with a high monomer concentration. Therefore, formation of wurtzite GaP phase is facilitated (Figure 3.27 b). In short, the formation of a zinc blende structure is favored with highly steric ligands such as trioctylamine, while wurtzite is dominant under less bulky linear alkyl amines (e.g. hexadecylamine).
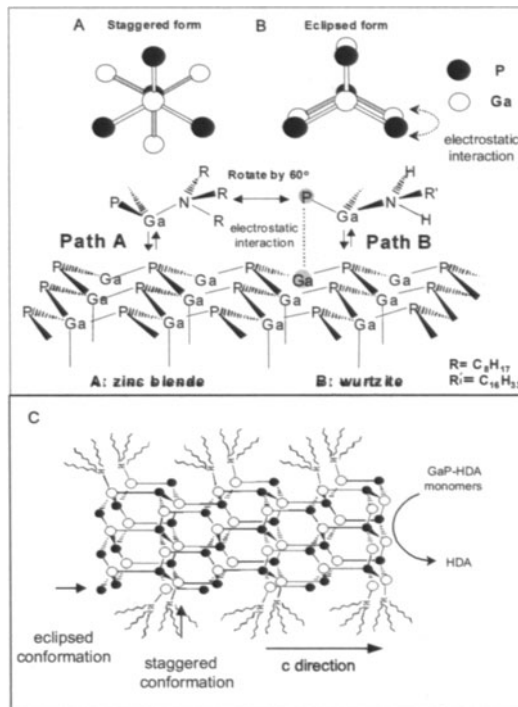
FIGURE 3.27. Dynamic steric ligand model. Steric and electronic effects on the crystalline phase (a-b) and the rod growth (c) of GaP nanocrystals. (Cheon, 2002, Ref. 30.)

Once the crystalline phase is determined, subsequent kinetic growth yields different types of shapes, which is also affected by the stereochemistry of ligands. When wurtzite seeds are formed, sterically bulky TOA selectively binds to the other faces (e.g., {100} and {110} faces) with a staggered conformation rather than to the {002} faces and blocks growth on these faces. On the other hand, GaP-HDA complexes continuously supply monomers on the {002} faces with high surface energy and therefore promote the growth in the c-direction of a rod structure (Figure 3.27 c).

3.4   CRITICAL PARAMETERS FOR ARCHITECTURE GUIDING PROCESSES OF NANOCRYSTALS

Since shape guiding process should also be operative in both 1-D and other more complex shapes (e.g. triangles, diamonds), it will be of particular interest to examine important parameters for selective growth and ultimate shape determinations. Until now, general perspectives that take into account other complex structures and their shape evolutions have been rare. Some recent studies have revealed a nice view of the controlling factors of nanocrystals ranging from isotropic (e.g. cubes, spheres) to anisotropic (e.g. rods) and in-between structures. Initially, the crystalline phase of the seeds at the nucleating stage is critical for directing the intrinsic shapes of nanocrystals due to its characteristic unit cell structure. In addition, further delicate shape control is also possible through the preferential growth of particular crystallographic surfaces of nanocrystals during kinetic controlled growth processes.

3.4.1   EFFECTS OF CRYSTALLINE PHASE OF NUCLEUS ON FINAL SHAPES

One of the critical factors that are responsible for shape determination of nanocrystals is the crystallographic phases of the initial seed during nucleation processes. The seed can potentially have a variety of different crystallographic phases and the stable phase is highly dependent on their environments. For example, by adjusting the initial temperature during the nucleation processes, their crystalline phase can be controlled. In the case of MnS semiconductor nanocrystals, the nuclei of rock-salt phase are more stable at high temperature (> 200 °C) and the formation of cubes of 30 nm are easily obtained after injection of the molecular precursor $Mn(S_2CNEt_2)_2$ into a hot solution containing alkylamine stabilizer (Figure 3.28).[26] In contrast, at temperatures below 200 °C, wurtzite structured nuclei are now more stable and preferred. Since the surface energy of the (001) face of the wurtzite phase is typically larger than that of the other faces due to its higher atomic density and number of dangling bonds, preferred growth through the c-axis is facilitated. As seen in figure 3.28, by simply lowering the growth temperature to 120 °C without changing any other growth parameters, 200 nm long nanowires of 2 nm in diameter are obtained.
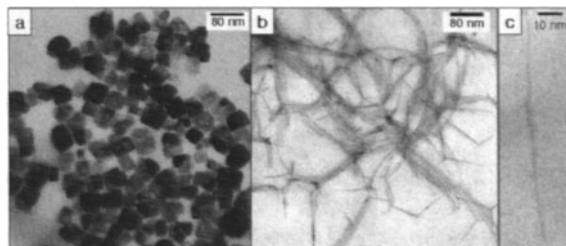
FIGURE 3.28. TEM images of MnS nanocrystals. (a) Cubes synthesized at 250 °C . (b) bundles of wires synthesized at 120 °C and (c) a TEM image of a monowire (2 nm in width). (From Cheon, 2002, Ref. 26.)

Shapes of CdS nanocrystals can also be adjusted by this temperature mediated phase control of initial seeds.[25] Under high temperature conditions (~ 300 °C), exclusive 1-D nanorod formation with purely wurtzite phased CdS is observed from high temperature stable wurtzite phased seeds, while at lower temperatures, zinc blende nuclei are now preferred and tetrahedral seeds with four {111} faces are formed. The epitaxial growth of wurtzite pods along the 00$\underline{1}$ direction from the {111} faces occurs and, as a result, CdS multipods (e.g. monopod, bipod, tripod, and tetrapod) are formed (Figure 3.29, 3.30, and Scheme 3.2, 3.3).
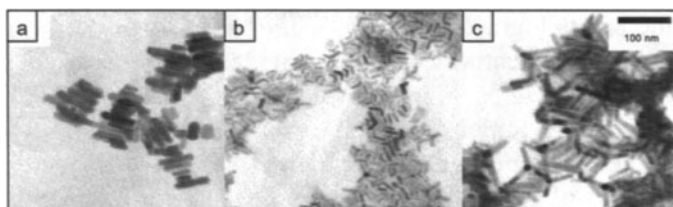
FIGURE 3.29. TEM images of temperature dependent shape change of CdS nanocrystals grown at (a) 300, (b) 180, and (c) 120 °C. Shape of CdS nanocrystals continuously changes from rods to bipods, tripods, and tetrapods. (From Cheon, 2001, Ref. 25.)
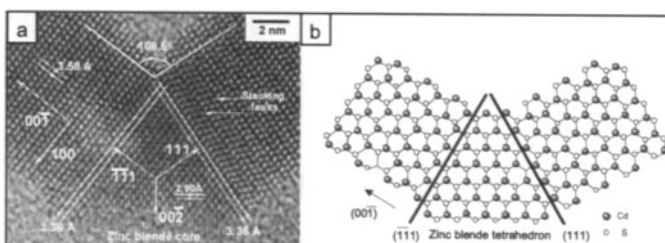
FIGURE 3.30. Atomic structure of bipod shaped nanocrystals (a) HRTEM image of CdS tetrapods and (b) 2-d projected model of bipod shaped CdS nanocrystals. (From Cheon, 2001, Ref. 25.)
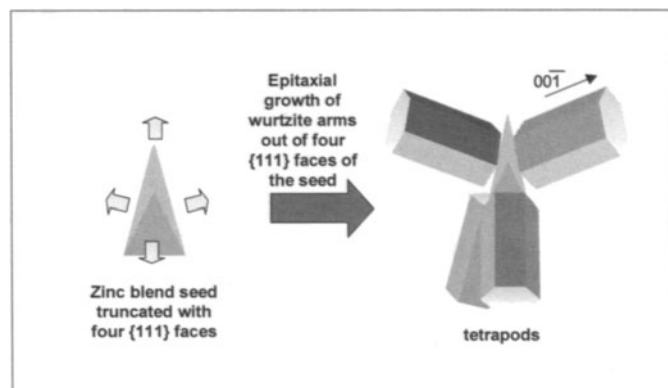
SCHEME 3.2. Growth processes of tetrapods. i) Zinc blende seed formation with T_d geometry ii) Epitaxial growth of wurtzite arms out of four {111} faces of the seed.
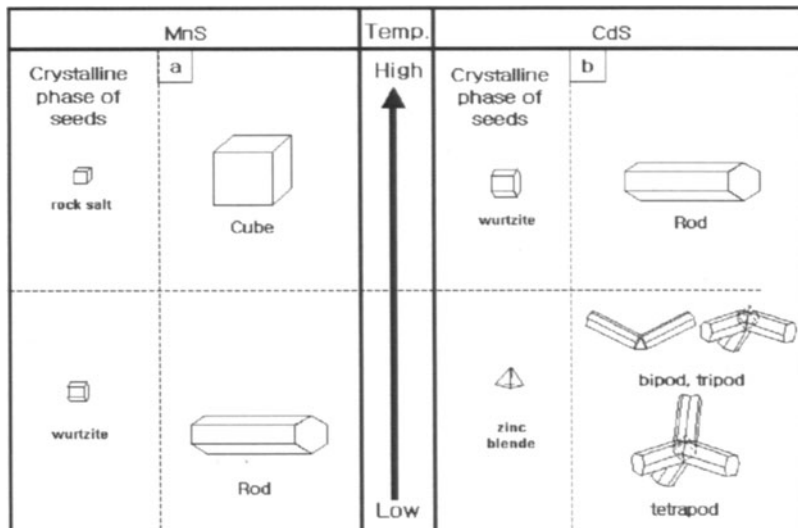
SCHEME 3.3. Shape changes of (a) MnS and (b) CdS nanocrystals by crystalline phase control of seeds.

3.4.2 SHAPE CONTROL UNDER KINETIC CONTROLLED PROCESSES AND CAPPING MOLECULAR EFFECTS

After the preferred crystalline phase has been determined in the nucleation stage, a balance between the kinetic growth and the thermodynamic growth regimes strongly governs the final architecture of the nanocrystals in the growth stage. Thermodynamically stable isotropic growth of nanocrystals is preferred in the thermodynamic growth regime that is characterized by a sufficient supply of thermal energy (kT) and low flux of monomers. In contrast,

in the non-equilibrium kinetic growth regime in which there is a high flux of monomers, selective anisotropic growth between different crystallographic surfaces is facilitated. There are at least four different parameters that can influence the growth pattern of nanocrystals (Figure 3.31). Intrinsic surface
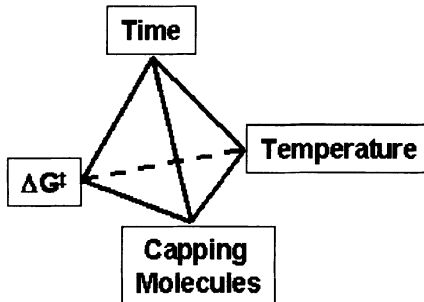
FIGURE 3.31. Critical parameters for architecture guiding processes of nanocrystals.

energy of the crystallographic face of the seed is also important since the kinetic energy barrier ($\Delta G^{\neq}$) is inversely proportional to the surface energy. These surface properties can also be tailored by the types and amounts of adsorbing organic capping molecules. The growth processes should be quenched in an appropriate time since longer times can result in the formation of thermodynamically stable shapes of nanocrystals. Finally, molecular precursors which can be decomposed under mild conditions (e.g. low temperature) are also critical for kinetic processes.

The shape evolution of PbS nanocrystals with symmetric rock salt structure is a good example.[20] Rapid injection of a PbS molecular precursor induces the formation of tetradecahedron seeds that are terminated by {100} and {111} faces and subsequent competitive growth on these two different types of crystalline faces determines the final shape (Figure 3.32. bottom). Typically, in the rock salt structure, the {111} surface has a higher surface energy than the{100} surface. When excess thermal energy is supplied by utilizing high growth temperatures (e.g. E=kT, T~250 °C), the thermodynamic regime governs the growth process and, due to faster growth on the {111} faces, the formation of cube shaped PbS nanocrystals is favored (Figure 3.35 c). However, in the presence of a strongly binding capping molecule (e.g. dodecanethiol), the thiol molecule binds to the {111} surface via a μ^3-Pb$_3$-SR bridging mode while weakly binding to the {100} faces. The surface energy of the {111} faces can selectively be lowered significantly relative to that of the {100} faces (Figure 3.33). Therefore, under the conditions of low temperature (~ 120 °C) and in the presence of a strongly binding dodecanethiol capping molecule, the growth process shifts into the kinetic growth regime, and growth on the {100} faces with high surface energy is preferred. This results in 1-D rod based single- and multi-pod structures (Figure 3.35 a).
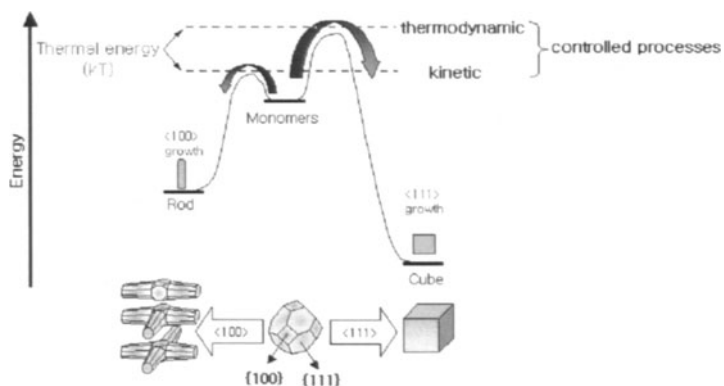
FIGURE 3.32. Schematic energy diagram of PbS nanocrystals and growth modes and final shape of nanocrystals grown along different growth directions from tetradecahedron seed
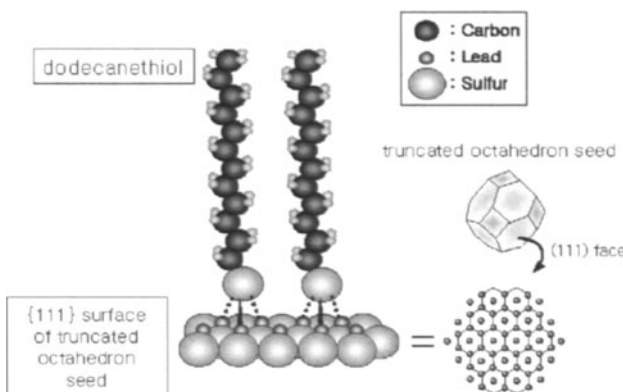
FIGURE 3.33. Strong μ^3-Pb$_3$-SR bridging mode of dodecanethiol on {111} surfaces of PbS nanocrystals.

HRTEM images of multi-pods can be good evidence for the preferable growth along the [100] directions. The image of tadpole shaped nanocrystals and lattice distance measurements indicates that the rod grows along the <001> direction. Hexagonal shape of the truncated octahedral seed with four {111} and two {100} faces was observed (Figure 3.34 a). In the case of the cross-shaped nanocrystals, [100] directional growth was also observed. The separation angle between the pods of the cross is 90° and an octagonal shape consistent with the [001] projection of a tetradecahedron is observed at the central junction of the cross (Figure 3.34. b). Moreover, at intermediate temperatures (e.g. 180 °C), as a transient species, star-shaped nanocrystals possessing both the characteristics of 0-D and 1-D structures are formed (Figure 3.35 b).
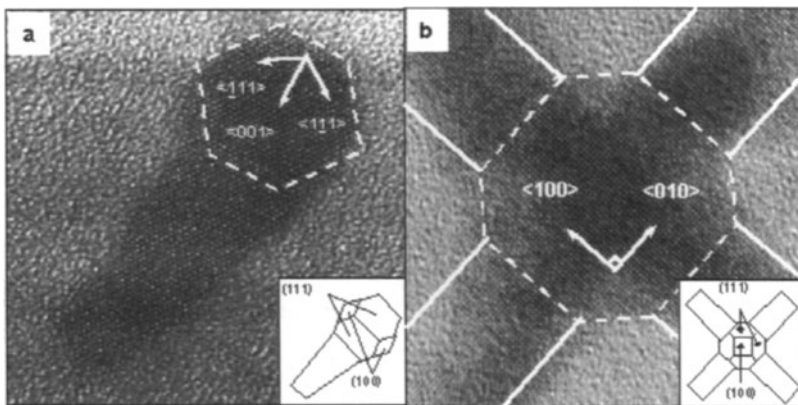
FIGURE 3.34. (a) A HRTEM image of tadpole shaped monopod with zone axis of [110]. (b) A HRTEM image of cross shaped tetrapod of PbS nanocrystals with zone axis of [001]. (From Cheon, 2002, Ref. 20.)
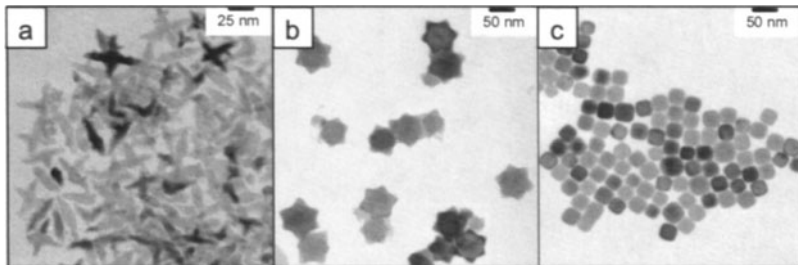
FIGURE 3.35. TEM images of (a) rod-based multipods, (b) star-shaped nanocrystals, and (c) cubes. (From Cheon, 2002, Ref. 20.)

Careful control of the growth regime and capping molecules also promotes the shape evolution of CdSe nanocrystals. As described in the previous section, CdSe rod growth was induced by introducing alkylphosphonic acids.[23]

Although the role of alkylphosphonic acids (APA) is not clear, the acids induce rapid growth along the 001 axis. At a low APA concentration, formation of spheres or short rods is favored. At a relatively high APA concentration, formation of long rods is preferred. At a very high APA concentration, the growth rate difference between the $(00\underline{1})$ face and other faces is accentuated and induces shrinking of the $(00\underline{1})$ face, which results in pencil and arrow shaped nanocrystals. Control of growth regimes also affects the final shape of CdSe. At low monomer concentrations, spherically shaped CdSe was produced. However, when a large amount of monomers was added via multiple injections, anisotropic

growth out of the {001} faces of spheres as induced. Therefore, teardrop- and rice- shaped nanocrystals were formed (Figure 3.36).[46,52]
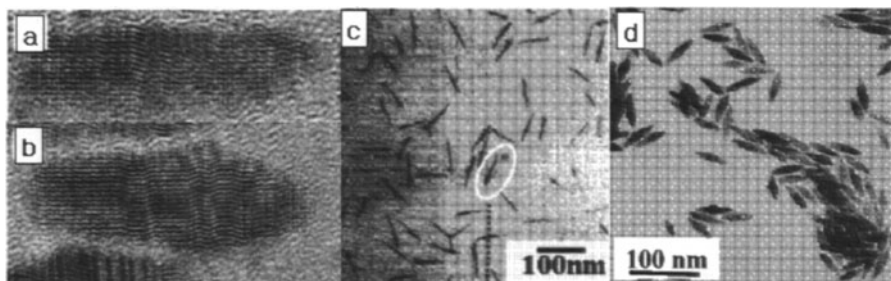
FIGURE 3.36. HRTEM image of (a) pencil-, (b) arrow-shaped CdSe nanocrystals. (From Alivisatos, 2000, Ref. 46) TEM image of (c) tadpole-, (d) rice-shaped CdSe nanocrystals. (From Peng, 2002, Ref. 52.)

Critical factors for architecture guiding processes are the crystal phase of the initial seeds, a delicate control between kinetic and thermodynamic growth regimes by varying temperature and monomer concentration, and surface energy control via changing capping molecules. With careful consideration of these parameters, it will be possible to control and program the geometry of nanoarchitectures.

3.5.   FUTURE DIRECTION

Recent developments on the shape control of colloidal nanobuilding blocks have been in quite fast track rapidly advancing after a rather long induction period since the discovery of 0-D building blocks such as CdSe. Various synthetic approaches have now been developed and many structurally unprecedented nanocrystals have been discovered in high quality. Novel properties and manipulations of these materials, especially 1-D rods, will enable the successful developments of nanodevices such as LEDs. There are also many other developments on the verge of breakthroughs to next generation devices. Even with these successes in the past few years, the syntheses have been rather limited to 1-D shape nanocrystals and a narrow range of specific materials systems. The success of this field depends heavily upon the development of more versatile, but reliable and simple synthetic schemes for the tailored architecture of nanobuilding blocks with desired components. At the same time, an understanding of the guiding laws of nanocrystals growth is of particular importance. Many new and as of yet undiscovered nanobuilding blocks will become the key components in next generation nanodevices with novel phenomena and exciting implications for nanoscience and nanotechnology.

ACKNOWLEDGEMENTS

REFERENCES

1. Present address: Department of Chemistry, Korea Advanced Institute of Science and Technology, Korea.
2. Chestnoy, N.; Hull R.; Brus, L. E. *J. Chem. Phys.* **1986,** *85,* 2237.
3. Steigerwald, M. L.; Brus, L. E. *Acc. Chem. Res.* **1990,** *23,* 183. (Reprinted in part with permission. Copyright 1990 American Chemical Society.)
4. Goldstein, A. N.; Echer, C. M.; Alivisatos, A. P. *Science* **1992,** *256,* 1425.
5. Murray, C. B.; Norris, D. J.; Bawendi, M. G. *J. Am. Chem. Soc.* **1993,** *115,* 8706. (Reprinted in part with permission. Copyright 1993 American Chemical Society.)
6. Vossmeyer, T.; Katsikas, L.; Giersig, M.; Popovic, I. G.; Weller, H. *J. Phys. Chem.* **1994,** *98,* 7665.
7. Lee, K. -B.; Lee, S.-M.; Cheon, J. *Adv. Mater.* **2001,** *13.* 517.
8. Kastner, M. A. *Rev. Mod. Phys.* **1992,** *64,* 489.
9. Klein, David L.; Roth, R.; Lim, A. K. L.; Alivisatos, A. P.; McEuen, P. L. *Nature* **1997,** *389,* 699.
10. Hu, J.; Li, L.; Yang, W.; Manna, L.; Wang, L.; Alivisatos, A. P. *Science* **2001,** *292,* 2060. (Reprinted with permission. Copyright 2001 Science.)
11. Park, J.-I.; Kang, N.-J.; Jun, Y.-w.; Oh, S. J.; Ri, H.-C.; Cheon, J. *ChemPhysChem.* **2002,** 543.
12. Bean, C.P.; Livingston, J. D. *J. Appl. Phys.* **1959,** 30.
13. Cullity, B. D. *Introduction to Magnetic Materials* Addison Wesley, London, **1972.**
14. Markovich, G.;Collier, C. P.; Henrichs, S. E.; Remacle, F.; Levine, R. D.; Heath, J. R. *Acc. Chem. Res.* **1999,** *32,* 415.
15. Postma, H. W. Ch.; Teepen, T.; Yao, Z.; Grifoni, M.; Dekker, C. *Science* **2001,** *293,* 76.
16. Huang, Y.; Duan, X. F.; Cui, Y.; Lauhon, L. J.; Kim, K. H.; Lieber, C. M. *Science* **2001,** *294,* 1313.
17. Rueckes, T.; Kim, K.; Joselevich, E.; Tseng, G. Y.; Cheung, C. L.; Lieber, C. M. *Science* **2000,** *289,* 94.
18. Hubbard, A. T. In *Surfactant Science Series*; Sugimoto, T., Eds.; Marcel Dekker Inc.: New York·Basel, 2000; Vol. 92.
19. Ahmadi, T. S.; Wang, Z. L.; Green, T. C.; Henglein, A.; El-Sayed, M. A. *Science* **1996,** *272,* 1924. (Reprinted with permission. Copyright 1996 Science.)
20. Lee, S.-M.; Jun, Y.; Cho, S.-N.; Cheon, J. *J. Am. Chem. Soc.* **2002,** *124,* 11244. (Reprinted in part with permission. Copyright 2002 American Chemical Society.)
21. Trindade, T.; O'Brien, P.; Zhang, X.; Motevallic, M. *J. Mater. Chem.*, **1997,** *7,* 1011.
22. Li, L.; Walda, J.; Manna, L.; Alivisatos, A. P.; *Nano. Lett.* **2002,** *2,* 557.
23. Peng, X.; Manna, L.; Yang, W.; Wickham, J.; Scher, E.; Kadavanich, A.; Alivisatos, A. P. *Nature* **2000,** *404,* 59. (Reprinted by permission from Nature copyright 2000 Macmillan Publishers Ltd.)
24. Jun, Y.; Choi, C.-S.; Cheon, J. *Chem. Commun.* **2001,** 101.
25. Jun, Y.; Lee, S.-M.; Kang, N.-J.; Cheon, J. *J. Am. Chem. Soc.* **2001,** *123,* 5150. (Reprinted in part with permission. Copyright 2001 American Chemical Society.)
26. Jun, Y.; Jung, Y.; Cheon, J. *J. Am. Chem. Soc.* **2002,** *124,* 615. (Reprinted in part with permission. Copyright 2002 American Chemical Society.)

27. Pacholski, C.; Kornowski, A.; Weller, H. *Angew. Chem. Int. Ed.* **2002**, *41*, 1188.

28. Tang, Z.; Kotov, N. A.; Giersig, M.; *Science* **2002**, *297*, 237.

29. Yeh, C.-Y.; Lu, Z. W.; Froyen, S.; Zunger, A. *Phys. Rev. B*. **1992**, *46*, 10086.

30. Kim, Y.-H.; Jun, Y.; Jun, B.-H.; Lee, S.-M.; Cheon, J. *J. Am. Chem. Soc.* **2002**, *124*, 13656. (Reprinted in part with permission. Copyright 2002 American Chemical Society.)

31. Trentler, T. J.; Hickman, K. M.; Goel, S. C.; Viano, A. M.; Gibbons, P. C.; Buhro, W. E. *Science* **1995**; *270*, 1791.

32. Morales, A. M.; Lieber, C. M. *Science* **1998**, *279*, 208.

33. Holmes, J. D.; Johnston, K. P.; Doty, R. C.; Korgel, B. A. *Science* **2000**, *287*, 1471. (Reprinted with permission. Copyright 2000 Science.)

34. Park, S.-J.; Kim, S.; Lee, S.; Khim, Z. G.; Char, K.; Hyeon, T. *J. Am. Chem. Soc.* **2000**, *122*, 8581. (Reprinted in part with permission. Copyright 2000 American Chemical Society.)

35. Cordente, N.; Respaud, M.; Senocq, F.; Casanove, M.-J.; Amiens, C.; Chaudret, B. *Nano. Lett.* **2001**, *1*, 565. (Reprinted in part with permission. Copyright 2001 American Chemical Society.)

36. El-Sayed, M. A. *Acc. Chem. Res.* **2001**, 34, 257. (Reprinted in part with permission. Copyright 2001 American Chemical Society.)

37. Feldheim, D. L.; Foss, Jr. C. A. *Metal Nanoparticles; Synthesis, Charaterization, and Applications*; Marcel Dekker, Inc.: New York·Basel, 2002; pp 163-182.

38. Chemseddine, A.; Moritz, T. *Eur. J. Inorg. Chem.* **1999**, 235.

39. Penn, R. L.; Banfield J. F. *Geochimica. Et. Cosmochimica. Acta.* **1999**, *63*, 1549.

40. Urban, J. J.; Yun, W. S.; Gu, Q.; Park, H. *J. Am. Chem. Soc.* **2002**, *124*, 1186.

41. Puntes, V. F.; Zanchet, D.; Erdonmez, C. K.; Alivisatos, A. P.; *J. Am. Chem. Soc.* **2002**, *124*, 12874. (Reprinted in part with permission. Copyright 2002 American Chemical Society.)

42. Chen, S.; Fan, Z.; Carroll, D. L. *J. Phys. Chem. B*. **2002**, *106*, 10777. (Reprinted in part with permission. Copyright 2002 American Chemical Society.)

43. Jin, R.; Cao, Y.; Mirkin, C. A.; Kelly, K. L.; Schatz, G. C.; Zheng, J. G. *Science* **2001**, *294*, 1901. (Reprinted with permission. Copyright 2001 Science.)

44. Bradley, J. S.; Tesche, B.; Busser, W.; Maase, M.; Reetz, M. T. *J. Am. Chem. Soc.* **2000**, *122*, 4631. (Reprinted in part with permission. Copyright 2000 American Chemical Society.)

45. Pinna, N.; Weiss, K.; Urban, J.; Pileni, M.-P. *Adv. Mater.* **2001**, *13*, 261.

46. Manna, L.; Scher, E. C.; Alivisatos, A. P. *J. Am. Chem. Soc.* **2000**, *122*, 12700. (Reprinted in part with permission. Copyright 2000 American Chemical Society.)

47. Murray, C. B.; Kagan, C. R.; Bawendi, M. G. *Science* **1995**, *270*, 1335. (Reprinted with permission. Copyright 1995 Science.)

48. Li, M.; Schnablegger, H.; Mann, S. *Nature* **1999**, *402*, 393. (Reprinted by permission from Nature copyright 1999 Macmillan Publishers Ltd.)

49. Murphy, C. J.; Jana, N. R. *Adv. Mater.* **2002**, *14*, 80.

50. Peng, Z. A.; Peng, X. *J. Am. Chem. Soc.* **2001**, *123*, 1389. (Reprinted in part with permission. Copyright 2001 American Chemical Society.)

51. Sugimoto, T. *Monodipersed Particles*; Elsevier: Amsterdam, 2001.

52. Peng, Z. A.; Peng, X. *J. Am. Chem. Soc.* **2002**, *124*, 3343. (Reprinted in part with permission. Copyright 2002 American Chemical Society.)

4

Nanoparticle Scaffolds for Devices and Sensors

Angel E. Kaifer

Center for Supramolecular Science and Department of Chemistry, University of Miami
Coral Gables, FL 33124-0431, U.S.A.

4.1. INTRODUCTION

Modified metal and semiconductor nanoparticles have become the subject of an extremely active field of chemical research in the last few years. This widespread interest is understandable considering the proliferation of simple chemical methods for the preparation of metal and semiconductor particles with sizes in the range 1-100 nm,[1] which is of great interest in emerging nanotechnologies. The properties of metal and semiconductor nanoparticles in this size range differ from those of the corresponding bulk materials and approach the molecular limit.[2] For the smallest nanoparticles, the distribution of electronic states departs from the usual band structure and discrete states will appear at the band edges. Electrons may undergo quantum confinement and these systems may exhibit unique electronic, magnetic and optical properties associated with the so-called *quantum dots*. Furthermore, as the size of the nanoparticle decreases, a larger fraction of the constituent atoms are located on its surface. This is particularly important when dealing with metals with applications in catalysis, because of the high cost associated with these materials.

Colloids, nanoparticles and *clusters* are all terms applied to describe these systems, which may often give rise to some confusion. From a historical perspective colloidal particles are considerably larger than a few

nanometers and are usually stabilized by electric charges. On the other hand, clusters are small atom groupings and their sizes tend to be rather small. The term nanoparticle is more general and can be applied to any kind of system as long as the characteristic dimensions are in the nanometer range. In this chapter, the preferred general term will be 'nanoparticle'. The term 'colloids' will be reserved for dispersions of electrostatically-stabilized particles with individual diameters above 10 nm and 'clusters' will only be used to describe systems containing a well-defined number of atoms and having diameters below 3 nm. While metal and semiconductor colloidal particles have been known for several decades (centuries in some specific cases, such as colloidal gold), it must be clearly recognized that the fast growth of research in the field of metal nanoparticles has followed the seminal work of Brust and Schiffrin.[3] These authors reported a rather simple solution method for the preparation of gold nanoparticles protected by monolayers of alkanethiolates. Alkanethiolate monolayers on planar gold surfaces are the most extensively studied class of self-assembled monolayers.[4] Brust, Schiffrin and coworkers showed that similar monolayers can be prepared around gold nanoparticles, endowing them with solubility in organic solvents and allowing their isolation as solids that can be re-dissolved and used at will, similarly to any molecular compounds.[5] Furthermore, this preparative methodology allows a reasonable degree of control on the size of the nanoparticles, and most groups have targeted the technologically attractive 1-5 nm size range.

In this chapter we will essentially focus on metal nanoparticles and their use as building blocks to prepare molecular devices and sensors. A good fraction of the chapter is thus devoted to the preparation and characterization of nanoparticles decorated with molecular recognition (binding) sites on their surfaces. These modified or derivatized nanoparticles are expected to combine the properties of their metallic cores with the molecular recognition ability of the binding sites present in their organic 'skins' or protecting monolayers. Novel properties required for applications as sensors and other devices are expected to result from an optimal combination of all these features. Finally, the emphasis in this chapter is squarely placed on nanoparticles modified with synthetic functional groups. Those readers interested in nanoparticle modification with biological materials are directed to Chapter 10.

4.2. NANOPARTICLES MODIFIED WITH MOLECULAR OR IONIC RECEPTORS

4.2.1. GENERALITIES

The attachment of organic molecules to metal and semiconductor nanoparticles affords an easy way to create chemical functionality on their surfaces. For instance, the particles can be made more hydrophobic by the surface attachment of lipophilic organic compounds.[5] Nanoparticles soluble in solvents as nonpolar as toluene and chloroform may thus be readily prepared. In general terms, the organic skin of the inorganic nanoparticle may determine or modify some of its properties. The capping or protecting organic monolayers can play very important roles in the overall chemistry of the particles and furnish them, for instance, with redox active or fluorescent functional features.[5] From the standpoint of building devices and, more specifically, sensors, it is desirable to express in these organic monolayers the ability to selectively recognize and bind target substrate compounds. In this regard, several decades of work on the development of host-guest binding interactions[6] provide a good number of systems to choose from.

4.2.2. HYDROGEN BONDING RECEPTORS

Hydrogen bonding is extremely important in biological systems and has thus played a crucial role in the development of synthetic host-guest chemistry.[7] Therefore, it is not surprising that hydrogen bonding receptors have been one of the first classes of molecular receptors expressed on the surface of nanoparticles. In 1997, the group of Fitzmaurice and co-workers started a long series òf reports on the modification of TiO_2 nanoparticles -- prepared by arrested hydrolysis of titanium tetraisopropoxide-- with the stabilizer N,N'-2,6-pyridinediylbis(undecamide) (compound **1** in Figure 4.1).[8] ^{1}H NMR spectroscopic data indicated that the two undecyl aliphatic chains of this compound stick to the surface of the nanoparticles and lead to the surface attachment of the diamidopyridine functionality. Using ^{1}H NMR and FT-IR spectroscopic data these authors demonstrated that the TiO_2-immobilized diamidopyridine group engages in three-point hydrogen bonding with uracyl derivatives (see, for instance, compound **2** in Figure 4.1) in $CDCl_3$ solution. Fitzmaurice coined the term *Heterosupramolecular Chemistry* to describe the formation of supramolecular host-guest complexes at the surface of the colloidal TiO_2 nanoparticles.[8] Later on, this group covalently attached a 4,4'-bipyridinium electron acceptor group to the uracyl derivative and demonstrated the photoinduced electron transfer from the

TiO_2 conduction band to the viologen group in the uracyl derivative within the resulting heterosupramolecular assembly.[9]
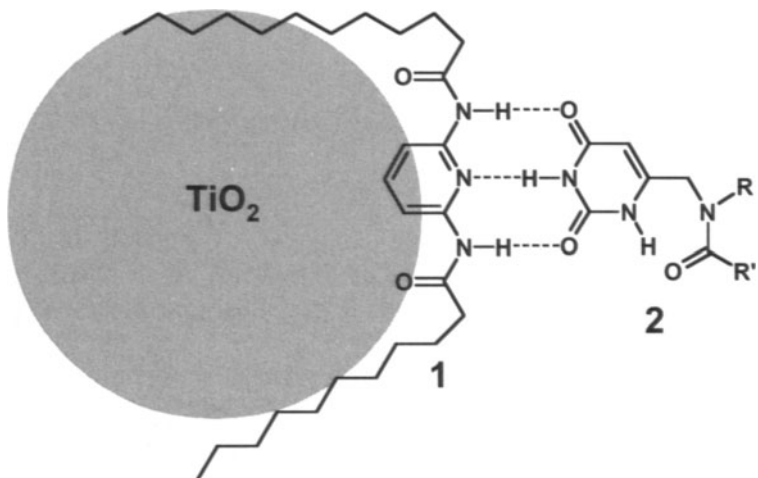
FIGURE 4.1. Fitzmaurice's heterosupramolecular hydrogen bonded complex on the surface of a titanium oxide nanoparticle.

A similar approach can be utilized to program the assembly of nanoparticles by preparing colloidal TiO_2 particles stabilized by diamidopyridine receptors, such as **1**, and colloidal TiO_2 particles stabilized by uracyl derivatives, such as **2**.[10] Mixing these two types of particles in chloroform solution yields assemblies in which the nanoparticles are connected by three-point hydrogen bonded complexes of the kind represented in the figure above. However, this general approach presents some difficulties because the hydrogen bonding sites are simply physisorbed onto the surface of the nanoparticle. Concerns about long-term stability and reproducibility will be more easily dispelled by the covalent immobilization of the receptor. In order to address these concerns, Fitzmaurice took advantage of the Brust and Schiffrin method[3] to prepare ~3 nm gold nanoparticles capped by monolayers of dodecanethiolate.[11] Refluxing these nanoparticles in a chloroform solution containing a mixture of dodecanethiol and 12-mercaptododecyl-1-uracyl replaces a small fraction of the unfunctionalized thiolates by uracyl-functionalized thiolates on the surface of the gold nanoparticles. This surface exchange reaction[12] affords a convenient way to introduce functional groups in the capping monolayer of the nanoparticles, without any significant changes in the nanoparticle size distribution. The degree of nanoparticle functionalization can be simply controlled by factors such as thiol ratios in the exchange solution. The resulting functionalized nanoparticles were shown to engage in hydrogen

bonding interactions with diamidopyridine derivatives in solution (see Figure 4.2), giving rise to three-point complexes similar to those previously employed by this group with modified colloidal TiO$_2$ particles.[11]
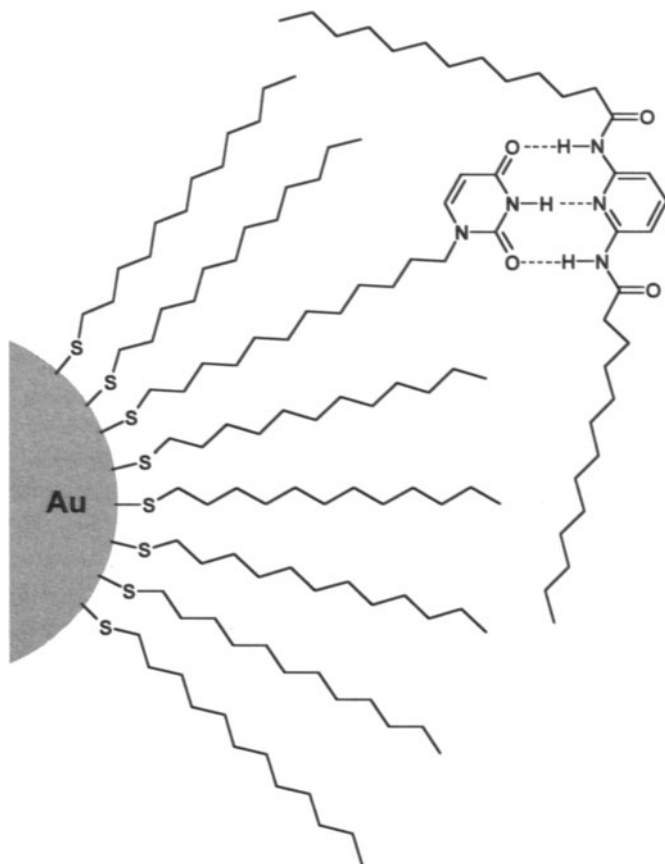
FIGURE 4.2. Fitzmaurice's hydrogen bonded complex between gold-immobilized uracyl groups and solution diamidopyridine derivatives.

This group further elaborated on this idea by modifying silver nanoparticles (~7 nm in diameter) with surface diamidopyridine receptors, which can engage in hydrogen bonding with bifunctional bis(uracyl) derivatives in chloroform solution.[13] The thiolate-capped silver nanoparticles were prepared by methods similar to Brust and Schiffrin's. The nanoparticle assemblies resulting from the interactions with the bis(uracyl) derivatives were characterized by NMR, FT-IR and Dynamic Light Scattering (DLS) spectroscopic data.

In 1999 Rotello and coworkers started their extensive investigation of thiolate-capped gold nanoparticles modified with hydrogen bonding

receptors. Initially, this group reported the preparation of octanethiolate-capped gold nanoparticles onto which diamidopyridine functional groups could be incorporated via place exchange reactions with suitably functionalized thiols.[14] The surface of the resulting typical gold nanoparticle (ca. 2 nm in diameter) is composed of 78 alkanethiols and 12 thiols functionalized with diamidopyridine receptors, capable of establishing hydrogen bonding interactions with flavins (Figure 4.3).
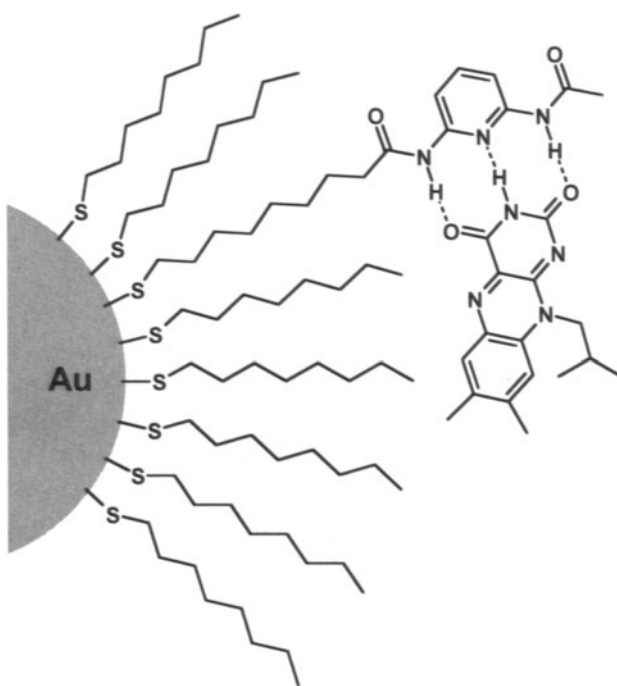
FIGURE 4.3. Rotello's hydrogen bonded complex between a flavin and a nanoparticle-immobilized diamidopyridine receptor.

The redox activity of flavins allows the examination of their binding to the nanoparticle-immobilized amidopyridine receptors in two oxidation states. From voltammetric data, the authors concluded that the one-electron reduced form of the flavin is more strongly bound than the oxidized form.[14] Rotello and coworkers elaborated further on this interesting system by adding another thiol --terminally functionalized with aromatic pyrene groups-- to their capping monolayers.[15] The idea is that the combination of hydrogen bonding, provided by the diamidopyridine subunits, and aromatic stacking, from the pyrene groups, would act synergistically and improve the binding properties of the sites created on the nanoparticle surfaces. Later on, this group very cleverly exploited the radial nature of these monolayers by realizing that, when the recognition functional groups are brought closer to

the gold surface, binding is enhanced.[16] This effect results from the increased cooperativity between the hydrogen bonding and π stacking components, as the two functionalities are forced closer together by shorter aliphatic tethers (Figure 4.4). Interestingly, since aromatic stacking disfavors binding of the more electron-rich, reduced flavin, the stability of the complex with the reduced flavin increases as the binding sites are pulled away from the gold surface.[16]
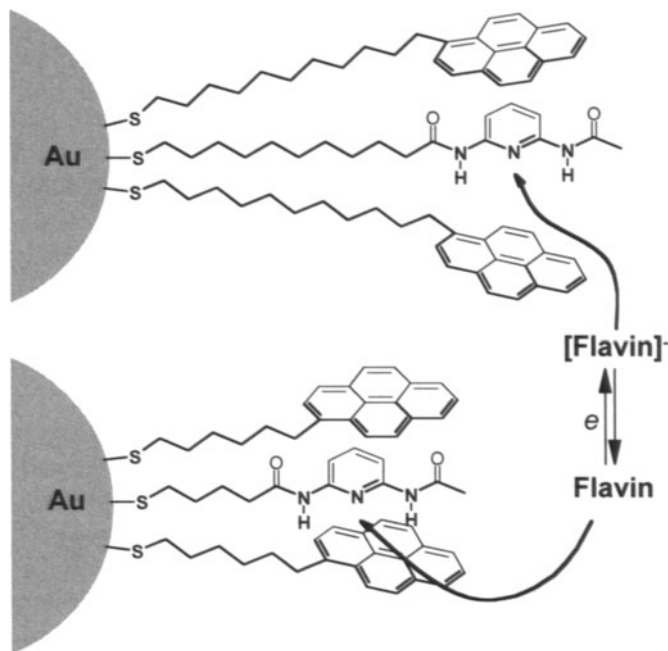
FIGURE 4.4. Schematic representation of the redox-induced selectivity associated with radial structural effects within the capping monolayers.

Rotello and coworkers have also investigated a number of fundamental points with alkanethiolate-capped nanoparticles. Their interest in probing hydrogen bonding within these monolayers led them to prepare a series of alkanethiols containing amide functional groups at variable distances from the thiol group. These amide-functionalized thiols were used in the preparation of capping monolayers and the extent of hydrogen bonding was investigated as a function of distance to the gold surface by NMR spectroscopy.[17] The relative protecting effect of the various amide-functionalized thiols was also studied through etching experiments with cyanide.[18] This group has also carried out interesting investigations on the interactions of gold nanoparticles with polymers having complementary binding sites,[19] which are described in more detail in Chapter 8.

4.2.3. CROWN ETHER RECEPTORS

Crown ethers have been extensively investigated as molecular receptors for alkali and alkaline-earth metal ions in nonaqueous solvents.[20,21] These cyclic polyether compounds are also effective receptors for ammonium ions.[22] In joint work with the Stoddart group, Fitzmaurice and coworkers prepared gold nanoparticles (~4 nm in diameter) protected by thiols bearing terminal dibenzo-24-crown-8 functional groups.[23] The resulting nanoparticles were characterized using elemental analysis, TEM and ^{1}H NMR spectroscopic data. The organic monolayer protecting these nanoparticles contains an average of 300 crown ether-functionalized thiol molecules. The guest selected for this study was the dibenzylammonium cation 3. Stoddart and coworkers had previously shown that guest 3 forms a stable pseudorotaxane in solution by threading through dibenzo-24-crown-8 (see Figure 4.5).[24]
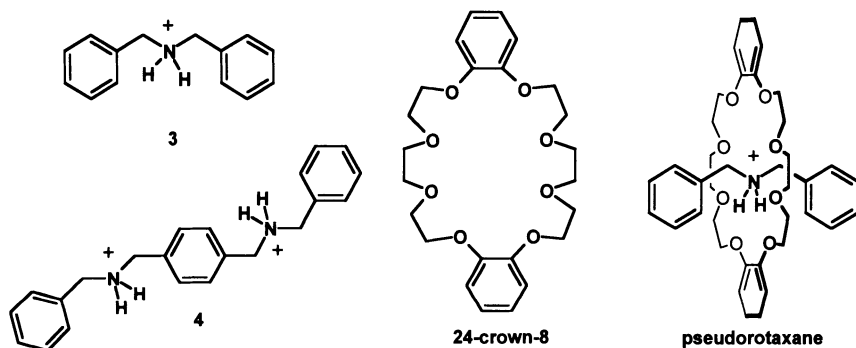
FIGURE 4.5. Structures of guests 3 and 4, host 24-crown-8 and the pseudorotaxane formed between guest 3 and 24-crown-8.

Using ^{1}H NMR spectroscopy these authors initially investigated the binding interactions of monocation 3 with the nanoparticle-immobilized crown ethers in CDCl$_3$ solution. The NMR data verified that pseudorotaxane complexes were formed on the surface of the nanoparticles.[23] Quantitative analysis of the NMR data revealed that ca. 84% of the crown binding sites were complexed with guest 3. The increased charge on the surface of the nanoparticles led to their slow precipitation from CDCl$_3$ solution. The nanoparticles could be re-dissolved by addition of about 10% CD$_3$CN. Further analysis of the NMR binding data suggests that the binding of guest 3 is cooperative. These authors continued their study of this host-guest system by using compound 4 (see Figure 4.5), which is capable of acting as an effective guest for the assembly of a ternary complex containing two 24-crown-8 hosts. In this series of experiments Fitzmaurice and coworkers utilized narrowly dispersed silver nanoparticles (~7 nm in diameter)

protected by dodecanethiol monolayers.[25] The crown ether binding sites were incorporated by place exchange reactions with alkanethiols containing terminal 24-crown-8 subunits. As anticipated the exposure of the resulting crown ether-functionalized silver nanoparticles to ditopic guest **4** in CDCl$_3$:CD$_3$CN (4:1, v/v) solution led to a slow, but gradual increase in the apparent hydrodynamic radius of the nanoparticles, as measured by DLS methods. This finding reflects the slow aggregation of the nanoparticles that is driven by the molecular connections created each time that guest **4** is bound by two crown ether units attached to different nanoparticles (Figure 4.6).
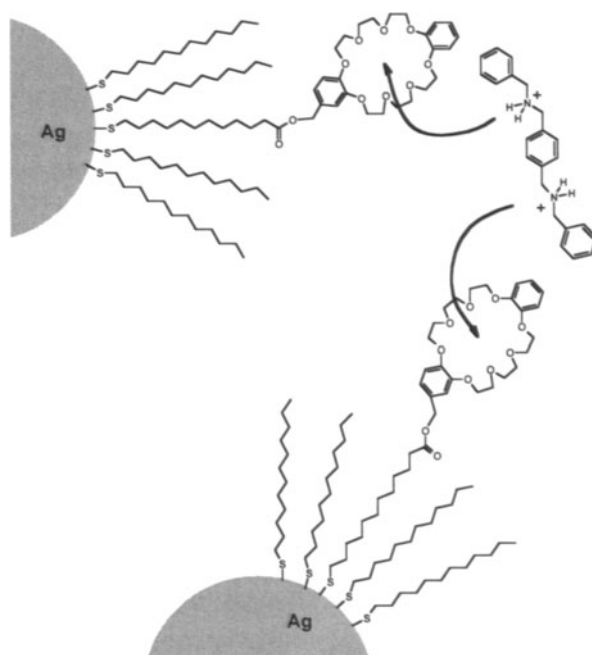
FIGURE 4.6. Aggregation of Fitzmaurice's silver nanoparticles resulting from the interparticle binding linkages established by dicationic guest **4**.

It is important to point out here that, in order to insure that guest **4** will bind to crown ethers attached to *different* nanoparticles, as opposed to crown ethers on the same nanoparticle, the crown ether units must be kept relatively far away from one another by 'dilution' with inert (dodecanethiol) molecules. Fitzmaurice and coworkers accomplished this by preparing dodecanethiol-capped silver nanoparticles onto which the crown ether-functionalized thiols were incorporated, in a subsequent step, through place-exchange reactions. This approach has a number of advantages. First, the preparation of alkanethiolate-capped metal nanoparticles follows established procedures and leads to well-characterized particles with relatively narrow

size distributions. Second, place exchange reactions[12] allow nanoparticle functionalization to an extent that can be readily controlled in each specific case using simple parameters, such as reaction times and thiol concentrations. Usually, thiol exchange reactions do not affect the preexisting size distribution. Furthermore, place exchange reactions lead to moderate loading levels of the incoming (functionalized) thiol, which typically results in dilution of the functional subunits in the surface of the nanoparticles. When the functional groups are binding sites, their surface separation may perhaps lead to lack of binding cooperativity, but also insures that ditopic guests may establish molecular linkages between hosts attached to separate nanoparticles.

4.2.4. Cyclodextrins

The cyclodextrins (CDs) are cyclic glucopyranose oligomers which constitute a well-known class of molecular receptors.[26,27] They have been extensively utilized in multiple applications due to their ability to form stable inclusion complexes in aqueous media. The cyclodextrins have a long history as stabilizers of metal colloidal particles.[28] However, in order to truly achieve their immobilization on metal nanoparticles, synthetic modification of the native CD receptors is necessary.

Native Cyclodextrins

OH

n = 6, α-CD
n = 7, β-CD
n = 8, γ-CD

Thiolated Cyclodextrins

SH

n = 6, SH-α-CD
n = 7, SH-β-CD
n = 8, SH-γ-CD
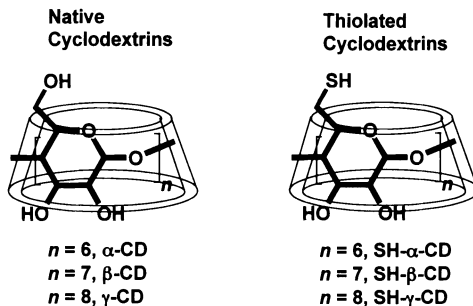
FIGURE 4.7. Native and thiolated cyclodextrins.

The author's group has followed this synthetic approach, replacing the primary hydroxyl groups on the smaller opening of the CD receptors by thiols.[29] The resulting thiolated CDs (see structures in Figure 4.7) can be covalently attached to a gold surface through the formation of multiple thiolate-gold bonds between each CD receptor and the surface. Upon chemisorption, the immobilized CD hosts are oriented with their wider opening pointing to the solution (away from the metal surface) in an optimum configuration to complex suitable guests present in the solution phase.[28] Furthermore, the polarity of the interface between the organic monolayer and the solution is determined by the presence of the secondary hydroxyl groups on the CDs, and nanoparticles modified with thiolated CDs

are expected to be water-soluble. This is particularly convenient because the host properties of the CDs are indeed optimized in aqueous media.[26,27]

Several procedures were used to prepare CD-capped gold nanoparticles. Initially, citrate-stabilized colloidal gold particles (~12 nm in diameter) were prepared and treated with small amounts of SH-β-CD.[30] In a slow surface modification process, due to the low solubility of the thiolated CD in aqueous media, some of the citrate molecules were displaced by CDs. The resulting particles, characterized by photon correlation spectroscopy (PCS), Scanning Electrochemical Microscopy (SEM) and FT-IR spectroscopy, responded to the addition of the ferrocene dimer **5** by undergoing a reversible flocculation process, which reflects the aggregation of the colloidal particles driven by the complexation of the dimer by two CD hosts attached to different particles (Figure 4.8).
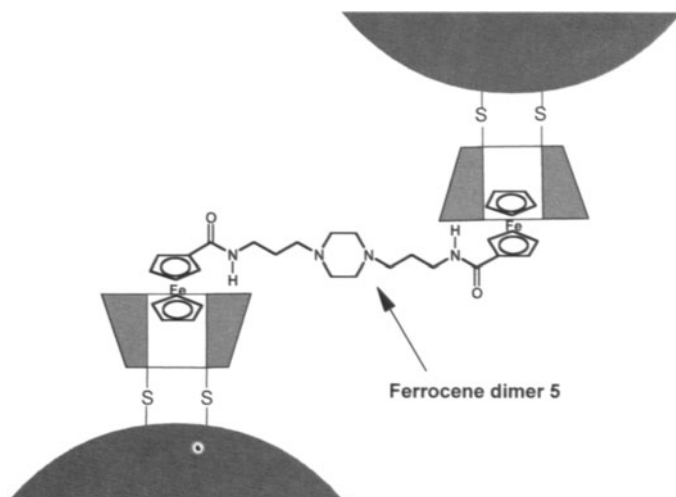
FIGURE 4.8. Aggregation of gold colloidal particles derivatized with thiolated β-CD through complexation of a ferrocene dimer.

This system shows flocculation properties that can be controlled via host-guest complexation. For instance, the rate of CD-modified colloid flocculation could be adjusted by adding variable concentrations of free β-CD to the solution, as the free CD competes with the particle-immobilized CD for the available ferrocene binding sites in dimer **5**. Similar effects were found when variable amounts of a monomeric ferrocene derivative were added to the solution.[30] Unfortunately, this methodology is limited by the fact that the CD hosts can only cover a moderate fraction of the total surface on the gold particles. Therefore, the author's group decided to develop a different procedure for nanoparticle derivatization with CDs.

Inspired by the work of Brust and Schiffrin,[31] we devised a method to prepare CD-capped gold nanoparticles in one step. In this procedure, a

solution of $AuCl_4^-$ and the corresponding thiolated CD in DMSO (or DMF) was quickly reduced by the fast addition of $NaBH_4$.[32] Gold nucleation and nanoparticle growth take place in the presence of the capping agent (the thiolated cyclodextrin) and, as expected, the average size of the final nanoparticles is determined by the S/Au ratio in the reaction mixture. The resulting CD-capped gold nanoparticles could be precipitated with CH_3CN, dried and re-dissolved in aqueous solution. Characterization by TEM, ^{1}H NMR and FT-IR spectroscopic data confirmed the structure and composition of the nanoparticles, which were prepared in different sizes through the range 2-7 nm.[32] Electrochemical data confirmed that the nanoparticle-immobilized CD hosts retain their binding ability and form inclusion complexes with ferrocenemethanol and adamantanol (Figure 4.9).
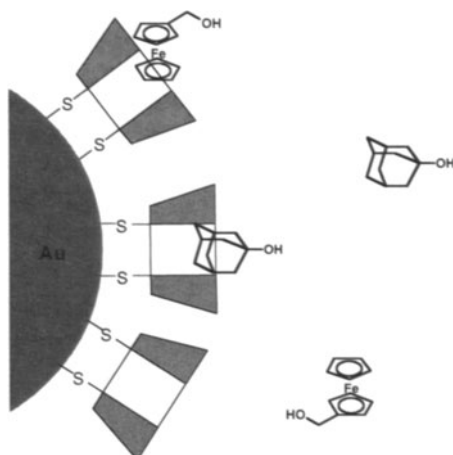
FIGURE 4.9. Competitive binding between ferrocenemethanol and adamantanol guests with the β-CD hosts immobilized on Au nanoparticles.

^{1}H NMR spectroscopic data confirmed that the CD surface coverage in these CD-capped gold nanoparticles was about 75%, which translates into 10-11 CD hosts on the surface of a single ~3 nm nanoparticle.[33] The large CD surface coverage attained in these nanoparticles affords the possibility of changing the polarity of their surfaces via complexation of appropriate guests. For instance, every compound in the series of cationic, amphiphilic ferrocene derivatives shown in Figure 4.10 is expected to bind to the β-CD hosts immobilized on these Au nanoparticles. However, only those guests with a sufficiently long aliphatic chain should be able to change the polarity of the nanoparticle surfaces and foster their transfer to a chloroform solution phase. This expectation was fully realized and our experiments revealed that only guests **9** and **10** were effective to accomplish the phase transfer of the hydrophilic β-CD-capped Au nanoparticles to chloroform solution.[33]

Compounds **6-8** were fully ineffective, although they were shown to bind to the CD receptors on the nanoparticles.
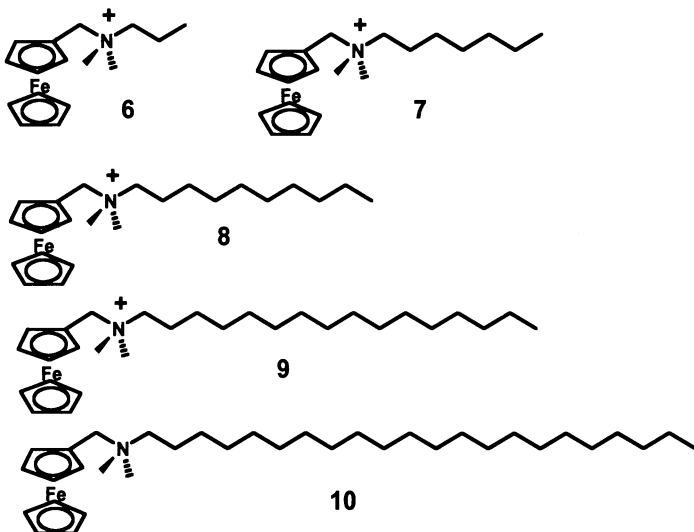
FIGURE 4.10. Ferrocene-containing guests surveyed as candidates to effect the transfer to chloroform of hydrophilic, CD-capped Au nanoparticles.

The structural composition of the assemblies formed upon extensive binding of guests **9** or **10** to the β-CD hosts on the surface of the nanoparticles and their transfer to chloroform solution is of considerable interest. A number of control experiments indicated that the presence of small amounts of water was crucial for their structural integrity, probably because the β-CD-ferrocene inclusion complex falls apart in the absence of water. All the experimental data point to assemblies in which the Au nanoparticles are surrounded by a thin aqueous layer containing the β-CD-ferrocene complexes and the counterions required to compensate for the positive charges on the ferrocene guests, with the aliphatic chains of **9** or **10** extending into the surrounding chloroform solution. These assemblies are conceptually similar to gold-filled reverse micelles.[33]

Fullerene C_{60} is known to form a stable complex with two molecules of γ-CD.[34,35] In this complex, the two CDs interact with opposite ends of the C_{60} molecule. This binding configuration coupled with the rigidity of the CD hosts immobilized on the surface of the nanoparticles opened up the possibility of using C_{60} molecules as noncovalent linkers between different γ-CD-capped nanoparticles. With this central idea in mind, the author's group carried out a series of experiments exposing stable aqueous dispersions of γ-CD-capped Au nanoparticles to minute amounts of C_{60}.[36] The extremely low solubility of this fullerene in aqueous solution could be enhanced by the presence of γ-CD binding sites. We were able to show that

the γ-CD Au nanoparticles (3.2 nm in diameter) increased the apparent aqueous solubility of C_{60} and that its solubilization led to the self-assembly of the nanoparticles, which formed network aggregates with diameters in the range of 200- 300 nm as measured by PCS and TEM.[36] The resulting aggregates could be reversibly broken up by the addition of free γ-CD host to the solution, as the free CD competes with the nanoparticle-immobilized CD for the limited amount of C_{60} molecules present in the solution. All these experimental data indicate that the aggregation results from the formation of 2:1 γ-CD-C_{60} complexes acting as multiple noncovalent linkages between the nanoparticles (Figure 4.11).
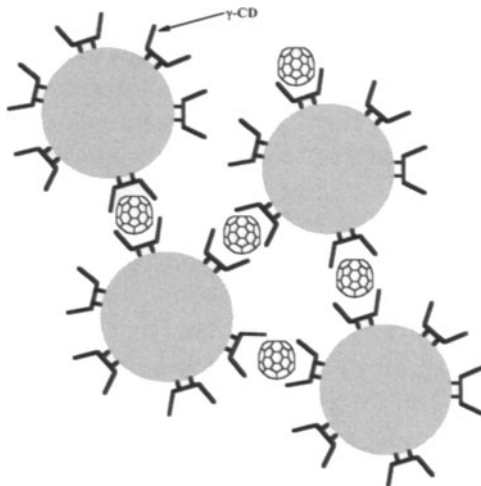
FIGURE 4.11. C_{60}-induced network aggregation of γ-CD-capped Au nanoparticles in aqueous solution.

4.2.5. ANION RECEPTORS

The recognition and binding of anions has a long history and the literature contains a large number of receptors designed with this main goal.[37] Astruc and coworkers have taken elements of this existing knowledge and applied them to the preparation of novel gold nanoparticles that serve as scaffolds for the construction of oxyanion binding sites.[38,39] These authors utilized gold nanoparticles capped with dodecanethiol or hexadecanethiol, which were prepared following Brust and Schiffrin's procedures. Their nanoparticles had an average diameter of 2.1 nm (270 Au atoms in the core) and 103 alkanethiolate chains.[39] In a second modification step, these nanoparticles were submitted to place-exchange reactions with alkanethiols terminated in amidoferrocenyl units. ^{1}H NMR spectroscopic analysis of the final nanoparticles was utilized to ascertain the extent of the exchange reaction, which varied depending on the reaction conditions and molecular

details of the system. The resulting Au nanoparticles contain variable numbers of amidoferrocenyl groups on their surfaces. Cyclic voltammetric experiments in CH_2Cl_2 solution revealed that the electrochemical oxidation of all the ferrocenyl groups attached to any of these nanoparticles takes place in a single voltammetric wave. In other words, the ferrocenyl groups behave as independent redox centers, without any detectable communication among them. This voltammetric wave departs slightly from the shape anticipated for perfectly reversible electrochemical systems. For instance, the cathodic peak in the reverse scan is generally sharper than the anodic peak in the forward scan, which can be attributed to some adsorption of the oxidized, ferrocenium form of the nanoparticles.[39]

Addition of the $H_2PO_4^-$ (as its tetrabutylammonium salt) to a CH_2Cl_2 solution of nanoparticles containing surface-immobilized amidoferrocenyl groups leads to substantial changes in the voltammetric response of this system. A new redox wave appears at more cathodic potentials in addition to the original wave for the oxidation of the ferrocenyl groups. The currents associated with the new wave increase, at the expense of the current levels of the original wave, as the concentration of added $H_2PO_4^-$ also increases. Eventually, when the concentration of $H_2PO_4^-$ is equivalent to the concentration of amidoferrocenyl units present in the solution, the original wave disappears and the new wave reaches full development. This electrochemical behavior reflects the binding of $H_2PO_4^-$ ions to the amide groups adjacent to the ferrocenyl units, which act as voltammetric reporters of the interaction. The cathodic shift observed in the oxidation potential means that the binding is stronger with the oxidized, positively charged forms of the ferrocenyl groups (see Figure 4.12) than with the reduced, neutral forms. It is also remarkable that the observed potential shift in the presence of $H_2PO_4^-$ (-220 ± 20 mV) is almost independent from the extent of amidoferrocenyl functionalization of the nanoparticle and the length of the alkanethiols used in the capping monolayer. However, the potential shift was observed to increase if the unsubstituted cyclopentadienyl ring of ferrocene was replaced by $C_5H_4COCH_3$ and decrease if replaced by pentamethylcyclopentadienyl. Other anions, such as HSO_4^- are also detected voltammetrically by these nanoparticles, but the magnitude of the observed anion-induced effects is much smaller. The authors conclude that as sensors for $H_2PO_4^-$ these functionalized nanoparticles compare favorably with ferrocenyl dendrimers in terms of ease of preparation and selectivity.[39]
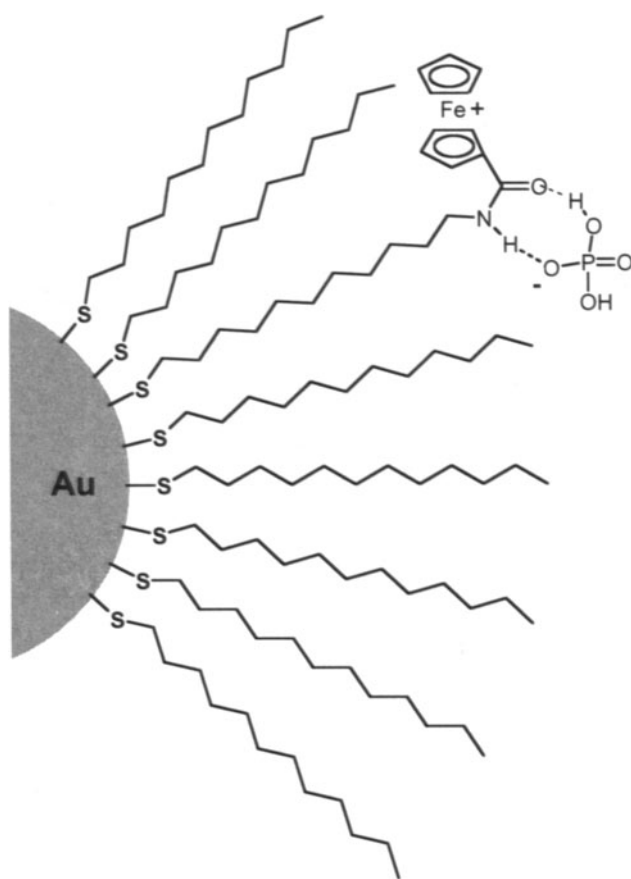
FIGURE 4.12. Binding of the dihydrogenphosphate anion to oxidized amidoferrocenyl sites on the surface of Astruc's alkanethiolate-capped Au nanoparticles.

4.2.6. OTHER RECEPTORS

The potential of metal nanoparticles as core building blocks for the synthesis of nanoscopic systems with designed surfaces has only begun to be exploited. A fascinating example of new directions that can be explored with these systems has been recently provided by the group of Penadés and coworkers, who prepared an interesting new class of glyconanoparticles.[40] These authors synthesized a series of carbohydrate-terminated disulfides (see Figure 4.13 for two examples) as monomers for the preparation of capping monolayers on Au nanoparticles. Using a modification of the procedures reported by Brust and Schiffrin, gold nanoparticles (~ 2 nm in diameter) were prepared and characterized by ^{1}H NMR, UV-Vis, FT-IR spectroscopic and TEM data. The nanoparticles contained from 60-100 carbohydrate-

terminated thiolate chains on their protecting monolayers and were found to be stable in aqueous solution for long periods of time, as anticipated from the water-solubility of the carbohydrate termini on their surfaces.

11, X = O
12, X = CH$_2$
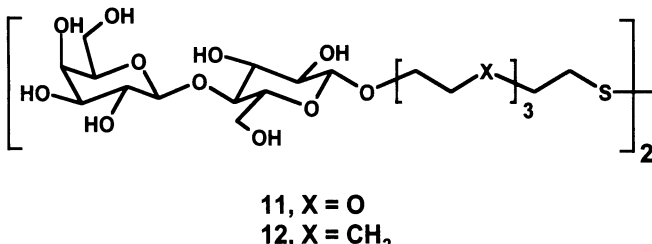
FIGURE 4.13. Two illustrative carbohydrate-terminated disulfides utilized in the preparation of Penadés' glyconanoparticles.

This group demonstrated that their glyconanoparticles aggregate in the presence of Ca^{2+} ions in the solution, to an extent that depends on the nature of the carbohydrate terminal groups.[40] This nanoparticle aggregation process is fully reversible as evidenced by the dissociation of the aggregates upon removal of the free Ca^{2+} ions (accomplished by addition of EDTA to the solution). This approach affords a flexible strategy for the preparation of polyvalent carbohydrate arrays with globular shapes, which can be used to investigate carbohydrate-carbohydrate recognition, as well as other interactions involving carbohydrate surfaces.

In an entirely different approach, the groups of Pasquato and Scrimin have functionalized the surface of dodecanethiolate-capped Au nanoparticles (2.2 nm in diameter) with *N*-methylimidazole functional groups.[41] Functionalization was accomplished via place-exchange reactions, using a methylimidazole-terminated alkanethiol to replace some of the dodecanethiol from the nanoparticle surfaces. In this particular case, extensive exchange takes place and the final nanoparticles were found to contain a roughly equimolar mixture of the unfunctionalized and functionalized thiols. The large concentration of methylimidazole groups on the nanoparticle surface permits their use as catalysts for the cleavage of 2,4-dinitrophenyl acetate.[41] This finding can only be rationalized if one accepts that the imidazole groups are acting cooperatively. The authors conclude that these nanoparticle systems resemble dendrimers, although the synthetic effort involved in their preparation is considerably less demanding.

The research work surveyed so far in this section relies on the preparation of nanoscopic assemblies containing metal cores and functionalized organic shells. While these systems are synthetically accessible, in the next section we will discuss thin film assemblies that can be prepared by simply exploiting the charges accumulated on the surface of metal colloidal particles.

4.3. THIN FILM SENSORS CONTAINING METAL COLLOIDAL PARTICLES

Metal colloidal particles are customarily covered with charged adsorbates that provide them with the necessary electrostatic stabilization. For instance, the very common gold colloidal particles prepared by citrate reduction of $AuCl_4^-$ solutions are covered and stabilized by adsorbed citrate ions. Therefore, these particles show a net negative charge. This fact has been exploited by Willner and coworkers to prepare a large number of thin film structures that can be used as sensors. This work has been recently reviewed by Shipway and Willner[42] and I will limit myself here to a brief exposition of the basic methodology. Essentially, thin film preparation relies on the compensation of the negative charges on the gold colloidal particles with appropriately functionalized organic cations, having the ability to recognize a specific type of substrate. The expectation is that the thin film will exhibit (a) enhanced electronic conductivity due to the presence of multiple gold particles, and (b) the molecular recognition properties afforded by the functionalized organic cations. Perhaps the prototypical example of these thin films is illustrated by those made using the tetracationic cyclophane receptor, cyclobis(paraquat-*p*-phenylene), **13**[4+] (Figure 4.14), which was first used by Stoddart and coworkers for the preparation of a large number of catenanes, rotaxanes, pseudorotaxanes and other topological molecules.[43-45]
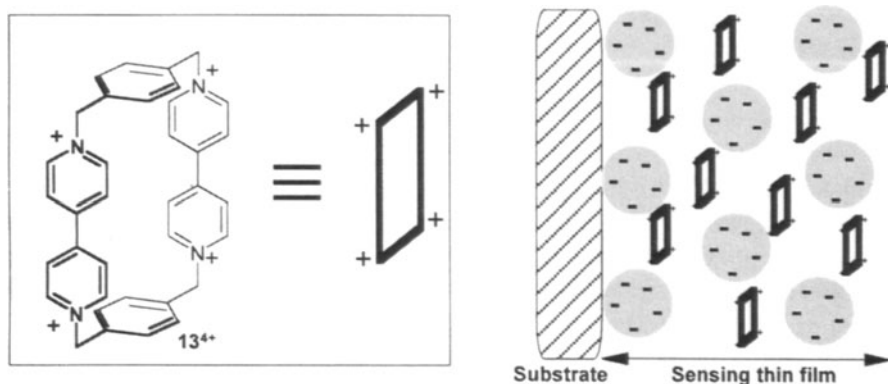
Figure 4.14. Structure of cyclophane receptor **13**[4+] and schematic representation of a supported thin film containing gold colloidal particles and tetracationic cyclophane receptors. The particles and the receptors are not drawn to scale.

This cyclophane receptor contains two paralell electron acceptor paraquat units lining its prismatic cavity and forms inclusion complexes with organic molecules containing electron rich aromatic residues. These complexes are stabilized by a combination of solvophobic and charge transfer

interactions.[46] The solubility of this receptor can also be adjusted by suitable counterion choices.

Willner and coworkers prepared these films by exposing a positively charged substrate (for instance, an indium tin oxide electrode derivatized with aminopropylsilane) to a solution of colloidal particles. This surface is subsequently exposed to a solution of the tetracationic cyclophane and the two-step process is repeated several times until the desired film thickness is reached. These authors have utilized electrochemical measurements to prove that hydroquinol derivatives, a well known class of guests for host 13^{4+}, penetrate the film and form inclusion complexes with the immobilized cyclophane hosts. Electrochemical measurements are very useful to monitor complex formation inside the film because the half-wave potential corresponding to the one-electron reduction of the paraquat groups in 13^{4+} is sensitive to host-guest complexation. In general terms, these thin films provide reasonable detection limits for appropriate guests and their selectivity is determined by the binding selectivity of the cationic host used in their preparation. Willner and coworkers have applied this approach to the quantitative detection of neurotransmitters.[47]

The same group has also reported a number of interesting results with composite films prepared by the incorporation of gold colloidal particles into hydrogel polymeric layers.[42] In a recent report, these authors took advantage of the thermosensitive properties of poly(N-isopropylacrylamide).[48] Basically, a gold electrode was covered with a layer of N-isopropylacrylamide, which was then polymerized *in situ*. At 20 °C the resulting polymer layer swells and allows electron transfer reactions between the underlying gold surface and redox active ferrocyanide and ferricyanide ions in the contacting solution. However, at 40 °C the polymer layer shrinks and the electron transfer is shut down. These swelling and shrinking cycles with the thermosensitive hydrogel layer are reproducible and can be repeated many times. Interestingly, gold colloidal particles (citrate-stabilized, 12 nm in diameter) can be introduced into the hydrogel layer when the shrunken polymer (40 °C) is allowed to swell in the presence of the colloidal particles. This 'breathing' process can be repeated and the gold loading of the hydrogel increases with the number of breathing cycles. As a result, the overall electrical resistance of the hydrogel film in its shrunken state decreases and so does the hindrance to the electron transfer reactions between the underlying gold surface and the redox active ions in the solution.[48]

Vossmeyer and coworkers have recently used thin films composed of gold nanoparticles and dendrimers for vapor sensing.[49] In their approach, these authors use dodecylamine-capped Au nanoparticles (~ 4 nm in diameter) and either poly(amidoamine) (PAMAM) or poly(propylene imine)

(PPI) dendrimers. The Au nanoparticle/dendrimer films were assembled layer-by-layer on amino-functionalized glass substrates. The films were characterized by UV-Vis spectroscopy, Atomic Force Microscopy (AFM) and electrical conductivity measurements. The latter property was found to be extremely sensitive to the presence of toluene, 1-propanol and water vapors. The selectivity of the film conductivity response was essentially controlled by the solubility properties of the dendrimers. These findings illustrate a very simple approach to sensor devices based on the electrical resistivity of composite metal nanoparticle/dendrimer films.[49]

4.4.   ORGANIZED NANOPARTICLE ASSEMBLIES

The organization of nanoparticles into assemblies with well-defined architecture may give rise to novel electronic, magnetic or optical properties. Furthermore, the creation of two- and three-dimensional arrays of nanoparticles is of considerable technological interest, as a first step in the application of these systems for information processing and storage.[50] Therefore, a substantial amount of work has been performed on this area. A comprehensive review of all this work would be impossible here due to space limitations. I will only discuss some illustrative examples. The reader is directed to Chapter 4 for a more extensive treatment.

The first goal in the assembly of nanoparticles is the creation of discrete nanoparticle assemblies, such as dimers, trimers, etc.. In 1997, Alivisatos and coworkers reported the preparation of linear arrays of DNA-linked gold particle dimers and trimers.[51] Two years later Novak and Feldheim reported the use of a series of thioacetyl-terminated phenylacetylene derivatives as linkers between gold and silver colloidal particles.[52] Addition of small amounts of these linkers to metal nanoparticle sols leads to the assembly of well-defined dimers, trimers or tetramers, according to the structure of the linker. Compelling TEM data were obtained to support the formation of the proposed nanoparticle assemblies. Furthermore, the UV-Vis spectroscopic data reveal that the surface plasmon resonance band of the 30-nm Ag particles is affected by the short interparticle distance in the assemblies.[52] The same group, in collaboration with Hupp and coworkers, used hyper-Rayleigh scattering spectroscopy to investigate the collective nonlinear optical behavior of these nanoparticle assemblies.[53] They found exceptionally large nonlinear optical responses that were strongly affected by the symmetry of the assembly and the interparticle distance.

The assembly of nanoparticles into two-dimensional arrays has indeed a long history.[54] Typically, the particles are protected by monolayers of hydrophobic organic molecules in order to favor their assembly into large

arrays with variable degrees of organization. Two-dimensional assembly is easier with small nanoparticles (diameter < 10 nm), while three-dimensional assembly normally prevails for larger metal particles. Wei and coworkers have recently reported a highly successful approach for the two-dimensional assembly of large (16-170 nm) gold colloidal particles at the air-water interface, which can then be transferred to planar substrates as hexagonal close-packed arrays.[55] The key issue is the selection of the organic capping agent. These authors chose to use tetrathiol resorcin[4]arene derivatives, functionalized with long aliphatic tails. These bowl-shaped receptors chemisorb to the surface of Au colloidal particles through their four thiol groups, while leaving the four aliphatic chains exposed to the solution. The resorcinarene-protected gold particles can be spread at the air-water interface and assembled into extremely large and well organized two-dimensional arrays, which could be readily transferred to solid substrates for TEM analysis. The particle size and the interparticle spacing exert a large influence on the optical properties of these two-dimensional arrays.[55]

One-dimensional nanoparticle arrangements have also attracted attention because of their potential applications as nanowires. In this regard, Schmid and coworkers performed fascinating experiments using nanoporous alumina as a template for the alignment of 1.4 nm Au_{55} clusters, enlarged to 4.2 nm by a ligand shell of thiol-functionalized silsequioxanes.[56] Their TEM data indicate that the experiments were successful using alumina membranes with 7 nm pores as templates, although the authors noted significant problems filling and packing the modified clusters into the pores. A more recent, template-free attempt to prepare wires from 15-30 nm gold nanoparticles uses a dielectrophoretic approach and leads to millimeter long wires, albeit their diameters are also in the micrometer regime.[57] Clearly, the one-dimensional arrangement of nanoparticles into well-defined wires of variable lengths is still an area in which a lot of progress needs to be made.

4.5. CONCLUSIONS AND OUTLOOK

Nanoparticle research is a vibrant field of research that currently attracts both chemistry and physics groups because of the considerable technological potential that these systems offer. The main goal of this Chapter has been to provide the reader with a survey of the recent research work on the modification of metal and semiconductor nanoparticles with monolayers of synthetic (non biological) organic molecules possessing active binding sites. The composite nanoscopic systems that are produced in this type of research work contain an inorganic core and an organic shell and are expected to derive interesting properties from both. Several classes of molecular

receptors have already been expressed on the protecting organic monolayers of metal nanoparticles. However, it is fair to state that this research field appears to be in its early stages of development. Most of the work reported thus far is concerned with nanoparticle preparation and characterization. Significant effort has been devoted to the characterization of binding events on the surface of the nanoparticles. However, most of this work has been done with nanoparticles dispersed in the solution phase. The last section of this chapter describes briefly some of the research work performed on the organized assembly of nanoparticles. Some of the most interesting possibilities of this research area may be realized with highly organized arrays of functionalized nanoparticles, where the binding activity of the functional groups may be rendered even more attractive by their spatial organization within the array. This idea still remains basically unexplored.

In general terms, we still lack versatile methods for the patterned assembly of nanoparticles. In this regard, it must be noted that Sagiv and coworkers are currently developing an interesting methodology for nanolithography on the surface of self-assembled monolayers that allows the construction of features of nanometer dimensions.[58] This methodology can be used to create nanoscopic patterns with metal nanoparticles on the surface of the monolayers. Clearly, this approach illustrates some of the possibilities on which we must expand to take full advantage of the size of the metal and semiconductor nanoparticles.

Finally, some nanoparticles offer unique properties that can be very advantageous in the design of sensor schemes. For instance, Wang and coworkers have recently developed a new nanoparticle-based protocol for detection of DNA hybridization in which they take advantage of the magnetic properties of the nanoparticles to induce their accumulation on an electrode surface, where the electrochemical stripping detection of the metal tags takes place.[59] It is easy to visualize other applications in which the ease of spatial accumulation of magnetic nanoparticles can be used to advantage from the standpoint of developing new sensor devices.

ACKNOWLEDGMENTS

REFERENCES

1.   Bönnemann, H.; Richards, R. M. *Eur. J. Inorg. Chem.* **2001**, 2455.

2. El-Sayed, M. *Acc. Chem. Res.* **2001**, *34*, 257.
3. Brust, M.; Walker, M.; Bethell, D.; Schiffrin, D. J.; Whyman, R. *J. Chem. Soc., Chem. Commun.* **1994**, 801.
4. Ulman, A. *Chem. Rev.* **1996**, *96*, 1533.
5. Templeton, A. C.; Wuelfing, W. P.; Murray, R. W. *Acc. Chem. Res.* **2000**, *33*, 27.
6. Lehn, J.-M. *Supramolecular Chemistry: Concepts and Perspectives;* VCH: Weinheim, 1995.
7. Prims, L. J.; Reinhoudt, D. N.; Timmerman, P. *Angew. Chem. Int. Ed.* **2001**, *40*, 2382.
8. Cusack, L.; Rao, S. N.; Wenger, J.; Fitzmaurice, D. *Chem. Mater.* **1997**, *9*, 624.
9. Cusack, L.; Marguerettaz, X.; Rao, S. N.; Wenger, J.; Fitzmaurice, D. *Chem. Mater.* **1997**, *9*, 1765.
10. Cusack, L.; Rizza, R.; Gorelov, A.; Fitzmaurice, D. *Angew. Chem. Int. Ed. Engl.* **1997**, *36*, 848.
11. Aherne, D.; Rao, S. N.; Fitzmaurice, D. *J. Phys. Chem. B* **1999**, *103*, 1821.
12. Ingram, R. S.; Hostetler, M. J.; Murray, R. W. *J. Am. Chem. Soc.* **1997**, *119*, 9175.
13. Fullam, S.; Rao, S. N.; Fitzmaurice, D. *J. Phys. Chem. B* **2000**, *104*, 6164.
14. Boal, A. K.; Rotello, V. M. *J. Am. Chem. Soc.* **1999**, *121*, 4914.
15. Boal, A. K.; Rotello, V. M. *J. Am. Chem. Soc.* **2000**, *122*, 734.
16. Boal, A. K.; Rotello, V. M. *J. Am. Chem. Soc.* **2002**, *124*, 5019.
17. Boal, A. K.; Rotello, V. M. *Langmuir* **2000**, *16*, 9527.
18. Paulini, R.; Frankamp, B. L.; Rotello, V. M. *Langmuir* **2002**, *18*, 2368.
19. Boal, A. K.; Ilhan, F.; DeRouchey, J. E.; Thurn-Albrecht, T.; Russell, T. P.; Rotello, V. M. *Nature* **2000**, *404*, 746.
20. Gokel, G. W. *Crown Ethers and Cryptands*; Stoddart, J. F., Ed.; Monographs in Supramolecular Chemistry; Royal Society of Chemistry: London, 1991.
21. Bradshaw, J. S.; Izatt, R. M.; Bordunov, A. V.; Zhu, C. Y.; Hathaway, J. K. In *Comprehensive Supramolecular Chemistry*; Atwood, J. L., Davies, J. E. D.; Macnicol, D. D., Vögtle, F., Eds.; Elsevier: New York, 1996; Vol. 1, Chapter 2.
22. Reference 20, Chapter 3.
23. Fitzmaurice, D.; Rao, S. N.; Preece, J. A.; Stoddart, J. F.; Wenger, S.; Zaccheroni, N. *Angew. Chem. Int. Ed.* **1999**, *38*, 1147.
24. Ashton, P. R.; Chrystal, E. J. T.; Glink, P. T.; Menzer, S.; Schiavo, C.; Spencer, N.; Stoddart, J. F.; Tasker, P. A.; White, J. P.; Williamns, D. J. *Chem. Eur. J.* **1996**, *2*, 709.
25. Ryan, D.; Rao, S. N.; Rensmo, H.; Fitzmaurice, D.; Preece, J. A.; Wenger, S.; Stoddart, J. F.; Zaccheroni, N. *J. Am. Chem. Soc.* **2000**, *122*, 6252.
26. Connors, K. A. *Chem. Rev.* **1997**, *97*, 1325.
27. Rekharsky, M. V.; Inoue, Y. *Chem. Rev.* **1998**, *98*, 1875.
28. See, for instance: Willner, I.; Mandler, D. *J. Am. Chem. Soc.* **1989**, *111*, 1330.
29. Rojas, M. T.; Königer, R.; Stoddart, J. F.; Kaifer, A. E. *J. Am. Chem. Soc.* **1995**, *117*, 336.
30. Liu, J.; Mendoza, S.; Román, E.; Lynn, M. J.; Xu, R.; Kaifer, A. E. *J. Am. Chem. Soc.* **1999**, *121*, 4304.
31. Brust, M.; Bethell, J.; Schiffrin, D. J.; Kiely, C. *J. Chem. Soc., Chem. Commun.* **1995**, 1655.
32. Liu, J.; Ong, W.; Román, E.; Lynn, M. J.; Kaifer, A. E. *Langmuir* **2000**, *16*, 3000.
33. Liu, J.; Alvarez, J.; Ong, W.; Román, E.; Kaifer, A. E. *J. Am. Chem. Soc.* **2001**, *123*, 11148.
34. Andersson, T.; Nilsson, K.; Sundahl, M.; Westman, G.; Wennerstrom, O. *J. Chem. Soc., Chem. Commun.* **1992**, 604.

35. Yoshida, Z.; Takekuma, H.; Takekuma, S.; Matsubara, Y. *Angew. Chem. Int. Ed. Engl.* **1994**, *33*, 1597.

36. Liu, J.; Alvarez, J.; Ong, W.; Kaifer, A. E. *Nano Lett.* **2001**, *1*, 57.

37. Beer, P. D.; Gale, P. A. *Angew. Chem. Int. Ed.* **2001**, *40*, 486.

38. Labande, A.; Astruc, D. *Chem. Commun.* **2000**, 1007.

39. Labande, A.; Ruiz, J.; Astruc, D. *J. Am. Chem. Soc.* **2002**, *124*, 1782.

40. De La Fuente, J. M.; Barrientos, A. G.; Rojas, T. C.; Rojo, J.; Cañada, J.; Fernández, A.; Penadés, S. *Angew. Chem. Int. Ed.* **2001**, *40*, 2258.

41. Pasquato, L.; Rancan, F.; Scrimin, P.; Mancin, F.; Frigeri, C. *Chem. Commun.* **2000**, 2253.

42. Shipway, A. N.; Willner, I. *Chem. Commun.* **2001**, 2035.

43. Anelli, P.-L.; Ashton, P. R.; Ballardini, R.; Balzani, V.; Delgado, M.; Gandolfi, M. T.; Goodnow, T. T.; Kaifer, A. E.; Philp, D.; Pietraskiewicz, M.; Prodi, L.; Reddington, M. V.; Slawin, A. M. Z.; Spencer, N.; Stoddart, J. F.; Vicent, C.; Williams, D. J. *J. Am. Chem. Soc.* **1992**, *114*, 193.

44. Amabilino, D. B.; Stoddart, J. F. *Chem. Rev.* **1995,** *95*, 2725.

45. Raymo, F. M.; Stoddart, J. F. *Chem. Rev.* **1999**, *99*, 1643.

46. Castro, R.; Berardi, M. J.; Córdova, E.; Ochoa de Olza, M.; Kaifer, A. E.; Evanseck, J. D. *J. Am. Chem. Soc.* **1996**, *118*, 10257.

47. Lahav, M.; Shipway, A. N.; Willner, I. *J. Chem. Soc., Perkin Trans. 2* **1999**, 1925.

48. Sheeney-Haj-Ichia, L.; Sharabi, G.; Willner, I. *Adv. Funct. Mater.* **2002**, *12*, 27.

49. Krasteva, N.; Besnard, I.; Guse, B.; Bauer, R. E.; Mullen, K.; Tasuda, A.; Vossemeyer, T. *Nano Lett.* **2002**, *2*, 551.

50. Feldheim, D. L.; Keating, C. D. *Chem. Soc. Rev.* **1998**, *27*, 1.

51. Peng, X.; Wilson, T. E.; Alivisatos, A. P.; Schultz, P. G. *Angew. Chem Int. Ed. Engl.* **1997**, *36*, 145.

52. Novak, J. P.; Feldheim, D. L. *J. Am. Chem. Soc.* **2000**, *122*, 3979.

53. Novak, J. P.; Brousseau, L. C.; Vance, F. W.; Johnson, R. C.; Lemon, B. I.; Hipp, J. T.; Feldheim, D. L. *J. Am. Chem. Soc.* **2000**, *122*, 12029.

54. See, for instance: Collier, C. P.; Vossmeyer, T.; Health, J. R. *Annu. Rev. Phys. Chem.* **1998**, *49*, 371.

55. Kim, B.; Tripp, S. L.; Wei, A. *J. Am. Chem. Soc.* **2001**, *123*, 7955.

56. Hornyak, G. L.; Kröll, M.; Pugin, R.; Sawitowski, T.; Schmid, G.; Bovin, J.-O.; Karsson, G.; Hofmeister, H.; Hopfe, S. *Chem. Eur. J.* **1997**, *3*, 1951.

57. Hermanson, K. D.; Lumsdon, S. O.; Williams, J. P.; Kaler, E. W.; Velev, O. D. *Science* **2001**, *294*, 1082.

58. Hoeppener, S.; Maoz, R.; Cohen, S. R.; Chi, L.; Fuchs, H.; Sagiv, J. *Adv. Mater.* **2002**, *12*, 1036.

59. Wang, J.; Xu, D.; Polsky, R. *J. Am. Chem. Soc.* **2002**, *124*, 4208.

5

Nanoparticles in Catalysis

Chuan-Jian Zhong*, Mathew M. Maye, Jin Luo, Li Han, Nancy Kariuki

Department of Chemistry, State University of New York at Binghamton, Binghamton, NY 13902.

5.1.   INTRODUCTION

Catalysis plays a vital role in providing fuels, fine chemicals, pharmaceuticals, and means for strengthening environmental safeguards. In comparison with many other fields of chemical and materials sciences, catalysis was perhaps one of the first fields to take advantage of nanotechnology. Supported noble metal catalysts with particle sizes down to a few hundred nanometers and zeolite catalysts with pore size of sub-nanometers, all developed in the 1950s-60s, are widely used in today's chemical processes. The field of catalysis continuously reinvents itself and become highly interdisciplinary. Many of the recent advances, some of which are discussed in this chapter, are a result of such interdisciplinary developments involving nanotechnology. The nanotechnology-guided design and fabrication of catalysts, enhancement of catalytic activity or selectivity, and reduction in cost of catalysts will have enormous impacts to the chemical industry. The ability to harness the large surface area-to-volume ratios and the unique binding sites of nanoparticles (1-100 nm), especially in heterogeneous catalysis, constitutes a major driving force in fundamental research and practical applications of nanoparticle catalysts. Importantly, deliberate tailoring of nanoparticle size, shape and surface could lead to improved or new catalytic properties. This aspect was indeed inspired by the surprising discovery of high catalytic activity of nanosized gold towards oxidation or reduction of hydrocarbons.[1-4] Gold is traditionally

113

considered catalytically inactive as a practical catalyst, but this property is completely changed when the size dimension is reduced to a few nm.

The design, fabrication, manipulation and characterization of nanoparticles ranging from sub-nm to ~100 nm are now in the center of catalysis and nanotechnology (Scheme 5.1). The goals are, (1) to develop design strategies to fabricate nanoparticle catalysts with precisely controlled size, shape, surface and spatial properties; (2) to apply nano-probes to characterize or manipulate the nanostructured catalysis, and (3) to gain fundamental understanding of the nanochemistry in nanoscale catalysis.
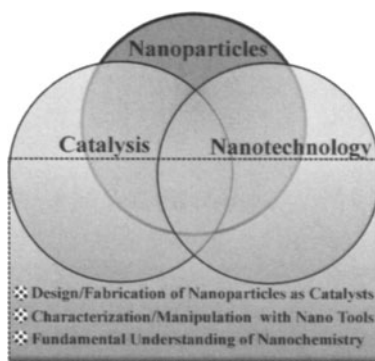
SCHEME 5.1. A schematic illustration of the interplay of nanoparticles and nanotechnology in catalysis

Two related challenges for developing nanometer-sized particles as catalysts are, 1) the preparation of controllable nanoscale dimensions, and 2) the prevention of the intrinsic propensity of aggregation of nanoscale materials. Aggregation of nanoparticles leads to eventual loss of the nanoscale catalytic activity in practical applications. The use of naked metal nanoparticle catalysts on supporting materials based on traditional preparative methods has been well demonstrated for different catalytic reactions.[5,6] Recently, nanoparticles capped in monolayers, polymers or dendrimers are rapidly emerging, demonstrating remarkable parallels to catalytic activities for supported nanoparticles. The catalysis includes those utilizing functional groups at the capping shell[7,8] and those exploiting surface sites on the nanocrystals.[5,6,9] The core-shell (CS) nanoparticles are explored as model building blocks towards catalytic materials by taking advantage of the diverse attributes, including size monodispersity, processibility, solubility, stability, tunability, self-assembly capability, and controllable optical, electronic, magnetic, and chemical/biological properties. Many types of nanoparticles could fit into the core-shell category by the broad definition that it consists of core and shell of different matters in close interaction, including inorganic/organic, inorganic/inorganic,

organic/organic, or inorganic/biological combinations.[10-20]   For example, polymer-mediated self-assembly of monolayer-functionalized Pd nanoparticles and SiO_2 particles through 'bottom-up' approach and thermal treatment have recently been demonstrated as highly reactive, recyclable heterogeneous catalysts for both hydrogenation and carbon–carbon bond formation reactions.[21]

There are several excellent reviews or book chapters that have described recent progress related to different aspects of catalysis using nanoparticles.[22-25]   In this chapter, we will focus on several latest developments by highlighting nanoscale manipulation and characterizations. This chapter is divided into four sections. The first section gives an overview of the fundamental issues of nanoparticles in catalysis and their challenges and opportunities. The next section outlines several approaches to the fabrication of nanoparticles. The third section describes the use of nanoparticles supported on oxides or electrode materials for catalysis. The gold nanoparticle catalysis will be highlighted. In the fourth section, relatively new strategies of using molecularly-engineered nanoparticles in catalysis will be discussed, which highlight the concept of molecularly-assembled nanoparticle catalysts and catalytic activation. The future prospectus will be discussed in the last section.

5.2.   FUNDAMENTAL ISSUES

A key process in a heterogeneous catalytic reaction is the interaction of the chemical reactants with surface sites of the catalyst. This interaction depends strongly on the surface properties of the catalyst. To maximize this interaction, the use of nanoparticles as catalysts has a number of important attributes including,

     Large surface area-to-volume ratio
     High surface concentrations of corner and edge atoms
     Low coordination numbers of surface atoms
     Unique electronic properties (e.g., quantum transition)

The basic relationship between the surface area to volume ratio or surface atoms to bulk atoms and the diameter of nanoparticle is illustrated in Figure 5.1 based on a spherical model for a gold nanoparticle. As the size of particle approaches a few nm, both surface area to volume ratio and surface to bulk atom ratio dramatically increase. In addition, the percentages of surface atoms in corner and edge vs. particle sizes, which can be calculated based on a octahedral model,[26] display dramatic increases when the size is decreased below a few nm, whereas the percentage of face atoms decreases.

For nanoparticles of ~ 1 nm size, more than ~70% atoms are at corners or edges. This aspect is important because chemisorption is highly dependent on the atomic scale surface morphology.
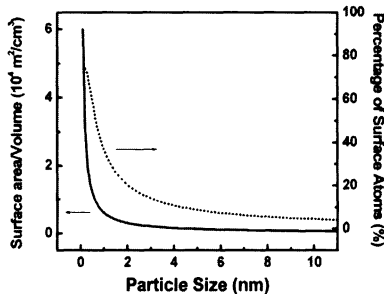
FIGURE 5.1. Surface area to volume ratio and percentage of surface atoms (%) as a function of particle diameter (for gold nanoparticles).

Although the large surface area-to-volume ratio of small metal or oxide particles has been explored for a long time in catalysis, the understanding of how the catalytic nanostructure can be fabricated in a controlled way is rather limited. The coupling between catalyst fabrication and nanotechnology is unique because nanoscale materials serve as "designer" building blocks for nanostructured catalysts, and advanced analytical tools provide abilities for studying the nanoscale catalytic properties. Recent advances in the synthesis of nanoparticles or nanotubes and the development of analytical tools such as scanning probe microscopy (scanning tunneling microscopy (STM) and atomic force microscopy (AFM)) have equipped us with the capability to address a number of important fundamental issues.

One issue concerns catalyst stability in fuel cell catalysts (e.g., hydrogen and methanol fuel cells). The propensity of poisoning by adsorbed reaction intermediate species poses a major problem to the sustenance of high catalytic activity of Pt-group catalysts.[27-30] For example, in "dual-pathway" mechanism for electrocatalytic oxidation of methanol and formic acid which involves dissociative chemisorption followed by oxygen/proton/electron transfer steps, the formation of a chemisorbed "poison" in competition with one or more adsorbed reaction intermediates was considered to be operative. Multi-component catalysts such as Pt/Ru and Pt-Ru-WO_3 have been demonstrated to minimize the poisoning propensity, including carbon–supported Pt/Ru alloy nanoparticles prepared from cluster precursors as an electrocatalyst in direct oxidation fuel cells. In a different approach, Au particles of less than 10 nm on metal oxide supports have been demonstrated by Haruta[1,2] to display extremely high catalytic activities for CO oxidation. The activation-size correlation of the particles in CO gas

phase was further shown by Goodman[31] to exhibit a band gap of metallic-insulator transition in 2~5 nm range. Another issue involves the propensity of aggregation of nanoparticles. The recent abilities in synthesizing molecularly-capped metal nanoparticles may emerge as an alternative solution because the capping agent serves as a protective layer. A critical question is then how to render the nanocrystal core catalytically active under the encapsulation. Answers should impact much of the recent studies of nanotechnology in catalysts. Schmid and co-workers showed that the deposition of surfactant-capped Pt nanoparticles on carbon support materials could be utilized as catalysts for electrocatalytic oxidation of methanol.[24] Another early example for the preparation of metal-organic cluster catalysts on supports involved reacting with surface functional groups (e.g., -OH) to immobilize[32] and then stripping the ligands off the clusters. In addition to these issues, a good understanding of the surface edges, corners, and ion vacancies and oxide species is also important, as recently demonstrated for MgO-CaO nanocrystal catalysts.[33]

The discovery of nanoscale gold catalysis[1,2] is perhaps a best example to illustrate these fundamental aspects. Important factors of nano gold catalysis have been shown to include low-coordination sites on surface, high mobility of surface atoms, high electronegativity, and high oxidation potential. These properties are largely determined by surface atoms. As revealed by model calculation (Figure 5.1),[26] the percentages of surface atoms at corners and edges increase sharply with size reduction. The relatively high mobility of corner or edge atoms at room temperature can be explained on the basis of band theory[3-4] and by melting point decrease of small particles. In the band theory, the spacing between adjacent energy levels ($\delta \approx E_F/n$, E_F - Femi energy level, n - number of atoms) is about 2.5×10^{-2} eV for a 2 nm core size, comparable to kT (2.6×10^{-2} eV). The temperature decrease of melting, $\Delta T = T_0 - T_r = 2T_0\sigma/\rho Lr$ (L: heat of fusion, r: radius, σ: surface tension coefficient of solid-liquid interface), predicts that the lowering of the melting point is inversely proportional to the power of the particle size.[34] For example, in comparison with the melting temperature of 1320 ^{0}C for bulk gold, gold particles of 2.5 nm diameter melts at ~600 ^{0}C. The surface melting temperature could be even lower since melting starts at the surface layer, demonstrating again the critical dependence of gold catalysis on the properties of surface atoms.

In addition to size effect, a fortunate combination of factors and conditions is required to achieve highly active and stable gold catalysts for CO oxidation. A number of possibilities are proposed to account for the catalytic activity, including a greater chemisorptive ability of surface atoms, a larger coverage of oxygen atoms on the peripheral interface between gold and the support, and a modification of the interfacial interaction to create

special catalytic sites near the support. Mechanistically, the oxidation of CO at gold catalyst[1-4] could occur: 1) exclusively on support, 2) exclusively on Au, and 3) preferentially on the edges of Au particles. While gold nanoparticle catalysis begins to show parallels with the growing numbers of applications for platinum catalysis achieved in the recent past,[35] precisely, why gold particles in restricted size range are catalytically active is still an important subject of current research. In recent reviews by Bond and Thompson,[3,4] gold is considered as a relatively new catalyst because of its weak chemisorption capability in comparison with Pt-group metals. For example, the initial enthalpy of chemisorption of oxygen can be related to enthalpy of formation of stable oxides (Au_2O_3), +19.3 kJ mol^{-1}, which means that gold does not form stable oxides, in contrast to oxides of other neighboring metals which have negative free energies of formation. Another hypothesis for the unique properties of gold nanoparticles involves the relativistic contraction of 6s level electrons.[4] Briefly, the innermost 1s electrons increase their speed to maintain their position as the atomic number increases. This has a relativistic effect on the mass, and 1s and all outer s electrons have to contract. The actual size of the 6s electron shell for Au and Pt is ~15% smaller than that in the absence of this effect. The chemistry is thus determined by the high energy and reactivity of the less-affected 5d electrons. This hypothesis accounts for the distinction of gold from its neighboring metals.[4]

5.3.   CHALLENGES AND OPPORTUNITIES

By taking advantage of advances in several areas of nanotechnology, especially nanofabrication methods and nanoscale analytical tools, we are now at a stage to create a new platform for catalyst design, preparation and characterization. Such a platform would involve interdisciplinary ideas, approaches and methodologies. The interdisciplinary effort could also form the basis for developing advanced nanoscale materials for sensors or biosensors, examples of which will be given towards the end of this chapter. Economically, the nanostructured catalysts could have a tremendous cost-saving impact on the multi-billion dollar chemical industry involving catalysts for synthetic processes, and have societal benefits in areas such as emission, pollution and breath alcohol detection. The benefits have recently been analyzed,[36] especially in the energy market, including oil, gas, fuel cells, environmental impact, etc.

A major challenge for exploring nanoparticles in heterogeneous catalysis is the control of size, shape, surface, and interparticle spatial properties. The nanostructures of many commercial catalysts are not well controlled and

their structure-activity relationships are poorly understood. This challenge requires new strategies and abilities that can manipulate nanoscale materials at high precision. There are many new synthetic or processing routes to prepare stable and catalytically active nanoparticles of high monodispersity, and many new analytical tools that probe nanostructured materials with atomic/molecular resolution. The various nanostructure fabrication methods and probing tools begin to accelerate the understanding of synthesis-structure-performance relationships of heterogeneous catalysts. The ultimate goal is to achieve catalyst by design with and high activity and 100% selectivity.[37]

One intriguing question is: can a general preparative route be developed towards nanostructured catalysts by which pre-engineered nanoparticles are assembled onto a desired platform for catalytic applications? Scheme 5.2 illustrates such a hypothesis. Surface-engineered nanoparticles are first assembled on a substrate via molecules or polymers. This assembly is then activated for a catalytic reaction (R → P). The activation may involve partial or complete removal of the surface molecules. A relevant question is then: why should one use capping/assembling molecules in the first place when the catalytic application involves their removal? The answer would be centered largely on the ability of the capping/assembling structures to precisely control or manipulate the size, shape, and interparticle spatial properties. The assembled nanostructure also provide controllable 3D catalytic access, in a way similar to zeolite catalysts with controllable pores. This could become a key area of nanotechnology in catalysis.
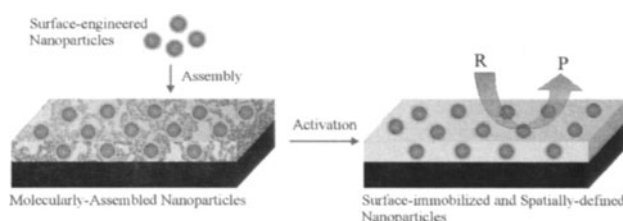
SCHEME 5.2. A schematic illustration of assembly and activation of surface-immobilized and spatially defined nanoparticles as catalysts.

In the next two sections, several examples will be shown to demonstrate the application of nanotechnology as a new advent in catalysis that may also prove valuable to emerging approaches, including combinatorial catalyst designs (e.g., synthesizing chemical libraries for rapid-screening nitroxyl radical catalysts for alcohol oxidation[38] and photochemical catalytic activities[39]).

5.4.   FABRICATION OF NANOPARTICLES AS CATALYSTS

The fabrication of nanoparticle and nanostructured catalysts is a key step in exploring nanoparticles in catalysis. Depending on the catalytic applications, numerous methods have been documented.[22-24] A large number of nanoparticle catalysts are based on Pt, Pd or alloys, whereas gold-based nanoparticles as catalysts are rapidly emerged in recent years. Table 3-1 summarizes several types of nanoparticle catalysts in terms of preparation and catalytic reaction, which is by no means exhaustive. Nanoparticles supported on oxides, encapsulated in polymers or dendrimers, and encapsulated in organic monolayers are of increasing interest, which are selectively outlined to illustrate both traditional and new approaches.

TABLE 5.1. Nanoparticles as Catalysts

Nanoparticle Catalyst	Preparation Method	Catalytic Reaction	refs
Pt (or Pd)-based			
Pt, Pt/Ru; Pt/Ni, Pt/Ru/Ni (3-4 nm)	Co-deposition; Repeated spontaneous deposition	electrooxidation of CO, methanol, formic acid	40-41
Pt, Pd in Al_2O_3 and polymer (2~5nm)	Radiolytic reduction	propene hydrogenation	42
PtRu (1.7 nm); Pt-Ni, Pt-Co (4 nm)	Co-precipitated; Co-reduction	Electrooxidation of methanol; redn. of O_2	43-45
Pd, Pt, Rh, Pd/Pt (1-4 nm)	Impregnation	hydrogenation of cyclooctadiene; CO oxidn.	46-47
Pt (28 nm)	Decomposed by electron beam	Dehydrogenation (cyclo-hexene), hydrogenation	48-49
Pt/Ru (1-2 nm)	decarbonylation	hydrogenation of dimethyl terephthalate	50
PtSn/C, Pt_3Sn/C (5-8 nm)	Deposition of metal precursors	methanol electrooxidation	51
Pd and SiO_2 (~1 nm)	2-phase synthesis, self-assembly	hydrogenation of 9-decen-1-ol and Heck coupling	21
Pt (7.1 nm) /carbon nanotubes(200 nm)	Chemical vapor deposition	O_2 reduction and methanol oxidation	52
Gold-based			
Au/TiO_2 (2-5nm)	Co-Precipitation	CO oxidn., Hydrogenation	2, 53
Au/TiO_2 (4nm)	Vapor Deposition	CO oxidn.	31
$Au/M(OH)_2$, M=Mn, Co, Ni, Zn, Cu (2-4 nm)	Impregnation of as-precipitated hydroxides	CO oxidn.,	54
Au_n (1-20 Au atoms)	Laser-induced vaporization	CO oxidation	55-56

Nanoparticle Catalyst	Preparation Method	Catalytic Reaction	refs
Au/ZrO$_2$, Au/SiO$_2$ (2-4 nm)	Impregnation	CO oxidation	57
Ni-Au/SiO$_2$/MgAl$_2$O$_4$ (3-10 nm)	Impregnation, co-Precipitation	Gas reforming of n-butane	58
Au$_n$/MgO (1-20 atoms)	Laser evaporation	CO oxidation	59
Au/TiO$_2$ (2 nm)	2-phase synthesis, Aero Gelation	CO oxidation	60
Au, Au/Pt (2-5 nm)	2-phase synthesis, self-assembly	CO, MeOH oxidation	61-66
Other Metals			
Ba hexaaluminate (3-10 nm); CeO2	Reverse emulsion; Magnetron sputtering	CH$_4$ combustion, SO$_2$ redn., CO & CH$_4$ oxidn.	67-68
Cu (3-6 nm)	Impregnation	Methanol, hydrocarbon conversion for fuel cells	69
V-Mg-O (187-299 m^2/g)	Hydrolysis and deposition	Oxidative dehydrogenation	70
TiO$_2$ (30 nm)	Commercial	Photodegradation of dye	71
Rh (2-3 nm)	Chemical reduction	hydrogenation of benzene and phenylacetylene	72
MoS$_2$ nanotubes (diameters: 25/12 nm)	Gas-solid reaction	methanation of CO and H$_2$	73
Dispersed in Polymers Pd/SiO$_2$/amine-polymer (2 nm)	self-assembly	Hydrogenation, Heck Reaction	21
Pt/polypyrrole (10 nm)	Electro-reduction	Methanol Electrooxidation	74
Pt-Ru-X (X=Au, Co, Cu, Fe, Mo, Ni)/Polyaniline(4 nm)	Electro-reduction	Methanol electrooxidation	75
Pt, Cu, Ag, Au, Pt, Pd, Ru, Fe/dendrimer(1–5nm).	Redn. in dendrimer-encapsulation	Hydrogenation, C-C coupling, O$_2$ reduction,	76-77
Au, Pt, Au/Pt, Pt/Ru /poly (N-vinyl-pyrrolidone) (1-5nm)	Polymeric incorporation	Oxidation, hydrogenation.	78-79
Pt/hyper-crosslinked polystyrene (1-6 nm)	Impregnation-reduction	Hydrogenation, Oxidation of L-sorbose	80
Pd/poly(N-vinyl-2-pyrrolidone) (3-6 nm)	Stepwise growth reaction	Suzuki reaction	81
Pt/Ppy (30-40 nm)	Electro-reduction	Methanol electrooxidation	82
Au/Pt (2-5 nm)	2-Phase synthesis/ electro-reduction	CO & Methanol Electrooxidation	83

5.5.   TRADITIONAL APPROACHES

The traditional approaches to preparing nanoparticles on supports involve co-precipitation, deposition-precipitation, ion-exchange, impregnation, successive reduction and calcination, etc. These methods have been widely used for preparing noble metal catalysts on support materials.[6] The preparation of gold nanoparticle catalysts, as recently reviewed by Bond and Thompson,[3,4] involved many of these methods. In the co-precipitation method, the support and gold precursors are brought out of solution as hydroxides by adding a base such as sodium carbonate. In deposition-precipitation method, the gold precursor is precipitated onto a suspension of the pre-formed support by raising the pH. In gold-phosphine complex method,[54] the complex is made to react with a freshly precipitated support precursor. There are also other procedures reported for nanoparticle catalyst preparation such as the use of colloids, grafting and vapor deposition.[4]

In these documented methods for the preparation of nanoparticle catalysts, the choice of support materials and the pretreatment of the nanoparticles before use are also very important. For gold nanoparticle catalysts, the use of the TiO_2 and Fe_2O_3 are demonstrated to be most effective.[1,2] In pretreatment of the supported catalysts, calcination is shown to be helpful. In general, the preparation of naked metal nanoparticles on support using the traditional approaches is very advantageous in terms of the exposure of the nanocrystal surface sites to catalytic reactions. A disadvantage is however the lack of control over size, shape and stability of the produced nanoparticles. It is especially difficult to process the nanoparticles once produced. Such controllability or processibility of size, shape and surface properties are important in delineating the size effect in nanostructured catalysis. An ideal nanoparticle catalyst system should be not only catalytically accessible but also morphological stable or controllable. The latter can be addressed by surface-capping approaches, as described next.

5.6.   SURFACE-CAPPING APPROACHES

In contrast to the traditional preparation methods, recent approaches to the fabrication of nanoparticles begin to explore surface-capping pathways in synthesis and processing. Because of the enhance stability against aggregation, such surface-engineering can overcome the weakness of the traditional approaches in controlling size, shape and surface properties. Different polymeric and molecular capping agents for the synthesis of Pt, Au and alloy nanoparticles of controllable size, shape and surface properties

have been well documented. The nanoparticles thus produced are often in the form of core-shell structure with polymers or monolayers as the shell and metal nanocrystals as the core. While the shell prevents aggregation and enhances stability of the nanocrystals, an inherent disadvantage is the blocking of the surface sites, which will be addressed in a later section.

The synthesis, characterization and application of organic monolayer-protected nanoclusters or nanoparticles have been extensively discussed in a number of articles,[6,10,11,84] including several chapters in this book. Among many synthesis methods, wet chemical synthesis is shown to be very effective in producing monodispersed nanoparticles. The two-phase synthesis protocol by Brust et al[85] is now widely used for fabricating stable and soluble gold and many other metal nanoparticles of a few nm core sizes. Briefly, this protocol involves transfer of $AuCl_4^-$ from aqueous to organic solution by a phase transfer reagent followed by reduction in the presence of thiols, producing thiolate-capped gold nanoparticles of a few nm core sizes (e.g., ~ 2 nm gold nanoparticles as shown in Figure 5.2B). Further modifications of the synthetic protocols or processing of the produced nanoparticles have been shown to produce a variety of chemically-tunable nanoparticles in terms of size, shape and surface properties.[86,87]

Perhaps one of the most important attributes of these nanoparticles is the core-shell reactivity that allows re-engineering or assembly of nanoparticles. In one type of core-shell reactivity, the capping molecules can be re-constituted to impart the desired functional properties, which was demonstrated in a place-exchange reaction first by Murray's group.[88] Our group demonstrated that the further manipulation of the reaction condition could lead to controllable assembly of the nanoparticles.[89] In another type of core-shell reactivity, the nanocrystal cores can be coalesced or re-shaped in a controlled way by thermally-activated core-shell reaction in solutions.[90,91] We termed this reactivity as a thermally-activated processing strategy for processing nanoparticle size, shape and surface properties. As was demonstrated for gold and alloy nanoparticles, the reaction could start from monolayer-capped Au or alloy nanoparticles of ~2 nm core sizes (Figure 5.2B), and undergo an evolution involving desorption of the shell molecules, coalescence of the nanocrystal cores, and re-encapsulation of the nanocrystals by the desired shell molecules. The resulting nanoparticles are narrowly sized with only 5~7% variation (e.g., 5.2   0.4 nm, Figure 5.2A).

The core-shell processing strategy has showed promises for the production of highly-monodispersed nanoparticle catalysts with controlled size, shape, composition and surface properties. Recently, this aspect is further refined by us[92] and several other research groups,[93-95] which expanded this strategy to produce monodispersed nanoparticles of different core sizes.
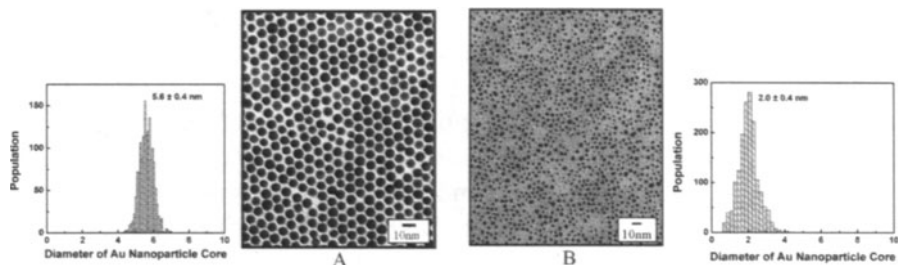
FIGURE 5.2. TEM micrographs and size distributions of gold nanoparticles of two different sizes (A: Au_{5-nm}; B: Au_{2-nm}). TEM Reproduced with permission from *Anal.Chim. Acta.,* **2002**, in press. Copyright 2002 Elsevier Science B.V.[92]

5.7. SURPPORTED NANOPARTICLE CATALYSTS

Although there were early examples using supported noble metal nanoparticle catalysts, the recent progress of nanotechnology in processing and nano-probing has led to refinement of preparation procedures and new or improved catalytic properties. The discovery of catalysis at gold nanoparticles supported on metal oxides is one example. There are also similar examples for other metal nanoparticles. These will be discussed in the following subsections.

5.7.1. GOLD NANOPARTICLE CATALYSTS

Nanoscale gold catalysis has attracted increasing interest largely because of Haruta's discovery of unprecedented catalytic activity and specificity of gold at nanometer sizes.[1,2] Gold in the bulk is chemically inert and has often been regarded to be poorly active as a catalyst. However, when the dimension of gold is reduced below ~10 nm, it turns out to be surprisingly active for many reactions such as CO oxidation, especially at low temperatures. The catalysis at oxide-supported gold nanoparticles begins to show parallels with the growing numbers of applications for platinum catalysis. The high activity of gold catalysts for CO oxidation requires gold particles less than 5 nm.[1-4] The correlation between catalytic activation and particle size for CO gas phase catalysis revealed a band gap of metallic-insulator transition in the 2~5 nm range.[31] Temperature-programmed combustion of CO on magnesia-supported gold clusters showed that Au_8 was the smallest catalytically active size.[96] Partial electron transfer from the surface to gold cluster was believed to play an essential role in the activation

of nanogold clusters.   As discussed earlier, the decrease of mean surface coordination number and the ready mobility of surface Au atoms, particularly at corner and edges, could lead to a greater chemisorptivity and a stronger interaction with the support which creates special gold sites near the support (Scheme 5.3).
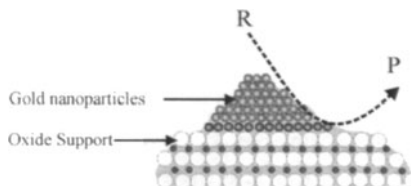
SCHEME 5.3. A schematic illustration of catalytic reaction at oxide-supported nanoparticle catalyst, Reprinted with permission from *Adv. Mater.* 2001, *13*, 1507. Copyright 2000 Wiley-VCH.[9]

The mechanism of CO oxidation at oxide (e.g., TiO_2, Al_2O_3)-supported gold nanoparticles is complex.[1-4]   Oxygen is required for CO to CO_2 oxidation, which can be from an adjacent water molecule, or from surface oxides that function as support or redox mediator. It is believed to involve chemisorption and oxygen transfer reactivity at the particle and particle-support interface. The proposed possible interfacial steps include,[3,4]

(1) $Au^0 + CO \rightarrow Au^0...CO_{ad}$
(2) $Au^{III} + OH^-_{ad} \rightarrow Au^{II}... OH_{ad}$
(3) $Au^0...CO_{ad} + Au^{II}...OH_{ad} \rightarrow Au^{II}...COOH_{ad} + Au^0$
(4) $O_2 + \square/AuO_x \rightarrow O_2^-...\square/AuO_x$
(5) $Au^{II}...COOH + O_2^-...\square/AuO_x \rightarrow Au^{II} + CO_2 + HO_2^-...\square/AuO_x$
(6) $Au^{II}...COOH + HO_2^-...\square/AuO_x \rightarrow Au^{II} + CO_2 + 2HO^-...\square/AuO_x$
(7) $Au^{II} + \square/AuO_x \rightarrow Au^{III} + \square^-/AuO_x$

where the square stands for adsorption sites on the nanocrystal.   The chemisorption sites involve Au^{III-II} oxidation states and surface hydroxyl species.   The presence of oxide support is a key element in steps 2-3.   A number of factors that play important roles in these interfacial steps include: (1) the large amount of surface atoms and their relatively high surface mobility; (2) the surface behave more like individual atoms than a collection of atoms; and (3) strong interaction of a large fraction of gold atoms with the oxide support.   The catalytic performance of Au is thus defined by contact structure, support selection, and particle size.   The contact structure is the most important because the perimeter interfaces around Au particles act as the reaction site.   As extensively studied for low-temperature CO oxidation on Au/TiO_2, the perimeter interface between Au particles and the support

serves a unique reaction site for the reactants adsorbed separately, one on Au and another on the support surfaces. These aspects have been recently reviewed by Haruta.[2,53] The catalytic properties of nanosized gold have attracted growing interests due to their potential applicabilities to many reactions of both industrial and environmental importance.

5.7.2. OTHER METAL NANOPARTICLE CATALYSTS

Catalysis on Pt-based metal or alloy nanoparticles has also attracted a great deal of interest in a number of areas, many of which have been extensively reviewed.[6] One important area is fuel cell technology, where the development of highly effective catalysts is critical. For example, Wieckowski[46] showed that Pt-based nanoparticle catalysts electrochemically deposited on electrode surfaces exhibited high activity for formic acid electrooxidation. The Pt nanoparticles decorated with controlled amounts of Pd/Ru showed the best performance with a steady-state oxidation current (~ 1 mA/cm^2 at 0.27 V vs. RHE), which is two orders of magnitude higher than that obtained from pure Pt. Within the dual path mechanism of formic acid oxidation, the direct CO_2 formation channel on Pt/Pd is much less affected by CO chemisorption than that on other catalysts. For methanol oxidation processes in the direct oxidation methanol fuel cell, Pt/Ni and Pt/Ru/Ni alloys were found to have excellent catalytic activities compared to those of pure Pt and Pt/Ru. The presence of Ni or Ru oxides was found to serve as the oxygen donors for the oxidation process. The change in the electronic structure of Pt in the alloys versus those in Pt and Pt/Ru collectively account for enhancement in rates of methanol oxidation.

Another intriguing example of nanoparticle catalysts involves the use of electron beam lithography to produce model nanoclusters on a substrate as catalysts. Somorjai[49] recently demonstrated the fabrication of Ag-based nanoclusters as a model catalyst for ethylene epoxidation. The aim was to understand the behavior of aggregates of metal atoms in determining product selectivity of chemical reactions. The catalyst is made of a square array of cylinder-shaped Ag nanoclusters of 20 nm in diameter, deposited on a 4-inch silicon wafer, pre-covered with a 10 nm thick film of α-alumina. The height of the particles and interparticle distance can vary, ranging from 15 to 100 nm. Although the particle size is relatively large due to the use of e-beam fabrication, this high-technology model nanocluster catalyst is an excellent example towards understanding the effect of particle size and spatial arrangement (or interparticle distance) of catalyst particles on reaction rates.

5.8.   ASSEMBLED NANOPARTICLE CATALYSTS

In comparison with the use of the supported nanoparticle catalysts, the concept of using surface-capped nanoparticles to assemble catalysts is relatively new.   Using various chemical methods, ligand-stabilized Pt or Pt/Pd nanoclusters (1-4 nm) prepared by Schmid[47,97] showed high catalytic activity for hydrogenation of olefins in both homogeneous and heterogeneous systems.   The catalytic activities for hydrogenation of 1,3-cyclooctadiene and methyl acrylate depend mainly on the particle size, i.e. the smaller the size, the higher the activity.   A strongly-interacting ligand like tetraoctylammonium halide and 1,10-phenanthroline can disturb the hydrogenation.   The activities of heterogeneous catalysts supported on charcoal depend strongly on the covering strength of the ligand stabilizer. Similarly, Pt/Ru alloy colloids prepared as precursors for fuel cell catalysts using an organometallic compound[44] possesses lipophilic surfactant stabilizers.   Prior to electrocatalysis, the surfactant is removed by reactive annealing in O_2 or H_2.   The catalytic activities with respect to CO and methanol oxidation were found to be practically identical to commercial Vulcan-supported Pt/Ru catalysts.

The use of polymer-hosted or -capped nanoparticles as catalysts is another area of increasing interest.   For example, using stepwise growth method, poly(N-vinyl-2-pyrrolidone)-stabilized Pd nanoparticles (3-7 nm) with varying particle size are prepared[42] as catalysts for the Suzuki reaction between phenylboronic acid and iodobenzene.   The size dependence of catalytic activity shows that the low-coordination number vertex and edge atoms on the particle surface are active sites.   Pt nanoparticles supported in nanoporous Al_2O_3 catalyst are prepared by reduction of K_2PtCl_4 in the presence of Al_2O_3 and poly(acrylic acid) as capping agent to protect against particle aggregation and produce various shapes.   The activation energy for the hydrogenation of propene is found to be about one-half that for catalysis by Pt deposited in SiO_2 and TiO_2 synthesized by using impregnation method. In a latest example, Rotello and co-workers demonstrated the preparation of polymer-mediated self-assembly of functionalized Pd and SiO_2 nanoparticles as catalysts through 'bottom-up' approach.[21]   The assembled nanoparticles after calcination is shown to be highly reactive for both hydrogenation and carbon–carbon bond formation reactions.   In addition to several examples of using conducting polymers to disperse electrodeposited metal nanoparticles as fuel cell catalysts,[74,75,82] the use of dendrimers for dispersing nanoparticles is another recent example.   Crooks and co-workers[76,77] have demonstrated the preparation by sequestering metal ions within dendrimers followed by chemical reduction to yield metal nanoparticles (1~5 nm).   The Pt nanoparticles in dendrimer exhibited remarkable catalytic activities towards

hydrogenation and carbon-carbon coupling reactions. Major attributes of the dendrimer encapsulation include uniform structure, stabilization against agglomeration, substantial fraction of active surface, access of small molecules, and tunable periphery to control solubility, which have been discussed in a recent review.[76]

As a model system to delineate size and interparticle spatial properties in catalysis, the viability of catalysis of organic monolayer-encapsulated gold or alloy nanoparticles have been recently investigated through core-shell nanostructured assembly on planar substrates (Scheme 5.2). This approach can in fact be applied to any type of substrate. Details of the assembly is described in the next subsection. The shell-based surface passivation, which concerns all catalytic applications of nanoparticles when the surface properties are exploited, depends on the nature of the interfacial reaction. The central question is thus how the nanocrystal core can be processed towards catalytically active sites. Upon catalytic activation, as will be discussed in a great detail in a later subsection, the core-shell assembled nanostructure undergoes structural or morphological changes within both the individual core-shell structure and the collective network environment. Unlike conventional colloids which are hardly processable due to the propensity of aggregation, the shell encapsulation imparts 3D structural framework to enhance catalyst stability.

These nanostructured catalysts were studied for electrooxidation of CO and methanol,[61-63] which are of tremendous interest because of fundamental significance and broad technological applications, including methanol oxidation fuel-cell technology and purification of air in gas products, long duration space travel, and conversion for automobile exhaust. Both CO and methanol can be electrocatalytically oxidized at the assembled Au or Au/Pt nanoparticles of 2-5 nm core sizes.[61-63] In the case of electrocatalytic oxidation of methanol at an activated $(Au-Pt)_{2-nm}$ nanoparticles on glassy carbon electrode (Figure 5.3),[62] the anodic peak current (i_{pa}) exhibits a linear relationship with methanol concentration, (insert). The peak potential closely matches the potential for Au oxide formation. In contrast, the peak current for the cathodic wave (i_{pc}) decreases with increasing methanol concentration. The opposite trend is suggestive of a catalytic mediation role by surface Au oxide species. Both i_{pa} and i_{pc} increase with scan rate, which resembles those observed for electrooxidation of methanol at Pt-based surface and of CO at core-shell Au nanoparticle assembly.[61] The gold component is predominantly responsible for the catalytic activity, since the Pt is only a small fraction of the alloy composition (~5%) and similar reactivity has been found for activated Au nanoparticle assembly.[63,65]
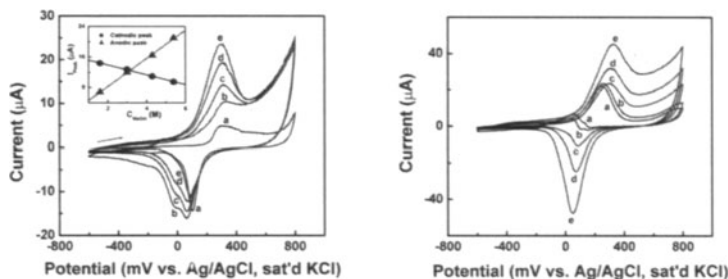
FIGURE 5.3. Left: Cyclic voltammetric curves for activated NDT-linked Au-Pt nanoparticles on glassy carbon electrode in electrolyte solution of 0.5 M KOH with methanol concentration of 0 (a), 1.6 (b), 3.0 (c), 4.3 (d) and 5.4 M (e). (electrode area: 0.07 cm^2. 50 mV/s). Right: Scan rate dependence in solution-e (10, 20, 50, 100, and 200 mV/s). [*Chem. Comm.* 2001,*5*, 473] Reproduced by permission of The Royal Society of Chemistry.[62]

Other alloy nanoparticles such as Au/Ni and Au/Fe have also been studied for these electrocatalytic reactions. It is known that Au nanoparticles supported on Fe_2O_3 are highly active catalysts for CO oxidation.[1,2] In view of the easy oxidation of Fe, the activated Au/Fe nanoparticle assembly may introduce Au/Fe_2O_3 as part of the nanocrystal composition. Preliminary catalytic current-potential data for methanol electrooxidation at an activated Au/Fe nanoparticle assembly showed a current density of ~ 26 mA/mg (0.23 V), which is remarkably close to those reported for commercial carbon-supported Pt/Ru catalyst (~40 mA/mg).[44] Many mechanistic issues are yet to be determined for fully assessing the observed catalytic activity.

5.9.   THE NANOPARTICLE ASSEMBLY

As noted earlier, there are many pathways towards nanoparticle assembly, including the dispersion of nanoparticles in polymers[74,75,98] or dentrimers[76,77] and the polymer-mediated self-assembly of functionalized Pd and SiO_2 nanoparticles.[21] Several approaches have also involved surfactant molecules[99] or polymers[81] as capping agents. In these approaches, the polymeric or molecular environment effectively suppressed the nanocrystal core-core aggregation. The assembly of monolayer-capped nanoparticles on a substrate as catalysts is another pathway. In particular, the assembly of nanoparticles on planar surfaces is often desired because the catalytic activities can be effectively probed using surface analytical tools such as STM and AFM. The use of molecular linkers such as ω-functionalized thiols has been widely reported for stepwise layer-by-layer or hydrogen-bonding polymeric assembly of nanoparticles.[100-103] In a recent approach, we

demonstrated a simple one-step pathway,[89] which exploits the surface exchange reactivity[88] of monolayer-capped nanoparticles towards thin film assembly. This approach is termed as one-step exchange-crosslinking-precipitation route.[89,104] One example involved the exchange of ω-functionalized alkyl thiols, e.g., 1,9-nonanedithiol (NDT), with decanethiolates (DT) capped on gold nanoparticles. The DT-NDT exchange reaction was followed by crosslinking, leading to nucleation and growth of a 3D network thin film. Another example involves hydrogen-bonding using carboxylic acid functionalized alkyl thiols, e.g., 11-mercaptoundecanoic acid (MUA). The DT-MUA exchange reaction was followed by hydrogen-bonding into a network thin film.
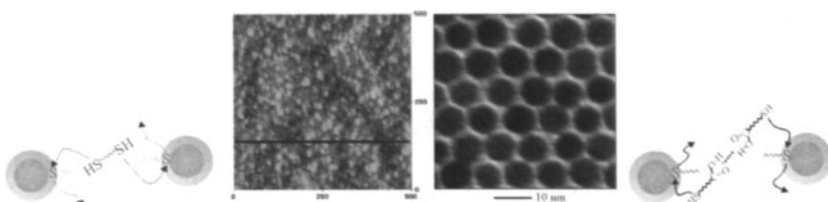
FIGURE 5.4. Left: AFM image for an NDT-linked Au_{2-nm} on annealed Au(111)/mica. Reprinted with permission from *Adv. Mater.* 2001, *13*, 1507 Copyright 2001 Wiley-VCH.[9] Right: TEM for MUA-linked Au_{6-nm} on carbon-coated Cu-grid. Reprinted with permission from *Chem. Mater*, 2002, in-press. Copyright 2002 American Chemical Society. [105]

The assembled nanoparticles, as shown in an atomic force microscopic (AFM) image for NDT-linked Au_{2-nm} on Au(111) and a TEM micrograph for MUA-linked Au_{6-nm} on carbon film (Figure 5.4), display individually-isolated character or highly ordered interparticle spatial property. It is important to note that both the crosslinking and the original capping molecules are present in the assembled nanostructure; the relative ratio depends on the extent of exchange.[99,105] The electronic conductivity, interfacial reactivity and nanoporous properties of these nanostructured films have been extensively characterized.[89,104-106] The conductivity depends on particle core size and linker chain length.[104,106] The nanostructure is nanoporous through which the interfacial reactivity and mass fluxes can be fine-tuned chemically or electrochemically.[107] The latter is desired for achieving catalytic access through the nanostructured pores in a way similar to zeolite-like pores. How to activate the catalytic activity of the nanocrystal cores is the focus of the next subsection.

5.10. THE CATALYTIC ACTIVATION

It is evident that the catalytic activity of the core-shell assembled nanoparticles requires the ability to manipulate the interparticle spatial and interfacial access properties. This ability is inherently linked to the controllable activation, or reconstitution of the shell components. This subsection focuses on catalytic activation. While there are a number of means for catalytic activation, we describe here electrochemical and thermal activation to illustrate the general concept. In each case, we also show the use of surface analytical techniques to probe the nanochemistry involved.

5.10.1. ELECTROCHEMICAL ACTIVATION

Electrochemical activation is well known in electrocatalysis,[108] which usually involves interfacial oxidative or reductive reconstitution. In the example shown in the previous section (Figure 5.3), the methanol oxidation wave was observed only after application of a polarization potential at $\sim$+800 mV to the assembled catalysts, a process we termed as electrochemical activation. The potential-induced catalytic activation of the assembled gold catalysts was further evidenced by the fact that the potential for CO or methanol oxidation closely matched the potential for gold oxide formation, implying the participation of Au oxide in the overall catalytic oxidation mechanism.

A number of analytical tools have been utilized to probe the structural and morphological reconstitution of the catalytic activation. One powerful technique involves electrochemical quartz-crystal nanobalance (EQCN)[63-65] which is highly sensitive to interfacial mass fluxes (0.1 ng). The quantitative correlation of the oxidation charge and the detected mass changes provides an assessment of the formation of oxide species (e.g., AuO_x, $AuOH_{ad}$) in the assembled catalysts and mass fluxes of reactant, product and solvent. The EQCN data (Figures 5.5) revealed changes in both current and mass curves for a NDT-linked Au_{2-nm} film during the catalytic activation process in an alkaline electrolyte. Both the oxidation and the reduction currents increase with the number of cycles, whereas the mass decreases gradually, reaching about 3500 ng/cm^2 after $\sim$18 cycles. The detected mass change corresponds to an equivalency of 80-90% loss of the thiolates in the catalyst film. Corresponding to the methanol oxidation wave at +215 mV, there is a mass wave which is absent in the control experiment (Figure 5.5), implying a predominant initial product release followed by formation of surface oxygenated species. The mass decrease detected for the cathodic wave (+ 62 mV) is in part attributed to the reduction of nanocrystal's surface oxygenated species or oxides, and in part to release of solvent or anions (OH$^-$) from the

nanostructure. The anodic charge, 1465 $\mu C/cm^2$ (corresponding mass change ~90 ng/cm^2), is much larger than the expected mass change. It follows that the charge is largely used in the oxidation process of methanol from the solution. The reduction charge, 164 $\mu C/cm^2$, corresponds to 0.56 nmoles/cm^2 coverage of Au(OH)$_3$. The electrogenerated oxide species were largely used in the electron mediation for methanol oxidation. The detected mass decrease for the reduction of the surface oxides is only 6% of a full monolayer coverage of oxide in the nanoparticle assembly, suggesting the formation of a hydrated metal oxide phase (e. g., Au$_2$O$_3$ nH$_2$O). For gold oxide, the hydration energy is negative, i.e., ΔG^0_{hydr} = -7.53 kcal/mol. The detected voltammetric and piezogravimetric characteristics are consistent with an expected equilibrium potential shift, $\Delta E_{eq} = \Delta E^0 = 0.054$ V.
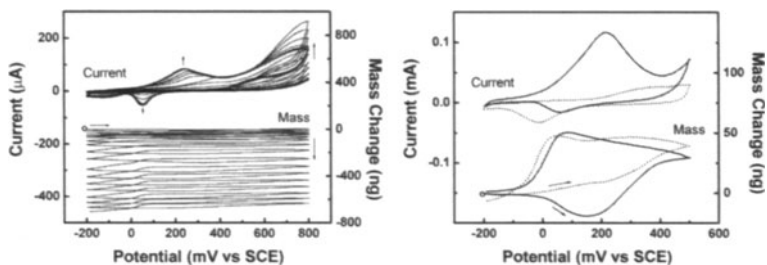
Figure 5.5. EQCN curves for electrochemical activation process (left), and the electrocatalytic oxidation of methanol (right) at the activated NDT-linked Au$_{2\text{-nm}}$ film electrode in 0.5 M KOH with 3.0 M methanol (solid line) and without (dash line). (50 mV/s). Reproduced with permission from *Catal. Today*, 2002, in-press. Copyright 2002 Elsevier Science B.V.[63]

The activity is dependent on the nature of the molecular linkers, which is reflected by the difference in peak current and potential. It is found that the MUA-linked Au$_{2nm}$ film is activated more easily than NDT-Au$_{2\text{-nm}}$ film of similar coverages, and displays a higher electrocatalytic activity with the peak potential of the oxidation wave being slightly lower (+280 mV) and peak current larger (by a factor of ~2) than those for NDT-linked film. The ready catalytic activation of the MUA-linked nanoparticles suggests the influence of the molecular structure on the open framework, the access of electrolytes, and the solubility of desorbed molecules. Insights into these issues require further structural and morphological information, which is discussed next based on results from a number of surface characterizations using infrared reflection spectroscopy (IRS), X-ray Photoelectron Spectroscopy (XPS) and atomic force microscopy (AFM).

IRS probes the shell or framework structural properties. The spectral features in the high-frequency region (Figure 5.6) are diagnostic of the methylene stretching bands (v_a(CH$_2$)~2920 and v_a(CH$_2$)~2950 cm^{-1}) in the

alkyl chains (NDT).[63] For the NDT-linked nanoparticle film, the significant reduction in absorbance after the catalytic activation is suggestive of the removal of the shell components from the nanostructured film, a result consistent with the EQCN-detected mass decrease upon catalytic activation, as described in the previous section.
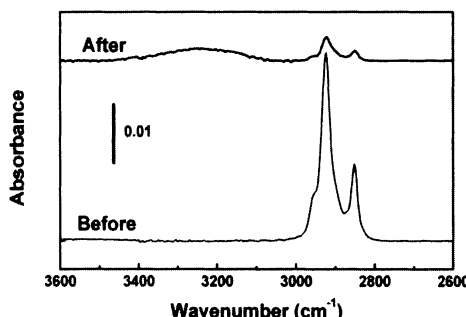
FIGURE 5.6. IRS spectra in high-frequency region for an NDT-Au$_{2nm}$ film on Au/glass before and after potential activation in an electrolyte solution of 0.5 M KOH with 3.0 M methanol. Reproduced with permission from *Catal. Today*, 2002, in-press. Copyright 2002 Elsevier Science B.V.[63]

XPS analysis of the nanostructured catalysts, on the other hand, provides important information on the identification of surface species on the activated nanocrystal cores.[66] The results for NDT-Au$_{2-nm}$ and MUA-Au$_{2-nm}$ films are analyzed in the regions of S(2p) (A) and O(1s) (B) (Figure 5.7). For the NDT-linked film, the S(2p) band intensity after activation is significantly reduced, indicating a partial removal of thiolates species (~75%). The envelope of the remaining (S2p) band (b) is suggestive of the presence of un-removed thiolates and weakly-bound -SH group from one end of NDT. The detection of the small 169.2 eV band is indicative of the presence of sulfonate species (-SO$_3^-$), qualitatively consistent with earlier findings in electrochemical oxidative desorption of self-assembled alkanethiolate monolayers on planar gold surfaces. A similar S(2p) spectral feature for the as-prepared MUA-linked film demonstrates the similarity of the Au-thiolate bonding. The absence of the higher-BE component is consistent with the more effective removal of thiolates than the case of the NDT-linked nanoparticles. In O(1s) region (B), an increase of the O(1s) band is detected at 532.4 eV for the activated NDT-linked film (a). In comparison with those observed for surface oxide species, this band is attributed to the formation of oxygenated species (oxides) on the gold nanocrystals, consistent with the application of an anodic potential (> +600 mV) in the alkaline electrolyte. For MUA-Au$_{2-nm}$ film (B), a similar conclusion can be reached based on the subtle changes in the O(1s) band position and intensity. The analysis is also consistent with spectral

deconvolution of the overlapping band components of Au(4f) bands, which revealed a combination of Au(0) and Au(I)/(III) components after the partial removal of thiolates. These could be due to Au(I) and Au(III) oxides (e.g., Au_2O_3, or $Au(OH)_x$). On the basis of the relative oxygen to sulfur ratios on the activated gold nanocrystals, the thiolates being removed include both DT and MUA molecules and the detected oxygen is largely from the surface oxides.
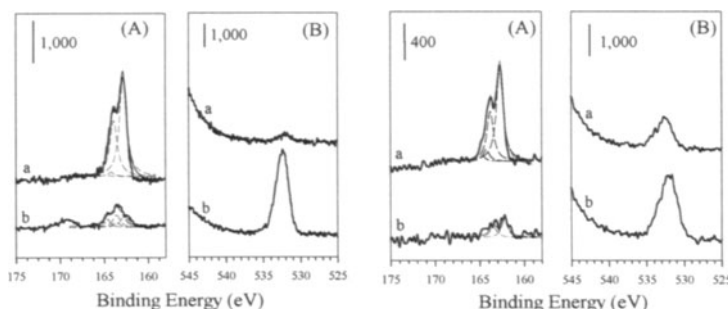
FIGURE 5.7. XPS spectra in regions of S(2p) (A) and O(1s) (B) for a NDT-Au_{2-nm} film (left A&B) and a MUA-Au_{2-nm} film (right A&B) before (a) and after (b) the electrochemical activation. Film thickness: ~ 13 equivalent layers. Reprinted with permission from *Langmuir*, 2002, *in-press*. Copyright 2002 American Chemical Society.[66]

The overall electrocatalytic reactions of CO or methanol are:

$$CO_{ad}/Au^0 + 2\ OH_{ad}/AuO_x - 2e^- \rightarrow Au^0/AuO_x + H_2O + CO_2$$
$$(CO_3^-/alkaline)$$
$$CH_3OH_{ad}/Au^0 + 6OH_{ad}/AuO_x - 6e^- \rightarrow Au^0/AuO_x + 5H_2O + CO_2$$
$$(CO_3^-/alkaline).$$
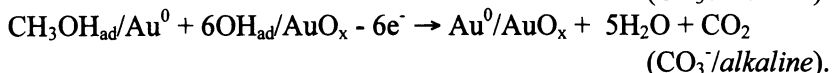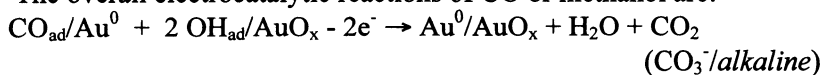
AFM studies provided further insights into the morphological changes of the nanostructured catalysts before and after catalytic activation.[63] Before activation (a), the overall surface morphology for a film of ~3 layers assembled on a glassy carbon electrode (Figure 5.8) is partly due to the surface roughness effect of the substrate. The particles appear somewhat larger than the core-shell particle size, but the cross-section view reveals an average height as expected for the particle size. In addition to tip-sample convolution effect, a number of additional factors include roughness of the glassy carbon surface, thickness of the film, and interparticle linkages of particles by the shell linkers. Images of a very thin film on flat surfaces (e.g., mica or annealed Au(111)) have in fact revealed that the height data are consistent with the particle sizes determined from TEM. After activation (b), there appears no significant change of size after the activation, at least within the resolution limit. The interparticle distance change is reflected by the

appearance of smoother domains after activation. The porous morphology is also evident.
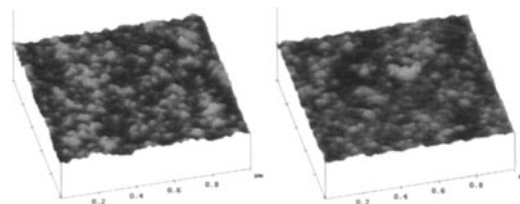
FIGURE 5.8. TM-AFM images for NDT-lined Au_{2-nm} on GC electrode before (left) and after (right) electrochemical activation in 0.5 M KOH with 3.0 M methanol. The film thickness is equivalent to ~3 layers of nanoparticles. Reprinted with permission from Reproduced with permission from *Catal. Today*, 2002, in-press. Copyright 2002 Elsevier Science B.V.[63]

As a rough estimate of the morphology change, the standard deviation (Rms) of the Z values suggests a smoothing effect by the activation. The smoother film morphology indicates that there is a rearrangement of the nanoparticles upon removal of some thiolates. The insignificant change in particle size or interparticle spatial property is indicative of the effective isolation of individual nanoparticles before and after the catalytic activation even though there is a rearrangement of the nanostructured particles. Further in-situ AFM probing of the electrochemical activation using a patterned nanoparticle assembly revealed a subtle swelling of the nanostructure after the activation, implying the morphological rearrangement due to fluxes across the nanostructure.

Two main conclusions can be drawn about the electrochemical activation: (1) there is a partial opening of the capping/linking nanostructure as a result of the removal of shell molecules; and (2) surface oxides are formed on the gold nanocrystals. On the basis of the recent proposal for catalytic oxidation of CO on oxide (e.g., TiO_2 and FeO_x)-supported Au catalyst[1-4] and surface oxygen ad-atom on gold,[109] the structure of the activated core-shell catalysts can be hypothesized as nanocrystal cores with a partial oxide encapsulation (Scheme 5.4). The uptake of oxygen forming gold oxides leads to the formation of pores, which could then be operative for admitting reactant or releasing product, and allowing catalysis to occur at the peripheral (interfacial) areas between core and shell involving Au or $Au^{\delta+}$ species. This would facilitate the chemisorption of CO or methanol on Au atoms of low coordination number and combination with OH species supplied by the contacting oxide shell. In comparison with catalytic peripheral sites on oxide-supported Au nanoparticles, the total amount of peripheral Au should be much larger for the AuO_x-capped nanoparticles. It is important to note

that the tendency of gold oxide formation is completely changed as a result of the size shrinkage in comparison with bulk gold.
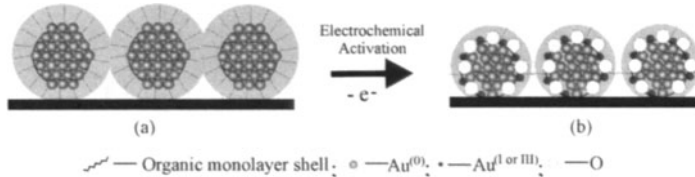
SCHEME 5.4. A schematic illustration of the electrochemical activation of the assembled nanoparticles. The shell is partially removed, and covered with oxides. The linker molecules are omitted in the drawing for simplicity. Reprinted with permission from *Langmuir*, 2002, in-press. Copyright 2002 American Chemical Society.[66]

5.10.2. THERMAL ACTIVATION

Thermolysis is another approach towards catalytic activation, which eliminates the use of electrolytes in electrochemical activation. Calcination of catalysts is well documented for catalyst pretreatment. The thermolysis of metal-carboxylate bridged gold nanoparticles[102] for preparing conductive films, the calcination of surfactant-capped Pt/Ru nanoparticles[44] or C-supported $PtRu_5C(CO)_{16}$[110] for preparing catalysts, and the thermal treatment of the polymer-mediated assembly of Pd and SiO_2 nanoparticle catalysts[21] are some of the recent examples. A key question is how the interparticle spatial and surface properties evolve controllably for the nanostructured catalysis, which is discussed in this subsection.

Using molecularly-wired gold nanocrystals on a mica substrate, we recently investigated thermal activation of the nanostructured catalysts for electrocatalytic oxidation of methanol.[111] The aim was to establish a thermal activation strategy viable for processing nanostructured catalysts via spatially-defined core-shell nanoparticle assembly. The thermogravimetric analysis of DT-capped Au_{2-nm} particles reveals a transition at 225 ^0C with an overall mass change (25%wt). Two possibilities were hypothesized for the thermal activation near this transition temperature. One involves partially-capped nanoparticles with intact core size and interparticle space, and the other, naked nanoparticles with larger but controllable core size. The interaction of the shell-opened nanocrystals with the substrate surface thus plays an important role in the eventual morphology of the nanoparticles.

These possibilities were examined by comparing the in-situ AFM images for a NDT-linked Au nanoparticle film on mica surface before and after the thermal treatment at 225 ^{0}C (Figure 5.9). The particles are clustered into wire or chain-like morphologies. The cross-section data suggest an overlapping of ~3 nanoparticles in average. The outline of individual nanoparticles is slightly blurred or not well resolved (a). After the treatment (b), the outline of individual particles is better resolved, but also the chain-like feature remains intact.
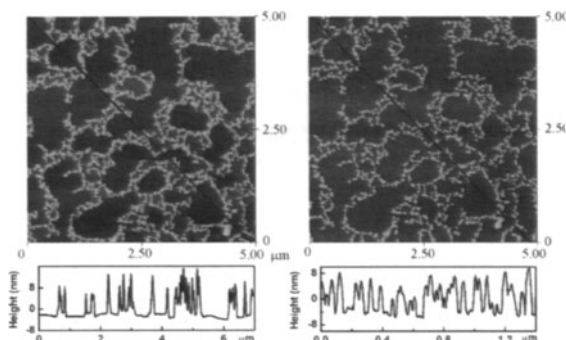
FIGURE 5.9. In-situ AFM images (5x5 μm^2) of a sub-monolayer film of NDT-Au_{2-nm} on mica before (a) and after (b) thermal activation (225 °C, 30 min) (acquired after cooling to RT). Cross-section view corresponds to the line drawn. Reprinted with permission from *J. Am. Chem. Soc.*, 2002, in-press. Copyright 2002 American Chemical Society.[111]

The removal of thiolates at this temperature was also supported by tapping-mode phase imaging data, which reveals that the dark phase contrast (associated with the thiol monolayer) for the as-prepared film is absent for the thermally treated. The height analysis of the cross-section data reveals 11.1   3.9 nm (a) and 13.1   3.4 nm (b), respectively, suggesting relatively little change in height. The small increase in particle size is believed to be due to localized aggregation largely from the overlapped particles. The unchanged interparticle spatial feature in the xy-plane demonstrates that the interparticle spatial property can be controlled even if there is a local aggregation from the overlapped nanoparticles. Both IRS and XPS data have evidenced the absence of any organic thiolates of the assembled nanoparticles after the thermal activation. It is thus viable to control the interparticle spatial properties by programming the temperature. The combination of the initial molecular wiring and the subsequent adhesive interaction of the particle to the substrate must have played an important role in the spatial fixation (Scheme 5.5).
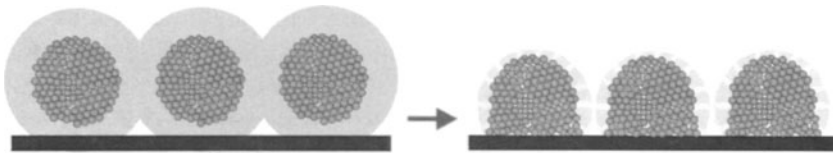
SCHEME 5.5. A schematic illustration of thermal activation of the core-shell assembled nanoparticles on a substrate surface. Reprinted with permission from *J. Am. Chem. Soc.* 2002, in-press. Copyright 2002 American Chemical Society.[111]

By further comparing the electrocatalytic activity between the thermally activated gold catalysts and the electrochemically activated catalysts, the anodic current density for the thermally-activated film is found to be twice as large as the electrochemically-activated catalyst (same film thickness). The oxidation potential is slightly less positive for the former than the latter. A closer examination reveals two overlapping anodic waves, indicating the existence of at least two different catalytic sites for the thermally-activated catalysts. The molecularly-wired nanoparticles can thus be thermally activated by manipulating temperature to produce nanoparticle catalysts with controllable size and largely intact interparticle morphology on surfaces. In view of the fact that dependencies of the interparticle morphology on temperature, wiring structure and substrate properties, these findings have important implications to the design of nanostructured catalysts via molecular wiring nanoparticles on a substrate.

5.11. CONCLUSIONS AND PROSPECTUS

We have shown that nanoparticles of controllable core size and surface properties can be synthesized, processed, manipulated, and probed for catalytic applications. The emerging nanotechnology is also shown to have significant impacts to catalysis. The oxide-supported, polymer or dendrimer encapsulated, molecularly-assembled monometallic/bimetallic/multi-metallic nanoparticle catalysts, and their combinations may eventually provide promising ventures with unprecedented opportunities to prepare nanostructured catalysts with precisely controlled size, shape, surface and spatial properties. The catalytic or electrocatalytic oxidations of CO and methanol are just some examples of the exploration. A more challenging issue in expanding these nanostructured catalytic concepts is the ability to manipulate nanoscale chemistry with 100% catalytic selectivity. Many areas of on-going work on core size, shape, composition and interparticle spatial properties involve the use of spectroscopic, microscopic and in-situ techniques to provide quantitative assessments of the nanostructural

evolution of catalytic sites, and theoretical modeling of nanocrystal's unique physical and chemical properties to understand the mechanistic aspects of the nanostructured catalysis.

It is important to note that the fundamental insights in developing nanoparticle catalysis could also form the basis of many new technologies. Microsensor technology is such an area where nanoparticles are used as catalytic components in sensing materials for the detection of analytes. For example, most commercial chemiresistor-type gas sensors use semiconductor materials (e.g., SnO_2),[112] and the response principle is based on the detection of changes in conductivity in the n-type material, either an increase as a result of releasing electrons from surface states in reducing gases (e.g., CO, CH_4), or an decrease as a result of space charge build up in oxidizing gases (e.g., NO_2). The main drawbacks include the lack of selectivity and high temperature ($>300^0C$) requirement. In addition to reducing operation temperatures[113,114], doping of semiconductor (e.g., SnO_2, SiO_2 or TiO_2) materials with metals (e.g., Pt, Pd, Au etc.)[112-114] modulates the Schottky barrier at the semiconductor/metal contact leading to different overall resistance. The distribution of the active metal nanosites and the reduction of interfacial potential barrier between semiconductor crystallites regulate electronic conductivity, catalytic activity and chemical specificity for enhancing sensory responses.

The field of nanostructured catalysis has benefited greatly from the development of advanced nanomaterials, which will undoubtedly continue as many new nanomaterials are rapidly emerging. One example is the use of carbon nanotubes for fabricating catalysts. Carbon nanotubes have extremely high surface area to volume (or weight) ratios, and can be conductive or semiconductive depending on diameter. The assembly and characterization of nanoparticles on such materials, as already demonstrated in recent reports (e.g., Pt-loaded carbon nanotubes for methanol oxidation),[52] will lead to enormous opportunities in nanotechnology, fuel cell catalysis, and environmental sensors. The precise manipulation of the surface and spatial properties is only at beginning. The question whether the nanostructured materials can in general be developed into designer catalysts of high catalytic activities and selectivities rests with our capabilities in controlled fabrication, effective activation, nanoscale manipulation, and analytical probing. A variety of advanced design strategies will quickly emerge by taking advantage of recent developments of nanotechnology, which will help us in the exciting advent towards "catalyst-by-design".

ACKNOWLEDGEMENTS

REFERENCES

1. Haruta, M. *Catal. Today*, **1997**, *36*, 153, and references therein.
2. Haruta, M.; Date, M. *Appl. Catal. A*, **2001**, *222*, 427.
3. Bond, G. C.; Thompson, D. T. *Gold Bulletin*, **2000**, *33*, 41; and refs therein.
4. Bond, G. C. *Gold Bulletin*, **2001**, *34*, 117.
5. Aiken III, J. D.; Finke, R. G. *J. Mol. Catal. A.*, **1999**, *145*, 1.
6. Klabunde, K. J.; Mulukutla, R. S. in *Nanoscale Materials in Chemistry*, Ed. by Klabunde, K. J., John Wiley & Sons, Inc., New York, **2001**, p.223.
7. Li, H.; Luk, Y.-Y.; Mrksich, M. *Langmuir*, **1999**, *15*, 4957.
8. Ingram, R. S.; Murray, R. W. *Langmuir*, **1998**, *14*, 4115.
9. Zhong, C. J.; Maye, M. M. *Adv. Mater.*, **2001**, *13*, 1507.
10. Templeton, A. C.; Wuelfing, W. P.; Murray, R. W. *Acc. Chem. Res.*, **2000** *33*, 27; and references therein.
11. Caruso, F. *Adv. Mater.*, **2001**, *13*, 11; and references therein.
12. Schneider, J. J. *Adv. Mater.*, **2001**, *13*, 529.
13. Schärtl, W. *Adv. Mater.* **2000**, *12*, 1899.
14. Whetten, R. L.; Khoury, J. T.; Alvarez, M. M.; Murthy, S.; Vezmar, L.; Wang, Z. L.; Stephens, P. W.; Cleveland, C. L.; Luedtke, W. D.; Landman, U. *Adv. Mater.* **1996**, *8*, 428.
15. Storhoff, J. J.; Mirkin, C. *Chem. Rev.*, **1999**, *99*, 1849.
16. El-Sayed, M. A. *Acc. Chem. Res.*, **2001**, *34*, 257.
17. Kiely, C. J.; Fink, J.; Zheng, J. G.; Brust, M.; Bethell, D.; Schiffrin, D. J. *Adv. Mater.*, **2000**, *12*, 640.
18. Peng, X.; Schlamp, M. C.; Kadavanich, A. V.; Alivisatos, A. P. *J. Am. Chem. Soc.*, **1997**, *119*, 7019.
19. Oldenburg, S. J.; Averitt, R. D.; Westcott, S. L.; Halas, N. J. *Chem. Phys. Lett.*, **1998**, *288*, 243.
20. Mbindyo, J. K. N.; Reiss, B. D.; Martin, B. R.; Keating, C. D.; Natan, M. J.; Mallouk, T. E. *Adv. Mater.*, **2001**, *13*, 249.
21. Galow, T. H.; Drechsler, U.; Hanson, J. A.; Rotello, V. M. *Chem. Commun.*, **2002**, 1076.
22. Klabunde, K. J. Ed., *Nanoscale Materials in Chemistry*, John Wiley & Sons, Inc., New York, **2001**.
23. Feldheim, D. L.; Foss, Jr. C. A. Eds., *Metal Nanoparticles: Synthesis, Characterization, and Applications*, Marcel Dekker, Inc., New York, **2002**.
24. Schmid, G.; Maihack, V.; Lantermann, F.; Peschel, S. *J. Chem. Soc., Dalton Trans.*, **1996**, 589.

25. Nalwa, H. S. Ed., *Handbook of Nanostructured Materials and Nanotechnology*, V.1-4, Academic Press, San Diego, **2000**.

26. Bond, G. C.; Thompson, D. T. *Catal. Rev.*, **1999**, *41*, 319.

27. Wasmus, S.; Kuever, A. *J. Electroanal. Chem.*, **1999**, *461*, 14.

28. Lipkowski, J.; Ross, P. N. Jr.; Eds., *Electrocatalysis, Frontiers in Electrochemistry*, VCH, New York, Vol. 5, **1997**.

29. Jarvi, T. D.; Sriramulu, S.; Stuve, E. M. *J. Phys. Chem. B.*, **1997**, *101*, 3649.

30. Tremiliosi, G.; Kim, H.; Chrzanowski, W.; Wieckowski, A.; Grzybowska, B.; Kulesza, P. *J. Electroanal. Chem.*, **1999**, *467*, 143.

31. Valden, M.; Lai, X.; Goodman, D. W. *Science*, **1998**, *281*, 1647.

32. Ley, K. L.; Liu, R. X.; Pu, C.; Fan, Q. B.; Leyarovska, N.; Segre, C.; Smotkin, E. S. *J. Electrochem. Soc.*, **1997**, *144*, 1543.

33. Sun, N. J.; Klabunde, K. J. *J. Am. Chem. Soc.*, **1999**, *121*, 5587.

34. Shi, F.G. *J. Mater. Res.*, **1994**, *9*, 1307.

35. Thompson, D. *Gold Bulletin*, **1998**, *31*, 111. & **1999**, *32*, 12.

36. *Nanocatalysis and the Energy Markets*, CMP Científica, Madrid, Spain, **2002**.

37. Liu, J. 224th ACS National Meeting (Boston, August 18-22, **2002**), CATL-18.

38. Reddington, E.; Sapienza, A.; Gurau, B.; Viswanathan, R.; Sarangapani, S.; Smotkin, E. S.; Mallouk, T. E. *Science*, **1998**, *280*, 1735.

39. Chen, J.; Ollis, D. F.; Rulkens, W. H.; Bruning, H. *Water Res.*, **1999**, *33*, 661.

40. Waszczuk, P.; Lu, G. Q.; Wieckowski, A.; Lu, C.; Rice, C.; Masel, R. I. *Electrochim. Acta*, **2002**, *47*, 3637.

41. Park, K. W.; Choi, J. H.; Kwon, B. K.; Lee, S. A.; Sung, Y. E.; Ha, H. Y.; Hong, S. A.; Kim, H.; Wieckowski, A. *J. Phys. Chem. B*, **2002**, *106*, 1869.

42. Yoo, J. W.; Hathcock, D.; El-Sayed, M. A. *J. Phys. Chem. A*, **2002**, *106*, 2049.

43. Schmidt, T. J.; Gasteiger, H. A.; Behm, R. J. *Electrochem. Commun.*, **1999**, *1*, 1.

44. Paulus, U. A.; Endruschat, U.; Feldmeyer, G. J.; Schmidt, T. J.; Bonnemann, H.; Behm, R. J. *J. Catal.*, **2000**, *195*, 383.

45. Paulus, U. A.; Wokaun, A.; Scherer, G. G.; Schmidt, T. J.; Stamenkovic, V.; Radmilovic, V.; Markovic, N. M.; Ross, P. N. *J. Phys. Chem. B*, **2002**, *106*, 4181.

46. Toshima, N.; Shiraishi, Y.; Teranishi, T.; Miyake, M.; Tominaga, T.; Watanabe, H.; Brijoux, W.; Bonnemann, H.; Schmid, G. *Appl. Organometal Chem.*, **2001**, *15*, 178.

47. Junges, U.; Schuth, F.; Schmid, G.; Uchida, Y.; Schlogl, R. *Ber. Bunsenges. Phys. Chem.*, **1997**, *101*, 1631.

48. Zhu. J.; Somorjai, G. A. *Nano Letters*, **2001**, *1*, 8.

49. Somorjai, G. A.; McCrea, K. *Appl. Catal. A – Gen.*, **2001**, *222*, 3.

50. Raja, R.; Khimyak, T.; Thomas, J. M.; Hermans, S.; Johnson, B. F. G. *Angew Chem. Int. Ed.*, **2001**, *40*, 4638.

51. Jones, F. E.; Milne, S. B.; Gurau, B.; Smotkin, E. S.; Stock, S. R.; Lukehart, C. M. *J. Nanosci. Nanotechnol.*, **2002**, *2*, 81.

52. Che, G.; Lakshmi, B. B.; Martin, C. R.; Fisher, E. R. *Langmuir*, **1999**, *15*, 750.

53. Haruta, M. *Cattech*, **2002**, *6*, 102.

54. Kozlov, A. I.; Kozlova, A. P.; Liu, H.; Iwasawa, Y. *Appl. Catal. A - Gen.*, **1999**, *182*, 9.

55. Sanchez, A.; Abbet, S.; Heix, U.; Schneider, W.-D.; Hakkinen, H.; Barnett, R. N.; Landman, U. *J. Phys. Chem. A.*, **1999**, *103*, 9573.

56. Wallace, W. T.; Whetten, R. L. *J. Am. Chem. Soc.*, **2002**, *124*, 7499.

57. Bailie, J. E.; Hutchings, G. J. *Chemm. Commun.*, **1999**, 2151.

58. Molenbroek, A. M.; Norskov, J. K.; Clausen, B. S. *J. Phys. Chem. B*, **2001**, *105*. 5359.

59. Heiz, U.; Sanchez, A.; Abbet, S.; Schneider, W.-D. *Chem. Phys.*, **2000**, *262*, 189.

60. Pietron, J. J.; Stroud, R. M.; Rolison, D. R. *Nano lett.* **2002**, *2,* 545.

61. Maye, M. M.; Lou, Y. B.; Zhong, C. J. *Langmuir,* **2000,** *16,* 7520.

62. Lou, Y. B.; Maye, M. M.; Han, L.; Luo, J.; Zhong, C. J. *Chem. Commun.,* **2001,** 473.

63. Luo, J.; Maye, M. M.; Lou, Y. B.; Han, L.; Hepel, M.; Zhong, C. J. *Catal. Today,* **2002,** in press.

64. Luo, J.; Lou, Y. B.; Maye, M. M.; Zhong, C. J.; Hepel, M. *Electrochem. Comm.,* **2001,** *3,* 172.

65. Luo, J.; Maye, M. M.; Han, L.; Zhong, C. J.; Hepel, M. *J. New Mater. for Electrochem. Systems,* **2002,** *5,* 237.

66. Maye, M. M.; Luo, J.; Lin, Y.; Engelhard, M. H.; Hepel, M.; Zhong, C. J. *Langmuir,* in press.

67. Zarur, A. J.; Ying, J. Y., *Nature,* **2000,** *403,* 65.

68. Tschope, A.; Liu, W.; Flytzanistephanopoulos, M.; Ying, J. Y., *J. Catal.,* **1995,** *157,* 42.

69. Hansen, P. L.; Wagner, J. B.; Helveg, S.; Rostrup-Nielsen, J. R.; Clausen, B. S.; Topsoe, H. *Science,* **2002,** *295,* 2053.

70. Pak, C.; Bell, A. T.; Tilley, T. D. *J. Catal.,* **2002,** *206,* 49.

71. Nasr, C.; Vinodgopal, K.; Fisher, L.; Hotchandani, S.; Chattopadhyay, A. K.; Kamat, P. V. *J. Phys. Chem.,* **1996,** *100,* 8436.

72. Pellegatta, J. L.; Blandy, C.; Colliere, V.; Choukroun, R.; Chaudret, B.; Cheng, P.; Philippot, K. *J. Mol. Catal. A – Chem.,* **2002,** *178,* 55.

73. Chen, J.; Li, S. L.; Xu, Q.; Tanaka, K. *Chem. Commun.,* **2002,** 1722.

74. Hepel, M. *J. Electrochem. Soc.,* **1998,** *145,* 124.

75. Lima, A.; Coutanceau, C.; Leger, J. M.; Lamy, C. *J. Appl. Electrochem.,* **2001,** *31* 379.

76. Crooks, R. M.; Zhao, M. Q.; Sun, L.; Chechik, V.; Yeung, L. K. *Acc. Chem. Res.,* **2001,** *34,* 181.

77. Chechik, V.; Crooks, R. M. *J. Am. Chem. Soc.,* **2000,** *122,* 1243.

78. Toshima, N.; Shiraishi, Y.; Teranishi, T. *J. Mol. Catal. A:,* **2001,** *177,* 139.

79. Wang, Y.; Toshima, N. *J. Phys. Chem. B.,* **1997,** *101,* 5301.

80. Sidorov, S. N.; Volkov, I. V.; Davankov, V. A.; Tsyurupa, M. P.; Valetsky, P. M.; Bronstein, L. M.; Karlinsey, R.; Zwanziger, J. W.; Matveeva, V. G.; Sulman, E. M.; Lakina, N. V.; Wilder, E. A.; Spontak, R. J. *J. Am. Chem. Soc.,* **2001,** *123,* 10502.

81. Li, Y.; Boone, E.; El-Sayed, M. A. *Langmuir,* **2002,** *18,* 4921.

82. Kulesza, P. J.; Matczak, M.; Wolkiewicz, A.; Crzybowska, B.; Galkowski, M.; Malik, M. A.; Wieckowski, A. *Electrochim. Acta,* **1999,** *44,* 2131.

83. Maye, M. M.; Luo, J.; Lou, Y.; Ly, N. K.; Chan, W.-B.; Phillip, E.; Hepel, M.; Zhong, C. J. in *Nanophase and Nanocomposite Materials IV,* Ed. by Komarneni, S.; et al., *Mat. Res. Soc. Symp. Proc.* V10.6.1, **2001,** Vol. 703.

84. Sun, S.; Murray, C. B.; Weller, D.; Folks, L.; Moser, A. *Science,* **2000,** *287,* 1989.

85. Brust, M.; Walker, M.; Bethell, D.; Schiffrin, D. J.; Whyman, R. *J. Chem. Soc., Chem. Commun.,* **1994,** 801.

86. Hostetler, M. J.; Wingate, J. E.; Zhong, C. J.; Harris, J. E.; Vachet, R. W.; Clark, M. R.; Londono, J. D.; Green, S. J.; Stokes, J. J.; Wignall, G. D.; Glish, G. L.; Porter, M. D.; Evans, N. D.; Murray, R. W. *Langmuir,* **1998,** *14,* 17.

87. Hostetler, M. J.; Zhong, C. J.; Yen, B. K. H.; Anderegg, J.; Gross, S. M.; Evans, N. D.; Porter, M. D.; Murray, R. W. *J. Am. Chem. Soc.,* **1998,** *120,* 9396.

88. Hostetler, M. J.; Templeton, A. C.; Murray, R. W. *Langmuir,* **1999,** *15,* 3782.

89. Han, L.; Maye, M. M.; Leibowitz, F. L.; Ly, N. K.; Zhong, C. J. *J. Mater. Chem.,* **2001,** *11,* 1258.

90. Maye, M. M.; Zheng, W. X.; Leibowitz, F. L.; Ly, N. K.; Zhong, C. J. *Langmuir*, **2000**, *16*, 490.

91. Maye, M. M.; Zhong, C. J. *J. Mater. Chem.*, **2000**, *10*, 1895.

92. Maye, M. M.; Han, L.; Kariuki, N.; Ly, N. K.; Chan, W.-B.; Luo, J.; Zhong, C. J. *Anal. Chim. Acta.*, in press.

93. Clarke, N. Z.; Waters, C.; Johnson, K. A.; Satherley, J.; Schiffrin, D. J. *Langmuir*, **2001**, *17*, 6048.

94. Chen, S. W.; Pei, R. J. *J. Am. Chem. Soc.*, **2001**, *123*, 10607.

95. Teranishi, T.; Hasegawa, S.; Shimizu, T.; Miyake, M.; *Adv. Mater.*, **2001**, *13*, 1699.

96. Sanchez, A.; Abbet, S.; Heiz, U.; Schneider, W. D.; Halkkinen, H.; Barnett, R. N.; Landman, U. *J. Phys. Chem. A*, **1999**, *103*, 9573.

97. Schmid, G.; Baumle, M.; Geerkens, M.; Heim, I.; Osemann, C.; Sawitowski, T. *Chem. Soc. Rev.*, **1999**, *28*, 179.

98. Kariuki, N. N.; Han, L.; Ly, N. K.; Peterson, M. J.; Maye, M. M.; Liu, G.; Zhong, C. J. *Langmuir*, **2002**, *18*, 8255.

99. Schmid, G.; West, H.; Malm, J.-O.; Bovin, J.-O.; Grenthe, C. *Chem. Eur. J.*, **1996**, *2*, 1099.

100. Bethell, D.; Brust, M.; Schiffrin, D. J.; Kiely, C. J. *J. Electroanal. Chem.*, **1996**, *409*, 137.

101. Musick, M. D.; Keating, C. D.; Keefe, M. H.; Natan, M. J. *Chem. Mater.*, **1997**, *9*, 1499.

102. Templeton, A. C.; Zamborini, F. P.; Wuelfing, W. P.; Murray, R. W. *Langmuir*, **2000**, *16*, 6682.

103. Boal, A. K.; Ilhan, F.; DeRouchey, J. E.; Thurn-Albrecht, T.; Russell, T. P.; Rotello, V. M. *Nature*, **2000**, *404*, 746.

104. Zheng, W. X.; Maye, M. M.; Leibowitz, F. L.; Zhong, C. J. *Anal. Chem.*, **2000**, *72*, 2190.

105. Han, L.; Luo, J.; Kariuki, N.; Maye, M. M.; Jones, V. W.; Zhong, C. J. *Chem. Mater.*, in press.

106. Leibowitz, F. L.; Zheng, W. X.; Maye, M. M.; Zhong, C. J. *Anal. Chem.*, **1999**, *71*, 5076.

107. Luo, J.; Kariuki, N.; Han, L.; Maye, M. M.; Moussa, L. W.; Kowaleski, S. R.; Kirk, F. L.; Hepel, M.; Zhong, C. J. *J. Phys. Chem. B*, **2002**, *106*, 9313.

108. Vayenas, C. G.; Bebelis, S.; Pliangos, C.; Brosda, S.; Tsiplakides, D. *Electrochemical Activation of Catalysis: Promotion, Electrochemical Promotion, and Metal-Support Interactions*, Kluwer Academic Publishers, New York, **2001**.

109. Burke, L. D.; Nugent, P. F. *Gold Bulletin*, **1998**, *31*, 39.

110. Nashner, M. S.; Frenkel, A. I.; Somerville, D.; Hills, C. W.; Shapley, J. R.; Nuzzo, R. G. *J. Am. Chem. Soc.*, **1998**, *120*, 8093.

111. Luo, J.; Jones, V. W.; Maye, M. M.; Han, L.; Kariuki, N. N.; Zhong, C. J. *J. Am. Chem. Soc.*, in press.

112. Capone, S.; Siciliano, P.; Barsan, N.; Weimar, U.; Vasanelli, L. *Sensor. Actuator. B - Chem.*, **2001**, *78*, 40.

113. Cabot, A.; Arbiol, J.; Morante, J. R.; Weimar, U.; Barsan, N.; Gopel, W. *Sensors and Actuators B*, **2000**, *70*, 87.

114. Grunwaldt, J.-D.; Baiker, A. *J. Phys. Chem. B*, **1999**, *103*, 1002.

6

Adventures with Smart Chemical Sensing

Electrooptically Responsive Photonic Crystals

Sanford A. Asher
Department of Chemistry
University of Pittsburgh

6.1   INTRODUCTION

There is intense interest in the development of photonic crystal materials for applications in optics, optical computing and for the control of electromagnetic radiation propagation.[1-3] The excitement in this area stems from the recent development of a deep understanding of light propagation within materials with periodic optical dielectric constant modulations, and the development of fabrication methods for forming these materials.[4]

The synthetic and fabrication communities have been challenged to develop photonic crystals with the appropriate crystal structures and the dielectric constant modulations that enable the photonic crystals to possess three-dimensional photonic bandgaps in the visible and near IR spectral regions.[5] Electromagnetic radiation within a bandgap would be unable to propagate in a 3-D photonic bandgap material at any angle; thus, unique phenomena would occur; for example, spontaneous emission would disappear. Any light in the bandgap that entered the 3-D photonic bandgap material, through a purposely fabricated defect structure, could be made to traverse tortuous paths, such as, for example, 90 ° bends, without significant intensity losses. These possibilities enable a number of fantasies, such as fabricating complex photonic chips made out of 3-D photonic bandgap

materials that contain numerous optical transistors and switching devices, all made from photonic crystals.

As discussed below, the future appears bright for the development of photonic crystals for the control of light propagation. The rate limiting step is the development of methods to fabricate appropriate materials to test recent theories for propagation and control of light in photonic materials.

The first fabrication methods for forming photonic crystals utilized crystalline colloidal self assembly.[6] In this approach highly charged monodisperse spherical colloidal particles were dispersed in pure water.

CCA Self-Assembly
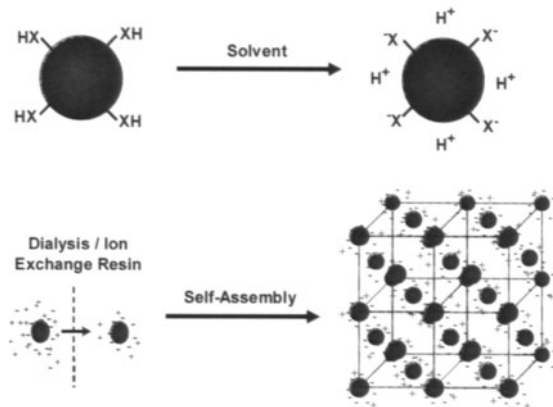
FIGURE 6.1. A dispersion of monodisperse colloidal particles with strong acid groups on their surfaces self assemble into fcc or bcc crystalline colloidal arrays in low ionic strength solution. Ions can be removed from colloidal dispersions by techniques such as dialysis, for example.

These spheres were functionalized with thousands of strong acid groups which ionized in water to result in a high surface charge (Figure 6.1). Because these highly charged spheres repel each other over macroscopic distances (Figure 6.2), the system finds a well defined minimum energy state. This minimum energy state involves the self assembly of these particles into an fcc lattice (a bcc structure is also observed under some conditions).

Monodisperse colloidal particles were first synthesized in the 1950's by Alfrey et al[7], a group from Dow Chemical. It was immediately obvious from TEM studies that these monodisperse polystyrene spherical particles easily formed highly ordered close packed arrays when aqueous dispersions of them were dried on TEM grids. Hiltner and Krieger[7,8] were among the first to note that cleaned dispersions of these monodisperse, charged particles would Bragg diffract visible light. The Asher group was the first to demonstrate that this colloidal crystalline array (CCA) self assembly could

be used to form large fcc single crystals, where the fcc (111) planes oriented parallel to the quartz plates which enclosed the crystal[6,9] (Figure 6.3). This enabled fabrication of photonic crystals which used the one dimensional fcc (111) plane band gap for filtering light in the visible spectral region.[6,9]

$$U(r) = \frac{Z^2 e^2}{\varepsilon} \left[\frac{e^{\kappa a}}{1 + \kappa a} \right]^2 \frac{e^{-\kappa r}}{r}$$

— Medium Dielectric Constant

— Interaction Potential Energy

$$\kappa^2 = \frac{4\pi e^2}{\varepsilon k_B T} \left(n_p Z + n_i \right)$$

— Ionic Impurities

— Dissociated Ions

— Reciprocal of Debye Layer Thickness
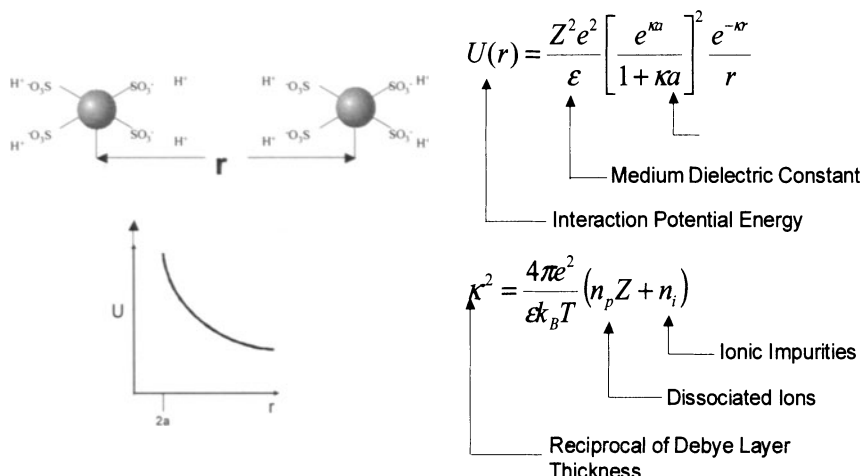
$1/\kappa$ in pure water is ~ 700 nm

FIGURE 6.2. CCA self assembly results from the electrostatic repulsion between colloidal particles. This interaction is modeled by the DLVO potential as increasing with the square of the colloidal particle charge, and inversely with the solution dielectric constant. It exponentially decreases with the Debye layer length, κ^{-1} which decreases with the solution ionic strength. The repulsion can be significant over macroscopic distances. For example, κ^{-1} is limited to 700 nm in pure water due to the concentrations of the H^+ and OH^-.

The Bragg diffraction efficiency of these CCA were extraordinarily high (Figure 6.3 and 6.4); for example, a thin 400 μm thick CCA of 270 nm diameter polystyrene spheres in water diffract away essentially all 488 nm light from a 1 W Ar laser, and allows brave observers to directly look down a lasing Ar^+ laser plasma tube.[6,9]

EG&G Princeton Applied Research Corp. was the first company to commercialize photonic crystals by manufacturing CCA filters for use in rejecting laser light. This commercialization occurred through their licensing of the first photonic crystal patents[6] from the University of Pittsburgh in the mid 1980's.

The major difficulty with the CCA photonic crystal devices is that they are potentially unstable, if not prepared with very pure materials and with careful attention to the sample container. CCA fabricated under appropriate conditions have shown over ten years of stability.
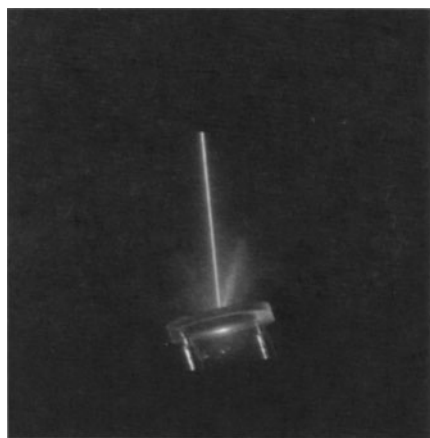
FIGURE 6.3. Diffraction of 488 nm laser light by an fcc CCA whose (111) planes diffract normally incident 1.4 μm light. The liquid CCA of 270 nm diameter spheres shows the diffraction of three beams from higher Miller indice planes. The ~100 μm thick fcc crystal is contained between two quartz plates. The fcc (111) planes spontaneously orient parallel to the quartz plate surfaces.
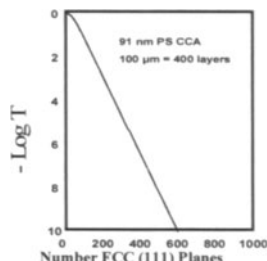
FIGURE 6.4. Calculated transmission through fcc CCA of 91 nm diameter polystyrene spheres in water diffracting 488 nm light. The transmittance is calculated to be less ~10^{-7} for 400 (111) planes, which corresponds to a CCA thickness of ~100 μm. Adapted from Spry and Kosan (ref. 13).

     The fcc lattice is kinetically stabilized by repulsive interactions. In the absence of these repulsive interactions these particles would flocculate as they reached their true equilibrium lowest energy state, the primary minimum. The CCA ordering will decrease if ionic impurities leach into the CCA. Further, the CCA must be sealed to avoid water evaporation. This is notoriously difficult to prevent since all organic materials have significant diffusion constants for water, and the optical devices must be contained in materials that transmit light. Further, the CCA transiently disorders due to mechanical shock.

The Asher group developed a much more rugged photonic crystal by embedding the CCA within a hydrogel matrix[10] (Figure 6.5). This was accomplished by UV photopolymerization of nonionic acrylamide and bisacrylamide derivatives and other crosslinkers and a UV photoinitiator that were added to the CCA. UV photopolymerization of these ~10 % acrylamide/bisacrylamide mixtures result in rugged polymerized CCA (PCCA) photonic crystals which are ~90 % water or other solvent. These PCCA are enabling photonic crystal structures, since they can be easily further processed to form more sophisticated functional photonic crystal materials.

PCCA Fabrication
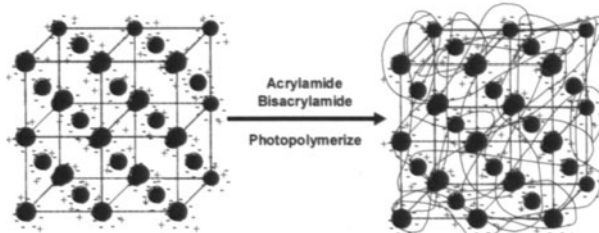
FIGURE 6.5. Synthesis of polymerized crystalline colloidal array (PCCA) by adding polymerizable monomers of acrylamide and bisacrylamide and a UV photoinitiator to a CCA. UV polymerization forms a hydrogel network around the CCA (~90 % water). The CCA crystal structure is maintained during polymerization and also upon hydrogel volume changes.

Another alternative to utilizing fragile CCA photonic crystals is to fabricate close-packed photonic crystals from monodisperse colloidal particles.[4,11] A number of groups have recently developed methods to grow highly ordered close packed arrays from solution dispersions of monodisperse particles. These methods rely on the controlled growth of particle layers on the growing crystal lattice surfaces. Additional processing of this lattice can form inverse opal structures. In this case, additional material is imbibed into the interstices between the close packed spheres. This material is then treated to remove the original close packed spheres,[11] leaving the material in the interstices between close packed arrays of air spheres.

6.2.   DIFFRACTION FROM CCA PHOTONIC CRYSTALS

6.2.1. DIFFRACTION EFFICIENCIES AND BAND GAPS

The diffraction from CCA photonic crystals made from ~120 nm polystyrene spheres in water is extremely efficient. For example, Figure 6.6 shows a transmission measurement of an fcc colloidal crystal[9] which is oriented with the normal to the fcc (111) planes parallel to the incident light propagation direction. The diffraction of light at ~500 nm gives rise to a symmetric bandshape in the Figure 6.6 extinction spectra, which are scaled as -log of the transmission.
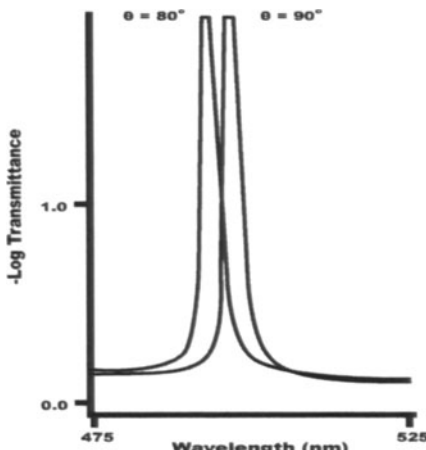
FIGURE 6.6. Extinction spectra of CCA of ~100 nm spheres. The diffraction band at ~500 nm shows a top hat profile since all incident light of a bandwidth of 5 nm is diffracted. The diffraction blue-shifts as the crystal is tilted to 80° off of the normal.

The simplest model for diffraction from these photonic crystals assumes the weak diffraction kinematic limit in which Bragg's law is operative: $\lambda_o \sim 2 \, n \, d \, \sin \theta$, where λ_o is the wavelength of light in vacuum, n is the average refractive index of the photonic crystal, d is the spacing of the lattice planes diffracting and θ is the Bragg glancing angle. In this model, CCA with numerous layers give rise to insignificant small diffraction bandwidths.

In contrast, diffraction from CCA of polystyrene spheres in water shows significant bandwidths; essentially all light that meets the diffraction condition is diffracted from even thin CCA (Figure 6.6). The extinction spectrum (shown giving a top hat profile with a ~5 nm bandwidth blue-shifts as the CCA is tilted off of normal (almost following Bragg's law). The finite

bandwidth occurs because the polymer spheres in water show large scattering cross sections for visible light. Thus, efficient diffraction occurs; the incident beam traversing the sample is highly attenuated as the diffracted beam grows in intensity. This incident beam attenuation limits the number of layers involved in diffraction and determines the bandwidth of diffraction. The stronger the diffraction, the fewer layers involved in the scattering, and thus, the broader the diffraction.[12]

We initially modeled the diffraction from polymer colloid CCA by using Dynamical Diffraction theory[12] as did Spry and Kosan.[13] Dynamical diffraction theory predicts highly efficient diffraction and successfully explains the sphere diameter, and the angular and wavelength bandwidth diffraction dependence. As pointed out recently by Mittelman and Colvin et al,[14] more sophisticated theoretical approaches are needed to model the photonic crystal diffraction for particles with a higher refractive indices and for polystyrene sphere sizes above ~150 nm.

The efficiency of diffraction increases as the modulation depth, $M_D = [(m_s / m_i)^2 - 1]$ of the diffracting particles increases, where m_s and m_i are the refractive indices of the spheres and the material in the interstices between spheres, respectively. Even more sophisticated theoretical approaches are required for larger values of M_D where multiple scattering dominates.[1-5] It appears clear from photonic crystal theory that fabrication of a 3-D photonic bandgap crystal in the visible spectral region lies just at the edge of what is possible given known materials. For example, a 3-D photonic bandgap is predicted to just occur in an inverse fcc crystal (the interstices have the larger refractive index) if the refractive index of interstices is 2.8 and the spheres are etched out and have the refractive index of vacuum.

The lack of a 3-D bandgap in the direct fcc lattice results because the diffracting planes are unable to diffract π polarized incident light[15] when $\theta = 45°$. This leaves a small solid angle for this light to propagate. No other planes are situated to diffract this light. Apparently, the inverse opal fcc structure closes this gap for sufficiently large refractive index differences between the interstices and the spherical voids.

The theories that are used to model CCA diffraction and to predict diffraction bandwidth do not yet include phonons and Debye-Waller phenomena which are known to contribute to diffuse scattering. Our examination of these phenomena in the early 90's found that diffraction from even well ordered CCA shows significant diffuse scattering from these dynamic phenomena as well as from static disorder such as defects.[16] Recent theoretical studies suggest that existence of 3-D photon bandgap materials is highly sensitive to lattice defects structures.

Figure 6.7 shows the diffraction spectra of 270 nm polystyrene sphere CCA in water along well defined crystalline planes. An *apparent* 3-D

photonic bandgap appears at ~600 nm where little light transmission occurs at any orientation of the crystal in the incident beam. Transmission experiments were performed where the crystal orientation was scanned over all possible incident angles. These experiments showed that all light propagation directions appear to be effectively closed. This 3-D bandgap is likely to be due in part to phenomena such as diffuse scattering and defect scattering.

Thus, some features of a 3-D photonic bandgap material appears to occur even for periodic materials that do not meet the strict conditions required for the opening of a gap. These easily fabricated polystyrene colloid photonic crystals, with their relatively small refractive index differences can be utilized to demonstrate interesting optical phenomena.
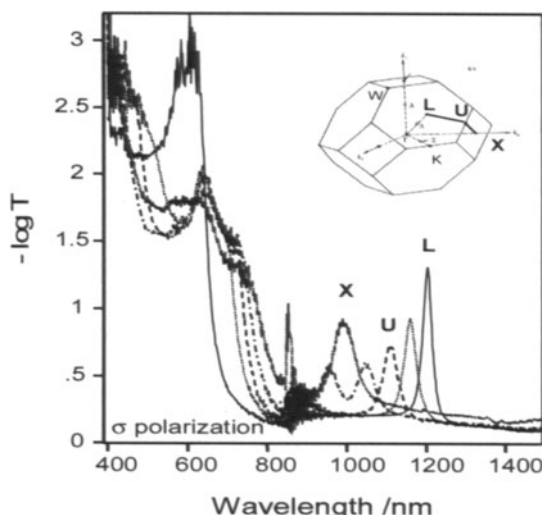
Figure 6.7. Extinction spectra of 125 μm thick CCA of 270 nm diameter polystyrene spheres in water recorded at different rotation angles within the L-U-X plane and with the incident light polarized perpendicular to the incident plane. The L direction corresponds to normal incidence, U is rotated by 35°, and X is rotated 55° from normal. As the sample is tilted, the (111) diffraction peak moves from ~1200 nm to ~1000 nm, where it is coincident with the (200) peak. The broad band at ~600 nm at normal incidence is a superposition of several peaks from the (200), (220), and (311) families of planes.

6.2.2. STANDING WAVE ELECTRIC FIELD LOCALIZATION

An important feature of photonic crystals is that they can be used to localize the electric field maxima of light within materials. This may be useful, for example, for increasing the nonlinear optical response of

materials. This electric field localization was recently demonstrated by Wang and Asher[18] in their study of the plasmon resonance extinction of a CCA of silver quantum dots contained within silica spheres. For example Figure 6.8 shows the concentration dependence of the CCA diffraction as well as the surface plasmon extinction of an aqueous CCA of 82 nm silica spheres containing Ag quantum dots. The dark curve in Figure 6.8 also shows for comparison the extinction of a random dispersion of these same spheres in a DMSO-water solution. All of the extinction spectra were normalized to the particle concentration of the random dispersion.
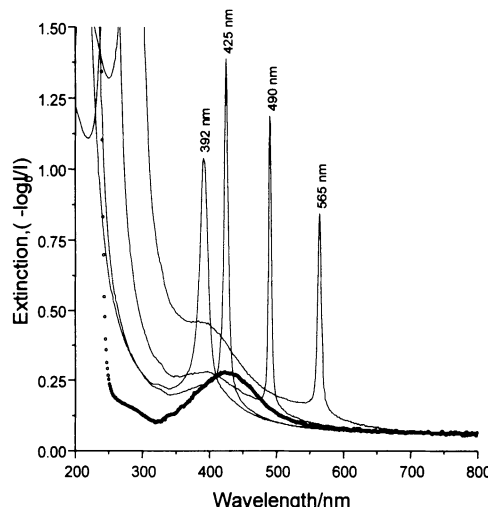
FIGURE 6.8. Comparison of extinction spectra of CCA of 82 nm diameter Ag@SiO$_2$ composite colloids at different particle concentrations (solid lines) to the extinction spectrum of a random dispersion of the particles in an n=1.47 water-DMSO refractive index matching solvent (heavy line). The extinction spectra are normalized to the particle concentration of the random refractive index matched dispersion (7.43 vol%).

The CCA fcc (111) plane spacing decreases as the sphere number density increases, which causes the diffraction band to blue-shift towards the plasmon absorption at ~430 nm. Surprisingly, the extinction spectrum showing the 425 nm diffraction peak displays a decreased plasmon absorption, much below that of the random dispersion. This clearly indicates that the transmitted light experiences a decreased plasmon resonance extinction.

Wang and Asher proposed that this decreased plasmon resonance extinction results from an analog of the Bormann effect observed in x-ray scattering, where the standing wave of the electromagnetic radiation in the periodic medium localizes the electric field in the low dielectric component (Figure 6.9), in the water in our case. This decreases the plasmon

absorption. In contrast, the diffraction on the blue side of the plasmon resonance localizes the electric field maxima in the high dielectric constant medium, giving rise to an increased plasmon absorption.

Spatial Concentration of Electromagnetic Field

**Electromagnetic standing wave produced
by incident and diffracted light**
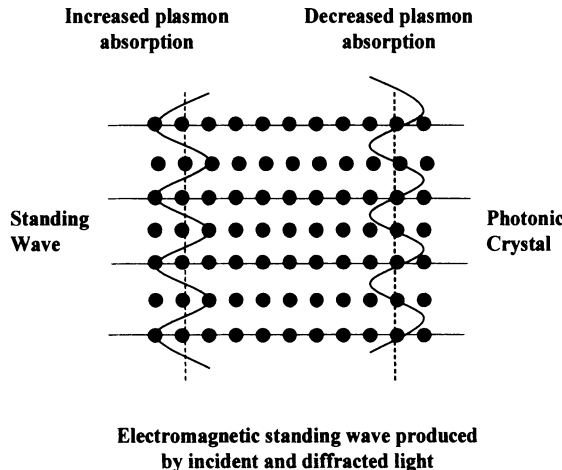
FIGURE 6.9. Schematic illustration of the Borrmann effect in a CCA photonic crystal. A standing wave is produced by the coupled incident and diffracted light. If the electric field maximum lies in the particle planes the absorption is a maximum, while if the electric field maximum lies between the particle planes, the absorption is a minimum.

This shows that the periodic spacing of a photonic crystal can be tuned to maximize the electric field within this periodic medium. This phenomenon has the potential to increase the nonlinear response of materials. In fact, it was recently used to increase the absorption of dyes on the red edge of the diffraction band. This was recently demonstrated by the Mallouk[19] group who showed a standing wave induced increased red edge absorption in a photonic crystal photovoltaic device that increased the solar photovoltaic efficiency by increasing the dye absorption bandwidth.

6.3. CCA OPTICAL SWITCHING AND OPTICAL LIMITING

The CCA diffraction can be altered by high intensity laser illumination.[20] Modest W/cm^2 laser fluences can heat absorbing CCA to induce temperature increases which induce a diffraction shifts. This phenomenon occurs because of the temperature dependence of the repulsive interactions between colloidal particles (Figure 6.10). The major impact of CCA heating, in the absence of photochemistry, is to decrease the value of ε, essentially the dielectric constant of water. This dielectric constant

determines the value of U(r) directly, as well as through κ, the reciprocal of the Debye length. A temperature increase decreases ε, which decreases the repulsion between spheres. This results in a local compression of the CCA by the surrounding colder CCA, which results in a local diffraction blueshift. An additional blue shift derives from the accompanying decrease in the average CCA refractive index.

This laser heating induced diffraction shift can be used for slow switching of transmission or diffraction from a CCA. However, attempts to speed up this process by faster heating, such as by pulsed laser sources disorder the CCA, probably due to shear forces induced by fluid motion. These liquid CCA may be too fragile for use in fast optical switching materials.

We also examined other CCA optical switching approaches. For example, we developed a synthesis for monodisperse, highly charged poly-N-isopropylacrylamide (NIPAM) colloidal particles.[21] These particles undergo a dramatic temperature dependent volume phase transition from a highly swollen polymer in water below room temperature, to a dramatically shrunken polymer above room temperature; the polymer shrinks by expelling water and becomes relatively hydrophobic. As shown in Figure 6.10A these spheres undergo a volume phase transition, where the diameter decreases from 300 nm to 100 nm as the temperature increases from 15 to 35 °C. The scattering power of the spheres, as measured by turbidity, increases dramatically for the shrunken spheres, because the sphere refractive index rapidly increases as the sphere volume decreases. These spheres readily self assemble into an fcc CCA which diffracts light in the visible spectral region. The diffraction of the fcc can be continuously controlled by controlling the CCA temperature. As shown in Figure 6.10 the CCA, which minimally diffracts 500 nm light at low temperature, diffracts essentially all of the incident 500 nm light at high temperature.

This CCA NIPAM volume phase transition phenomenon may be useful for fabricating optical switches or optical limiters. For example, optical limiting applications would utilize incident laser heating as the actuating temperature increase. Unfortunately, the switching times for these NIPAM CCA are slow (sec). Attempts to heat the sample quickly with pulsed or CW laser sources result in transient sample disorder. Presumably, the liquid CCA ordering is too fragile to permit fast switching.

6.4.   POLYMERIZED COLLOIDAL ARRAY SWITCHING AND OPTICAL LIMITING

As discussed above we fabricated more robust photonic crystal materials by polymerizing acrylamide hydrogels around the CCA lattice of colloidal particles.[10]   These polymerized CCA (PCCA) possess the responsive properties of hydrogels.
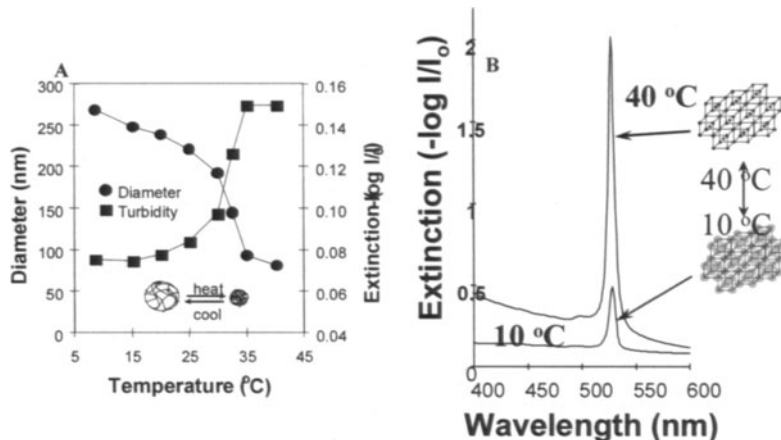
FIGURE 6.10. A: Dependence of diameter of monodisperse N-isopropylacrylamide colloids on temperature. The diameter was monitored by quasielastic light scattering. The temperature dependence of the turbidity of a random dispersion is also shown. B: Dependence of diffraction of a CCA of these colloidal particles at 10 and 40 °C.

Normal acrylamide hydrogels in water show little volume response to changes in temperature or aqueous solution ionic strength. However, large hydrogel volume changes can be induced by altering the surrounding hydrogel solvent composition which alters the free energy of mixing of the hydrogel with the solvent[22] A PCCA relative volume change of dV/V results in a relative CCA lattice spacing change and a relative diffraction wavelength change of $dl/l = d\lambda/\lambda \sim 1/3 \, (dV/V)$, for small volume changes. Obviously, these hydrogel volume changes can be used to tune the PCCA diffraction wavelength.

These PCCA can also be chemically functionalized to make them responsive to temperature, photon flux and their chemical environment. This enables novel photonic switching materials which can be used for photonic control of diffraction and for fabricating chemical sensing photonic crystals.

6.4.1. PCCA THERMAL DIFFRACTION SWITCHING PHENOMENA

The kinetics of hydrogel volume phase transitions depends on the effective size of the hydrogel. ~100 μm thick hydrogels respond in time scales of seconds. The response is slow because any hydrogel volume change must macroscopically transport water into or out of the hydrogel. Theory[23] indicates that the response is diffusion-like in nature, and should scale as $t \sim l^{2}$. Thus, faster PCCA volume phase transitions require smaller hydrogel length scales. For example, if we utilize ~100 nm hydrogels we expect ~1 μsec time scales.

In fact, this expectation is met. Figure 6.11 shows the temperature dependence of diffraction from a PCCA array of NIPAM colloidal particles lightly polymerized into a PCCA hydrogel. After these NIPAM spheres self-assembled into a CCA lattice they were lightly polymerized into an acrylamide/bisacrylamide PCCA. This permanently localized the sphere centers of mass at the fcc lattice sites. As expected, the CCA diffraction efficiency dramatically increases as the temperature increase causes the NIPAM spheres to collapse (Figure 6.11). Because the centers of mass of the individual spheres are locked onto an fcc lattice, this array of NIPAM spheres does not disorder upon laser heating. In fact it shows very fast (μsec) optical switching.
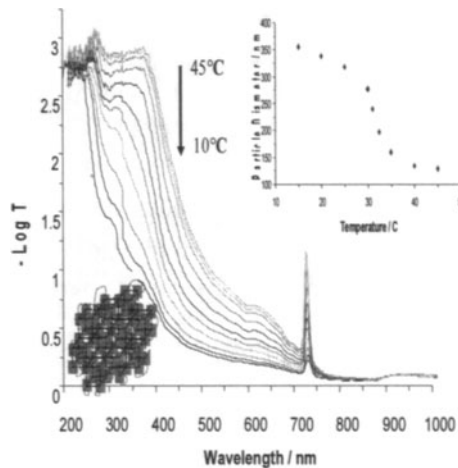
FIGURE 6.11. Temperature dependence of diffraction from PCCA of NIPAM spheres. The inset shows the temperature dependence of the diameter of the individual spheres in water. The diffraction efficiency increases with temperature as the sphere size decreases. The peak at ~730 nm results from diffraction by the fcc (111) plane. The shoulder at ~630 nm is from a higher Miller index plane and indicates that the fcc planes have buckled. Diffraction at shorter wavelengths derive from higher index planes and second order diffraction[17].

Figure 6.12 shows the time dependence of diffraction from the PCCA of NIPAM spheres subsequent to excitation by a 3 nsec pulse of 1.9 μm light that is absorbed by the surrounding H_2O/D_2O medium. This near IR light, is converted to heat in the psec time domain, to give rise to a ~ 10 °C T-jump. The diffraction efficiency increase shows a short 1 μsec time constant which accounts for 26 % of the diffraction increase, while the remaining efficiency increase derives from slower 20 μsec and 200 μsec dynamics. The 600 nm peak derives from diffraction from the fcc 111 planes while the diffraction at 300 nm derives from second order diffraction. The broad diffraction between 300 and 600 nm derives from diffraction from misaligned planes.
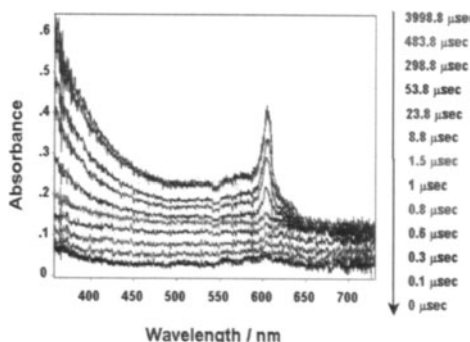
FIGURE 6.12. Time dependence of diffraction of PCCA of NIPAM spheres shown in Figure 6.11. The PCCA was excited by a 3 nsec 1.9 μm IR pulse which generates a ~10°C T-jump. A xenon flashlamp interrogates the transmission at different delay times. The transmission spectrum is monitored by a fiber optic diode array spectrometer.

Obviously, the use of ~100 nm spheres enables fast μsec optical switching times. In fact, we should be able to achieve even faster switching behavior by constructing photonic crystals out of even smaller particles.

6.4.2. PCCA PHOTOCHEMICAL SWITCHING PHENOMENA

We have also developed photochemically switchable PCCA[24] by covalently attaching azobenzene derivatives. The trans ground state of azobenzene in solution shows a strong near UV absorption band at ~360 nm (Figure 6.13). Monophotonic excitation within this absorption band converts the trans form to the cis form which displays a weak~460 nm absorption. The cis form shows a large activation barrier which prevents conversion back into the trans ground state, such that at room temperature in the dark,

the cis form PCCA is stable for more than one week. Population of the cis derivative red shifts the PCCA 710 nm fcc (111) diffraction band to 730 nm due to the cis derivative's increased dipole moment, which results in a more favorable free energy of mixing. This redshifted diffraction can be completely reset to 710 nm by excitation in the visible to convert the cis to the trans derivative. Because this PCCA is macroscopic, these photochemically induced diffraction shifts are slow and occur ~10 sec after 3 nsec UV or visible excitation. This PCCA response is obviously too slow for optical switching or optical limiting applications, but could be useful for memory devices. Excitation in the UV writes information in the form of redshifts in the diffraction which creates an image. Subsequent excitation in the visible erases the stored information. Readout occurs at wavelengths that do not cause diffraction shifts.
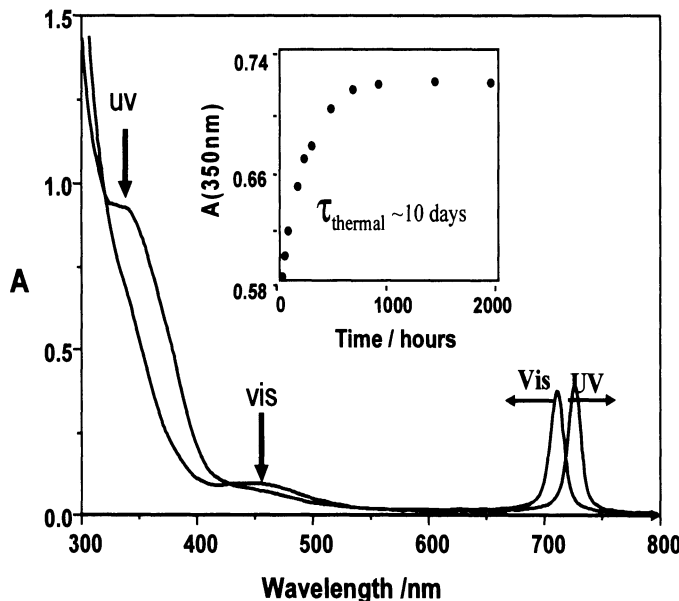
FIGURE 6.13. Optical switching of azobenzene functionalized PCCA. UV light transfers trans ground state azobenzene to the cis form while visible light transfers cis azobenzene to the trans form. The more favorable free energy mixing of the cis form results in a diffraction redshift of the fcc (111) diffraction from 710 to 730 nm. Inset shows that cis form is stable for ~10 d.

Interestingly, we also observe fast (300 nsec) diffraction shift dynamics in this system.[24] Excitation in the UV results in a prompt ~5 nm red-shift which relaxes back to the initial diffraction in ~1 msec time, and which evolves in the multisecond time scale to a stable cis red shifted diffraction. We are continuing to investigate these phenomena.

6.4.3. PCCA REFRACTIVE INDEX DIFFRACTION SWITCHING PHENOMENA

We are also developing a fast optical switching photonic crystal[25] where the PCCA colloidal particles have the real part of their refractive index matched to that of the medium (Figure 6.14). Thus, under normal circumstances the array does not diffract light. However, these colloidal particles also have an imaginary component of their refractive index which selectively absorbs incident laser irradiation.[26,27] The resulting particle temperature increase causes the particle refractive index to diverge from that of the medium. Thus, upon high laser fluences the array refractive index modulation "pops up" to diffract away in incident laser wavelength.[25]

Time Dependence of Submicron Periodic Thermally Non-Linear Crystalline Colloidal Array

83 nm spheres
$n_p = 9 \times 10^{13}$ spheres/cc $\lambda_m = 514.5$ nm
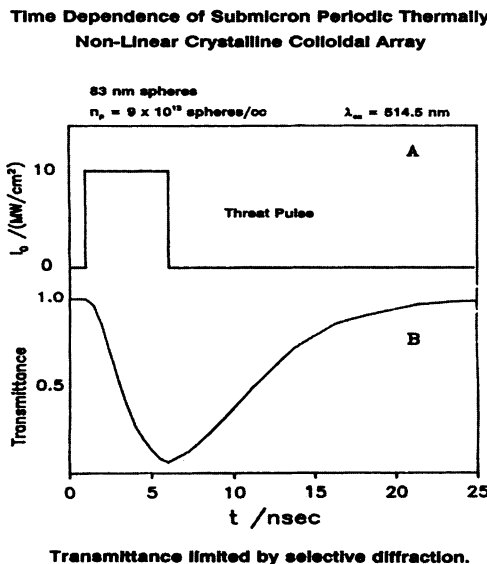
FIGURE 6.14. Concept for optical limiting involving absorbing colloidal particles (n_p) that are refractive index matched to the medium (n_m). At normal incident intensities the system transmits light except for a ~45 % attenuation by absorption[25]. High intensity illumination heats the spheres, lowers their refractive index and causes the CCA refractive index modulation to "pop up" to diffract away the incident light.

Concept for Creating Nonlinear Optical Switch

★ Low intensity illumination :

CCA

100% transmission

index matched: $n_p = n_m$

★ High intensity illumination causes the refractive index of the spheres and the medium to mismatch and Bragg diffraction occurs.

CCA

no transmission
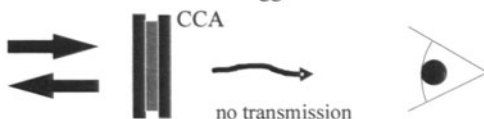
index mismatched: $n_p \neq n_m$

FIGURE 6.15. Calculated response[25] of CCA of absorbing 83 nm diameter spheres (9 X 10^{13} spheres/cm^3) which are initially refractive index matched to the medium. Excitation by a 5 nsec incident pulse with a fluence of 10 MW/cm^2 causes the array diffraction to "pop up" and to diffract away greater than 90 % of the incident light within within 6 nsec.

Most polymers show a temperature dependence of the refractive index, $dn/dT \sim -10^{-4}$ T^{-1}. Thus, a temperature increase of 10 °C should decrease the PARTICLE refractive index by 0.001. This value of $\Delta n = n_p - n_m$ for a PCCA of ~100 nm diameter particles is calculated to be sufficient to diffract away most of the light meeting the Bragg condition.[25]

We also calculated[25] that we could use nsec pulsed lasers to selectively heat the PCCA colloidal particles, and this temperature increase would stay localized within the ~100 nm colloidal particles over nsec time intervals to selectively decrease the sphere refractive index compared to the medium.[25] A modeling of this system (Figure 6.15) indicated that optical limiting should occur in the ~5 nsec time scale for fluences of less than 10 MW/cm^2.

Experimental Setup For Measuring Optical Switching Nonlinearity
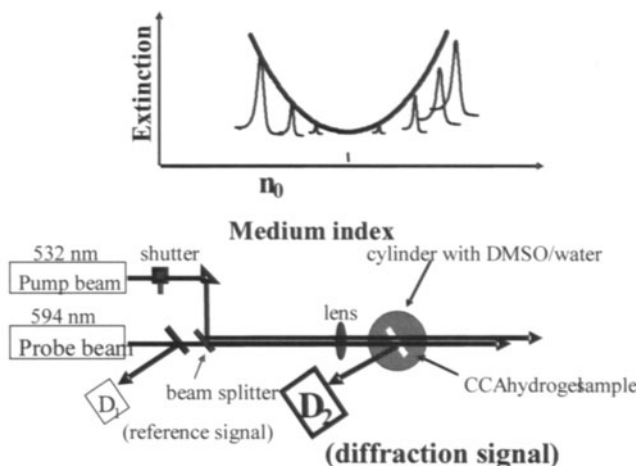
FIGURE 6.16. Top curve shows the dependence of diffraction on the refractive index difference between the particles and the medium. The diffracted intensity is zero when the refractive indices are equal and increases symmetrically with the absolute difference. Bottom: Experimental setup for monitoring diffraction from CCA shown in Figure 6.15. A 532 nm laser pulse (5 nsec duration) incident on the CCA heats the absorbing colloidal particles. A 594 nm delayed probe pulse is also generated by a dye laser excited by the 532 nm pulse. Two diodes monitor the relative intensity of the 594 nm probe pulse as well as the intensity diffracted by the CCA.

To test this switching mechanism we developed a synthesis of highly charged fluorinated colloidal particles containing absorbing dye.[26] These fluorinated particles have a refractive index of 1.38 and are easy to refractive index match to a mainly aqueous medium typical of PCCA.

We examined the optical switching by using a 3 nsec 532 nm pulsed laser which was absorbed by the PCCA colloidal particles.[25] We also utilized a 594 nm probe pulse which was diffracted by the heated CCA array (Figure 6.16).

As shown by Figure 6.17 we observe an increase in diffraction with increasing pump pulse energy when our colloidal particles have a refractive index below that of the medium ($n_p < n_m$). Larger pump pulse energies result in even smaller values of n_p, which increases the refractive index mismatch, which increases the diffraction. The dip at 0.6 mJ gives rise to a ~50 °C temperature increase to the polymer glass transition temperature. Higher pulse energies disrupt the PCCA ordering.

Figure 6.17 shows that the pump pulse does not alter the diffraction, if the spheres do not contain dye to absorb the light. Alternatively, if the dyed

colloidal particles have a refractive index greater than that of the medium, $(n_p > n_m)$ pump heating decreases n_p which decreases the refractive index mismatch which decreases the diffraction efficiency.
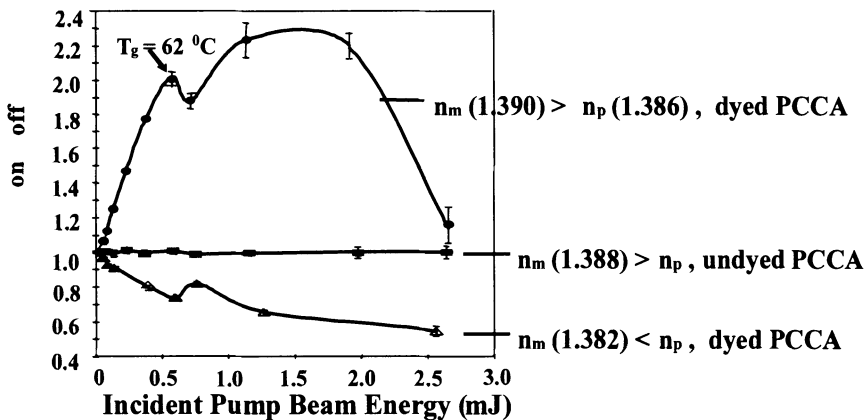
FIGURE 6.17. Pulse energy dependence of the relative diffraction (relative to that in the absence of the pump pulse) from the CCA of Figure 6.15. The middle curve is for undyed spheres that do not change refractive index. The top curve is for particles with a refractive index smaller than that of the medium, while the bottom curve is for particles with refractive index greater than that of the medium.

We examined the time dependence of these pump induced diffraction changes. Figure 6.18 shows that the maximum diffraction change is delayed by about 3 nsec from the pump pulse, as predicted.

Thus, we observe the predicted photonic crystal diffraction switching. Unfortunately, initial measurements only found 3 % diffraction switching efficiencies,[25] more recent studies have observed 7 % switching efficiencies. We are presently characterizing the phenomena that limit these efficiencies. These phenomena appear to be related to those contributing to the nsec diffraction peak shift dynamics observed for the azobenzene PCCA hydrogels briefly discussed above.
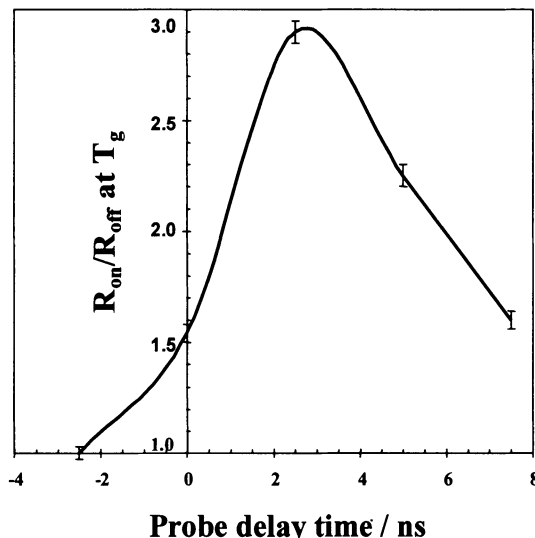
FIGURE 6.18. Probe delay time dependence of CCA diffraction. The maximum diffraction occurs at ~3 nsec after the pump pulse.

6.5.   PCCA PHOTONIC CRYSTAL CHEMICAL SENSING MATERIALS

A crosslinked hydrogel is a responsive soft material whose volume is controlled by three competing phenomena,[22] the free energy of mixing of the hydrogel polymer with the medium, electrostatic interactions of charges bound to the hydrogel and the restoring forces due to the hydrogel crosslinks (Figure 6.19). The free energy of mixing of the hydrogel with the medium involves the entropic propensity of the hydrogel to fill all space (analogous to the entropy increase associated with the expansion of an ideal gas), and an enthalpic term which accounts for molecular interactions of the hydrogel with the medium.

The electrostatic free energy gives rise to osmotic pressures associated with electrostatic interactions between bound charges and osmotic pressures due to the changes in the water chemical potential associated with the immobilization of counterions within the hydrogel to the bound charges. Each charge immobilizes at least one counterion, to give rise to a hydrogel Donnan potential in low ionic strength solutions, which causes water to flow into or out of the hydrogel. Finally, the configurational entropy of the hydrogel crosslinked chains act to constrain the hydrogel volume.
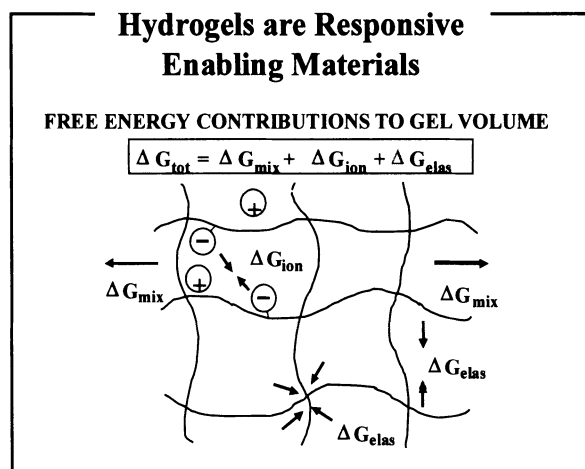
FIGURE 6.19. The hydrogel volume depends upon the free energy of mixing, the free energy of ionic interactions and the free energy associated with the elastic constraints of the hydrogel crosslinks.

We have functionalized[22] the PCCA with molecular recognition agents to create intelligent PCCA (IPCCA) which can be used for chemical and temperature sensing applications. These molecular recognition agents are designed to actuate PCCA hydrogel volume changes as they interact with their targeted analytes. These volume changes alter the embedded CCA lattice constants, which result in diffraction wavelength shifts which directly report on the concentration of analyte or temperature.

6.5.1. TEMPERATURE SENSING IPCCA SENSORS

The temperature sensors utilize the previously discussed volume phase transitions of NIPAM. We can fabricate a NIPAM PCCA temperature sensor by polymerizing a polystyrene colloid CCA in a NIPAM hydrogel.[21] Figure 6.20 shows that the temperature induced NIPAM volume phase transition shifts the diffraction from the near IR into the near UV as the PCCA temperature is varied between 15 and 40 °C. Thus, this PCCA material functions well as a highly sensitive temperature sensor.

The NIPAM volume phase transition, is driven by the temperature dependent free energy entropic term. The NIPAM hydrogel shrinks in order to minimize the surface area of hydrogel polymer contacting the water medium; water contacting the hydrophobic hydrogel must be highly ordered. The entropic penalty for this ordering of water at the polymer hydrogel interface increases linearly with temperature. At some temperature this becomes sufficiently unfavorable that it cannot be balanced by the expansion entropic free energy and the enthalpic term associated with the free energy

of mixing. This results in a shrinkage of the NIPAM hydrogel as it minimizes the surface area exposed to water.
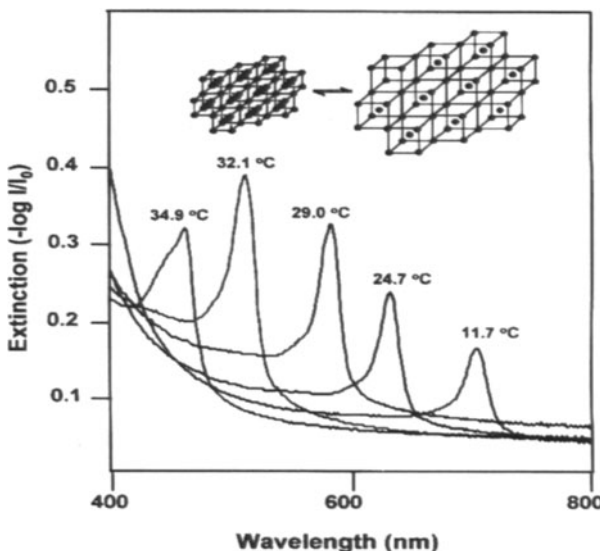
FIGURE 6.20. Temperature dependence of diffraction from a PCCA of polystyrene colloidal particles polymerized into a poly-N-isopropylacrylamide hydrogel. The diffraction shifts from ~720 nm at 12 °C to 460 nm at 34.9 °C. The diffraction shifts result from a volume phase transition due to free energy of mixing changes of the polymer with water as the temperature is altered.

6.5.2. ELECTROSTATICALLY DRIVEN CHEMICAL IPCCA SENSORS

Our first photonic crystal chemical sensors utilized a Donnan potential to drive the volume phase transition used for chemical sensing.[22] A vinyl-crown ether derivative with a high affinity for Pb^{2+} was polymerized into a PCCA (Figure 6.21). Ligation of the Pb^{2+} dication by the crown ether in the PCCA results in immobilization of its counterions, which causes a Donnan potential which induces an osmotic pressure which swells the hydrogel. nM to mM concentrations of Pb^{2+} are easily detected. The diffraction red shift reaches a maximum of ~650 nm and then decreases at concentrations above ~1000 ppm, due to the decreasing Donnan potential at the elevated solution ionic strengths that accompany the higher solution Pb^{2+} concentrations. This Pb^{2+} sensor can be immersed directly in the analyte solution to determine the analyte concentration by measuring the wavelength of light diffracted at normal incidence, for example. Alternatively, we demonstrated that this sensor material can be glued to the end of a fiber optic to determine the concentration remotely.[22]
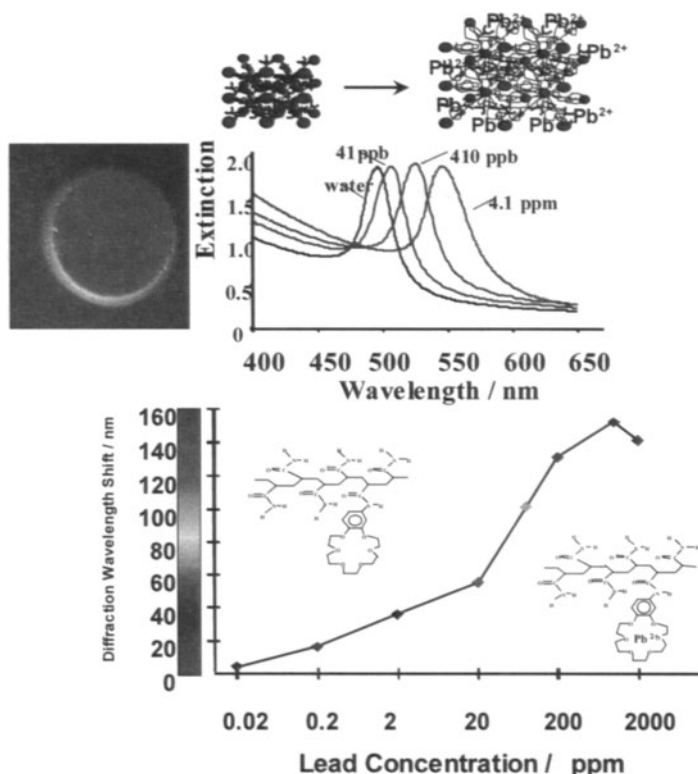
FIGURE 6.21. IPCCA containing 18-crown-6 recognition group has a high affinity for Pb^{2+}. Top left: photograph showing red (center) diffraction from originally blue (outer edges) IPCCA, after placing a drop of 8 mM $Pb(NO_3)_2$ on IPCCA. Dependence of diffraction peak and diffraction peak wavelength on Pb^{2+} concentration.

The selectivity's of these IPCCA sensing materials are determined by the selectivity's of their molecular recognition agents. Because this 18-crown-6 derivative[22] has a binding affinity for Ba^{2+} comparable to that for Pb^{2+}, Ba^{2+} is a significant interferant.

We fabricated a glucose sensing IPCCA by utilizing the enzyme glucose oxidase (GOD).[22] GOD converts glucose to gluconic acid. During this reaction a flavin is reduced in the enzyme. This anionic flavin acts as an anion immobilized on the hydrogel, which gives rise to a Donnan potential which swells the PCCA in proportion to the glucose concentration. This GOD PCCA operates as a steady-state sensor since oxygen in solution reoxidizes the flavin. When oxygen is excluded concentrations of glucose as low as 10^{-12} M are easily determined.[22]

We recently developed another glucose IPCCA sensor that also utilizes a Donnan potential by attaching boronic acid recognition groups to the PCCA.[28] Boronic acid derivatives are known to bind to the cis diols of

carbohydrates such as glucose. The binding of glucose to neutral boronic acid derivatives shifts the boronic acid equilibrium towards the anionic boronate form. This anionic boronate attached to the hydrogel results in a Donnnan potential induced osmotic pressure which swells the PCCA. As shown in Figure 6.22, this IPCCA is an excellent glucose sensor in low ionic strength aqueous solutions. The solid line through the diffraction shift data derives from a detailed hydrogel volume phase transition model which accurately models the IPCCA response.
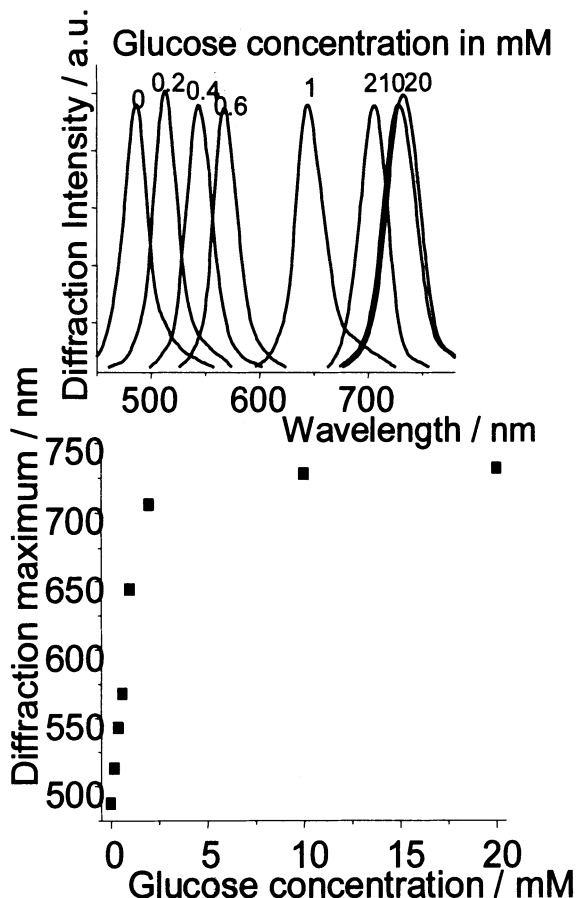
FIGURE 6.22. Glucose concentration dependence of diffraction from boronic acid IPCCA. The IPCCA in pure water redshifts as the glucose concentration increases until ~5 mM glucose concentration where the response saturates.

We also developed pH and ionic strength sensors which also utilized the hydrogel Donnan potential.[29] The pH sensor utilizes a covalently attached group which titrates in the pH range of interest. For example, to sense pH values between 4 to 8 we utilized carboxyl groups formed by the hydrolysis of the amide groups of the polyacrylamide PCCA. As the pH

changes the fraction of protonated carboxlys change and the hydrogel changes its volume. This IPCCA can determine solution ionic strengths if used at pH values where significant carboxylates exist, because the Donnan potential decreases with solution ionic strength.
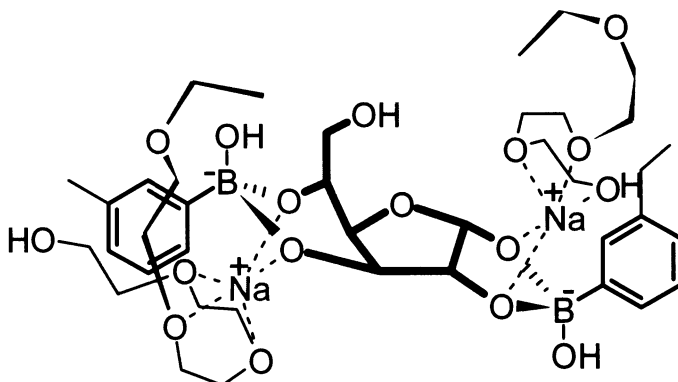
FIGURE 6.23. Model of glucose crosslinks across two boronates in IPCCA. The polyethylene glycol localizes two Na^+ cations at the boronates to reduce electrostatic repulsion between them.

6.5.3. CROSSLINKING DRIVEN IPCCA CHEMICAL SENSORS

We have also developed a sensor for glucose for use in high ionic strength bodily fluids based on glucose induced hydrogel crosslinking.[30] This sensor, which also utilizes boronic acids, also incorporrates polyethylene glycols. This IPCCA senses glucose through the crosslinks glucose forms through its two appropriately oriented cis diols (Figure 6.23). The formation of these crosslinks shrink the hydrogel as shown in Figure 6.24 for glucose concentrations between 0 and 10 mM glucose (the physiological ranges of glucose in tear fluids and blood) which blue shift the diffraction. Higher glucose concentrations break the crosslinks when individual glucose molecules saturate the individual boronic acid groups. We are now also able to fully model this sensor response using our fundamental understanding of the hydrogel volume phase transitions and the relationship between crosslinks and the IPCCA elastic constant. Our intention is to utilize these sensors for the noninvasive monitoring of glucose in the tear fluid of patients with diabetes mellitus.
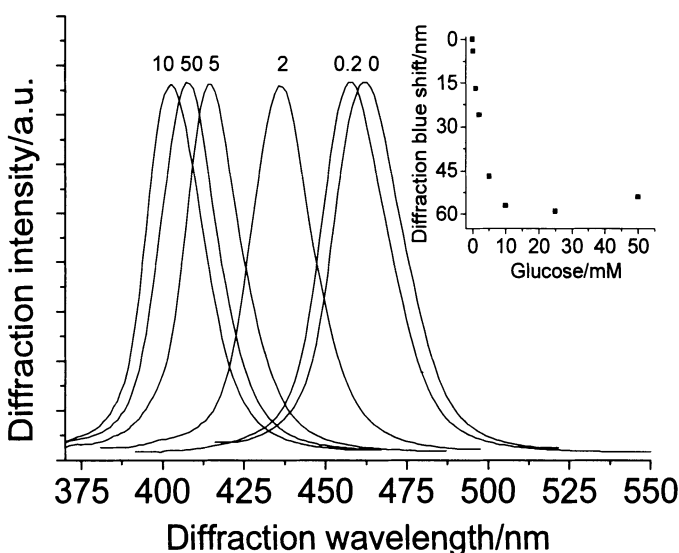
FIGURE 6.24. Glucose concentration dependence of diffraction of the 4-amino-3-fluorophenylboronic acid BA-AA-PEG sensor in 2 mM tris-HCl (pH 7.4) and 150 mM NaCl. Inset: Dependence of diffraction peak shift on glucose concentration.

6.6.   CONCLUSIONS

As discussed above we are able to construct novel responsive photonic crystal materials which have promise for optical switching as well as chemical sensing devices. These materials interact with light due to their highly ordered CCA array. The prospects for these materials looks very bright to us.

ACKNOWLEDGEMENTS

REFERENCES

1. Joannopoulos, J.D.; Meade, R.D.; Winn, J.N. *"Photonic Crystals:Molding the Flow of Light"*Princeton University Press, New York, **1995**.
2. (a) Ibanescu, M.; Fink, Y.; Fan, S.; Thomas, E.L.; Joannopoulos, J.D. *Science* **2000**, *289*, 415; (b) Maldovan, M.; Urbas, A.M.; Yufa, N. W.; Carter, C.; Thomas, E.L. *Phys. Rev. B.* **2002**, *65*, 165123; (c) Soukoulis, C. M. Nanotechnology. **2002**, *13*, 420-423.

3. Sakoda,K. *"Optical Properties of Photonic Crystals"*, Springer Series in Optical Sciences **2001**.

4. (a)Krauss , T. F.; De La Rue, R. M. .*Prog. Quant. Elect.* **1999**,*23*, 51-96; (b) Ozin , G. A.; Yang, S. M. *Adv. Func. Mat.* **2001**,*11*, 95-104.(c) Jiang, P.; Ostojic, G. N.; Narat, R.; Mittleman, D.V.; Colvin, L. *Adv. Mat.* **2001**, *13*, 389-393.(d) Norris, D. J.; Vlasov, Y. A. *Adv. Mat.* **2001**, *13*, 371-376.

5. (a) Busch, K.; John, S. *Phys. Rev. E.* **1998**, *58*, 3896-3908 .(b) Biswas, R. M.; Sigalas, M.; Subramania, G.; Soukoulis , C. M.; Ho, K. M. *Phys. Rev. B.* **2000**, *61*, 4549-4553.

6. (a) Carlson, R. J.; Asher, S. A. *Appl. Spectrosc.* **1984**, *38*, 297-304.(b) Flaugh, P. L.; O'Donnell, S. E.; Asher, S. A. *Appl. Spectrosc.* **1984**, *38*, 847-850 .(c) Asher, S. A. *U.S. Patent.* **1986**, # 4,627,689, # 4,632,517.(d) Asher, S. A.; Flaugh, P. L.; Washinger, G. *Spectroscopy* . **1996**, *1*, 26-31.

7. (a)Alfrey, T. Jr.; Bradford, E. B.; Vanderhoff, J. W.; *J. Opt. Soc. Am.* **1954** *44*, 603-609; (b) Krieger, I.M.; O'Neill, F. M. *J. Am. Chem. Soc.* **1968**,*90*, 3114.

8. (a)Hiltner, P. A.; Krieger, I. M. *J. Phys. Chem.* **1969**, *73*, 2386. (b) Hiltner, P. A.; Papir, Y. S., Krieger, I. M. J. *Phys. Chem.* **1971**, *75*, 1881.

9. Flaugh, P. L.; O'Donnell, S.; EAsher, S. A. *Appl. Spectrosc.* **1984**, *38*, 847-850.

10. (a)Asher, S. A.; Holtz, J.; Liu L.; Wu, Z. *J. Am. Chem. Soc.* **1994**, 4997-4999 (b) Asher,. S. A.; S. Jagannathan, S. U.S. Patent # 5, **1994**, 281,370.(c) Haacke, G.;Panzer, H. P; Magliocco, L. G.; Asher, S.A. U.S. Patents # 5, **1993**, 266,238. #5,368,781 1994.

11. (a) Park, S. H.; Xia, Y. *Chem. Mat.* **1998**, 10, 1745; (b) Gates, B.; Qin, D.; Xia, Y. *Adv. Mat.* **1999**, 11, 466; (c) Zakhidov, A.; Baughman, R. H.; Iqbal, Z.; Cui, C.; Khayrullin, I.; Dantras, S.; Marti, J.; Ralchenko, V. G. *Science* **1998**, 282, 897; (d) Wijnhoven, J. E. G.; Vos, W. L. *Science* **1998**, 281, 802; (e) von Blaaderen, A.; Rue, R.; Wiltzius, P. *Nature* **1997**, 385, 241; (f) Jiang, P. ; Bertone, J. F.; Hwang, K. S.; Colvin, V. L. *Chem. Mater.* **1999**, 11, 2132.

12. Rundquist, P. A.; Photinos, P.; Jagannathan, S.; Asher, S. A. *J. Chem. Phys.* **1989**, 91, 4932-4941.

13. Spry, R. J.; Kosan, D. J. *Appl. Spectrosc.* **1986**, 40, 782.

14. Mittleman, D. M.; Bertone, J. F.; Jiang, P.; Hwang, K. S.; Colvin, V. L. *J. Chem. Phys.* **1999**, 111, 345.

15. Pan, G.; Sood, A. K.; Asher, S. A. *J. Appl. Phys.* **1998**, 84, 83-86.

16. (a)Rundquist, P. A.; Kesavamoorthy, R.; Jagannathan, S.; Asher, S. A. *J. Chem. Phys.* **1991**, 95, 1249-1257; (b) Rundquist, P. A.; Kesavamoorthy, R. ; Jagannathan, S.; Asher, S. A. *J. Chem. Phys.* **1991**, 95, 8546-8551.

17. Liu, L.; Li, P.; Asher, S. A. *J. Am. Chem. Soc.* **1997**, 119, 2729-2732.

18. Wang, W.; Asher, S. A. *J. Am. Chem. Soc.* **2001**, 123, 12528-12535.

19. Mallouk, T.; et al. *J. Am. Chem. Soc.* In press 2003.

20. (a) Rundquist, P. A.; Jagannathan, S.; Kesavamoorthy, R.; Brnardic, C.; Xu, S.; Asher, S.A. *J. Chem. Phys.* **1991**, 94, 711-717; (b) Kesavamoorthy, R.; Jagannathan, S.; Rundquist, P. A.; Asher, S. A. *J. Chem. Phys.* **1991**, 94, 5172-5179.

21. Weissman, J. M.; Sunkara, H. B.; Tse , A. S.; Asher, S. A. *Science* **1996**, 274, 959-960.

22. (a) Holtz, J. H.; Asher, S. A. *Nature.* **1997,** 389, 829-832; (b) Holtz, J. H.; Holtz, J. S. W.; Munro, C. H.; Asher, S. A. *Anal. Chem.* **1998,** 70, 780-791.

23. (a) Tanaka, T.; Hocker, L. O.; Benedek, G.B. *J. Chem. Phys*. **1973,** 69, 5151; (b) Tanaka, T.; Filmore, D. J. *J. Chem. Phys.* **1979,** 70, 1214; (c) Peters, A.; Candau, S. J. *Macromolecules.* **1986,** 19, 1952; (d) A. Peters and S.J. Candau, *Macromolecules.* 21, 2278 **1988**; (e) Li, Y.; Tanaka, T. *J. Chem. Phys.* **1990,** 92, 1365; (f) Annaka, M.; Tanaka, T. *Nature.* **1992,** 355, 430; (g) Durning, C. J.; Mormon, Jr., K. N. *J. Chem. Phys.* **1993,** 98, 4275; (h) Tokita, M.; Miyamoto, K.; Komai, T. *J. Chem. Phys.* **2000,** 113,1647.

24. Reese, C.; Mikonin, A.; Asher, S. A. *Adv. Func. Mat.* **2003,** *Submitted.*

25. Kesavamoorthy, R.; Super, M. S.; Asher, S. A. *J. Appl. Phys.* **1992,** 71, 1116-1123.

26. (a) Asher, S. A.; Kesavamoorthy, R.; Jagannathan, S.; Rundquist, P. *SPIE Vol. 1626 Nonlinear Optics III*, **1992,** 238-241; (b) Pan, G.; Kesavamoorthy, R.; Asher, S. A. *Phys. Rev. Lett.* **1997,** 78, 3860-3863; (c) Pan, G.; Tse, A. S.; Kesavamoorthy, R.; Asher, S. A. *J. Am. Chem. Soc.* **1998,** 120, 6518-6524; (d) Pan, G.; Kesavamoorthy, R.; Asher, S. A. *J. Am. Chem. Soc.* **1998,** 120, 6525-6530.

27. Tse, A.; Wu, Z.; Asher, S. A. *Macromolecules* **1995,** 28, 6533-6538.

28. Asher, S. A.; Alexeev, V. L.; Goponenko, A. V.; Sharma, A. C.; Lednev, I. K.; Wilcox, C. S.; Finegold, D. N. *J. Am Chem. Soc.* **2003,** 125, 3322-3329.

29. Lee, K.; Asher, S. A. *J. Am. Chem. Soc.* **2000,** 122, 9534-9537.

30. Alexeev, V. L.; Sharma, A. C.; Goponenko, A.V.; Das, S.; Lednev, I. K.; Wilcox, C. S.; Finegold, D. N.; Asher, S. A. *Anal. Chem,* **2003,** 75, 2316-2323.

7

PLASMONIC NANOMATERIALS

Enhanced Optical Properties From Metal Nanoparticles and their Ensembles

Alexander Wei
Department of Chemistry, Purdue University

7.1. INTRODUCTION

The first examples of nanotechnology, some historians might be inclined to argue, could very well be accredited to some glassblowers from the days of imperial Rome. Those ancient craftsmen were able to embed colloidal metal particles within their glassy works to enhance their lustrous qualities. Although they were most likely unaware of the nanoscopic nature of these inclusions, this did not prevent them from appreciating the enigmatic hues produced upon a change of incident light. One of the most striking examples of such Roman glasses is the famed Lycurgus cup, which dates back to the 4th century A.D. The chalice has a dark greenish tint under reflected lighting, but when illuminated from behind the goblet appears red colors are attributed to the optical responses of colloidal gold particles dispersed throughout the glass. Similar phenomena are also featured in the stained-glass windows of many medieval cathedrals, most often from colloidal particles of coinage metals such as copper and gold (red) or silver (yellow).

FIGURE 7.1. The Lycurgus cup (4th century A.D.) appears green when viewed with reflected light (left), but red when illuminated from behind (right). Printed with permission from the National British Museum of History.

Although the technology for producing metal-stained glass had been practiced for centuries, the source of their brilliant colors remained shrouded in mystery until the mid-nineteenth century, when Faraday published his seminal experiments ascertaining the colloidal nature of "red gold."[1] Faraday's work, followed by contributions from Tyndall, Mie, and many others, provided the foundations for understanding the physical behavior and optical responses of metal nanoparticles.

The purpose of this chapter is to review both basic concepts and current developments in the optical properties of metal nanoparticles, particularly gold and silver, and to highlight opportunities for applying such materials to applications which can benefit from their sensitive and tunable electromagnetic responses. Chemical sensing, biomedical imaging, high-throughput screening analysis, and nanoscale photonics are some of the many prospects which have sparked a resurgence of interest in this venerable class of nanomaterials. These activities have been further motivated by recent advances in metal nanoparticle synthesis, nanoscale self-assembly and lithography, and by a growing appreciation for the collective optical responses of metal nanoparticles in ensemble states.

7.2.   SURFACE PLASMONS IN SPHERICAL METAL NANOPARTICLES

The strong optical extinctions of conductive metal nanoparticles arise from an electrodynamic phenomenon known as surface plasmons. These are generated by the collective excitation of free electrons in response to a

characteristic electromagnetic frequency, very much similar to the function of a radio antenna. The physical nature of surface plasmons will be discussed here in sufficient detail for making useful connections between metal nanostructures and their optical properties; for a more comprehensive treatise on the physics of surface plasmons, the reader is directed to the monographs by Raether[2] and by Kreibig and Vollmer.[3]

Surface plasmons can be categorized into two types: localized plasmon resonances, in which incident light is absorbed or scattered by the oscillating electric dipoles within a metal nanoparticle, and surface plasmon polaritons, which propagate along metal surfaces in a waveguide-like fashion until released at some distance from their point of origin (see Figure 7.2). The former are important for generating local field factors, which enhance linear and nonlinear optical effects near the metal surface. However, metal nanostructures often support both types of plasmons simultaneously; in fact, it can be difficult to decouple one from the other, resulting in a confusion of terms. Nevertheless, the plasmonic coupling of metal nanoparticles with light enhances a broad range of useful optical phenomena, such as resonant light scattering (RLS), surface plasmon resonance (SPR), and surface-enhanced Raman scattering (SERS), all of which have tremendous potential for ultrasensitive chemical and biomolecular detection and analysis.

FIGURE 7.2. Incident light on nanostructured metal surfaces can generate localized (standing) plasmon resonances (*left*) as well as surface plasmon waves (*right*). Excitation of conduction electrons (red) produces local electromagnetic fields (pink) near the metal surfaces.

7.3.   SURFACE PLASMONS: THEORETICAL CONSIDERATIONS

In the simplified case of a metal nanosphere with radius R much smaller than the incident wavelength (a condition commonly referred to as the quasi-static approximation), the plasmon response is essentially dipolar in nature. The strength and frequency of this resonance is related to the total number of electrons in the oscillating dipole (defined essentially by the particle volume, or R^3), the complex dielectric function $\varepsilon(\omega)$, and the dielectric constant of the local medium ε_d. The plasmonic response is directly measurable by optical extinction and can be quite intense; for example, the molar extinction

coefficient (ϵ) for 30-nm Ag particles in water at plasmon resonance ($\omega_{SP} =$ 3.25 eV, or $\lambda_{SP} = 380$ nm) is on the order of $10^{10} M^{-1} cm^{-1}$.

Extinction includes both absorption and scattering components, which have different scaling relationships with nanoparticle size. The absorption cross section (a theoretical area value used to quantify the number of photons interacting within that region) increases linearly with particle volume, whereas the scattering cross section is relatively smaller but scales with volume squared. Such power functions are approximate and deviate significantly for particles above the quasi-static size limit.

The dipolar plasmon response (oscillator strength) of the nanoparticle is often defined by its polarizability, which can be expressed in terms of the parameters above by the electrostatic Clausius–Mossotti equation (also known as the Lorentz-Lorenz equation):

$$\alpha = 4\pi\varepsilon_0 R^3 \left| \frac{\varepsilon - \varepsilon_d}{\varepsilon + 2\varepsilon_d} \right| \tag{1}$$

The resonance condition leading to maximum polarization is $|\varepsilon + 2\varepsilon_d| = 0$, requiring $\varepsilon(\omega)$ to be negative. However, the complex dielectric function must be divided into real and imaginary components $\varepsilon'(\omega)$ and $\varepsilon''(\omega)$ in order to remove the phase-dependent term from the equation; resonance is thus achieved when $\varepsilon'(\omega) = -2\varepsilon_d$ and $\varepsilon''(\omega) \ll 1$. The dielectric function is negative when ω is below some threshold frequency ω_p, known also as the plasma frequency. The relationship between $\varepsilon(\omega)$ and ω_p can be illustrated by the Drude model, a conceptually useful description of free-electron behavior in metals. Here $\varepsilon'(\omega)$ and $\varepsilon''(\omega)$ can be approximated in terms of ω_p and Γ, the plasmon relaxation frequency:

$$\varepsilon'(\omega) \approx 1 - \frac{\omega_p^2}{\omega^2 + \Gamma^2} \tag{2}$$

$$\varepsilon''(\omega) \approx \frac{\omega_p^2 \Gamma}{\omega(\omega^2 + \Gamma^2)} \tag{3}$$

Applying these relations to Eq. (1) yields a Drude resonance frequency $\omega_D = \omega_p / \sqrt{2\varepsilon_d + 1}$ when $\varepsilon''(\omega)$ is small. The plasma frequency ω_p is a bulk material property and is scale-invariant within the quasi-static limit. However, the Drude free-electron response varies with geometric shape, which suggests a useful theoretical handle for predicting characteristic

resonance frequencies of ellipsoids (nanorods) and other anisotropic particles as a function of aspect ratio.

Unfortunately the free-electron model cannot be directly applied toward calculating the plasmonic response of most metals of interest, because of the additional electric susceptibility introduced by interband transitions between the outermost d and s orbitals at optical frequencies (threshold excitation energies for Ag($4d{\rightarrow}5s$) and Au($5d{\rightarrow}6s$) are close to 3.9 and 1.8 eV, respectively). These electronic excitations couple strongly with the free-electron response, resulting in large changes to $\varepsilon'(\omega)$ and $\varepsilon''(\omega)$; in addition, they can provide a significant relaxation (damping) mechanism for plasmon decay, reducing the quality of the optical resonance. In the case of Ag, interband transitions are responsible for changes in the resonance condition and the subsequent frequency difference between the theoretical Drude response (ω_D = 5.6 eV) and the observed plasmon resonance (ω_{SP} = 3.6 eV). In the case of other metals such as Au and Cu, $\varepsilon''(\omega)$ cannot be neglected at optical frequencies so the resonance condition derived from Eq. (1) is no longer strictly applicable.

Exact solutions for the optical properties of metal nanostructures can be obtained instead using electrodynamic Mie theory, whose formulations are derived from Maxwell's equations. Application of Mie theory requires the input of ε_d and $\varepsilon(\omega)$ as a function of frequency for a given particle size, either as experimental values or as numerical approximations. Various optical functions can be calculated with great accuracy; for example, extinction and optical conductivity (ε''/λ) spectra of Cu, Ag, and Au particles in the quasi-static limit were calculated using Eq. (4), with the effect of ε'' on the resonance band plainly visible (see Figure 7.3).[3] The calculated extinctions reproduce the experimental spectra with a high degree of fidelity, although the effect of certain physical parameters cannot be accounted for, such as surface charge from the electrostatic double layer.

$$\sigma_{ext}(\omega) = \frac{12\pi\varepsilon_d^{3/2}R^3\omega}{c}\left|\frac{\varepsilon''}{(\varepsilon'+2\varepsilon_d)^2+(\varepsilon'')^2}\right| \qquad (4)$$

Mie theory has been used to estimate variations in the electrodynamic response due to particle size, anisotropy, and other extrinsic parameters, independently from changes in the optical material function. This includes metal nanoparticles beyond the quasi-static limit ($2R/\lambda$ > 0.05), whose plasmon resonances are redshifted by phase retardation and broadened by radiation damping (*vide infra*). Higher-order plasmon modes also become significant; for example, quadrupole resonances in Ag and Au particles can be observed in optical extinction spectra starting from ~60 nm.
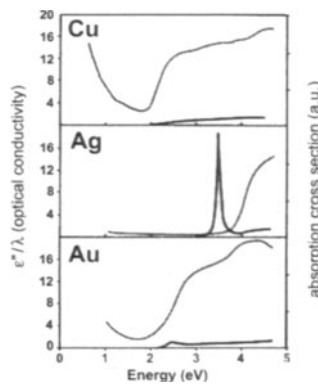
FIGURE 7.3. Optical conductivity (ε''/λ, in gray) and extinction spectra (in black) of Cu, Ag, and Au nanoparticles calculated as a function of photon energy ($2R = 10$ nm, $\varepsilon_d = 1$). The relative intensity of absorption by Ag is much higher than that of Au or Cu (adapted from Ref. 3).

Another important transition takes place in the mid-nanometer size regime: scattering supersedes absorption as the dominant optical response, at about 60 nm for Ag and 80 nm for Au. Dipole (S_1) scattering typically provides the largest contribution, followed by quadrupole (S_2) scattering.[4] As particles continue to increase in size, the various absorption and scattering modes reach a maximum, then fade away until only the bulk optical properties of the metal remain. Theoretical Mie absorption and scattering properties for Ag and Au particles of various size in water have been calculated by Yguerabide,[5] and are reproduced here to illustrate the dramatic effect of size on plasmonic response (see Figures 7.4 and 7.5 and Tables 7.1 and 7.2).
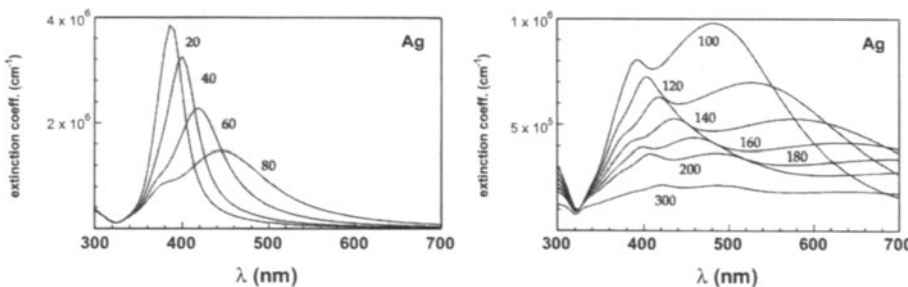
FIGURE 7.4. Mie extinction properties of spherical Ag nanoparticles in water, calculated as a function of diameter (adapted from Ref. 5).
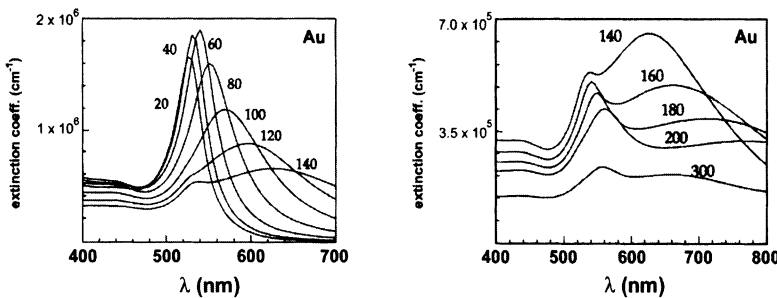
FIGURE 7.5. Mie extinction properties of spherical Au nanoparticles in water, calculated as a function of diameter (adapted from Ref. 5).

TABLE 7.1. Mie extinction properties for Ag nanoparticles as a function of size (adapted from Ref. 5). $^a\lambda_{max}$ values are calculated for dipolar, quadrupolar and higher-order plasmon resonances [latter two in brackets]. ^{b}Coefficients are calculated at maximum extinction. $^cC_{sca}$ = scattering cross section. $^d\varphi$ = relative scattering efficiency.

$2R$ (nm)	λ_{max} (nm)^a	ϵ (M^{-1} cm^{-1})^b	C_{sca} (cm^2)^c	φ (C_{sca}/C_{ext})^d
20	390	4.16×10^9	6.42×10^{-13}	0.041
40	400	2.87×10^{10}	2.78×10^{-11}	0.255
60	420	6.75×10^{10}	1.41×10^{-10}	.0550
80	445 [380]	1.04×10^{11}	2.92×10^{-10}	0.741
100	485 [390]	1.35×10^{11}	4.28×10^{-10}	0.835
120	530 [400]	1.66×10^{11}	5.57×10^{-10}	0.844
140	580 [415]	1.98×10^{11}	6.88×10^{-10}	0.913
160	640 [445] [390]	2.97×10^{11}	8.97×10^{-10}	0.819
180	[460] [400]	3.41×10^{11}	1.13×10^{-9}	0.848
200	[485] [405]	4.04×10^{11}	1.35×10^{-9}	0.876
300	[490] [420]	8.0×10^{11}	2.7×10^{-9}	0.877

TABLE 7.2. Mie extinction properties for Au nanoparticles as a function of size (adapted from Ref. 5). $^a\lambda_{max}$ values are calculated for dipolar, quadrupolar and higher-order plasmon resonances [latter two in brackets]. ^{b}Coefficients are calculated at maximum extinction. $^cC_{sca}$ = scattering cross section. $^d\varphi$ = relative scattering efficiency.

$2R$ (nm)	λ_{max} (nm)^a	ϵ (M^{-1} cm^{-1})^b	C_{sca} (cm^2)^c	φ (C_{sca}/C_{ext})^d
20	535	1.57×10^9	8.36×10^{-14}	0.014
40	535	1.63×10^{10}	6.05×10^{-12}	0.100
60	545	5.32×10^{10}	6.33×10^{-11}	0.313
80	555	1.14×10^{11}	2.31×10^{-10}	0.546
100	575	1.62×10^{11}	4.56×10^{-10}	0.739
120	605	2.07×10^{11}	6.90×10^{-10}	0.876
140	635 [535]	2.46×10^{11}	8.79×10^{-10}	0.940
160	665 [540]	2.80×10^{11}	1.02×10^{-9}	0.963
180	720 [550]	3.14×10^{11}	1.16×10^{-9}	0.974
200	780 [560]	4.51×10^{11}	1.38×10^{-9}	0.788
300	[660] [555]	7.98×10^{11}	2.94×10^{-9}	0.968

7.4. SURFACE PLASMONS AND THE MATERIAL FUNCTION

We have touched on the fact that the free-electron plasmon response can be strongly influenced by interband transitions, a property of the bulk metal. Several other material factors also have an influential role on surface plasmons and $\varepsilon(\omega)$: (a) the electron mean free path, (b) the skin depth, and (c) local medium effects, including surface adsorption. These are discussed in some detail below for the case of spherical, crystalline metal nanoclusters.

7.4.1. SIZE CONFINEMENT EFFECTS ON THE PLASMON BAND

Metal nanoparticles exhibit peak broadening when their diameters are much less than the electron mean free path L_e, a material-dependent property describing the quasi-elastic scattering of conduction electrons (L_e in bulk Ag and Au are about 50 and 40 nm, respectively). The effective path length L_r decreases almost linearly with $2R$, corresponding with a change in $\varepsilon(\omega)$ from the bulk dielectric function. Broadening of the plasmon band in Ag and Au nanoparticles becomes evident for $2R < 10$ nm; the plasmon resonance frequency is not affected, but the relaxation rate Γ increases with a $1/R$ relationship due to the greater electron scattering by the particle surface (see Figure 7.6).[6] In the case of the very smallest nanoclusters ($2R < 2$ nm), it has been argued that the local density of states may be reduced to the extent that they no longer form a continuous band structure. Experimental evidence for quantum size effects has recently been obtained in the form of electrochemical "Coulomb staircase" measurements on single gold nanoclusters, with redox-like behavior observed for particles with diameters well below 2 nm.[7] Quantum-mechanical effects of a different sort have also been established in the ensemble electronic states of metal nanoparticle superlattices, as shall be discussed in a later section (cf. Section 4.2a).

7.4.2. SKIN DEPTH

The incident lightwave on a bulk metal surface has a fairly low penetration depth, with an exponential attenuation of electric field strength below the surface (see Figure 7.2, *right*). The electric field within the metal can be expressed as a function of depth z:

$$|\mathrm{E}(z)| = |E_0| e^{-z/\delta} \tag{5}$$

Here the skin depth δ is defined as

$$\delta = \frac{c}{\omega k} = \frac{\lambda}{2\pi k} \tag{6}$$

where k is the absorption coefficient of the metal. The bulk refractive index n and the absorption coefficient k are related to the complex dielectric function by $n + ik = \sqrt{\varepsilon' + i\varepsilon''}$, so k can be expressed solely in terms of the dielectric function as

$$k = \sqrt{\frac{\sqrt{(\varepsilon')^2 + (\varepsilon'')^2} - \varepsilon'}{2}} \tag{7}$$

Calculations of δ using Eqs. (6) and (7) at different optical wavelengths suggest an average value of ~30 nm for both Ag and Au, with an exceptionally large value of ~80 nm near the plasmon resonance in the case of Ag. This reaffirms the dipolar nature of localized plasmon resonances for nanoparticles with diameters on the order of L_e, and suggests the onset of multimodal plasmon modes in larger metal nanoparticles. A low skin depth also promotes the propagation of surface plasmon polaritons in anisotropic metal nanostructures such as nanorods, with intriguing consequences for their optical emissions.
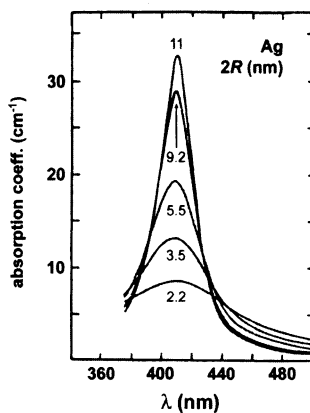

FIGURE 7.6. Size confinement effects on the plasmon resonance band for Ag nanoparticles, calculated using bulk dielectric constants (adapted from Ref. 3).

7.4.3. LOCAL DIELECTRIC AND SURFACE EFFECTS.

Coupling between the Drude free-electron response and interband excitations can be weakened by modulating ε_d, such that the Drude frequency is shifted away from the electronic transition threshold (see Section 2.1). An especially dramatic effect can be expected in the case of Cu, which has a significant $\varepsilon''(\omega)$ at plasmon frequencies above 2 eV (see Figure 7.3). By embedding Cu nanoparticles in transparent media with $\varepsilon_d >$ 5, the plasmon resonance frequency of Cu nanoparticles can be lowered to below 2 eV, resulting in a large enhancement in optical extinction (see Figure 7.7).[8] Metal nanoparticles are also solvatochromic; polymer-stabilized Au particles dispersed in organic solvents of varying refractive indices ($n = 1.33$–1.60) demonstrated a shift in absorption from red to purple ($\lambda_{SP} = 520$–545 nm), accompanied by an increase in extinction intensity.[9] The experimental data was found to be in excellent agreement with Mie theory, based on the changes in ε_d.
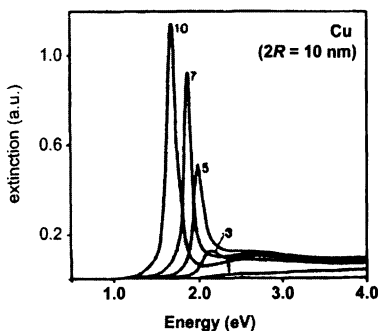

FIGURE 7.7. Extinction peaks of Cu nanoparticles embedded in various dielectric media (ε_d).[3]

Surface adsorbates (ligands) can also influence the optical properties of metal nanoparticles. Strongly adsorbing anions and chemisorptive surfactants such as thiols accelerate plasmon relaxation, resulting in peak broadening (vide supra). This effect has been attributed to a reduction in conduction electron mobility, due to electronic coupling between the plasmon and charge-transfer bands formed by the metal–adsorbate complex.[10] Strong optical resonance can be restored in some cases by cathodic (negative) charging, which induces ligand desorption.

7.4.4. PLASMON DECAY AND RADIATIVE DAMPING

The quality of the dipolar plasmon response depends both on the intensity of polarizability and the coherence lifetime of the collective

oscillations. The latter is determined by the dephasing (or decay) of the collective dipole, which is characterized by the relaxation constant $T_2 = 2\hbar/\Gamma$. Plasmon relaxation occurs by radiative damping and also by nonradiative electronic mechanisms such as interband transitions (*vide supra*). Radiative damping of an oscillating electronic dipole is the electromagnetic equivalent of mechanical damping in a vibrating system, with the conduction electrons providing an effective mass.

Both radiative damping and polarizability increase with particle volume, such that the increased dipole oscillator strength is accompanied by broadening of the optical response. Radiative damping also scales with $1/\lambda^3$, with a consequently reduced effect on plasmons at lower frequencies. Radiative damping in single metal nanoparticles has recently been measured by Klar *et al.* using near-field scanning optical microscopy, which permitted quantitative determination of plasmon linewidths (Γ) from individual nanoparticles.[11] These were narrower than that produced by bulk measurements, and yielded an excellent correlation between experiment and Mie theory.

As a practical rule of thumb, damping and phase-retardation effects in spherical nanoparticles will have a compromising effect on optical emission and field-enhanced applications such as SERS when $2R/\lambda > 1/\pi\sqrt{\varepsilon_d}$ (approximately 0.24 in water).[12,13] However, it is important to mention that radiative damping is not necessarily dependent on the overall particle volume, but rather on those portions which define an 'optical domain.' This point will become clear when discussing the optical properties of anisotropic structures such as nanorods and nanowires.

7.4.5. ANISOTROPIC METAL NANOPARTICLES

An important feature of dipolar plasmon resonance is its high sensitivity to shape anisotropy: isolated spherical nanoparticles typically support a single resonance frequency, whereas anisotropic particles such as rods and triangles will exhibit at least one additional plasmon mode, as well as large redshifts in plasmon resonance. Electric birefringence is also enhanced by structural anisotropy, and can be used in conjunction with optical extinction to estimate particle eccentricity.[14] Modifications to the original Mie theory (by Gans) have permitted the optical response of anisotropic nanoparticles to be calculated and compared with analytical measurements. Both theoretical and experimental investigations of anisotropic metal nanoparticles indicate several important differences in their enhanced optical properties when compared with those of spherical nanoparticles.

7.4.6. SURFACE PLASMONS IN METAL NANORODS AND NANOWIRES

According to Mie–Gans theory, cylindrical nanorods support two distinct plasmon modes: a transverse mode oscillating perpendicular to the principal axis, and a longitudinal resonance with a coaxial polarization. Several groups have shown that both frequencies are determined by the particle's aspect ratio.[15,16] The longitudinal plasmon mode can be strongly redshifted into the NIR: for example, Au nanorods dispersed in water with aspect ratios of ~4:1 exhibit longitudinal plasmon resonances centered at 800 nm, whereas nanorods with aspect ratios of ~9:1 exhibit resonances centered at 1.3 μm (see Figure 7.8). In contrast, the transverse plasmon resonance shifts toward shorter wavelengths with increasing aspect ratio, until an asymptotic value is reached (~500 nm).
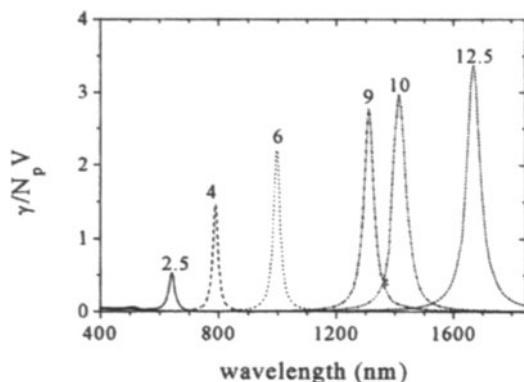

FIGURE 7.8. Longitudinal plasmon resonances calculated for Au nanorods in water with different aspect ratios, based on electrodynamic Mie–Gans theory (adapted from Ref. 15).

Methodologies for synthesizing metal nanorods are now well established. Nanoparticle-seeded growth mediated by cationic surfactants can produce cylindrically symmetric nanorods with aspect ratios as high as 20:1, with diameters on the order of 10–20 nm.[17,18] For thicker nanorods (> 20 nm), pulsed electrodeposition into metallized nanoporous membranes has been demonstrated to produce nanorods of any aspect ratio.[19,20] The latter synthetic method offers excellent control over nanorod dimensions: rod thickness is predetermined by pore diameter, whereas rod length is a direct function of deposition time or coulombs (current × time). In addition, the electroplating solution can be interchanged to enable the preparation of bi-, tri-, or multimetallic nanorods. This has been recently demonstrated in the production of submicron "nano-barcodes," in which several different metals can be incorporated into the nanorod, with each segment producing its own

characteristic plasmonic response.[21,22] These are currently being marketed as single-particle optical labels for various bioanalytical applications.[23]
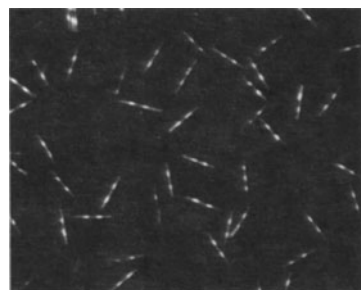

FIGURE 7.9. Optical micrograph (160×, N.A. = 1.4, λ = 405 nm) of bimetallic 'striped' Ag–Au nanorods, approximately 300 nm × 6 μm.[23]

A very important optical quality of Au nanorods is their low rate of plasmon decay, which reduces the linewidth of their optical response. A recent single-particle scattering study by Sönnichson *et al.* provided FWHM linewidths of individual Au nanospheres and nanorods, with the latter producing higher quality resonances due to reduced radiative damping effects.[24] Spherical nanoparticles with plasmon resonances centered at 800 nm produced emissions with broad linewidths (Γ = 0.9 eV, or ~500 nm), whereas nanorods at the same resonance frequency produced much narrower emission peaks (Γ = 0.1 eV, or ~50 nm). The plasmon linewidths are limited by nonradiative damping effects caused by the intraband transitions in gold ($\Gamma \sim \hbar/T_1^{1B}$) but remain narrow even at longer wavelengths, and are only slightly broader than those derived from electrodynamic calculations (cf. Figure 7.8). It is interesting to note that even very long metal nanowires (~30 nm × 6 μm) retain high optical scattering efficiency without significant line broadening (λ_{SP} = 520 nm).[22] The nanowires' transverse plasmon resonances are evidently unperturbed by radiative damping, which suggests that the plasmon relaxation rate is unaffected by dimensional changes normal to the direction of polarization.

The distinction of transverse and longitudinal modes in plasmonic nanowires gives rise to an interesting dichotomy: electric polarizations in the transverse direction can propagate as surface plasmon waves along the nanowire's principal axis. Optical input energy can be transported as surface-bound plasmon waves and be re-emitted as light at the far end of the nanowire, provided that propagation is favored over absorption or emission. This suggests possible applications in the emerging area of nanophotonics, in which electromagnetic information can be processed and directed at nanometer length scales.

An elegant study by Dickson and Lyon demonstrates the critical role of the dielectric function in plasmon propagation, using 20-nm Au and Ag nanowires coupled to an evanescent light source (see Figure 7.10).[25] In both cases, irradiation of 820-nm light at one end (input) produces scattered light at the other (output), but when 532-nm light is used only the Ag nanowire supports plasmon propagation. Efficient optical energy transport is not observed in Au nanowires presumably because of their significant absorption at that wavelength. Very interestingly, a bimetallic Au–Ag nanowire exhibits *unidirectional* plasmon propagation at 820 nm, with efficient transport only in the Au→Ag direction— in other words, a nanophotonic diode. The full potential of plasmonic nanowires and nanostructured heterojunctions as components in photonic circuits and devices remains to be discovered.
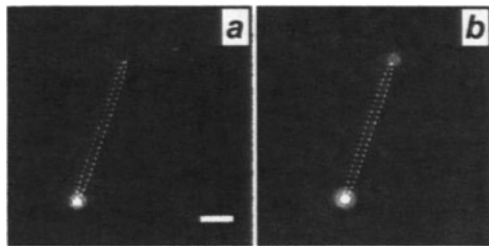

FIGURE 7.10. Optical image of 20 nm × 4.7 μm Au nanorod, with the lower end exposed to evanescent illumination at (*a*) 532 nm and (*b*) 820 nm.[25] A dotted outline of the nanorod has been drawn as a visual aid. Scattering is only observed from the input end in (*a*) whereas both ends emit light in (*b*), indicating plasmon propagation at 820 nm. Scale bar = 1 μm.

7.4.7. SURFACE PLASMONS IN METAL NANOPRISMS AND POLYHEDRA

Electrodynamic calculations can also be extended to nanoparticles with anisotropy in three dimensions (nanoprisms and polyhedra). Schatz and co-workers have used numerical methods such as discrete dipole approximation (DDA) to calculate the extinction properties and local field factors of Ag trigonal prisms and truncated tetrahedra under polarized light.[26] As in the case of the nanorods, shape plays a critical role in the dipolar resonance frequencies of the plasmon modes. The lowest-energy plasmon peak is largely determined by the tip-to-tip distance on the triangular nanoparticles, but even a slight truncation of the vertices will result in a sizable shift to shorter wavelengths (see Figure 7.11). The DDA calculations also reveal a significant quadrupolar resonance at higher frequencies, a plasmon mode often obscured in isolated spherical particles of comparable size.
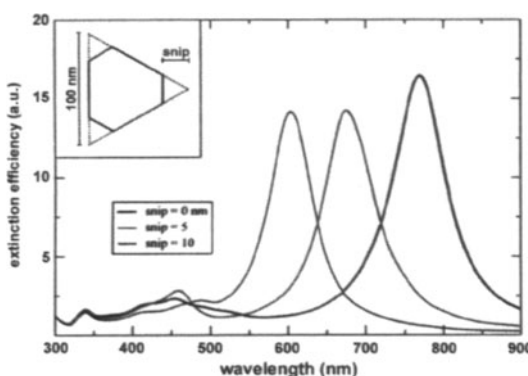
FIGURE 7.11. Calculated extinction spectra for 100-nm Ag trigonal prisms with truncations (see inset) of 0 nm (*left*), 5 nm (*middle*), and 10 nm (*right*).[26b] Prism thickness is 16 nm.

A comparison of experiment and theory reveals similar trends with respect to dielectric effects on plasmon resonances in triangular nanoprisms, although discrepancies due to surface oxidation and other environmental factors prevent complete convergence. Other polyhedra with less pronounced anisotropies exhibit smaller shifts in plasmon resonance: single-particle scattering studies of spheroidal, pentagonal, and triangular Ag nanoparticles have demonstrated a shape-dependent trend in optical response, with the latter experiencing the greatest average shift toward longer wavelengths.[27]

Methodologies for synthesizing metal nanoprisms with controlled dimensions are presently under development. One of the first reliable methods for fabricating triangular nanoprisms was developed by Van Duyne and coworkers, in which a hexagonally close-packed monolayer of colloidal spheres served as a template for metal vapor deposition.[28] The "nanosphere lithography" approach provides access to truncated tetrahedral metal islands with in-plane diameters ranging from ~20 nm to hundreds of nanometers depending on the size of the particles in the colloidal mask, and heights of 5–50 nm as a function of the metal evaporation rate (see Figure 7.12). The plasmon resonances of triangular Ag particles are size-tunable and have reasonably narrow linewidths, with primary extinction maxima ranging from 550 nm to 6.0 μm, well into the mid-infrared range.[29]

Solution syntheses of metal polyhedra have recently been achieved with some degree of control. A report by Jin *et al.* demonstrates a novel photoinduced method of converting spherical Ag nanoparticles into triangular prisms with variable in-plane diameters but nearly uniform thicknesses.[30] Also worth mentioning is the synthesis of metal nanoparticle cubes by Sun and Xia, whose anisotropic growth is surfactant-mediated.[31]
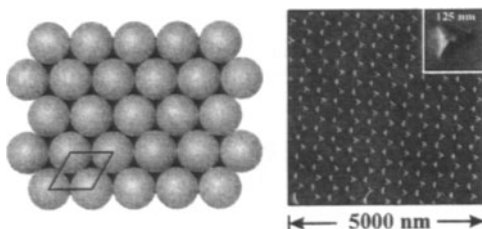
FIGURE 7.12. Nanosphere lithography.[28] A monolayer of close-packed microspheres (*left*) is exposed to thermally evaporated metal (Ag), then removed by sonication in organic solvent to reveal a periodic array of truncated tetrahedrons.

With respect to applications, the plasmonic responses of triangular nanoparticles have demonstrated a remarkably high sensitivity to changes in their local environment. For example, shifts in the surface plasmon resonance (SPR) wavelength due to alkanethiol adsorption were sufficiently sensitive that a difference of two carbons (e.g., C10 vs. C12 thiol) gave a differential response of ~8 nm in the extinction maxima.[32] These SPR shifts have proven to be useful for biomolecular sensing: functionalizing the nanoprisms' surfaces with biotinylated ligands enabled them to detect streptavidin binding events· at very low concentrations, with saturation adsorption at 100 pM and limits of detection in the low picomolar range ($\Delta\lambda$ ~4 nm).[33] By comparison, nonspecific protein adsorption induced only a 2-nm redshift in the resonance peak. Additional peakshifting could be induced by adding biotinylated Au nanoparticles as secondary labels, whose near-field coupling with the metal substrate provides a mechanism for enhancing SPR sensitivity.[34] In fact, electromagnetic coupling plays a key role in the plasmonic responses of metal nanoparticle ensembles, and can enhance their optical properties by many orders of magnitude.

7.5. METAL NANOPARTICLE ENSEMBLES

Up to this point we have focused on the optical properties of isolated metal nanostructures, with minimal interactions between particles. However, some of the highest signal amplifications have been achieved using nanoparticles with strong electromagnetic coupling. For example, many of the early SERS observations in the late 1970's and early 1980's were performed using kinetic aggregates of Ag and Au nanoparticles.[35] Unfortunately, reproducible activities from such substrates has been poor; although there is strong evidence that aggregated nanoparticles contain "hot spots" which produce the great majority of the enhanced Raman intensities, they vary widely from sample to sample and often disappear after a few

days' aging. This variability is made all the more frustrating by several fairly recent reports of single-molecule SERS spectroscopy;[36] while the detection of individual molecules is possible, the conditions which enable reproducible single-molecule analysis have not yet been established.

It is not terribly surprising that the complexity of disordered aggregates have been slow to yield the secrets of these elusive but potentially enormous optical enhancements. In the last few years significant progress has been made in the electromagnetic theory of metal–dielectric interfaces, both for periodic nanostructures[37] and for fractal aggregates.[38] There have also been several important advances in the self-assembly of discrete or periodically ordered metal nanostructures, and continued progress along both of these lines can be expected to produce some concrete answers. Here we shall review several recent studies on discrete nanoparticle aggregates (clusters), two-dimensional (2D) arrays, and three-dimensional (3D) aggregate structures. It will become evident that in addition to particle size and shape, interparticle spacing (δ) is a critical parameter to the collective optical properties of nanoparticle ensembles.

7.4.1. DISCRETE METAL NANOPARTICLE CLUSTERS

Nanoparticles separated by a few diameters begin to experience significant electromagnetic dipole coupling, which gives rise to additional plasmon modes. Effective-medium theories such as the Maxwell-Garnett formula have been used to approximate the optical responses of coupled nanoparticles up to a certain point, but these lose their accuracy if the spacing is much less than one particle diameter ($\delta < 1.5R$). Simulations based on generalized Mie theory[3,39] or numerical approaches such as DDA[26] appear to provide more consistent models of collective optical properties, for N-particle systems of discrete size. These have been used to predict the extinction and absorption cross sections of specific aggregate structures, such as chained particles in linear or bent conformations (see Figure 7.13). Overall, the calculated optical responses are quite similar to those determined for anisotropic particles; linear chains (resembling nanorods) produce longitudinal plasmon resonances at strongly redshifted wavelengths, whereas close-packed aggregates (resembling prisms) exhibit less pronounced shifts in their collective plasmon resonance frequencies.
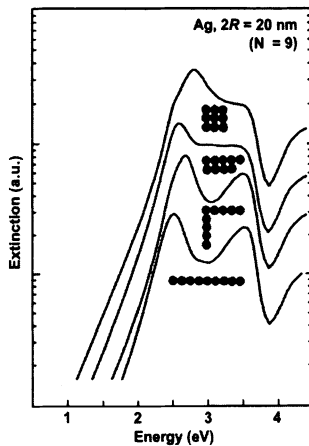
FIGURE 7.13. Extinction spectra of 20-nm Ag particle aggregates in different geometries, as calculated by generalized Mie theory (adapted from Ref. 3).

More recent theoretical treatments have given emphasis to the local electromagnetic fields generated near the metal nanoparticle surfaces, with the objective of defining regions with the highest field factors (often quantified as function of $|E/E_0|$) for a given frequency ω. This is especially important for surface-enhanced spectroscopies such as SERS, in which signals are amplified as a function of $G_{EM} = |E(\omega)/E_0(\omega)|^2 \cdot |E(\omega')/E_0(\omega')|^2$, where ω and ω' are the incident and Stokes-shifted frequencies, respectively.[40] In the simplest case of a two-sphere system, it is well known that local field factors are greatest when the two particles are almost touching. Käll and coworkers have performed electrodynamics calculations on pairs of Au and Ag particles (10–90 nm) separated by as little as 1 nm, and suggested G_{EM} values in excess of 10^{11} for the best cases.[41] These "hot spots" are exquisitely sensitive to interparticle spacing; changes in δ by just a few nanometers can cause the local enhancements to drop by several orders of magnitude (see Figure 7.14). The calculations imply that nanoparticle dimers may have potential as substrates for routine single-molecule SERS, given a reliable method for localizing analytes in regions of high field.

So far, successful methods of organizing nanoparticles into ensembles of well-defined size and shape have mostly relied on lithographically defined surfaces[42] or on serially directed assembly using scanning probe microscopy tips.[43] Surprisingly, there are few reports for producing even dimers of metal nanoparticles in a controlled fashion by self-assembly. A recent contribution to this area from Feldheim and coworkers uses a tectonic approach, in which the aggregation of metal nanoparticles is coordinated by a rigid, multivalent organic ligand.[44] Dimers, trimers, and tetrahedral clusters of colloidal Ag

and Au nanoparticles could be prepared and partially separated by gradient centrifugation.[45] The reduced symmetry of the nanoparticle trimers enhances their nonlinear optical properties; for example, the hyper-Raman scattering efficiency per unit nanoparticle (8 nm) was shown to be nearly an order of magnitude higher for noncentrosymmetric trimers versus dimers or monomers.[46]
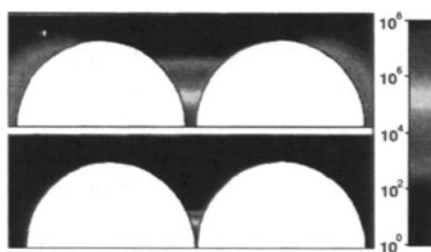

FIGURE 7.14. Electrodynamics simulation of local field enhancements (G_{EM}) between two 90-nm Ag particles ($\varepsilon_d = 1$) at different interparticle separations ($\delta = 5.5$ and 1.0 nm).[41]

7.4.2. PERIODIC METAL NANOPARTICLE 2D ARRAYS

7.5.2.1. COLLECTIVE OPTICAL PROPERTIES OF SMALL NANOPARTICLE ARRAYS

There have been numerous studies on the self-assembly and collective properties of 2D nanoparticle superlattices, the great majority of which have been prepared from metal particles in the 2–10 nanometer size range. Such ensembles have been reviewed elsewhere;[47] in brief, while several important advances have been made in correlating physical properties with 2D periodic structure, many more relationships remain to be elucidated. An important challenge to this effort is the development of reliable methods for fabricating arrays with excellent long-range order, a subject which has remained an active area of investigation.[48]

With respect to optical properties, Heath and coworkers have established quantitative relationships between the periodic structure and the dielectric function of 2D metal nanoparticle ensembles.[49,50] Hexagonally close-packed (hcp) arrays of Ag nanocrystals (2–6 nm) were self-assembled on air–water interfaces and subjected to gradual changes in surface pressure in a Langmuir trough (see Figure 7.15). Compression of the monolayer films increased their nonlinear optical responses as well as their reflectance. These could be parameterized in terms of $D/2R$, a ratio between the average center-to-center distance ($2R + \delta$) and the unit particle diameter.
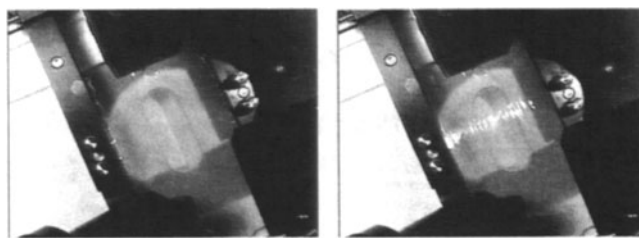
FIGURE 7.15. Close-packed monolayer of butanethiol-coated 3.5-nm Ag particles (center) in a Langmuir trough.[50] *Left*, Ag nanoparticle film under low surface compression; *right*, same film under slightly greater compression, but with a substantially higher reflectance.

For $D/2R$ values between 1.7 and 1.2, it was determined that quantum-mechanical exchange interactions play a significant role in the collective optical properties of the nanoparticle arrays, particularly in their nonlinear optical responses. Second-harmonic generation (SHG) was observed to have an exponential dependence on D with a maximum response at $D/2R \sim 1.2$, whereas local field factors provided only a minor contribution to SHG enhancement.[51] In addition, the linewidth of optical reflectance narrowed as $D/2R$ approached 1.2, due to greater electronic delocalization and less scattering from the particle surface (cf. Section 2.2a).

Further decreases in interparticle spacing resulted in an abrupt loss of reflectance and SHG, signifying the onset of a quasi-continuous metallic state. The insulator-to-metal transition was observed to be reversible, as decompression of the monolayer films to $D/2R > 1.2$ restored the strong optical response. The complex dielectric function $\varepsilon(\omega)$ could be derived from constants n and k, which in turn were obtained from bulk optical measurements at different stages of compression. It was determined that the free-electron (Drude-like) behavior of the metallic phase shifts $\varepsilon'(\omega)$ toward negative values, whereas $\varepsilon''(\omega)$ is relatively unaffected by changes in spacing.[52] A decrease in $\varepsilon'(\omega)$ corresponds to a higher absorption coefficient k especially when $\varepsilon'(\omega) < 0$ (cf. Eq. (7)), and is thus largely responsible for the significant loss in linear optical response at low values of $D/2R$.

It is worth mentioning that long-range order can also be a significant factor in the arrays' collective properties. This has been demonstrated to be an important parameter for electronic transport: the current–voltage relationship of highly crystalline nanoparticle arrays varies as a simple power function,[53] whereas disorder introduces nonlinear scaling behavior.[54] With regard to optical properties, nonlinear effects are also promoted by lattice disorder; small (~10%) fluctuations are sufficient to break the symmetry within the superlattice, enhancing second-order polarizability (χ^2) and the subsequent SHG.[55] However, at very small interparticle distances the

effects of local disorder are dominated by exchange coupling, and thus have only a minor effect on SHG intensity.

7.5.2.2. COLLECTIVE OPTICAL PROPERTIES OF LARGE NANOPARTICLE ARRAYS

Metal particles in the mid-nanometer size range (20–200 nm) are also important candidates for self-assembly because of their size-dependent optical properties, but their strong interaction potentials can promote kinetic aggregation, resulting in poorly organized structures. This can be viewed as a problem in dispersion control; if repulsive interactions can offset particle self-attraction at close range, one should be able to achieve conditions for thermodynamically controlled self-organization. Earlier demonstrations by Schmid[56] and by Giersig and Mulvaney[57] have indicated that colloidal Au particles can be assembled into 2D domains with local order. Beyond that however, there have been relatively few studies in which large (>20 nm) metal nanoparticles are organized into periodic superlattices.

A general method for organizing metal nanoparticles into self-assembled 2D arrays has recently been developed by Wei and coworkers, using multivalent macrocyclic surfactants known as resorcinarenes.[58] These compounds are capable of extracting colloidal Au particles from aqueous suspensions and dispersing them into organic solvents or at air–water interfaces.[59] In the latter case, resorcinarene-stabilized nanoparticles as large as 170 nm could spontaneously organize into monoparticulate films with long-range order (see Figure 7.16).[60] Careful inspection of the TEM images reveals an inverse correlation between array periodicity and interparticle spacing, most likely as a result of greater van der Waals attraction with unit particle size. The particle diameter-to-spacing ($2R/\delta$) ratios range from about 15 to well over 100, well beyond the metal–insulator threshold defined by the Heath group.[49]
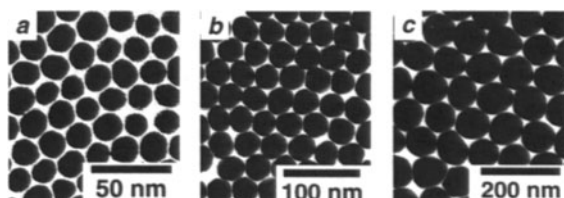

FIGURE 7.16. Self-organized 2D arrays of large Au nanoparticles.[60] Unit particle sizes: (a) 16 nm; (b) 34 nm; (c) 87 nm.

The 2D arrays exhibit size-dependent optical extinction and reflectance at visible and NIR wavelengths, and have been found to be excellent substrates

for SERS.[61] Surface-averaged Raman signals generated from the adsorbed resorcinarenes could be optimized as a function of periodicity and excitation wavelength, with cross sections enhanced by as much as 10^7. The observed trends are in accord with theoretical calculations describing electromagnetic SERS,[62] and also with earlier SERS studies on disordered metal colloid aggregates.[63] However, the resorcinarene-stabilized nanoparticle arrays have considerable advantages in reproducibility and stability, and retain essentially all SERS activity more than a year after self-assembly. Additional signal enhancement could be obtained by increasing the solid angle of incidence and collection; the angle-dependent Raman intensities suggest that surface plasmon polaritons in the Au nanoparticle films contribute significantly to the SERS effect.

The large Au nanoparticle arrays are capable of detecting exogenous analytes by SERS and thus have potential as spectroscopic chemical sensors.[61] Volatile organic compounds adsorbed onto the array surface produce a detectable signal within seconds; however, theoretical calculations indicate that detection limits can be further lowered by adjusting the interparticle spacing. Incremental changes in δ will delocalize field intensities, but at the same time increase the available sampling space for analyte detection. Recent calculations by Genov *et al.* indicate that the surface-averaged enhancement factor G_R (as opposed to the local factor G_{EM}) from periodic nanoparticle arrays can be maximized as a function of excitation wavelength at a given value of $2R/\delta$.[64] The resonant G_R values can surpass those produced by disordered metal–dielectric films by several orders of magnitude (see Figure 7.17).
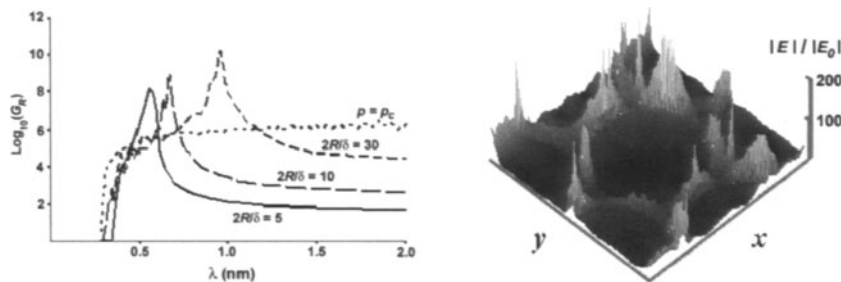

FIGURE 7.17. *Left*, numerical calculations of surface-averaged field enhancements (G_R) from 2D hexagonal superlattices with diameter–spacing ratios of 5, 10, and 30, versus a random metal–dielectric film at the percolation threshold ($p = p_c$). *Right*, local field distribution within a hexagonal lattice produced by *p*-polarized light ($\lambda = 600$ nm, $2R/\delta = 10$, $E_0 = E_y$).[64]

7.4.3. METAL AND METAL–DIELECTRIC NANOPARTICLES IN 3D SUPERLATTICES

In addition to enhancing spontaneous emission events such as SERS, metal nanoparticle superlattices may also be capable of blocking electromagnetic radiation at select frequencies, i.e. possess a photonic band gap. Photonic crystals with band gaps in the visible to NIR range have been highly sought after as a way to manipulate the flow of light.[65] In principle, a photonic band gap can be engineered from nearly any type of material by periodically modulating its dielectric properties. However, lattices with relatively low dielectric contrast are not optimal materials for designing photonic band gaps at optical wavelengths. Metal–dielectric periodic nanostructures are capable of much stronger optical modulation; "inverse-opal" metal-coated colloidal crystals have recently been fabricated, and have some promise as photonic band-gap materials.[66]

Theoretical studies by Moroz indicate that plasmonic colloidal crystals can support a complete photonic band gap in the visible and even the near-UV range.[67] Close-packed, face-centered cubic (FCC) crystals of colloidal Ag particles were calculated to have tunable band gaps, at frequencies defined by the particle radius and plasma wavelength (R/λ_p) and with gap widths ($\Delta\omega/\omega_c$) between 5 and 10%. The photonic band gaps were predicted to be greatest for colloidal crystals with $R/\lambda_p > 0.9$; in the case of Ag, 3D arrays of large, submicron-sized particles would be needed to produce band gaps for visible wavelengths.

A related study by Zhang *et al.* suggest that tunable photonic band gaps can also be made using metal-coated, core–shell nanoparticles as 3D array elements.[68] The band gaps of these materials are predicted to be less dependent on long-range order, a critical and challenging issue in the self-assembly of colloidal crystals. Photonic band gaps have been calculated for FCC lattices of SiO_2/Ag core–shell nanoparticles of different sizes and packing densities: 500/50-nm core–shell particles at 45% packing density are expected to have a robust band gap centered at $\lambda = 1.5$ μm, whereas 160/50-nm core–shell particles at 42% packing density are expected to have a band gap across the visible spectrum.

A number of reports have recently been published on the preparation and optical properties of nanoparticles with dielectric cores and metallic shells. Halas and coworkers have fabricated semicontinuous Au and Ag nanoshells by electroless deposition onto submicron silica particles.[69] Extinctions could be tuned as a function of shell thickness and core diameter, from the visible to the mid-IR range; the latter were produced by nanoparticles with high core–shell aspect ratios.[70] Highly monodisperse core–shell nanoparticles can be crystallized into 3D arrays with colorful Bragg reflections (see Figure

7.18). An interesting variant reported by Graf and van Blaaderen involves the growth of a second dielectric shell around the metal-coated nanoparticle.[71] The outermost SiO_2 shell reduces the van der Waals interactions considerably, and permits their self-organization into colloidal crystals with fractional densities close to that proposed by Zhang et al.[68]
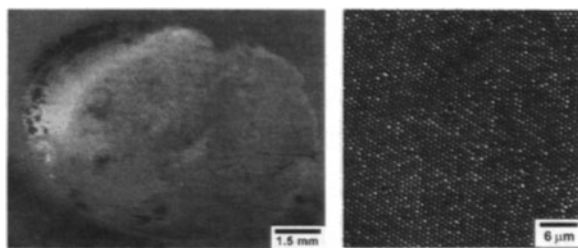

FIGURE 7.18. Colloidal crystals of core–shell nanoparticles formed in aqueous solution.[71] *Left,* photograph of crystal comprised of SiO_2/Au core–shell nanoparticles (core = 205 nm, shell = 31 nm); *right,* top layer of SiO_2/Au nanoparticle superlattice.

7.4.4. NONPERIODIC NANOPARTICLE ENSEMBLES

Many of the structure–property relationships which have been defined for 2D and 3D arrays are also qualitatively observed in disordered metal nanoparticle ensembles. Large changes in optical extinction and scattering are readily achieved by ligand-induced aggregation, with direct applications toward chemical and biomolecular sensing.[72] One of the best-known examples is the colorimetric detection of DNA polynucleotides by Mirkin and coworkers.[73] The technology is remarkably simple: 13-nm Au particles functionalized with two different oligonucleotide probes undergo hybridization with complementary (target) DNA strands, turning the solution from red to blue. The colorimetric "spot test" assay is capable of detecting antisense oligonucleotides in femtomole quantities (nanomolar concentrations), and can differentiate single-nucleotide mismatches as a function of a characteristic melting temperature. The magnitude of the color change (due to the increased electromagnetic coupling within the DNA–nanoparticle network) is dependent both on the effective interparticle distance between nanoparticles and on aggregate size. Hybridization with antisense oligonucleotides of different lengths revealed marked differences in the kinetics of aggregate formation, with gradual increases in average cluster size correlating with changes in optical extinction.[74]

As mentioned earlier, nonperiodic nanoparticle ensembles can also enhance spontaneous emission events such as SERS,[63] albeit with some degree of variability. One practical method of preparing SERS substrates

with fairly reliable and stable enhancements is to adsorb metal nanoparticles onto amine or thiol-functionalized substrates. Submonolayer ensembles of colloidal metal particles can be prepared with packing densities of up to 30% (see Figure 7.19, *left*), which is well below the close-packing limit (~90%) but sufficient to produce significant electromagnetic coupling and SERS.[75,76] Electrostatic self-assembly of Au nanoparticles on spherical submicron particles has also been reported recently;[77] in this case, packing densities on the order of 50% can be achieved by increasing the nanoparticles' surface potentials, with a concomitant enhancement in electromagnetic coupling (see Figure 7.19, *right*).
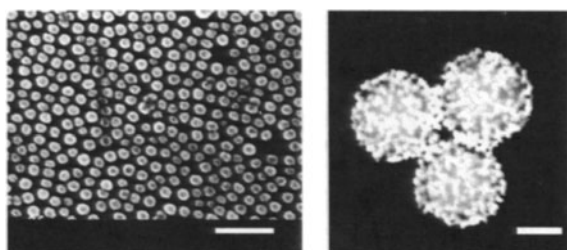

FIGURE 7.19. *Left*, planar ensemble of ~40-nm Au particles adsorbed onto thiol-functionalized SiO$_2$.[75] *Right*, spherical core–shell ensembles of 30-nm particles adsorbed onto amine-functionalized SiO$_2$ particles (390 nm).[77] Scale bar = 200 nm in both cases.

7.6. CONCLUSION

In closing, the sundry topics described in this chapter represent only a fraction of the areas in which plasmonic nanomaterials have found application. There is a strong need for further developments in theory and computational methods to predict collective electromagnetic behavior, and also for new methods of anisotropic nanoparticle synthesis and their controlled assembly into novel plasmonic nanostructures. As nanotechnology continues to evolve, these directions will become increasingly defined by their near- or long-term potential for function and application. Chemical and bioanalytical nanosensors have already reached a remarkably advanced stage of development, with detection and analysis bordering on the single-molecule limit. Biomedical optics also promises to be a fruitful field for plasmonic applications, given the biological inertness of gold and the relative transparency of human tissue to NIR wavelengths. Lastly, the emerging area of nano-photonics is anticipated to have long-term impact on telecommunications and device integration, with possible added benefits for the first two application areas.

ACKNOWLEDGEMENTS

REFERENCES

1   Faraday, M. *Phil. Trans. Royal Soc. London* **1857**, *147*, 145.
2   Raether, H. *Surface Plasmons on Smooth and Rough Surfaces and on Gratings*; Höhler, G.: Berlin, 1988; Vol. 111.
3   Kreibig, U.; Vollmer, M. *Optical Properties of Metal Clusters*; Springer: New York, 1995; Vol. 25.
4   Kreibig, U.; Zacharias, P. *Z. Physik* **1970**, *231*, 128.
5   Yguerabide, J.; Yguerabide, E. E. *Anal. Biochem.* **1998**, *262*, 137-56.
6   Kreibig, U. *Z. Physik* **1970**, *234*, 307.
7   Chen, S.; Ingram, R. S.; Hostetler, M. J.; Pietron, J. J.; Murray, R. W.; Schaaff, T. G.; Khoury, J. T.; Alvarez, M. M.; Whetten, R. L. *Science* **1998**, *280*, 2098-101.
8   Ruppin, R. *J. Appl. Phys.* **1986**, *59*, 1355-59.
9   Underwood, S.; Mulvaney, P. *Langmuir* **1994**, *10*, 3427-30.
10 Mulvaney, P. *Langmuir* **1996**, *12*, 788-800.
11 Klar, T.; Perner, M.; Grosse, S.; von Plessen, G.; Spirkl, W.; Feldmann, J. *Phys. Rev. Lett.* **1998**, *80*, 4249-52.
12 Gersten, J. I.; Weitz, D. A.; Gramila, T. J.; Genack, A. Z. *Phys. Rev. B* **1980**, *22*, 4562-71.
13 Wokaun, A.; Gordon, J. P.; Liao, P. F. *Phys. Rev. Lett* **1982**, *48*, 957-60.
14 Wiesner, J.; Wokaun, A. *Chem. Phys. Lett.* **1989**, *157*, 569-75.
15 van der Zande, B.; Böhmer, M. R.; Fokkink, L. G. J.; Schönenberger, C. *Langmuir* **2000**, *16*, 451-58.
16 Foss, C. A., Jr.; Hornyak, G. L.; Stockert, J. A.; Martin, C. R. *J. Phys. Chem.* **1994**, *98*, 2963-71.
17 Yu, Y.-Y.; Chang, S.-S.; Lee, C.-L.; Wang, C. R. C. *J. Phys. Chem. B* **1997**, *101*, 6661-64.
18 Jana, N. R.; Gearheart, L.; Murphy, C. J. *J. Phys. Chem. B* **2001**, *105*, 4065-67.
19 Cepak, V. M.; Martin, C. R. *J. Phys. Chem. B* **1998**, *102*, 9985-90.
20 Shemilov, K. B.; Moskovits, M. *Chem. Mater.* **2000**, *12*, 250-54.
21 Nicewarner-Peña, S. R.; Freeman, R. G.; Reiss, B. D.; He, L.; Peña, D. J.; Walton, I. D.; Cromer, R.; Keating, C. D.; Natan, M. J. *Science* **2001**, *294*, 137-41.
22 Mock, J. J.; Oldenburg, S. J.; Smith, D. R.; Schultz, D. A.; Schultz, S. *Nano Lett.* **2002**, *2*, 465-69.
23 Walton, I. D.; Norton, S. M.; Balasingham, A.; He, L.; Oviso, D. F.; Gupta, D.; Raju, P. A.; Natan, M. J.; Freeman, R. G. *Anal. Chem.* **2002**, *74*, 2240-47.
24 Sönnichsen, C.; Franzl, T.; Wilk, T.; von Plessen, G.; Feldmann, J. *Phys. Rev. Lett.* **2002**, *88*, 077402.
25 Dickson, R. M.; Lyon, L. A. *J. Phys. Chem. B* **2000**, *104*, 6095-98.
26 (a) Jensen, T.; Kelly, L.; Lazarides, A.; Schatz, G. C. *J. Cluster Sci.* **1999**, *10*, 295-317. (b) Kelly, K. L.; Coronado, E.; Zhao, L. L.; Schatz, G. C. *J. Phys. Chem. B* **2003**, *107*, 668-77.

27   Mock, J. J.; Barbic, M.; Smith, D. R.; Schultz, D. A.; Schultz, S. *J. Chem. Phys.* **2002**, *116*, 6755-59.

28   (a) Hulteen, J. C.; van Duyne, R. P. *J. Vac. Sci. Technol. A* **1995**, *13*, 1553-58. (b) Hulteen, J. C.; Treichel, D. A.; Smith, M. T.; Duval, M. L.; Jensen, T. R.; van Duyne, R. P. *J. Phys. Chem. B* **1999**, *103*, 3854-63. (c) Haynes, C. L.; Van Duyne, R. P. *J. Phys. Chem. B* **2001**, *105*, 5599-611.

29   Jensen, T. R.; Malinsky, M. D.; Haynes, C. L.; Van Duyne, R. P. *J. Phys. Chem. B* **2000**, *104*, 10549-56.

30   Jin, R.; Cao, Y.; Mirkin, C. A.; Kelly, K. L.; Schatz, G. C.; Zheng, J. G. *Science* **2001**, *294*, 1901-03.

31   Sun, Y.; Xia, Y. *Science* **2002**, *298*, 2176-79.

32   Malinsky, M. D.; Kelly, K. L.; Schatz, G. C.; Van Duyne, R. P. *J. Am. Chem. Soc.* **2001**, *123*, 1471-82.

33   Haes, A. J.; van Duyne, R. P. *J. Am. Chem. Soc.* **2002**, *124*, 10596-604.

34   (a) Buckle, P. E., *et al. Biosens. Bioelectron.* **1993**, *8*, 355-58. (b) He, L.; Musick, M. D.; Nicewarner, S. R.; Salinas, F. G.; Benkovic, S. J.; Natan, M. J.; Keating, C. D. *J. Am. Chem. Soc.* **2000**, *122*, 9071-77.

35   For a comprehensive review of the early research on SERS, see: Moskovits, M. *Rev. Mod. Phys.* **1985**, *57*, 783-826.

36   (a) Kneipp, K.; Wang, Y.; Kneipp, H.; Perelman, L. T.; Itzkan, I.; Dasari, R. R.; Feld, M. S. *Phys. Rev. Lett.* **1997**, *78*, 1667-70. (b) Nie, S.; Emory, S. R. *Science* **1997**, *275*, 1102-06. (c) Xu, H. X.; Bjerneld, E. J.; Kall, M.; Borjesson, L. *Phys. Rev. Lett.* **1999**, *83*, 4357-60.

37   Garcia-Vidal, F. J.; Pendry, J. B. *Phys. Rev. Lett.* **1996**, *77*, 1163-66.

38   (a) Stockman, M. I.; Shalaev, V. M.; Moskovits, M.; Botet, R.; George, T. F. *Phys. Rev. B* **1992**, *46*, 2821-30. (b) Sarychev, A. K.; Shalaev, V. M. *Phys. Rep.* **2000**, *335*, 275-311.

39   Quinten, M. *J. Cluster Sci.* **1999**, *10*, 319-58.

40   Weitz, D. A.; Garoff, S.; Gramila, T. J. *Opt. Lett.* **1982**, *7*, 168-70.

41   Xu, H.; Aizpurua, J.; Käll, M.; Apell, P. *Phys. Rev. E* **2000**, *62*, 4318-24.

42   For some recent examples, see: (a) Ivanisevic, A.; Im, J.-H.; Lee, K.-B.; Park, S.-J.; Demers, L. M.; Watson, K. J.; Mirkin, C. A. *J. Am. Chem. Soc.* **2001**, *123*, 12424-25. (b) Lu, Y.; Yin, Y.; Li, Z.-Y.; Xia, Y. *Nano Lett.* **2002**, *2*, 785-88.

43   For a recent example, see: Maier, S. A.; Brongersma, M. L.; Kik, P. G.; Meltzer, S.; Requicha, A. A. G.; Atwater, H. A. *Adv. Mater.* **2001**, *13*, 1501-05.

44   Novak, J. P.; Feldheim, D. L. *J. Am. Chem. Soc.* **2000**, *122*, 3979-80.

45   Novak, J.; Nickerson, C.; Franzen, S.; Feldheim, D. L. *Anal. Chem.* **2001**, *73*, 5758-61.

46   Novak, J.; Brousseau, L. C.; Vance, F. W.; Johnson, R. C.; Lemon, B. I.; Hupp, J. T.; Feldheim, D. L. *J. Am. Chem. Soc.* **2000**, *122*, 12029-30.

47   (a) Collier, C. P.; Vossmeyer, T.; Heath, J. R. *Annu. Rev. Phys. Chem.* **1998**, *49*, 371-404.

48   Some recent examples include: (a) Whetten, R. L., *et al. Acc. Chem. Res.* **1999**, *32*, 397-406. (b) Pileni, M. P. *J. Phys. Chem. B* **2001**, *105*, 3358-71. (c) Lin, X. M.; Jaeger, H. M.; Sorensen, C. M.; Klabunde, K. J. *J. Phys. Chem. B* **2001**, 3353-57.

49   (a) Collier, C. P.; Saykally, R. J.; Shiang, J. J.; Henrichs, S. E.; Heath, J. R. *Science* **1997**, *277*, 1978-81. (b) Shiang, J. J.; Heath, J. R.; Collier, C. P.; Saykally, R. J. *J. Phys. Chem. B* **1998**, *102*, 3425-30.

50   Markovich, G.; Collier, C. P.; Henrichs, S. E.; Remacle, F.; Levine, R. D.; Heath, J. R. *Acc. Chem. Res.* **1999**, *32*, 415-23.

51   Collier, C. P.; Henrichs, S.; Heath, J. R. *Philo. Mag. B* **1999**, *79*, 1299-305.

52   Henrichs, S. E.; Collier, C. P.; Saykally, R. J.; Shen, Y. R.; Heath, J. R. *J. Am. Chem. Soc.* **2000**, *122*, 4077-83.

53   Parthasarathy, R.; Lin, X.-M.; Jaeger, H. M. *Phys. Rev. Lett.* **2001**, *87*, 186807.

54   (a) Remacle, F.; Levine, R. D. *J. Am. Chem. Soc.* **2000**, *122*, 4084-91. (b) Beverly, K. C.; Sampaio, J. F.; Heath, J. R. *J. Phys. Chem. B* **2002**, *106*, 2131-35.

55   Remacle, F.; Collier, C. P.; Heath, J. R.; Levine, R. D. *Chem. Phys. Lett.* **1998**, *291*, 453-58.

56   Schmid, G.; Lehnert, A.; Kreibig, U.; Adamczyk, Z.; Belouschek, P. *Z. Naturforsch.* **1990**, *45b*, 989-994.

57   (a) Giersig, M.; Mulvaney, P. *J. Phys. Chem.* **1993**, *97*, 6334-36. (b) Giersig, M.; Mulvaney, P. *Langmuir* **1993**, *9*, 3408-13.

58   (a) Wei, A.; Kim, B.; Pusztay, S. V.; Tripp, S. L.; Balasubramanian, R. *J. Inclusion Phenom. Macrocyclic Chem.* **2001**, *41*, 83-86.

59   Balasubramanian, R.; Kim, B.; Tripp, S. L.; Wang, X.; Lieberman, M.; Wei, A. *Langmuir* **2002**, *18*, 3676-81.

60   Kim, B.; Tripp, S. L.; Wei, A. *J. Am. Chem. Soc.* **2001**, *123*, 7955-56.

61   Wei, A.; Kim, B.; Sadtler, B.; Tripp, S. L. *ChemPhysChem* **2001**, *2*, 743-45.

62   (a) Aravind, P. K.; Nitzan, A.; Metiu, H. *Surface Sci.* **1981**, *110*, 189-204. (b) Wang, D.-S.; Kerker, M. *Phys. Rev. B* **1981**, *24*, 1777-90. (c) Liver, N.; Nitzan, A.; Gersten, J. I. *Chem. Phys. Lett.* **1984**, *111*, 449-54. (d) Zeman, E. J.; Schatz, G. C. *J. Phys. Chem.* **1987**, *91*, 634-43.

63   (a) Blatchford, C. G.; Campbell, J. R.; Creighton, J. A. *Surface Sci.* **1982**, *120*, 435-55. (b) Kneipp, K.; Dasari, R. R.; Wang, Y. *Appl. Spectrosc.* **1994**, *48*, 951-55. (c) Maxwell, D. J.; Emory, S. R.; Nie, S. *Chem. Mater.* **2001**, *13*, 1082-88.

64   Genov, D.; Wei, A.; Sarychev, A. K.; Shalaev, V. M. Unpublished results.

65   Joannopoulos, J. D.; Meade, R. D.; Winn, J. N. *Photonic Crystals: Molding the Flow of Light;* Princeton University Press: Princeton, 1995.

66   Braun, P. B.; Wiltzius, P. *Curr. Op. Colloid Interface Sci.* **2002**, *7*, 116-23.

67   Moroz, A. *Phys. Rev. Lett.* **1999**, *83*, 5274-77.

68   Zhang, W. Y.; Lei, X. Y.; Wang, Z. L.; Zheng, D. G.; Tam, W. Y.; Chan, C. T.; Sheng, P. *Phys. Rev. Lett.* **2000**, *84*, 2853-56.

69   (a) Oldenburg, S. J.; Averitt, R. D.; Westcott, S. L.; Halas, N. J. *Chem. Phys. Lett.* **1998**, *288*, 243-47. (b) Jackson, J. B.; Halas, N. J. *J. Phys. Chem. B* **2001**, *105*, 2743-46.

70   Oldenburg, S. J.; Jackson, J. B.; Westcott, S. L.; Halas, N. J. *Appl. Phys. Lett.* **1999**, *75*, 2897-99.

71   Graf, C.; van Blaaderen, A. *Langmuir* **2002**, *18*, 524-34.

72   Shipway, A. N.; Katz, E.; Willner, I. *ChemPhysChem* **2000**, *1*, 18-52.

73   Elghanian, R.; Storhoff, J. J.; Mucic, R. C.; Letsinger, R. L.; Mirkin, C. A. *Science* **1997**, *277*, 1078-81.

74   Storhoff, J. J.; Lazarides, A. A.; Mucic, R. C.; Mirkin, C. A.; Letsinger, R. L.; Schatz, G. C. *J. Am. Chem. Soc.* **2000**, *122*, 4640-4650.

75   Chumanov, G.; Sokolov, K.; Gregory, B. W.; Cotton, T. M. *J. Phys. Chem.* **1995**, *99*, 9466-71.

76   (a) Freeman, R. G., *et al. Science* **1995**, *267*, 1629-32. (b) Grabar, K. C.; Freeman, R. G.; Hommer, M. B.; Natan, M. J. *Anal. Chem.* **1995**, *67*, 735-43. (c) Grabar, K. C., *et al. J. Am. Chem. Soc.* **1996**, *118*, 1148-53.

77   Sadtler, B.; Wei, A. *Chem. Commun.* **2002**, 1604-05.

8

Nanoparticle Polymer Ensembles

Amitav Sanyal, Tyler B. Norsten and Vincent M. Rotello*
Department of Chemistry, University of Massachusetts, Amherst MA 01003, U.S.A.

8.1. INTRODUCTION

   Self-assembly of nanoparticles mediated by polymers provides access to stabilized metal and semiconductor nanocomposites as well as allows for the fabrication of new structured nanoscale materials. Several attributes of the individual building blocks such as the size and shape of individual metal clusters, composition of the monolayer, and functional groups on the polymers allows control over the properties of these nanocomposites. Additional control over the structure and morphology of such nanocomposites can be induced by changes in the polymer structure. Such construction of composite materials using the assembly of nanoscopic building blocks or the 'bottom-up' approach provides a methodology complementary to 'top-down' lithographic methods. The 'bottom-up' approach provides access to structures smaller and with greater 3-dimensional control than is possible through sophisticated lithographic techniques such as electron-beam lithography.[1] Successful integration of these two approaches is a challenge that needs to be addressed. Such multi-scale engineering would allow fabrication of intricate functional devices with atomic level structural control that manifests and spans itself into the macroscopic world and thus could provide a successful integration of the two approaches.
   The present chapter will focus on selected examples, which we feel highlight the available methodologies currently employed for synthesis of polymer-based nanoparticle composites. This chapter is not intended to be an

exhaustive review of the literature, where necessary readers are directed to articles and reviews pertinent to the area. Keeping in mind that interest in developing nanostructured catalysts geared a lot of the initial work in this field an entire section is devoted to the design of catalytic nanocomposite based catalysts, while the remaining sections describes the use of polymers to assemble nanoparticles into various interesting and potentially useful architectures.

8.2. ASSEMBLY OF POLYMER-NANOPARTICLE COMPOSITE MATERIALS

Polymer matrices embedded with metal and semiconductor nanoparticles provide materials that possess the unique properties arising from the nanoscopic size and shapes of the metal clusters. These materials also possess the processing and handling advantages of bulk materials.

Traditionally polymer-nanoparticle composites have been prepared by *in situ* generation of metal nanoclusters by chemical reduction of a metal salt contained within a polymer matrix (Figure 8.1). The polymer matrix not only acts as a template for their synthesis but also imparts the necessary stability by providing a barrier against agglomeration of the metallic nanoparticles formed during and after the reduction process. A variety of different polymers (homopolymers, block copolymers and dendrimers) have been used to create ordered nanocomposite materials for various applications (Figure 8.1).

A different approach towards polymer-nanoparticle composites involves the assembly of polymer scaffolds with preformed Monolayer Protected Clusters (MPCs) (Figure 8.2). The surface monolayer prevents the metal clusters from agglomerating and provides ease of handling and processing. Choice of appropriate ligands on the monolayer and functional groups on the polymer provides the required interfacial interactions between the monolayer functional groups and the polymer backbone which allows MPCs to be readily dispersed into polymer matrices. Over the past several years others and we have demonstrated that the latter approach offers an attractive and versatile alternative approach towards the fabrication of new composite materials.
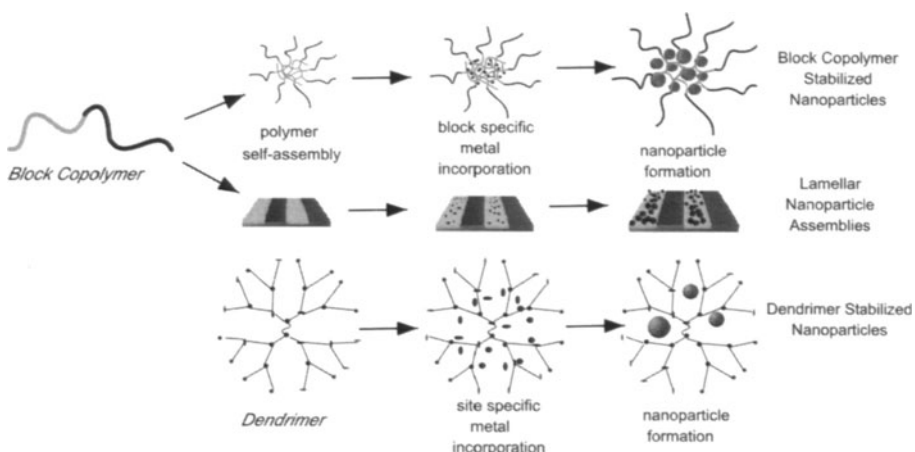
FIGURE 8.1. *In situ* formation of nanoparticles within polymer matrices.
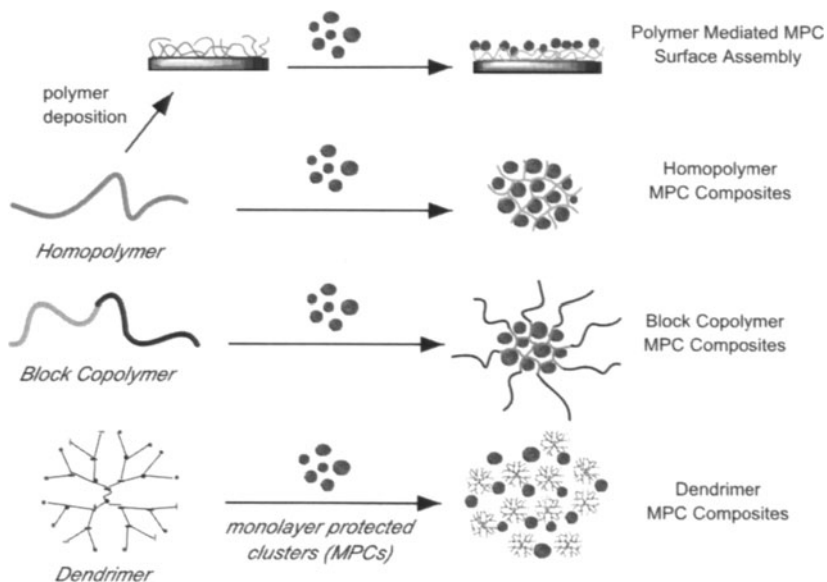
FIGURE 8.2. Polymer mediated assembly of monolayer-protected clusters (MPCs) into various ordered structures.

8.3.   NANOPARTICLE BUILDING BLOCKS AND
POLYMER SCAFFOLDS

8.3.1. NANOPARTICLE BUILDING BLOCKS

Typically polymer-nanoparticle composites have been synthesized by following either of the two strategies presented above. Although the most widely used route generally involves using the polymer as both a template for the formation of nanoparticles as well as a steric stabilizer to prevent agglomeration after nanoparticle formation, easy availability of several stabilized MPCs in recent years is attracting attention to the assembly strategy involving these preformed nanoparticles. Alkanethiolate stabilized gold clusters synthesized by the solution-phase method developed by Brust and Schiffrin (Figure 8.3),[2] has been widely used in the latter approach. In the Brust-Schiffrin procedure gold salt is chemically reduced by a hydride reducing agent in the presence of thiol capping ligands to obtain the desired monolayer protected nanoparticles. MPCs with a wide range of core sizes (1.5 - 8 nm) can be prepared by varying the stoichiometry of the metal salt to capping ligand.
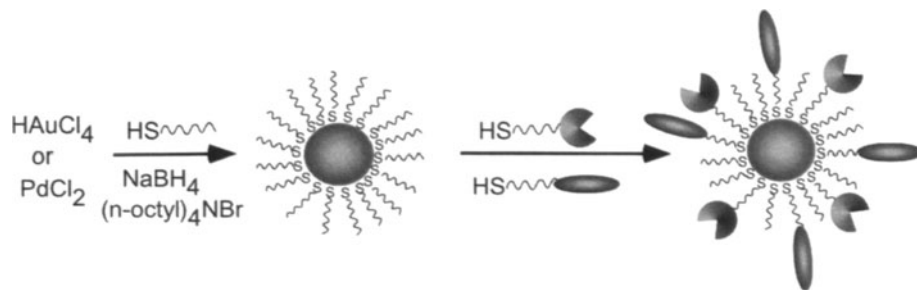

FIGURE 8.3. MPC synthesis using the Brust and Schiffrin procedure, followed by MMPC synthesis via the Murray place exchange reaction.

Modification of the monolayer using a simple ligand place-exchange reaction, where new incoming thiol ligands displace monolayer thiols on the parent MPC, opens access to a wide variety of functionalized Mixed Monolayer Protected Clusters (MMPCs).[3] Such ligand place-exchange reactions allow one to design nanoparticles with functional groups complementary to groups on the polymer strands. This provides efficient incorporation of the MMPCs into the polymeric matrix by maximizing the interfacial interactions between the building blocks.

Gold MPCs have emerged as excellent components or building blocks for the fabrication of nanoscale architectures since they can be synthesized in

various sizes with narrow polydispersities. The alkanethiolate monolayer not only provides the required stability and ease of handling (i.e. dissolution into various solvents and other matrices) without significant degradation but is also easily characterized using standard solution-phase techniques such as Nuclear Magnetic Resonance (NMR), Infrared (IR) and UV-Vis spectroscopy.[4]

Although a variety of other metallic, bimetallic and semiconductor nanoparticles other than gold and silver are available,[5] the conditions of their formation are quite harsh, which substantially reduces the variety of functionalities that can be incorporated into the capping monolayer. This limits the ability for these nanoparticles to be organized into extended ordered structures. Efforts focused on developing new procedures and modifying existing procedures to permit a wider variety of functionalities onto these nanoparticles are emerging continuously.

In addition to the functional aspects, the regular shape and size of the MPCs makes them excellent 'building blocks' for the fabrication of ordered structures in the mesoscopic size range. Utilization of such building blocks in a programmed self-assembly strategy would provide part of the solution to the problem of multiscale fabrication as discussed earlier. Much research has focused upon the chemical behavior and physical properties of these nanoparticles, however, their successful incorporation into desired functional ensemble is yet in its infancy.

8.3.2. POLYMER SCAFFOLDS

Polymers are large macromolecules comprised of multiple repeat units in a linear array (e.g. homopolymers and block copolymers) or a branched fashion, as is the case with star polymers. Recent progress in synthetic polymer science, especially in the area of 'living' polymerization techniques, has provided access to diblock and triblock copolymers with a wide range of functionality and narrow polydispersity. The synthetic methodologies for the synthesis of the polymers employed in various examples presented will not be covered here since it is not the focus of this chapter, but several excellent reviews are available.[6]

Block copolymers represent an interesting class of materials due to their unique ability to form microphase-separated domains. Diblock copolymers where the two blocks are chemically distinct can undergo microphase separation due to the immiscibility of the different blocks with each other or with a solvent. Various morphologies such as spheres, cylinders and lamellae are obtainable just by controlling the molecular weights and volume fractions of the individual blocks. Several examples highlighting the utilization of such self assembled polymeric templates for the incorporation

of nanoparticles or their precursor metal salts into specific polymer blocks will be discussed later in the chapter.

Dendrimers are hyperbranched molecules that possess repeat units that cascade outward from a central core.[7] A dendrimer molecule is made up of three components: a core, repeating branches, and peripheral groups. The 'generation' or the size of the dendrimer largely defines its shape. Higher generation dendrimers are more spherical in shape with large inner voids, whereas lower generation dendrimers are flat. The peripheral groups can be tailored to provide control over properties such as adhesion and solubility. Synthetic methodologies employed for making dendrimers allows precise control over the location of the functional groups. While on one hand dendrimers with appropriate internal functional groups can be used to sequester precursor metal salts or nanoparticles and thus act as templates and particle stabilizers, the higher generation dendrimers with appropriate peripheral groups can be used as building blocks to synthesize nanocomposites with precise control over interparticle distances between MMPCs.

Recent focus has also been on the use of biopolymers such as DNA to assemble and organize nanoparticles. Since the degree of non-covalent complementarity between these biopolymers can be readily controlled they are attractive scaffolds. The self-assembly of nanoparticle-biopolymer interactions is not covered here, however several recent reports exemplify this type of assembly strategy which show promise in the area of biosensor development.[8]

8.4. POLYMER-NANOPARTICLE ASSEMBLIES FOR CATALYIC APPLICATIONS

Methodologies for creation of stable nanoparticle assemblies possessing an open, porous framework are vital for the design of efficient catalysts. Nanoparticles possess the high surface area to volume ratio required for the efficient heterogeneous catalysts. Noble metals such as palladium, platinum etc. are widely used for catalysis in numerous important chemical transformations, including hydrogenation, oxidation, and Heck coupling.[9] Increased stability, improved processability, recyclability and solubility in a variety of organic solvents are among the benefits of immobilizing metal nanoparticles in polymeric matrices. The choice of polymeric matrix depends upon the type of metal ion precursors needed to be sequestered, compatibility with the reaction conditions leading to nanoparticle formation as well as the catalytic process. It has also been demonstrated that it is

possible to fine tune the reactivity and selectivity of such nanocomposites by judicious choice of the polymer.

Nanoparticle-based palladium catalysts within the micelles of amphiphilic block copolymers have been studied extensively by Antonietti and coworkers.[10] They utilized a poly-4-vinylpyridine-*b*-polystyrene (P4VP-*b*-PS) block copolymer and Pd(OAc)$_2$ as the palladium source for the preparation of metal colloids (Figure 8.4). Colloidal morphologies can be obtained in a controlled fashion by careful choice of the method of reduction. A "raspberry morphology" is created with rapid reduction *versus* a "cherry morphology" with a slower reduction rate.[11] Colloidal aggregates with the "raspberry morphology", where the particle size is smaller demonstrated excellent catalytic activity in the carbon-carbon bond forming Heck reaction. The polymer bound Pd nanoparticle catalyst showed similar reactivities but higher stabilities as compared to other widely used phosphine ligand/Pd complexes.
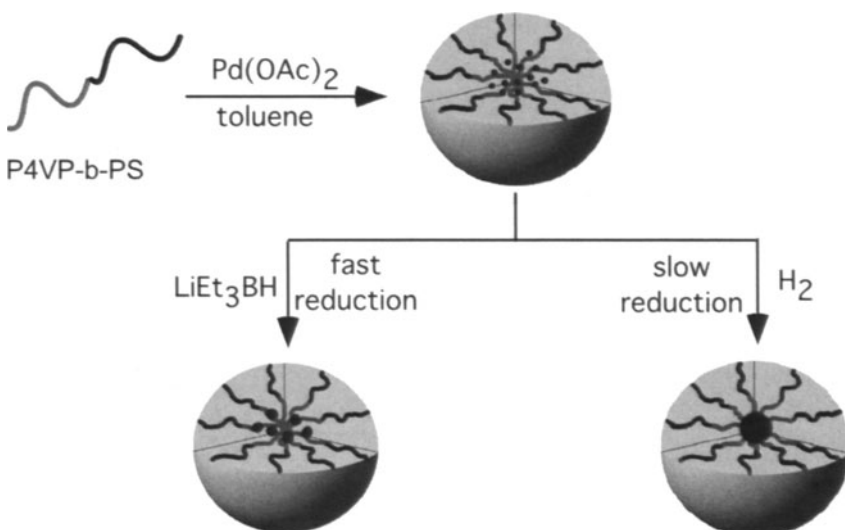
FIGURE 8.4. P4VP-*b*- PS block copolymer micelles for the preparation of palladium colloids.

Recent reports by El-Sayed and coworkers have shown that palladium nanoparticles stabilized by poly(N-vinyl-2-pyrrolidone) (PVP) can be used effectively as catalysts in aqueous media.[12] They obtained good conversions for the Suzuki coupling reaction using 40% ethanol in water as a solvent under reflux. However improvement in catalyst stability is necessary for the recyclability as precipitation of the palladium metal occurs towards the end of the reaction. Analysis of size distribution of the nanoparticles before and after the reaction using TEM revealed that during the course of the reaction Ostwald ripening leads to increase in the size of the nanoparticles which

precipitate out of solution. As a result, the effective catalyst concentration in solution decreases that leads to diminished catalytic activity in the subsequent cycle.[13]

Liu and coworkers have used cross-linked nanospheres prepared using triblock copolymer for encapsulating Pd nanoparticles.[14] Micelles of polyisoprene-*b*-poly(2-cinnamoyloxyethyl methacrylate)-*b*-poly(*tert*-butyl acrylate) (PI-*b*-PCEMA-*b*-P*t*BA) formed in 65% hexane/THF mixture were photocrosslinked. The resulting nanospheres consisted of PI coronas, crosslinked PCEMA shells and P*t*BA cores. Hydroxylation of the terminal isoprene units provided water-dispersibility and subsequent hydrolysis of the PtBA groups provided poly(acrylic acid) (PAA) cores capable of complexing PdCl$_2$. Loading of PdCl$_2$ into the acrylic acid core followed by reduction using hydrazine yielded polymer stabilized palladium nanoparticles (Figure 8.5). These nanosphere-based catalysts were used to study hydrogenation reactions of tetraethylallylammonium bromide, vinylacetic acid, methylmethacrylate and ethylene glycol dimethylacrylate.
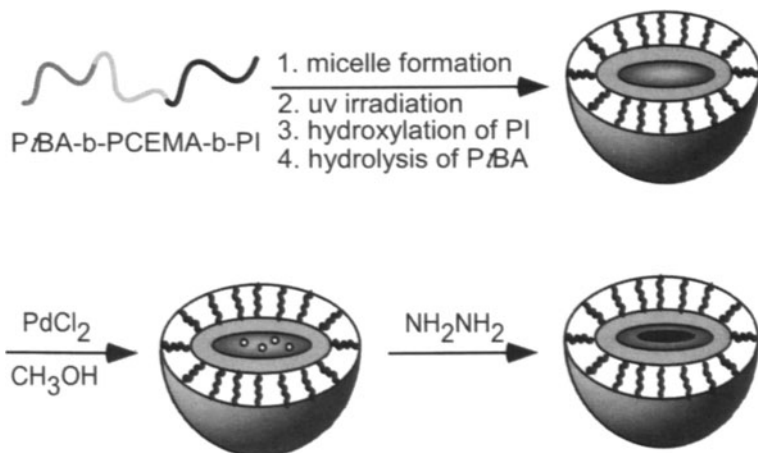
FIGURE 8.5. Triblock copolymer nanospheres encapsulating Pd nanoparticles.

Catalytic activity of these palladium containing nanospheres can be tuned by changing the pH since the core of the nanospheres are pH responsive. The charged core of the nanospheres regulates the transport of charged substrates into the nanospheres depending on the pH. Thus, when the reaction is carried out at pH=10, an increase in the rate of hydrogenation of the positively charged tetraethylallylammonium bromide is observed. Also as expected, a decrease in rate of hydrogenation of vinyl acetic acid is seen under the same conditions. The encapsulated catalyst has slightly lower reaction rates

compared to palladium black due to reduced mass transport of the reactants into the catalyst as a result of the outer polymer shells.

Mecking and coworkers reported the use of amphiphilic hyperbranched poly(glycerols) to prepare catalytically active and stable palladium colloids.[15] Precursor palladium salts (e.g. $PdCl_2$, $Pd(OAc)_2$) solublized by the hyperbranched polymer in nonpolar solvents such as toluene and chloroform was slowly reduced using hydrogen to yield stable colloidal palladium. Hydrogenation of cyclohexene using the polyglycerol supported palladium colloid proceeded with high turnover frequency (700 turnovers h^{-1}). The authors suggest that the weakly coordinating polyglycerols can avoid any risk of ligand poisoning that may result in the nitrogen-based polymeric systems due to stronger coordination between the polymer and the nanoparticle surface. Furthermore, no precipitation of palladium colloid and no significant decrease in rate of subsequent reactions using the recycled catalyst were observed.

Although the polymer casing provides the required stability and solubility to the catalytically active nanoparticles in a given reaction medium, this also tends to be a drawback of polymer supported catalysts because the substrates must find their way through the stabilizing polymer shell to reach the active metal surface. This ultimately results in inefficient mass transport mechanisms for these types of catalysts thus lowering their turnover capacity.

As an alternative to the polymer stabilized nanoparticle catalysts described above, we recently reported the fabrication of porous catalyst systems using directed self-assembly of nanoparticles. Macromolecular assemblies can be obtained using mixed monolayer protected clusters (MMPCs) of catalytically active metals as building blocks in the presence of a suitable polymeric mediator. Removal of the stabilizing polymers and monolayer ligands through calcination provides materials with improved access to the catalytically active sites.

Preliminary studies highlighting the concept of self-assembly based creation of new multi-component materials was reported for a polymer mediated three-component system. The nanocomposite material was obtained by employing carboxylic acid functionalized gold and SiO_2 nanoparticles, and an amine-functionalized polystyrene random copolymer.[16] Electrostatic attraction between the basic polymer and the acidic nanoparticles results in the formation of the nanocomposite material. Addition of the polymer to a mixture of the two nanoparticles results in well-integrated nanocomposites. On the other hand, mixing of one of the MPCs with the polymer followed by addition of the other nanoparticle results in segregated cluster where the nanoparticles added later in the assembly process are exposed on the surface of the resulting final aggregate.

Fabrication of high-efficiency palladium catalysts was investigated using the above assembly strategy.[17] Catalytically active Pd-COOH nanoparticles were assembled on a preformed SiO_2-COOH/poly-NH_2 scaffold. High exposure of the catalytically active metal on the surface of the final aggregate is obtained as a result of assembly strategy. A highly porous Pd-SiO_2 composite free of any polymer and organic monolayer is obtained upon calcination of the three-component aggregate (Figure 8.6).
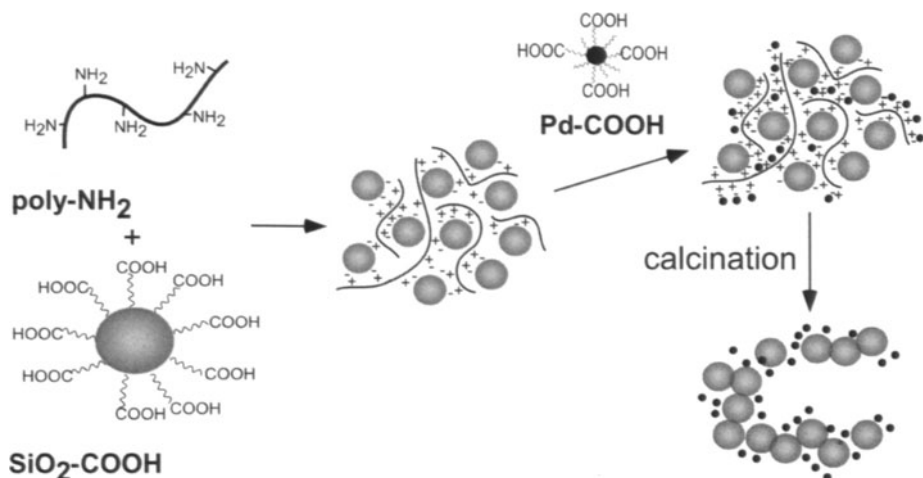

FIGURE 8.6. Three component self-assembly strategy for the formation of SiO_2 stabilized Pd nanoparticle catalyst.

Hydrogenation of 9-decen-1-ol was investigated using the calcinated aggregates. Excellent turnover frequencies (TOF) (10,100 h^{-1} for the 1:1:1 w/w/w composition of Pd/Si/polymer, respectively) were observed for the new catalyst system, compared to the 7200 h^{-1} found under the same conditions using the commercial 1% Pd/C catalyst (Figure 8.7). More importantly, the same catalyst system also proved highly effective for Heck coupling reactions of electronically activated bromoarenes and styrene or methyl acrylate at very low catalyst loadings (0.045 mol% of Pd).
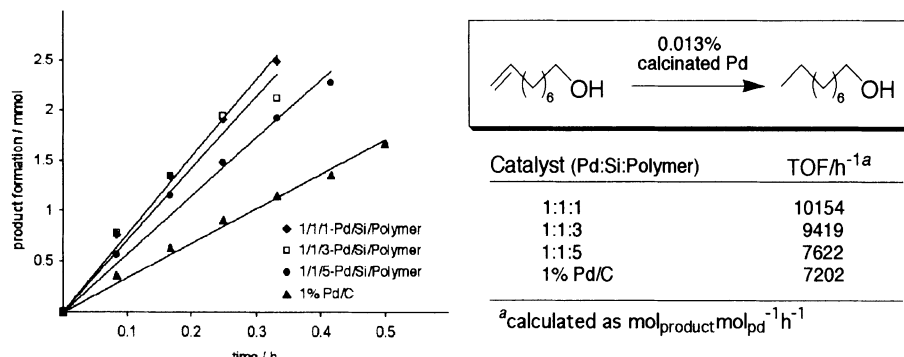
FIGURE 8.7. Relative rates of reaction and turnover frequencies in hydrogenation reaction with different polymer ratios.

Several advantages of nanoparticle based catalyst systems over the commonly used homogeneous Pd-catalysts make them attractive candidates. Typically no activation by additional ligands such as phosphines is required. Furthermore, heterogeneous nanoparticle catalysts are easier to separate from their reaction mixtures and to recycle them without too much compromise in their catalytic activity. The combination of these attributes makes them attractive catalysts for use in various industrial processes.

8.5. FABRICATION OF POLYMER-MEDIATED ORGANIZED NANOPARTICLE ASSEMBLIES

The ability to be able to control the assembly of nanoparticles into discrete organized assemblies is of broad interest in the field of nanotechnology.[18] Distinctive magnetic, electronic and optical behaviors displayed by complex, three-dimensional nanocomposites are highly dependent on the size of the nanoparticles as well as the distance between them. A valuable method in achieving controlled assemblies of nanoparticles is via utilization of diblock copolymers. Depending on the monomer choice, two chemically discrete fragments are present in diblock copolymers. Due to microphase separation, these two segments can arrange into a variety of structural morphologies, which can be controlled by the adjustment of the individual block lengths.[19] The choice of the blocks affects the self-assembly of the copolymer to form patterns which will accommodate metallic nanoparticles via either complexation of the specific polymeric domains with the nanoparticle or employment of selective wetting of the metal clusters.

Eisenberg and coworkers demonstrated that by controlling the size of micro compartments in copolymers it is possible to do a size-controlled synthesis of the metal nanoparticle clusters. In one of the earlier examples,

Eisenberg and coworkers synthesized metal nanoparticle clusters using ionomers as templates.[20] They have investigated the morphology of the ionomers with ionic groups positioned at different lengths on the styrene-based backbone. The choice of ionic monomer controlled the size of the ionic microdomains in these copolymers. By changing the ionic block length, the radii of the ionic core could be altered between 15-100 nm. The increase in the side chain length resulted in larger and more organized ionic aggregates. This handle on the ionic aggregate size was utilized for controlled nanocluster synthesis.
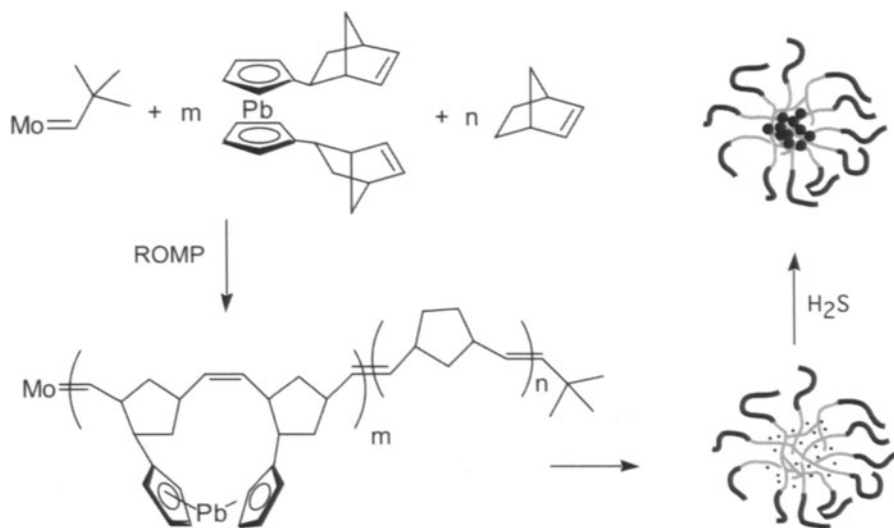
FIGURE 8.8. Nanoparticle-polymer composite synthesis via Schrock's organometallic diblock copolymer.

Schrock and coworkers demonstrated that microphase separated domains in organometallic copolymers act as nanosize reactors for the synthesis of small semiconductor nanoparticles.[21] They synthesized the block copolymers via ring opening metathesis polymerization of norbornene and a Pb coordinated norbornene polymer. Upon treatment with H_2S, PbS clusters with a diameter of 2-4 nm were formed (Figure 8.8).

The same group later utilized a diblock copolymer made from of methyl-tetracyclododecene (MTD) and phosphine functionalized norbornene to create silver containing spherical microdomains. Silver nanoparticle precursors were formed via complexation of (Ag(Hfacac)(COD)) and the phosphine ligands within the core of the solvent stabilized micelles.[22] Heating a solvent cast film comprised of the metal salt containing diblock

and MTD homopolymer to 90 °C for 5 days in water resulted in the formation of single metal clusters within the original microdomains.

The effective steric stabilization ability of poly[dimethylsiloxane-b-(3-cyanopropyl)methylsiloxane-b-dimethylsiloxane] (PDMS-PCPMS-PDMS) triblock copolymers for colloidal cobalt particles has been demonstrated by Riffle and coworkers.[23] They utilized the block copolymer micelles as reaction sites for cobalt carbonyl thermolysis reaction. The PCPMS blocks orient toward the interior of the micelle while the outer PDMS blocks provides stability to the micelles. Introduction of $Co_2(CO)_8$ in the copolymer followed by heating resulted in cobalt nanoparticles at the interior of these micelles. The size of the nanoparticles could be controlled via adjusting the cobalt carbonyl to copolymer ratio.

Contrary to the approach of utilizing the polymer as the template and growing the nanoparticles in isolated compartments, we have taken a 'bricks and mortar' approach. This self-assembly strategy is composed of recognition element functionalized nanoparticles as the 'bricks' and the complementary recognition element bearing polymer as the 'mortar'. Organized discrete assemblies can be created via this methodology and then be transferred onto surfaces to be used to create devices and sensors in the 2 - 40 nm range. The recognition element on the nanoparticle is the thymine functionality whereas the complimentary recognition element on the polystyrene based polymer is the diaminotriazine with the specific three-point hydrogen bonding between them holding the structure together (Figure 8.9).

Addition of a triazine-substituted random copolymer (poly-triaz) to concentrated solution of thymine-functionalized gold nanoparticles (Au-thy) in non-polar solvents, results in the formation of insoluble aggregates.[24] The role of specific hydrogen-bonding interactions in the formation of polytriaz/Au-thy aggregates were proven by the control experiment where the Au-thy was replaced by the methylated thymine (Me Au-thy). Usage of nanoparticles bearing the methylated thymine ligands did not result in any precipitation since the hydrogen bonding is completely disrupted. The TEM images of the THF-soluble fraction of the poly-triaz/Au-thy precipitate revealed the formation of large spherical clusters approximately 100 nm in diameter comprised of 3000-7000 individual gold particles (Figure 8.10). Small-Angle X-ray Scattering (SAXS) analysis of the aggregates indicates that the nanoparticles are regularly dispersed with a separation of 6.4 ± 0.3 nm (center to center).

Well-defined size and morphology of the aggregates can be achieved via thermal control of the assembly process. With the decrease in the assembly process temperature, the size of the nanoparticle assembly formed increases. Highly size-dispersed networks of spherical aggregates were obtained at by

performing the assembly at 10 °C, while performing the aggregation at -20 °C yields even larger, individual aggregates. These aggregates are 5-10 times larger than the aggregates formed at 23 °C, ranging 0.5-1 μm in diameter and comprising of 0.6-5.0 million (!) individual Au-thy nanoparticles, and are among the most complex synthetic self-assembled structures ever constructed.
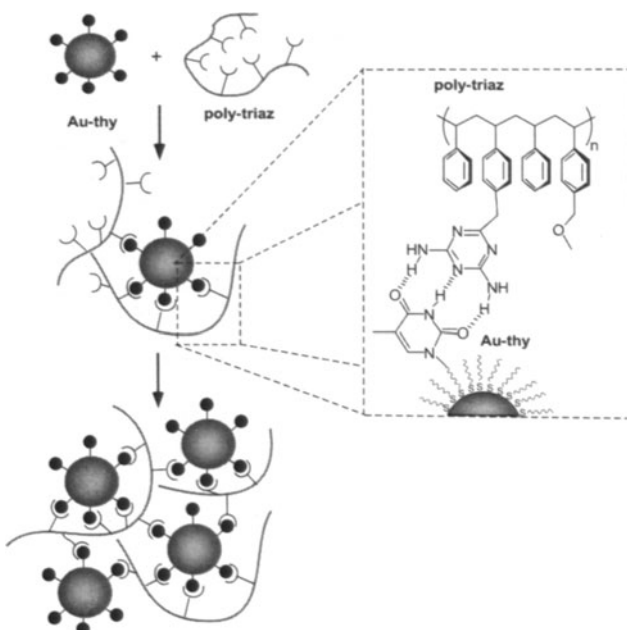

FIGURE 8.9. Three-point hydrogen bonding recognition between thymine-capped gold nanoparticles and diaminotriazine-functionalized polymer leads to extended network formation.
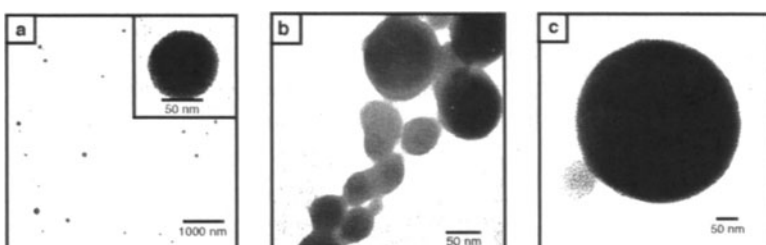
FIGURE 8.10. (a) TEM of Au-thy/poly-triaz aggregates formed at 23 °C. Inset: representative self-assembled nanoparticle-polymer microsphere. (b) TEM of Au-thy/poly-triaz aggregate network formed at 10 °C. (c) TEM of Au-thy/poly-triaz spherical aggregate formed at -20 °C.

Utilization of the gold nanoparticles as building blocks allows tuning the interfacial interactions between the nanoparticle and the polymer by

introducing additional ligands into the monolayer using a Murray displacement reaction. Similarly the polymeric backbone can also be readily functionalized with additional functional groups apart from the recognition units. In a follow up study secondary interactions such as π stacking were utilized in combination with the primary three-point hydrogen bonding interaction to provide additional control on the overall assembly process.[25] Various combinations of nanoparticle and polymer consisting of either an electron-rich anthracene moiety or an electron poor napthalimide moiety in conjunction with a primary hydrogen-bonding element were synthesized. The study revealed that weaker secondary interactions play an important role in the aggregate formation and the overall aggregate morphology is manifested by supramolecular events occurring at the nanoparticle-polymer interface.

Limited control over the size and the morphology of the aggregates was possible by carrying out the assembly at different temperatures. We rationalized that perhaps control over the aggregation process could be achieved by employing a diblock copolymer where one of the blocks is functionalized with the recognition units and the second block is unfunctionalized.[26] In this approach the functionalized block will drive the assembly process, while the inert second block will prevent extensive network formation. The overall core size should depend primarily on the length of the functionalized block capable of incorporating nanoparticle, (Figure 8.11).
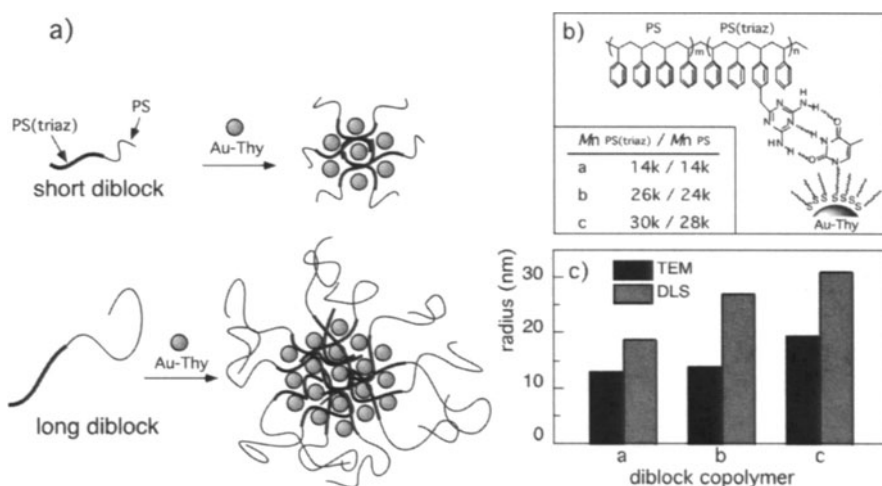

FIGURE 8.11. (a) Schematic representation of block lengths controlling nanoparticle core and corona size. (b) Different length PS(triaz)-*b*-PS polymers assembled with Au-thy. (c) Observed nanoparticle core size by TEM compared to hydrodynamic radius of the micelles observed by DLS.

Control of aggregate size using diblock copolymers was demonstrated by employing three symmetric diblock copolymers (Figure 8.11b) with varying total lengths. TEM analysis of the aggregates obtained on combining Au-thy with the various polymers (a-c) revealed increasing core sizes of 13.2 ± 1.3 nm, 13.9 ± 1.2 nm and 19.4 ± 1.8 nm, respectively (Figure 8.12). Dynamic Light Scattering (DLS) experiments reveal the effective hydrodynamic radii R_h (core and polystyrene corona) to be 18.7, 27.1 and 31.1 nm for the polymers (a-c), respectively. Comparison of the core size to the overall aggregate size observed by DLS suggests that the polymer segments within the core are extended as compared to the unfunctionalized polystyrene block lying in the exterior (Figure 8.11c).
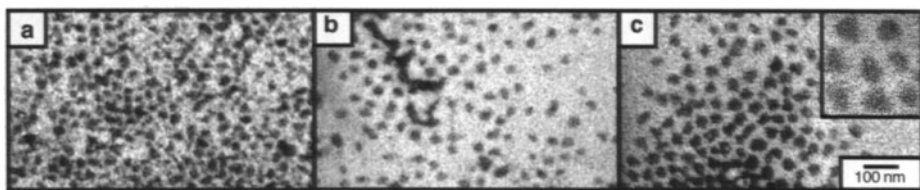
Figure 8.12. Increase in core size of the aggregates with increasing functionalized block length as observed using TEM

8.6. ORGANIZED POLYMER-NANOPARTICLE ASSEMBLIES ON SURFACES

As seen in earlier examples, polymers have been used to ordered nanoparticle arrays and assemble nanoparticles into discrete ordered entities extending into the micro-scale realm. In some applications, the controlled ordering at this level may be adequate; nevertheless higher degrees of ordering is required for functional device applications such as nanoelectronics or optical or magnetic storage media. It is essential to fabricate not only highly *ordered* arrays but arrays that are also highly *extended* over vast distances for fabrication of such devices (nm→cm).

Möller and coworkers have utilized micelles made of diblock copolymers of polystyrene-polyvinylpyridine (PS-*b*-PVP)[27] and polystyrene-polyethylene oxide (PS-*b*-PEO)[28] for synthesis of several metallic and semiconductor nanoparticles. The pyridine units within the micellar core of PS-*b*-PVP can uptake transition metal salts due to hard acid/soft base interactions (Figure 8.13). Size-controlled synthesis of gold nanoparticles can be achieved by controlling the amount of the precursor salt. Upon transfer onto a flat surface the micelles containing the gold salt assemble into

a quasihexagonal packing arrangement. Subsequent treatment with oxygen plasma completely removes all of the polymeric material yielding highly ordered bare gold nanoclusters.[29] Simply changing the amount of metal salt within the micelle allows one to obtain cluster sizes from 1 to 15 nm, whereas changing the length of the blocks allows one to adjust the interparticle distances from 30 to 140 nm.
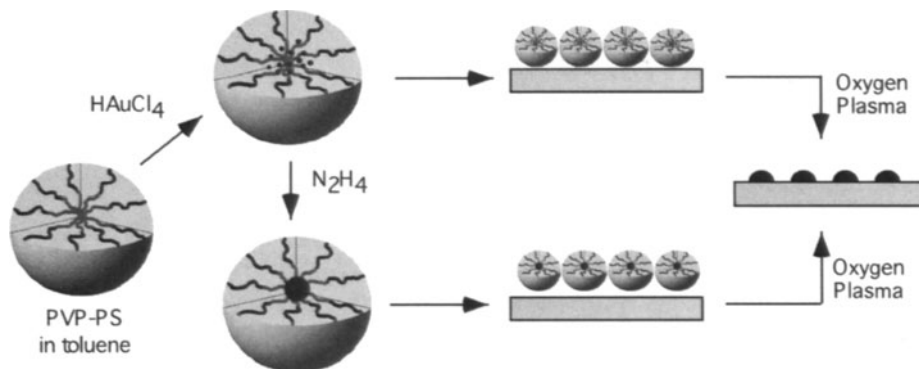

FIGURE 8.13. Deposition of nanoparticles in a block copolymer micelle onto a surface for creation of an ordered array of bare nanoparticles.

Schmid and coworkers were able to assemble [Au$_{55}$(Ph$_2$PC$_6$H$_4$SO$_3$H)$_{12}$Cl$_6$] clusters onto poly(ethyleneimine) (PEI) covered surfaces using an approach similar to Decher's[30] layer-by-layer (LBL) assembly of oppositely charged polyionophores (Figure 8.14).[31] Along with hexagonally close packed arrangement of the clusters ordered on the surface, they found large domains of nanoparticles with an unusual cubic lattice structure. The authors suggest that use of PEI with a low M_w (60,000) allows the polymer to uncoil on the surface creating a more ordered polymer template. The nanoparticles are packed immediately next to one another since there is no hindrance from the polymer. Several examples of LBL assemblies of polymers with gold,[32] semiconductor[33] or magnetic nanoparticles,[34] have also been reported.

Using phosphine-functionalized norbornene block copolymers Schrock and coworkers were able to form ordered surface assemblies of silver and gold nanoparticles.[35] The phosphine-containing block of the copolymer can selectively coordinate to gold and silver coordination complexes in benzene. Lamellar structures were obtained from films cast from the silver coordinated block copolymers, while those cast from the gold solutions gave cylinders. Thermally annealing the films yielded striped domains of silver nanoparticles (2-10 nm in diameter) and spherical domains of gold nanoparticles (1.5-4 nm). Long range ordering was observed in both cases and the interdomain spacing correlated to the length of the unfunctionalized

block. Incorporation of zinc and cadmium into similar norbornene block copolymers leads to the formation of metal sulfides within specific lamellar block copolymer microdomains.[36]
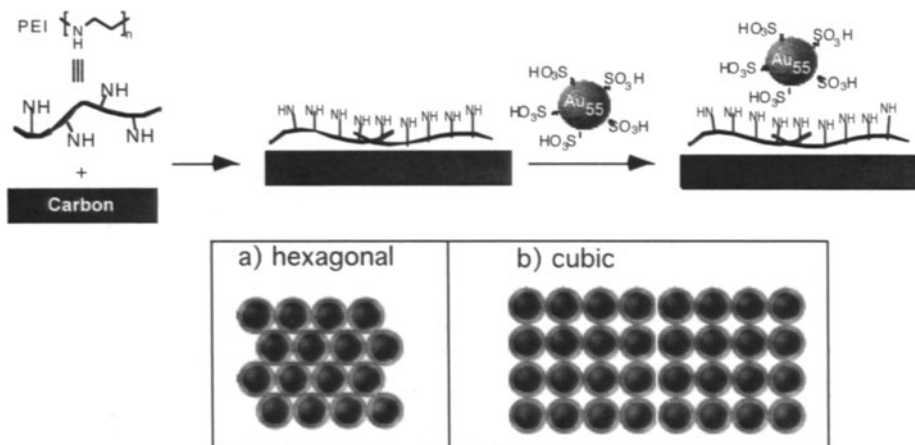

FIGURE 8.14. Poly(ethyleneimine) mediated assembly of sulfonated gold nanoparticles arranging into: (a) hexagonal and (b) cubic packed formations.

Lopes and Jaeger demonstrated that ultrathin films of microphase separated diblock copolymers could be utilized as templates for the incorporation of metal nanoclusters with near complete selectivity in the desired domain.[37] Thin films containing alternating domains of PS and PMMA obtain from a PS-*b*-PMMA diblock copolymer were exposed to metal vapors (Figure 8.15). The PS domains preferentially absorb Au and Ag, while the PMMA domains show preference for In, Pb, Sn, and Bi. Nearly perfect selectivity is observed for the adsorption of Ag in the PS domain. In the cases of partial uptakes, annealing the system above the glass transition temperature of the diblock copolymer could increase selectivity. Distinct separate nanoparticles arrays or metal nanowires were obtained
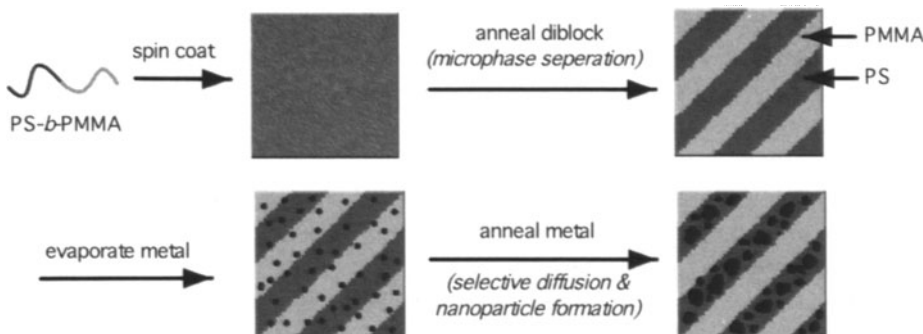

FIGURE 8.15. Ordered arrays of nanoclusters and nanowires in phase separated PMMA-*b*-PS diblock copolymer films.

depending upon the number of deposition cycles and annealing sequences. In the case of the *nanowire* linear current-voltage (*I-V*) characteristics were observed over a wide range of conditions, whereas the discrete assembly of *nanoparticle*s exhibited highly non-linear *I-V* profiles.

8.7.   DENDRIMERS IN CATALYTIC AND ASSEMBLY

Recently, the use of dendrimers as the organic component in the fabrication of metal cluster containing nanocomposites has attracted wide attention. Compared to hyperbranched polymers dendrimers can be synthesized with near perfect control over size and functional group placement. Similar to polymeric micelles, the interiors of dendrimers have been used as nanocompartments for the synthesis of stabilized metal clusters. Esumi *et al.* demonstrated that dendrimers could act as stabilizers by preparing gold colloids using photoreduction of $HAuCl_4$ in the presence of PAMAM dendrimers.[38] Amis and co-workers reported an extensive study of nanocomposites obtained from various generations of PAMAM dendrimers as templates for reduction of $HAuCl_4$ in aqueous solution using sodium borohydride.[39] Under certain experimental conditions they found that the lower generation dendrimers (G2 – G4) acts as colloidal stabilizers whereas the higher generation dendrimers (G6 – G9) behave as 'nanoreactors' for isolated cluster formation within the dendrimer.

Dendrimer based catalytically active nanocomposites have been designed by Crooks and co-workers using poly(amidoamine) (PAMAM) and poly(propyleneimine) (PPI) dendrimers as templates for the *in situ* generation of palladium nanoparticles.[40] The metal salt is sequestered inside the dendrimer by complexation to the interior tertiary amine groups followed by reduction to produce zero-valent metal nanoparticles. Size selective hydrogenation of α-substituted allyl alcohols could be achieved by employing these hydroxy terminated PAMAM/palladium nanocomposites (Figure 8.16).[41] Turnover frequencies of all the substrates decreased with increase in the dendrimer-generation (G4OH→ G6OH→G8OH). Furthermore, within a given generation of dendrimer smaller turnover frequencies were observed for larger substrates. Steric crowding at the periphery of the dendrimer, which increases with the dendrimers generation, regulates the flow of substrates into these microreactors. In essence the periphery of the dendrimer behaves like a nanofilter, which regulates access to the catalytically active site for the incoming substrates. The same group has also demonstrated that such dendrimer-based zero valent metal clusters can be utilized for hydrogenation and Heck coupling reactions in environmentally benign solvents as supercritical CO_2.[42]
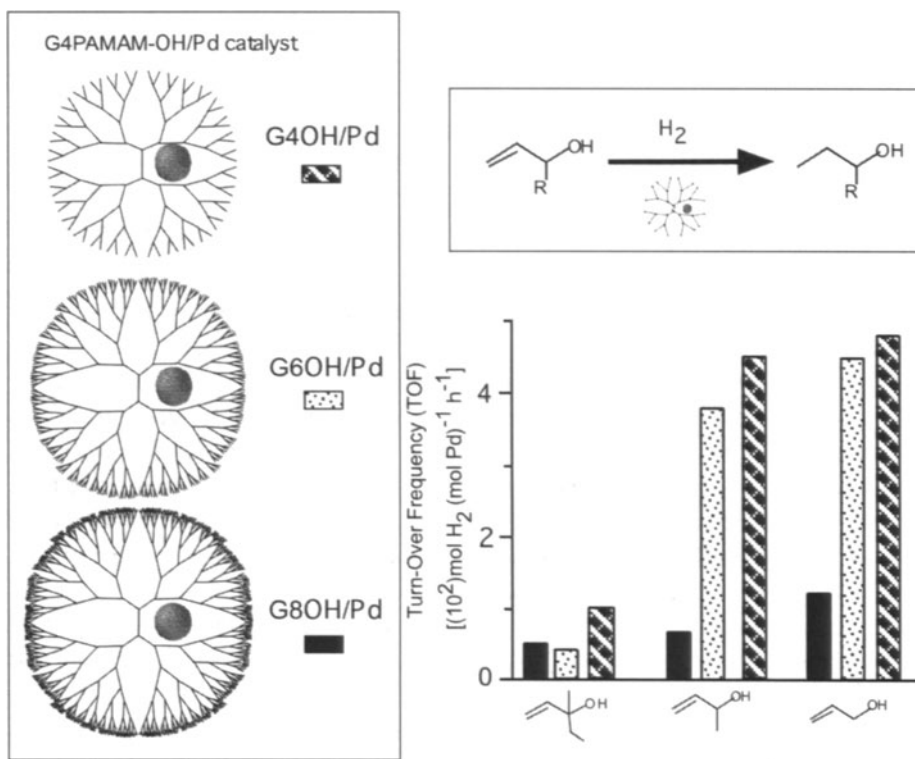
FIGURE 8.16. PAMAM stabilized Pd nanoparticle catalyzing the hydrogenation of α substituted allyl alcohols, and TOFs of the hydrogenation reactions of various allyl alcohols with generation 4, 6 and 8 dendrimers.

Creation of nanoparticle assemblies with control over the interparticle spacing is an important goal in nanotechnology. Electronic, optical and magnetic properties of the nanocomposite materials can be tuned by changing the spacing between the individual metal clusters. The size dependent properties of different generations of dendrimers makes them attractive building blocks to both assemble and control interparticle distances between nanoparticles. We recently reported that control over morphology and inter-cluster distances can be obtained for nanocomposites obtained using PAMAM dendrimers and carboxylic acid functionalized gold nanoparticles.[43] Formation of aggregates is driven by electrostatic self-assembly between the dendrimer and nanoparticle components by salt bridge formation between a carboxylic acid ligands on the gold nanoparticle and the terminal amine groups on PAMAM dendrimers. Control over interparticle spacing can be achieved in a systematic manner by simply changing the dendrimer generation (Figure 8.17).
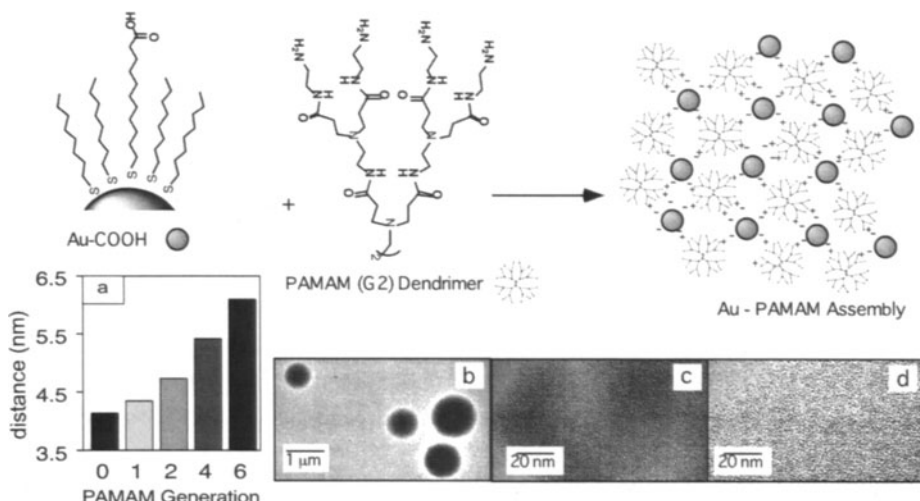
FIGURE 8.17. Electrostatic self-assembly of carboxylic acid gold nanoparticles and PAMAM dendrimers.

The resulting assemblies were obtainable in two distinct morphologies by adjusting the ratios of the MMPC to dendrimer. TEM analysis revealed that extended network-like structures with little evidence of spatial control were obtained using a low dendrimer to colloid ratios. Switching to high ratios of dendrimer to MMPC (10:1 based on functional group equivalence) resulted in micron size spherical aggregates (0.5-1.5μm in diameter, Figure 8.17b). In these assemblies, qualitative differences in inter-MMPC spacing could be readily discerned using TEM (Figure 8.17 c-d). Quantitative measurement to correlate of interparticle spacing within the aggregates to the generation of the dendrimer employed for the assembly was obtained using SAX. As expected, assemblies with greater interparticle spacing are obtained as the MPCs are assembled with larger dendrimers (G0→G1→G2→G4→G6, Figure 8.17a).

Self-assembled multilayer films of dendrimer-nanoparticles have been utilized for chemical vapor sensing. Vossmeyer and coworkers designed a sensor for detection of volatile organic compounds (VOCs). They utilized multilayer films of gold nanoparticles assembled using disulfide-functionalized polyphenylene dendrimers on glass substrates containing interdigitated electrodes. Apart from crosslinking the nanoparticles, the dendrimer also provides a porous framework for efficient analyte uptake.[44] The use of nanoparticles provides a high surface-to-volume ratio leading to excellent signal transduction through the film. Exposure to VOCs such as toluene and tetrachloroethylene induces a change in electrical resistance through the films. Higher selectivity is observed for non-polar solvents compared to polar solvents since the former is readily solublized by the

hydrophobic dendrimer. The same group later extended this work using poly(propylene imine) and PAMAM dendrimers as scaffolds.[45] Incorporating the hydrophilic PAMAM dendrimer allows an efficient device for water vapor sensing. This example highlights the versatile nature of such self assembly based fabrication strategy since a change in the specific application of the device is possible simply by tuning one of the building blocks.

8.8.   CONCLUSION

Nanocomposite materials fabricated using polymer-mediated self-assembly of nanoparticles is a versatile and effective tool for the advancement of nanotechnology. The ability to control properties of the polymer, and the nanoparticle core and shell at the molecular level provides access to a wide variety of materials with tunable properties. This 'mix and match' approach, coupled with the wealth of structures obtainable through self-assembly make polymer-nanoparticle composites potentially useful for a variety of applications. Nanoparticle chemistry and polymer self-assembly are disciplines in their own right but it is the combination of both which provides a powerful platform for device fabrication. The complexity and the resulting utility of nanoparticle-polymer composites will increase dramatically as we gain better understanding and control of the underlying self-assembly processes.

ACKNOWLEDGMENTS

REFERENCES

1. (a) Jager, E. W. H.; Smela, E.; Inganas, O. *Science* **2000**, *290*, 1540. (b) Chen, Y.; Pepin, A. *Electrophoresis* **2001**, *22*, 187. (c) Craighead, H. G. *Science* **2000**, *290*, 1532. (d) Wallraff, G. M.; Hinsberg, W. D. *Chem. Rev.* **1999**, *99*, 1801.
2. Brust, M.; Walker, M.; Bethell, D.; Schiffrin, D. J.; Whyman, R. *J. Chem. Soc., Chem. Commun.* **1994**, 801.
3. Templeton, A. C.; Hostetler, M. J.; Warmoth, E. K.; Chen, S. W.; Hartshorn, C. M.; Krishnamurthy, V. M.; Forbes, M. D. E.; Murray, R. W. *J. Am. Chem. Soc.* **1998**, *120*, 4845.
4. Templeton, A. C.; Wuelfing, M. P.; Murray, R. W. *Acc. Chem. Res.* **2000**, *33*, 27.

5. (a) Toshima, N.; Yonezawa, T. *New. J. Chem.* **1998**, 1179, and references cited therein. (b) Schmidt, G.; Bäumle, M.; Geerkens, M.; Heim, I.; Osemann, C.; Sawitowski, T. *Chem. Soc. Rev.* **1998**, *28*, 179.

6 . (a) Matyjaszewski, K.; Xia, J. *Chem. Rev.* **2001**, *101*, 2921. (b) Hawker, C. J.; Bosman, A. W.; Harth, E. *Chem. Rev.* **2001**, *101*, 3661. (c) Hadjichristidis, N.; Pitsikalis, M.; Pispas, S.; Iatrou, H. *Chem. Rev.* **2001**, *101*, 3747.

7. Newkome, G. R.; Moorefield, C. N.; Vögtle, F. *Dendritic Molecules – Concepts, Syntheses, Perspectives*; .VCH: Weinheim, 1996.

8. (a) Cao, Y. C.; Jin, R.; Mirkin, C. A. *Science*, **2002**, *297*, 1536. (b) Mucic, R. C.; Storhoff, J. J.; Mirkin, C. A.; Letsinger, R. L. *J. Am. Chem. Soc.* **1998**, *120*, 12674. (c) Elghanian, R.; Storhoff, J. J.; Mucic, R.C.; Letsinger, R. L.; Mirkin, C. A. *Science*, **1997**, *277*, 1078.

9. (a) Clapham, B.; Reger, T. S.; Janda, K. D. *Tetrahedron* **2001**, *57*, 4637. (b) Aiken, J. D.; Finke, R. G. *J. Mol. Catal. A-Chem.* **1999**, *145*, 1. (c) Centi, G.; Perathoner, S. *Curr. Opin. Solid State Mat. Sci.* **1999**, *4*, 74.

10. Forster, S.; Antonietti, M. *Adv. Mater.* **1998**, *10*, 195.

11. Klingelhofer, S.; Heitz, W.; Greiner, A.; Oestreich, S.; Forster, Antonietti, M. *J. Am. Soc. Chem.* **1997**, *119*, 10116.

12. Li, Y.; Hong, X. M.; Collard, D. M.; El-Sayed, M. A. *Org. Lett.* **2000**, *2*, 2385.

13. Narayanan, R.; El-Sayed, M. A. *J. Am. Chem. Soc.* **2003**, *125*, 8340.

14. Underhill, R. S.; Liu, G. *Chem. Mater.* **2000**, *12*, 3633.

15. Mecking, S.; Thomann, R.; Holger, F.; Sunder, A. *Macromolecules* **2000**, *33*, 3958.

16. Boal, A. K.; Galow, T. H.; Ilhan, F.; Rotello, V. M. *Adv. Funct. Mater.* **2001**, *11*, 461.

17. Galow, T. H.; Drechsler, U.; Hanson, J. A.; Rotello, V. M. *Chem. Commun.* **2002**, 1076.

18. (a) Shipway, A. N.; Katz, E.; Willner, I. *ChemPhysChem.* **2000**, *1*, 18. (b) Murray, C. B.; Kagan, C. R.; Bawendi, M. G. *Annu. Rev. Mater. Sci.* **2000**, *30*, 545. (c) Forster, S.; Plantenberg, T. *Angew. Chem.. Int. Ed. Engl.* **2002**, *41*, 688.

19. Russell, T. P. *Curr. Opin. Colloid Interface Sci.* **1996**, *1*, 107.

20. Moore, R. B.; Bittencourt, D.; Gauthier, M.; Williams, C. E.; Eisenberg, A. *Macromolecules,* **1991**, *24*, 1376.

21. Sankaran, V.; Cummins, C. C.; Schrock, R. R.; Cohen, R. E.; Silbey, R. J. *J. Am. Chem. Soc.* **1990**, *112*, 6858.

22. Ng Cheong Chan, Y.; Schrock, R. R.; Cohen, R. E. *J. Am. Chem. Soc.* **1992**, *114*, 7295.

23. Rutnakornpituk, M.; Thompson, M. S.; Harris, L. A.; Farmer, K. E.; Esker, A.R.; Riffle, J. S.; Connolly, J.; St. Pierre, T. G. *Polymer,* **2002**, *43*, 2337.

24. Boal, A. K.; Ilhan, F.; DeRouchey, J. E.; Thurn-Albrecht, T.; Russell, T. P.; Rotello, V. M. *Nature,* **2000**, *404*, 746.

25. Boal, A. K.; Gray, M.; Ilhan, F.; Clavier, G. M.; Kapitzky, L.; Rotello, V. M. *Tetrahedron* **2002**, *58*, 765.

26. Frankamp, B. L.; Uzun, O.; Ilhan, F.; Boal, A. K.; Rotello, V. M. *J. Am. Chem. Soc.* **2001**, *124*, 892.

27. (a) Möller, M.; Kunstle, H.; Kunz, M. *Synth. Met.* **1991**, *41*, 1159. (b) Spatz, J. P.; Sheiko, A.; Möller, M. *Macromolecules* **1996**, *29*, 3220.

28. Spatz, J. P.; Roescher, A.; Möller, M. *Adv. Mater.* **1996**, *8*, 337.

29. Spatz, J. P.; Mössmer, S.; Hartmann, C.; Möller, M. *Langmuir* **2000**, *16*, 407.

30. Decher, G. *Science* **1997**, *277*, 1232.

31. Schmidt, G.; Bäumle, M.; Beyer, N. *Angew. Chem. Int. Ed.* **2000**, *39*, 181.

32. (a) Hao, E.; Lian, T. *Chem. Mater.* **2000**, *12*, 3392. (b) Schmitt, J.; Decher, G.; Dressick, W. J.; Brandow, S. L.; Geer, R. E.; Shashidhar, R.; Calvert, J. M. *Adv. Mater.* **1997**, *9*,

61. (c) Feldheim, D. L.; Grabar, K. C.; Natan, M. J.; Mallouk, T. E. *J. Am. Chem. Soc.* **1996**, *118*, 7640.

33. Gao, M.; Zhang, X.; Yang, B.; Li, F.; Shen, J. *Thin Solid Films* **1996**, *284-285*, 242.

34. Sun, S.; Anders, S.; Haumann, H. F.; Thiele, J.-U.; Baglin, J. E. E.; Thomson, T.; Fullerton, E. E.; Murray, C. B.; Terris, B. D. *J. Am. Chem. Soc.* **2002**, *124*, 2884.

35. Ng Cheong Chan, Y.; Schrock, R. R.; Cohen, R. E. *Chem. Mater.* **1992**, *4*, 24.

36. Cummins, C. C.; Schrock, R. R.; Cohen, R. E. *Chem. Mater.* **1992**, *4*, 27.

37. (a) Lopes, W. A.; Jaeger, H. M. *Nature* **2001**, *414*, 735. (b) Lopes, W. A. Phys. Rev. E., **2002**, *65*, 031606, 1.

38. Esumi, K.; Suzuki, A.; Aihara, N.; Torigoe, K. *Langmuir* **1998**, *14*, 3157.

39. Grohn, F.; Bauer, B. J.; Akpalu, Y. A.; Jackson, C. L.; Amis, E. J. *Macromolecules* **2000**, *33*, 6042.

40. Crooks, R. M.; Zhao, M.; Sun, L.; Chechik, V.; Yeung, L. K. *Acc. Chem. Res.* **2001**, *34*, 181.

41. Niu, Y.; Yeung, L. K., Crooks, R. M. *J. Am. Chem. Soc.* **2001**, *123*, 6840.

42. Yeung, L. K.; Lee, C. T.; Johnston, K. P.; Crooks, R. M. *Chem. Commun.* **2002**, 2290.

43. Frankamp, B. L.; Boal, A. K.; Rotello, V. M. *J. Am. Chem. Soc.* **2002**, *124*, 15146.

44. (a) Vossmeyer, T.; Guse, B.; Besnard, I.; Bauer, R. E.; Müllen, K.; Yasuda, A. *Adv. Mater.* **2002**, *14*, 238.

45. Krasteva, N.; Besnard, I.; Guse, B.; Bauer, R. E.; Mullen, K.; Yasuda, A.; Vossmeyer, T. *Nano Lett.* **2002**, *2*, 551.

9

Electrostatic assembly of nanoparticles

Murali Sastry

National Chemical Laboratory, Pune – 411 008, INDIA.

E-mail : sastry@ems.ncl.res.in

9.1. INTRODUCTION

There is much excitement in the study of nanoscale matter with respect to their fundamental properties, organization to form superstructures and applications. The unusual physicochemical and optoelectronic properties of nanoparticles are primarily due to confinement of electrons within particles of dimensions smaller than the bulk electron delocalization length, this process being termed quantum confinement.[1-3] The exotic properties of nanoparticles have been considered in applications such as optoelectronics,[4] catalysis,[5] reprography,[6] single-electron transistors (SETs) and light emitters,[7] non-linear optical devices[8] and photoelectrochemical applications.[9] Magnetic nanoparticles are being viewed with interest from a fundamental point of view (superparamagnetism in the nanoparticles)[10] as well as in applications such as magnetic memory storage devices,[11] magnetic resonance image enhancement[12] and magnetic refrigeration.[13] The ability to tune the optical absorption/emission properties of semiconductor nanoparticles (the so-called "quantum dots") by simple variation in nanoparticle size is particularly attractive in the facile band-gap engineering of materials[14] and the growth of quantum dot lasers.[15] More recently,

nanoscale matter has been looked at with interest for potential application in nanocomputers, synthesis of advanced materials, energy storage devices, electronic and optical displays, chemical and biosensors as well as biomedical devices.[16] It is expected that some of the more immediate applications of nanoparticles will be in medical diagnosis and therapeutics. Exciting examples include detection of genetic disorders using gold nanoparticles,[17,18] color-coded fluorescent labeling of cells using semiconductor quantum dots[19,20] and cell transfection for gene therapy and drug delivery.[21]

While the exotic properties of individual (non-interacting) nanoparticles is well documented and understood, in many situations it would be desirable to assemble the nanoparticles either in solution or on suitable substrates, link them in some manner and make them "talk" to each other. In more scientific terms, tailoring the *collective properties* of nanoparticle ensembles is also an important aspect of nanotechnology.[22] The ultimate goal, insofar as the growth of nanoparticle superstructures is concerned, is the realization of crystals of nanocrystals wherein both the size of the nanoparticles and the interparticle separation in the film may be tailored at will and thus, enable one to tune the collective properties of the ensemble. For example, stringing together metal nanoparticles into linear superstructures with a view to using them as waveguides for electromagnetic energy transport is a recent exciting concept with clear application potential.[23]

The key steps involved in realizing nanoparticle superstructures are the synthesis of nanoparticles and thereafter, assembling them by a variety of methods. In this chapter, I will not dwell upon the different methods for synthesis of inorganic nanoparticles – this is a mature field with a large number of recipes available for the growth of nanoparticles of different chemical compositions, sizes, polydispersity and shape. I will instead focus on the assembly of inorganic nanoparticles into superstructures of varying topological complexity in solution (section 1.1) and in thin film form (section 1.2) using electrostatic interactions as the driving force for assembly. Electrostatic interactions play an important role in many chemical and biological processes[24] and enjoy a number of advantages over other interactions such as covalent and hydrogen bonding. Electrostatic interactions are isotropic, reasonably strong and long-range and can be tuned to be attractive or repulsive thereby provided one with the additional degree of freedom to disassemble nanoparticles superstructures. Electrostatic interactions as a glue for nanoparticle assembly enables easy extension of the methodologies to biological templates (such as proteins, DNA and cell membranes), which are often charged.

9.2. ELECTROSTATIC NANOPARTICLE ASSEMBLY IN SOLUTION

Inorganic nanoparticles such as gold, silver, CdS etc. require to be stabilized against aggregation in aqueous environments. This may be conveniently accomplished by covering the surface of the nanoparticles (termed 'functionalization' or 'derivatization) with ionizable groups such carboxylic acid and amine groups. In the case of noble metal and metal sulfide quantum dots, ω-functionalized thiol derivatives are normally used to modify the surface of the nanoparticles. Thiol groups are known to chemisorb on nanoparticles of the above chemical compositions while the terminal ionizable functional groups enable stabilization of the particles via repulsive Coulombic interactions.[25-28] The surface chemistry required for modification of nanoparticles of other chemical compositions such as oxides would necessarily be different but a similar strategy based on bifunctional molecules can be adopted. Deliberate and careful screening of the repulsive interactions of nanoparticle surface-bound functional groups may then be carried out to promote controlled aggregation of the particles in solution. The repulsive electrostatic interactions between charged nanoparticles may be modulated by controlling the extent of ionization of functional groups on the surface (as demonstrated for cysteine-capped silver nanoparticles by Sastry and co-workers[29]) or by screening the interactions by addition of salt (carboxylic acid derivatized gold nanoparticles, Murray and co-workers[30]). In a different approach, oppositely charged nanoparticles have also been mixed together to yield interesting superstructures in solution.[31,32] This approach is illustrated below with two examples.

The controlled aggregation oftiopronin-capped gold nanoparticles synthesized in an aqueous medium upon addition of Cu^{2+} ions was studied by Murray and co-workers.[30] Tiopronin ligands bound to the surface of gold nanoparticles possess one free carboxylic acid group each and thus Cu^{2+} ions may be bound to carboxylate ions under suitable pH conditions. Binding of the Cu^{2+} ions leads to screening of the repulsive interactions between the gold nanoparticles and eventual precipitation of the particles (Figure 9.1, Ref. 30). This process is fully reversible and upon addition of either sodium acetate or acetic acid, the aggregated gold nanoparticles go back into solution as well-dispersed particles (Figure 9.1). Upon addition of acid, protonation of the acid
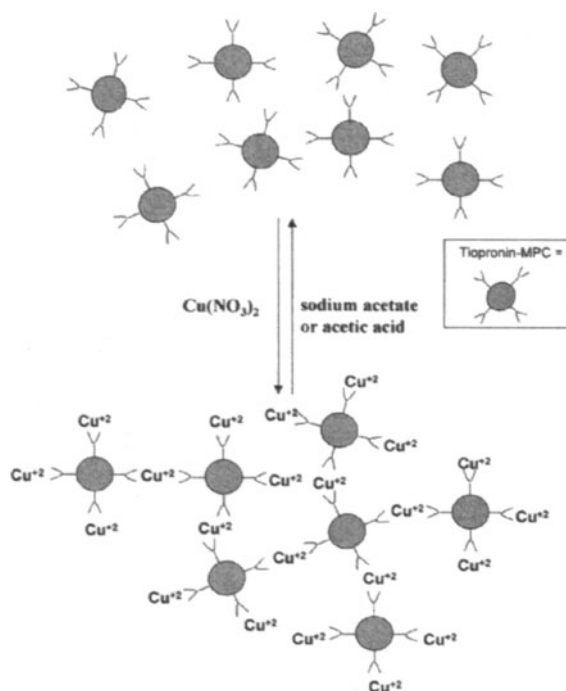
FIGURE 9.1. Cartoon illustration of reversible aggregation of tiopronin MPCs using Cu^{2+}-carboxylate chemistry and disaggregation by addition of sodium acetate or acetic acid (reprinted with permission from Ref. 30, © 2000 American Chemical Society).

groups is close to 100 % and suppresses complexation of Cu^{2+} ions with the nanoparticles and consequently, their aggregation as well.[30] These authors have also shown that Cu^{2+}-carboxylate chemistry can be used to electrostatically assemble tiopronin-capped gold nanoparticles onto self-assembled monolayers (SAMs) of mercaptoundecanoic acid on gold thin films.[30] This aspect will be discussed in some detail later.

The aggregation of gold nanoparticles consequent to screening of the repulsive interactions between the particles is generally a rapid process and results in aggregates with no particular long-range order among the particles themselves. Towards obtaining nanoparticle assemblies with a periodic three-dimensional structure in solution, Kolny, Kornowski and Weller[32] have investigated the highly controlled electrostatically driven aggregation of 2 nm CdS nanoparticles during mixing of positively and negatively charged quantum dots of CdS. The charge on the CdS nanoparticles was determined by the nature of terminal functional groups. This is illustrated in Figure 9.2 (a) along with the process for obtaining crystalline assemblies of CdS quantum dots in solution (b). Indeed, the nature and stability of aggregates
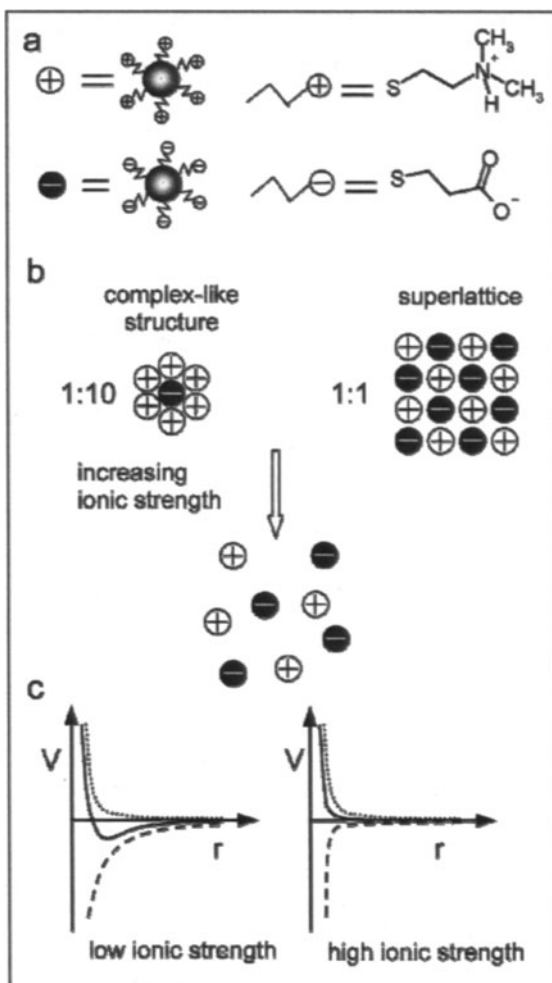
FIGURE 9.2. Schematic diagram of positively and negatively charged nanoparticles obtained by modification of the surface with thiol compounds (a), of the principle of superlattice formation (b) and of controlling the interaction between the nanoparticles by adjusting the ionic strength (c). (Reprinted with permission from Ref. 32, © 2002 American Chemical Society).

formed could be tailored by varying the ratio of positively charged to negatively charged CdS nanoparticles in the mixture. Significant excess of any of the two components resulted in stable aggregates in solution while an equi-molar mixture lead to the formation of an insoluble precipitate in water. Increasing the ionic strength in solutions with aggregates lead to re-dispersion of the particles as illustrated in the potential energy diagram of Figure 9.2(c).

That the 1 : 1 aggregates of positively and negatively charged CdS nanoparticles are crystalline is shown in Figure 9.3 which shows the powder

X-ray diffraction (XRD) patterns of aggregates obtained in a fast (curve a) and slow aggregation process (curve b). The important point to note is the
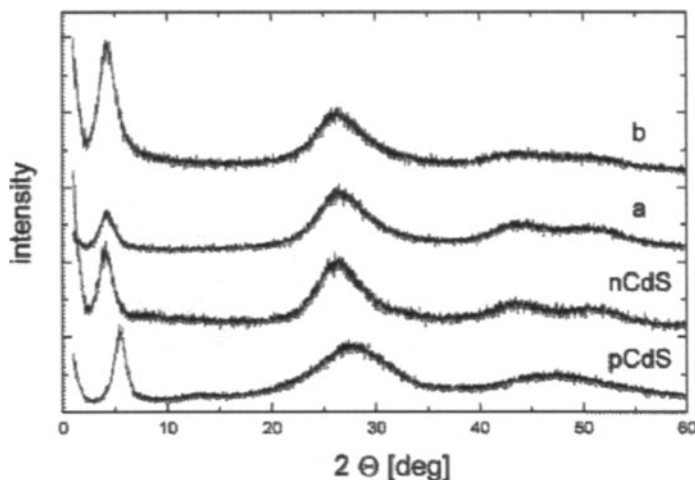
FIGURE 9.3. Powder X-ray diffraction patterns of fast and slowly aggregated samples (a and b) of pCdS and nCdS (normalized to the integrated peak intensities in the wide angle region ($20° < 2\theta < 60°$). (Reprinted with permission from Ref. 32, © 2002 American Chemical Society).

presence of diffraction peaks in the region $2 - 5°$ clearly indicating the existense of long-range order in the CdS nanoparticles in the aggregates.[32]

9.3.   ELECTROSTATICALLY DRIVEN NANOPARTICLE ASSEMBLY IN THIN FILMS

Commercial exploitation of many properties of nanoparticles, especially in the optoelectronics industry, would require the assembly of nanoparticles in the form of thin films either as monolayers or multilayer superlattices. A number of different methods exist for the electrostatic assembly of inorganic nanoparticles on charged surfaces such as those presented by SAMs, Langmuir-Blodgett films, biomacromolecules such as DNA, polyelectrolytes etc. A few illustrative examples of each approach are presented below.

9.3.1. ELECTROSTATIC ASSEMBLY OF NANOPARTICLES ON SELF-ASSEMBLED MONOLAYERS

It is well-known that immersion of films of coinage metals such as gold, silver and copper in organic solutions of alkanethiols results in the spontaneous assembly of densely packed monolayers of the alkanethiols on the substrate surface.[33] These monolayers have been termed 'self-assembled monolayers' or SAMs.[33] As in the case of surface modification of nanoparticles, ω-functionalized thiol derivatives may be used to form SAMs on suitable planar surfaces. A variety of terminal functional groups may be envisaged to modify the surface properties of the underlying substrate but what is pertinent to this study is the presence of ionizable terminal functional groups in the SAMs for electrostatic assembly of charged inorganic nanoparticles. A number of groups have used electrostatic attractive forces between charged SAMs and oppositely charged nanoparticles[30,34-38] to assemble thin films of the nanoparticles.

Gole, Sainkar and Sastry have demonstrated that SAMs of 4-aminothiophenol (4-ATP) chemisorbed on thin films of gold may be used to electrostatically bind with silver nanoparticles charged negatively with carboxylic acid functionality by simple immersion of the SAMs in the aqueous nanoparticle solution.[35] Detailed quartz crystal microgravimetry (QCM) measurements carried out on the silver nanoparticle films assembled onto SAMs of 4-ATP as a function of pH of the silver nanoparticle solution indicated that the density of nanoparticles on the SAM surface was a strong function of the solution pH. Figure 9.4 shows equilibrium percentage surface coverage of the silver nanoparticles determined from the QCM measurements as a function of solution pH. It is seen from this figure that maximum silver nanoparticle uptake occurs at ca. pH 9 and falls away on either side of this critical pH value. This may be understood in terms of the electrostatic interaction between the positively charged terminal amine groups in the SAM and negatively charged carboxylate ions on the silver nanoparticle surface, which would be clearly pH-dependent. Above pH 9, the protonation of the amine groups in the SAM would progressively decrease while a similar behavior occurs below pH 9 for the carboxylic acid groups on the silver nanoparticle surface (see schematic, inset of Figure 9.4). Thus, the surface coverage of the silver nanoparticles could be easily varied by pH-dependent modulation of the electrostatic interactions. Indeed, the silver nanoparticle assembly process could be reversed by immersion of the films formed at pH 9 in silver colloidal solutions held at pH 5 and 11.[35]
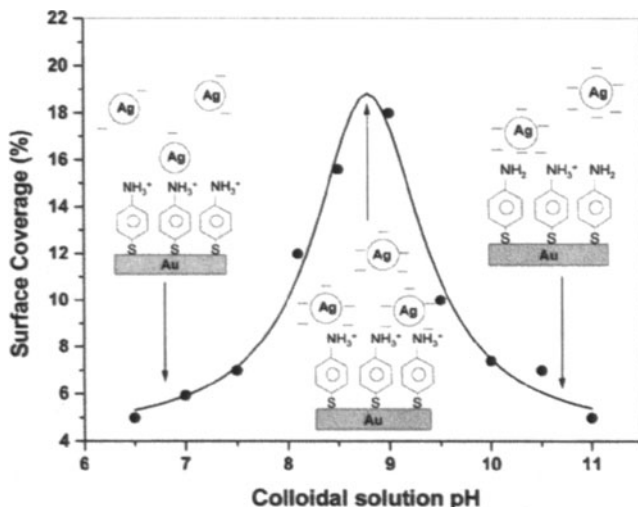
FIGURE 9.4. Surface coverage of 4-CTP-capped silver colloidal particles on 4-ATP SAMs plotted as a function of colloidal solution pH used for the formation of the colloidal particle films. The schematics show the nature of electrostatic coordination in the different pH regimes. (Reprinted with permission from Ref. 35, © 2000 American Chemical Society).

In a different approach based on SAMs, Auer et al. have shown that bis-benzamidines could be used as positively charged bifunctional electrostatic linker molecules in the assembly of negatively charged gold nanoparticles on negatively charged mercaptoundecanoic acid (MUA) SAMs on gold surfaces[34] as illustrated in Figure 9.5. In the first step, SAMs of MUA are assembled on
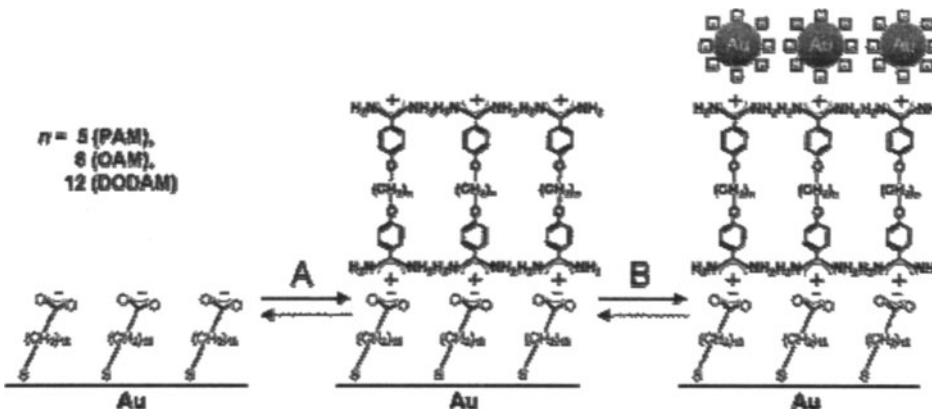
FIGURE 9.5. Schematic representation of the consecutive build-up of a SAM/nanoparticle composite by means of electrostatic interactions. Three different bis-benzamidines were used to serve as linking layers. $n=5$ pentamidine (PAM), $n=8$ octamidine (OAM), and $n=12$ dodecamidine (DODAM). (Reprinted with permission from Ref. 34, © 2000 American Chemical Society).

the surface of gold thin films. This leads to exposure of the carboxylic acid functional groups on the surface of the SAM, which may be ionized to render the monolayer negatively charged (Figure 9.5). In the second step, a monolayer of bis-benzamidine molecules is assembled electrostatically. The bifunctional nature of this molecule enables reversal of the sign of the charge of the underlying MUA SAM and thereby, assembly of negatively charged gold nanoparticles on the MUA-bis-benzamidine bilayer in the final step (Figure 9.5). The number of methylene units in the linker molecule was varied from 5 to 12 and the electrostatic assembly of gold nanoparticles on the MUA SAM was studied using ellipsometry. It was observed that the quality of the linker molecule layer (in terms of density of molecules in the linker layer) strongly influenced the coverage of gold nanoparticles on the MUA SAM being maximum for the DODAM linker film.[34]

As briefly described in section 1.1, Murray and co-workers have used carboxylate-Cu^{2+} chemistry to assemble nanoparticles in solution.[30] These authors have also shown that such an approach can be used to assemble *multilayers* of tiopronin-capped gold nanoparticles on SAMs of mercaptoundecanoic acid (MUA).[30] This is accomplished in the following sequential manner (Figure 9.6). In the first step, compact, SAMs of MUA are formed on gold thin films. Thereafter, the MUA SAMs are immersed in an ethanolic solution of Cu^{2+} ions to bind the ions to the free, terminal carboxylate ions in the MUA SAM (Figure 9.6, step a). This process leads to charge reversal on the SAM and further immersion of the Cu^{2+} ion-covered MUA SAM in a solution containing tiopronin-capped gold nanoparticles leads to the formation of a monolayer of gold nanoparticles on the surface of the SAM (Figure 9.6, step b). Simple repetition of steps a and b sequentially was shown to lead to the formation of multilayers of the tiopronin-gold nanoparticles on the underlying MUA SAM.[30]
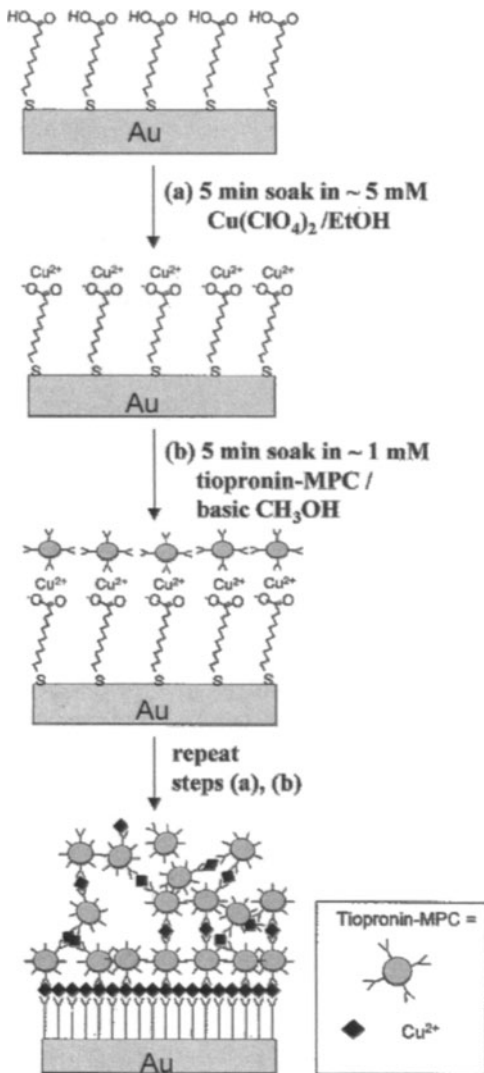
FIGURE 9.6. Cartoon representation of Tiopronin-MPC film formation. Step a : exposure of mercaptoundecanoic acid (MUA) monolayer to Cu^{2+} solution. Step b : exposure of Cu^{2+}-carboxylates to basic methanol suspension of tiopronin-MPC. The above two steps are repeated to construct multilayers of tiopronin-MPC held together by Cu^{2+}-carboxylate bonds. (Reprinted with permission from Ref. 30, © 2000 American Chemical Society).

Soft lithographic techniques applied to SAMs enables the formation of patterned nanoparticle structures. The most popular of the lithographic techniques for creating patterned structures in SAMs is based on micro-contact printing (μCP).[39] In μCP, an elastomeric PDMS stamp, inked with an appropriate solution of alkanethiol, is brought into contact with the surface of a substrate to transfer the ink molecules to those regions of the

substrate that contact the stamp.[39] It is a rapid and parallel process wherein large areas (~ 50 cm^2) can be patterned in a single impression. He et al. have demonstrated that μCP could be used to create patterned SAMs consisting of spatially well-separated regions bearing amine/thiol functionality and methyl functionality.[37] During immersion of the patterned SAMs in gold nanoparticle solution, these authors have observed attachment of gold nanoparticles at sites exposing thiol/amine functionality.[37] The patterned assembly of gold nanoparticles on mixed amine/methyl-terminated μCP SAMs is clearly seen in Figure 9.7, which shows the tapping
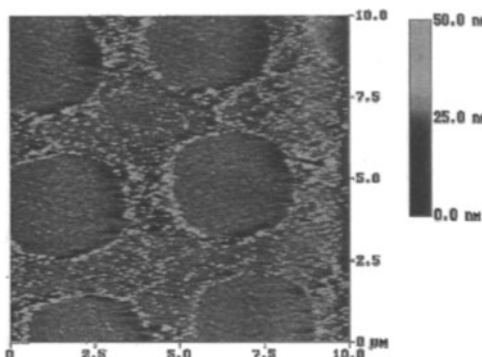
FIGURE 9.7. Tapping mode AFM image of patterned Au nanoparticles structure constructed by selectively anchoring Au colloidal on $-NH_2$ regions using a patterned SAM as a template. (Reprinted with permission from Ref. 37, © 2000 American Chemical Society).

mode atomic force microscopy (AFM) image of nanoparticles. The regions populated by the gold nanoparticles are regions with amine groups exposed and are clearly structured on a micron scale. He et al. concluded that the nanoparticles were bound to the amine groups via attractive electrostatic interaction between the negative charges on the gold nanoparticle surface and positive charges on the protonated amine regions.[37]

9.3.2. ELECTROSTATIC ASSEMBLY OF NANOPARTICLES AT THE AIR-WATER INTERFACE

The air-water interface has long been recognized as an excellent medium for the assembly of inorganic ions,[40,41] biomacromolecules such as proteins[42] and DNA[43,44] and inorganic nanoparticles. Insofar as nanoparticles are concerned, a number of different variants of the technique may be considered depending on the chemical nature of the surface of the nanoparticles. If the nanoparticles are hydrophobic, they may be simply floated on the surface of water, compressed into a close-packed monolayer and transferred onto suitable solid supports by the versatile Langmuir-Blodgett method.[45-48] The use of Coulombic or electrostatic interactions in

nanoparticle assembly at the air-water interface has been till now the most popular approach. Fendler and co-workers published the first report on using electrostatic interactions for the assembly of size-quantized CdS nanoparticles.[49] Nanoparticles of metals such as silver[50-57] and gold;[52,55,58,59] semiconductor quantum dots such as CdS[49,60] and CdTe;[61] oxides such as SiO_2, TiO_2,[62] Fe_3O_4[63] and γ-Fe_2O_3[64] and latex spheres[65] have since been assembled from solution at the air-water interface using electrostatic interactions.

The basic ingredients of the electrostatic assembly of nanoparticles with oppositely charged Langmuir monolayers are illustrated in Figure 9.7. In this particular example, nanoparticles in the aqueous subphase are derivatized with carboxylic acid functionality. Upon spreading a Langmuir monolayer of a cationic lipid such as octadecylamine (ODA) on the subphase surface held at a pH where both the carboxylic acid groups on the nanoparticle surface and the amine groups in the Langmuir monolayer are fully charged (pH ~ 5), the nanoparticles are attracted to the Langmuir monolayer on the surface of water through attractive coulombic interactions. This process results in the assembly of the nanoparticles at the interface in the form of a monolayer that can be easily transferred by the LB technique onto solid substrates (Figure 9.8). An important feature of this method is that the extent of ionization of the complementary functionalities at the air-water interface and on the surface of nanoparticles
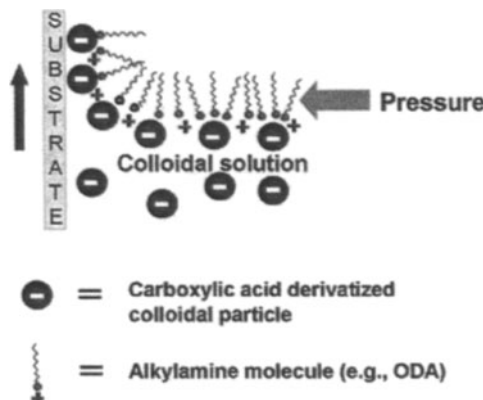
FIGURE 9.8. Scheme showing the electrostatic assembly of negatively charged nanoparticles present in the subphase with positively charged Langmuir monolayers of octadecylamine and their transfer onto suitable solid substrates by the Langmuir-Blodgett technique. (Reprinted with permission from Ref. 57, © 2002 American Chemical Society).

may be easily controlled by simple variation in the pH of the nanoparticle subphase. Sastry and co-workers have shown that this method can be used to assemble negatively charged silver nanoparticles of varying density at the

air-water interface with ODA Langmuir monolayers.[51] This may be conveniently demonstrated by quartz crystal microgravimetric (QCM) analysis of Langmuir-Blodgett films of the ODA-silver nanoparticle complexes formed at the air-water interface as a function of the subphase pH. QCM is a powerful technique for measuring minute changes in mass deposited on a piezoelectric quartz crystal and is ideally adapted for studying processes such as nanoparticle assembly on surfaces etc. Figure 9.9 shows a plot of the QCM mass uptake recorded from LB films of ODA complexed with carboxylic acid derivatized silver particles at two different subphase pH conditions (pH 9 and 12) as a function of thickness of the films. The first observation is that the mass uptake is essentially linear with number of monolayers of the silver nanoparticles transferred onto the quartz crystal. This indicates that the density of the silver nanoparticles in each of the layers is constant indicating fairly good lamellar ordering in the film. The second observation is that the slope of the curves corresponding to LB films formed at pH 9 and 12 is quite different and is smaller for the pH 12 case. This indicates that the mass uptake per monolayer is lower at high pH indicating a smaller concentration of silver nanoparticles in this film. This may be rationalized in terms of a simple electrostatic model. The pK_b of the ODA molecules in the Langmuir monolayer is ~ 10.5 and therefore, at a subphase pH of 9, both the ODA molecules and carboxylic acid groups on the silver
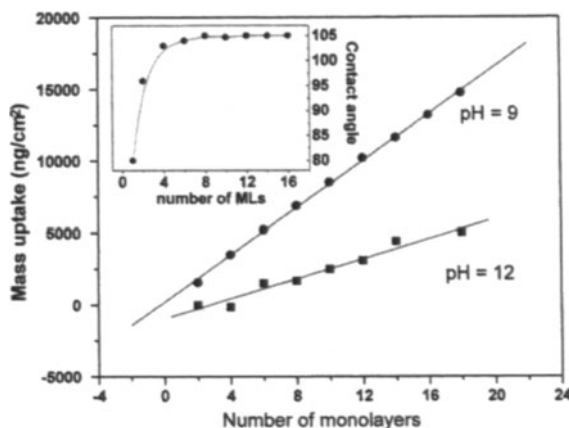
FIGURE 9.9. QCM mass uptake with time as a function of the number of monolayers transferred with the hydrosol at pH = 9 (filled circles) and pH = 12 (filled squares). The solid lines are linear least squares fits to the data. The inset shows the contact angle variation with the number of monolayers transferred onto lead arachidate coated quartz substrates. (Reprinted with permission from Ref. 51, © 1997 American Chemical Society).

are fully ionized leading to maximum attractive electrostatic interaction and consequently, maximum density of the silver nanoparticles in each of the monolayers. At pH 12, however, the ODA molecules are not protonated and

hence, there is no driving force for the assembly of silver nanoparticles at the air-water interface. The finite mass uptake observed at pH 12 is due to deposition of ODA monolayers without silver nanoparticles.[51] The inset of Figure 9.9 is a plot of the contact angles measured for a sessile water drop on LB films of ODA-silver nanoparticles of varying thickness. The contact angle increases steeply from $80°$ to $105°$ by the time 3 monolayers are deposited indicating that the hydrocarbon chains of the ODA molecules are exposed and that the film grows in a lamellar fashion. The work from the Sastry group on electrostatic complexation of nanoparticles at the air-water interface has been recently reviewed.[57]

Kang and co-workers have used electrostatic interactions to bind γ-Fe_2O_3 nanoparticles of 8.3 nm diameter at the air-water interface with Langmuir monolayers of arachidic acid.[64] In the pH regime 3.5-5, the colloidal solutions of γ-Fe_2O_3 were observed to be extremely stable indicating that the particles were stabilized electrostatically. A detailed ξ potential study was carried out on aqueous colloidal solutions of γ-Fe_2O_3 as a function of pH and it was observed that in the pH window 3.5 to 5, the particles were positively charged. The positive charge on the γ-Fe_2O_3 nanoparticles was then used by the authors to bind them at the air-water interface with negatively charged Langmuir monolayers of arachidic acid. A detailed investigation of the nanoparticle domain formation at the air-water interface and magnetic properties of LB films of the γ-Fe_2O_3 nanoparticles was carried out using a plethora of techniques.[64]

Figure 9.10 shows plots of the π-A isotherms recorded from Langmuir monolayers of arachidic acid on pure water (top) and a subphase of γ-Fe_2O_3 nanoparticles at pH 3.5 and temperature of 20 °C (bottom). A small expansion in the monolayer was observed in the π-A isotherms of arachidic acid on the γ-Fe_2O_3 nanoparticle subphase relative to that of arachidic acid on pure water. This expansion was attributed to complexation of γ-Fe_2O_3 nanoparticles at the interface and is a feature observed by other authors using different nanoparticle systems.[51] Kang and co-workers also performed surface potential measurements during compression of the monolayer and observed saturation in the surface potential at nearly identical limiting areas per molecule for the pure water and γ-Fe_2O_3 nanoparticle subphase cases.

The inset of Figure 9.10 shows Brewster angle microscopy (BAM) images recorded from the monolayers under different stages of compression, the images corresponding to the points identified on the π-A isotherms.
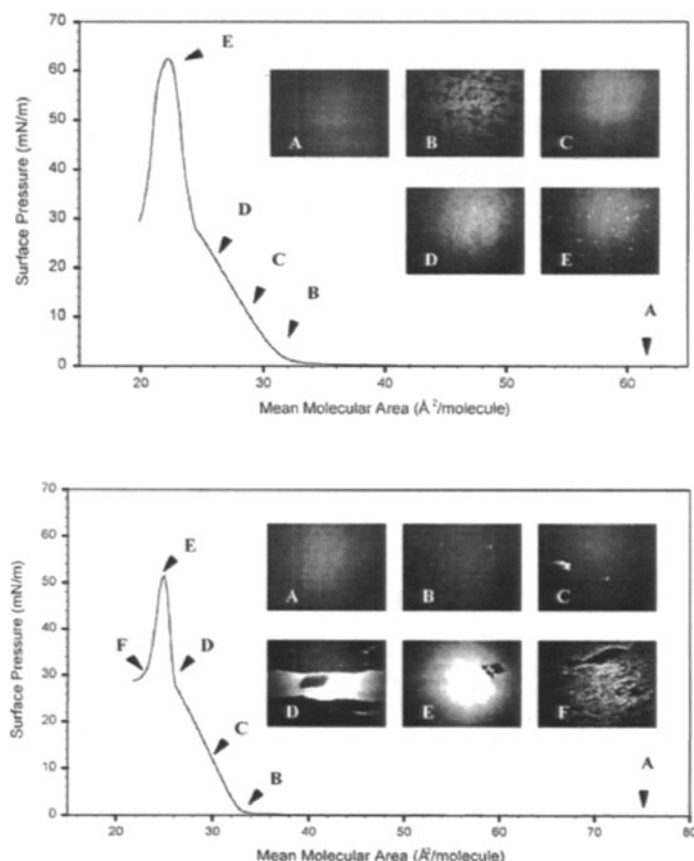
FIGURE 9.10. Pressure area isotherm and BAM images of arachidic acid on a subphase of pure water (top) and on a hydrosol of γ-Fe_2O_3 nanoparticles (bottom) with pH 3.5 at 20 °C. (Reprinted with permission from Ref. 64, © 2002 American Chemical Society).

In the coexisting liquid crystalline-gaseous phase (points A and B), the arachidic acid monolayer is completely homogeneous both on plain water (Figure 9.10, top) and on the γ-Fe_2O_3 subphase (Figure 9.10, bottom). Further compression of the arachidic acid monolayer results in BAM images characteristic of a liquid crystalline phase on pure water (C and D, images on top) while the formation of domains is indicated in the BAM images for the monolayer under similar compression conditions (D, image at the bottom). The domain formation is driven by complexation of the γ-Fe_2O_3 nanoparticles with the arachidic acid monolayer. The domains are fairly rigid till the collapse pressure (image E, lower panel) while at point F above the collapse pressure the BAM image of the arachidic acid-γ-Fe_2O_3 nanoparticles shows striations indicating rupture of the monolayer (image F, lower panel).

The magnetic properties of a 100 monolayer LB film of the γ-Fe_2O_3 nanoparticles complexed with arachidic acid was studied by vibrating

sample magnetometry. Figure 9.11 shows the magnetization data obtained as a function of applied magnetic field for this film at room temperature (plot at the top) and at 20 K (plot at the bottom).
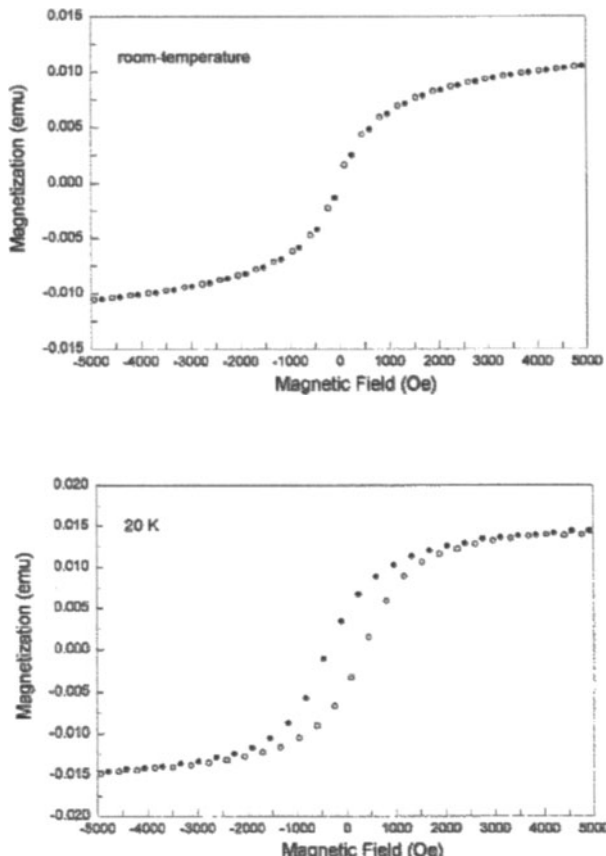
FIGURE 9.11. Magnetic hysteresis loop for nanocomposite Langmuir-Blodgett film of arachidic acid /γ-Fe_2O_3 nanoparticles of 100 layers at room temperature. The lack of hysteresis indicates the composite has superparamagnetic properties (top). Magnetic hysteresis loop for a Langmuir-Blodgett film of arachidic acid/γ-Fe_2O_3 nanocomposite of 100 layers at 20 K. The presence of hysteresis at low temperature indicates that the γ-Fe_2O_3 nanoparticles undergo a superparamagnetic/single domain transition (bottom). (Reprinted with permission from Ref. 64, © 2002 American Chemical Society).

A comparison of the two magnetic hysteresis loops shows that while there is no hysteresis at room temperature (indicating that the particles are superparamagnetic), hysteresis occurs at 20 K with a 425 Oe coercivity. This behavior indicates that the nanoclusters are magnetically frozen below the blocking temperature and undergo a superparamagnetic to single domain transition.[64]

9.3.3. LAYER-BY-LAYER NANOPARTICLE ASSEMBLY DRIVEN BY ELECTROSTATIC INTERACTIONS

The first report on the electrostatically driven layer-by-layer self-assembly of inorganic colloidal particles on planar surfaces may be traced to the seminal work of Iler.[66] Iler showed that oppositely charged silica and alumina particles could be electrostatically self-assembled in multilayer structures by alternatively immersing the substrate in the two colloidal solutions. However, true layer-by-layer growth was not fully established in this case.[66] Since then, the group lead by Decher has been very active in this field and have demonstrated the layer-by-layer electrostatic self-assembly of cationic and anionic polyelectrolytes as well as multilayer structures consisting of combinations of charged colloidal particles including biomacromolecules such as DNA.[67] Many groups worldwide have now used electrostatically driven layer-by-layer assembly to realize structures containing proteins/polyeletrolytes;[68] polyelectrolye/inorganic nanoparticle sandwich structures with nano-magnetite,[69] TiO_2/CdS,[70] SiO_2, TiO_2 and CeO_2,[71] Au[72-74] alternating layers of positively charged gold and negatively charged silver particles[75] as well as quantum dots of CdSe.[76] We have shown that gold nanoparticles rendered amphoteric using the amino acid, valine, may also be electrostatically assembled in a layer-by-layer fashion by suitably changing the pH of the gold colloidal solution.[77]

The layer-by-layer (LBL) assembly process is illustrated by an example from the work of He et al.[74] Poly(amidoamine) (PAMAM) dendrimers were used as polymeric templates/stabilizers/reservoir for the synthesis of gold nanoparticles.[74] Growth of gold nanoparticles within the dendrimer structures is accomplished by mixing dilute aqueous solutions of the PAMAM dendrimer and chloroauric acid. This results in the electrostatic entrapment of the $AuCl_4^-$ ions with the protonated amine groups of the dendrimer. In-situ reduction of the gold ions resulted in the formation of gold nanoparticles in the size range 5-20 nm which were extremely stable in the PAMAM matrix.

The electrostatic LBL assembly of the positively charged gold nanoparticle-PAMAM dendrimers on a negatively charged substrate is illustrated in Figure 9.12. The substrate surface is first treated with poly(dimethyl diallylammonium chloride) (PDAC), a cationic polyelectrolyte that renders the substrate surface positively charged. Thereafter, a layer of poly(sodium 4-styrenesulfonate) (PSS) was deposited on the PDAC layer to reverse the sign of the charge on the substrate surface (Figure 9.12). Immersion of this film in the Au nano-PAMAM dendrimer solution leads to the electrostatic assembly of the gold nanoparticles on the primed substrate surface.
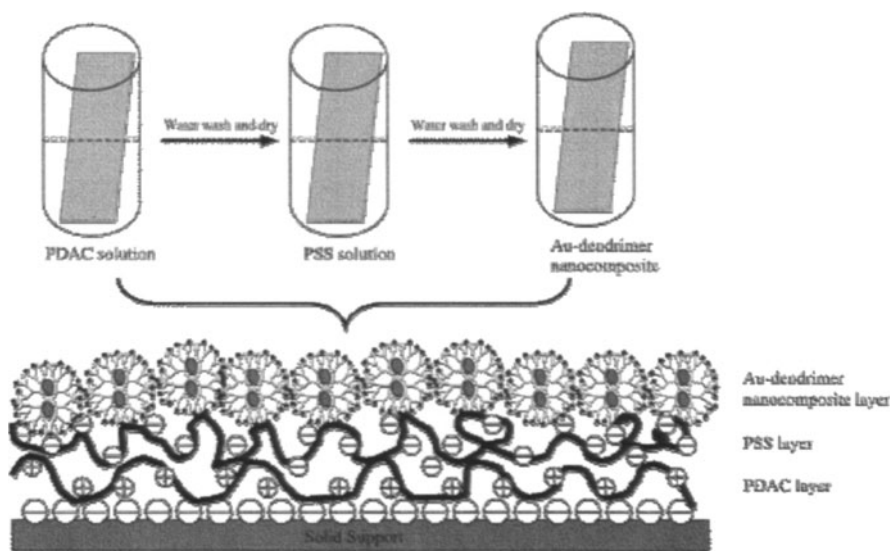
FIGURE 9.12. Schematic illustration of the procedure for fabrication of the PSS/Au-dendrimer nanocomposite film on the negatively charged substrate and the architecture of the resulting film. *(Reprinted with permission* from Ref. 74, © 1999 American Chemical Society).

As in the case of electrostatically assembled nanoparticles on SAMs,[30] this process may be repeated to yield multilayer sandwich structures of the Au nano-PAMAM and PSS. The UV-vis absorption spectra recorded from the PSS-Au nano-PAMAM films of different thicknesses is shown in Figure 9.13. At low film thickness (Figure 9.13a), a weak absorption centered around 550 nm can be observed which becomes more prominent as the number of Au nanoparticle layers increases. For film thicknesses of 8 bilayers of PSS-Au nano-PAMAM and above, a well-defined absorption band at 549 nm is clearly seen (Figure 9.13b) which increases monotonically with intensity as the number of nanoparticle layers increase. This absorption band is due to excitation of surface plasmon vibrations in the gold nanoparticles in the film and the fact that the intensity of the absorbance at 549 nm increases linearly with the number of Au nanoparticle monolayers (Figure 9.13b, inset) indicates that the films grown in a regular, lamellar fashion with negligible variation in the gold nanoparticle density in each of the layers.[74]
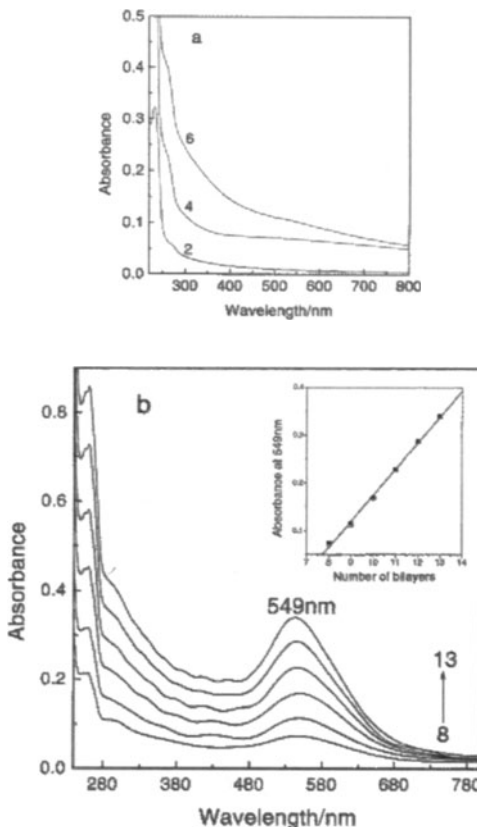
FIGURE 9.13. UV-vis absorption spectra of PSS/Au-dendrimer nanocomposite multilayers on a quartz slide. (a) Curves corresponding to adsorption of 2, 4, and 6 alternate PSS/Au-dendrimer bilayers. (b) Curves corresponding to adsoption of 8-13 PSS/Au-dendrimer complex bilayers. The inset shows the increase in absorbance at 549 nm with the number of bilayers. *(Reprinted with permission* from Ref. 74, © 1999 American Chemical Society).

An interesting application of such electrostatically assembled layered nanoparticle systems as Zener diodes has been demonstrated by Cassagneau et al.[76] Self-assembled structures of CdSe nanoparticles (*n*-type layer) and poly(3-methylthiophene)/poly(pyrrole) (*p*-type layer) were investigated and it was demonstrated that these structures showed excellent rectification behavior in the forward bias direction while Zener breakdown was observed during reverse bias.[76] Another important application of the electrostatic LBL assembly approach in realizing superstructures for application in molecular and supramolecular devices was addressed by Hao et al.[70] Semiconductor nanoparticles such as TiO_2 have important applications in photocatalysis and solar energy conversion. However, a drawback in the use of titania nanoparticles is the rapid recombination of the excited electron-hole pair. Combining two different semiconductor nanoparticles wherein one

semiconductor has a large band gap and energetically low-lying conduction band with another possessing a small band gap and energetically high-lying conduction band leads to the possibility of electron transfer between the nanoparticles thereby more efficient and longer charge separation. With this application in mind, Hao et al. have demonstrated the electrostatic LBL assembly of cationic TiO_2 and anionic CdS nanoparticles using the polyelectrolytes PSS and PDAC[70] and have studied the photoelectron energy conversion in such nanoparticle composite films using surface photovoltage spectroscopy. They observed that connection of the TiO_2 and CdS nanoparticles resulted in an efficient separation of the photogenerated charge carriers.[70]

Electrostatic LBL assembly of inorganic nanoparticles may also be accomplished on the surface of (sub)micron sized polymer spheres.[78,79] Caruso et al. have shown that anionic SiO_2 nanoparticles of ca. 25 nm diameter may be assembled on the surface of 640 nm diameter negatively charged polystyrene (PS) latex particles using the cationic polyelectrolyte poly(diallyldimethylammonium chloride) PDADMAC as the electrostatic 'glue'. The sequential assembly process leading to a PS core and multilayer SiO_2-PDAC shell structure is illustrated in Figure 9.14.
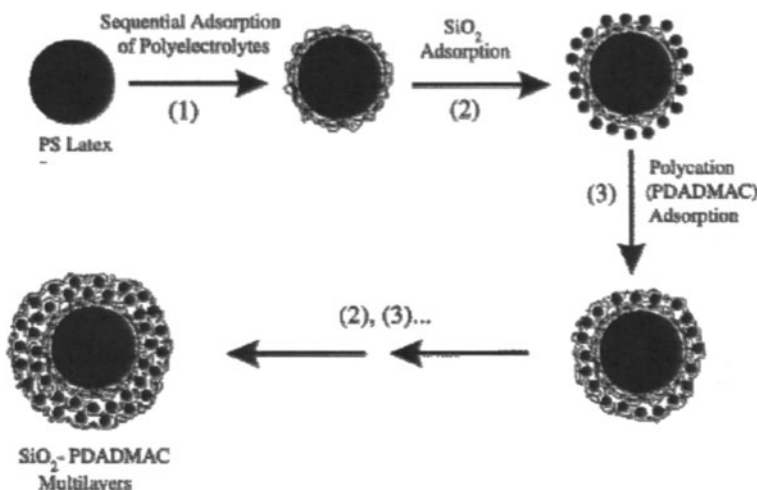
FIGURE 9.14. Schematic illustration of the assembly of composite multilayers on PS lattices. The first stage involves the sequential adsorption of oppositely charged polyelectrolytes (PDADMAC/PSS/PDADMAC) (Pr$_3$) (step 1) in order to produce a smooth and positively charged outer surface to facilitate the adsorption of negatively charged SiO_2. Subsequent alternate adsorption of SiO_2 (step 2) and PDADMAC (step 3) results in SiO_2-PDADMAC multilayers being formed on the PS lattices. (Reprinted with permission from Ref. 78, © 1998 American Chemical Society).

SiO$_2$-PDADMAC films of thickness ranging from a few tens to hundreds of nanometers on the PS latex core particles were prepared by the authors. A similar methodology was used by Dong and co-workers to assemble close-packed shells of silver nanoparticles on PS latex spheres.[79] The silver nanoparticles were rendered positively charged by capping with 4-aminothiophenol molecules and thereafter electrostatically bound to the surface of 1.5 μm diameter PS latex particles which were charged negatively by adsorption of a layer of PDADMAC followed by the anionic polyelectrolyte, PSS. The authors showed that the extent of silver nanoparticle binding to the latex spheres could be varied by modulating the electrostatic interaction between the positively charged silver nanoparticles and negatively charged PS latex spheres by simple solution pH variation. This is illustrated in the scanning electron microscopy (SEM) micrographs of the PS-core-Ag nano shell structures formed at different pH and of different shell thickness (Figure 9.15). The polymer core can be etched away to leave behind structures with hollow centers.
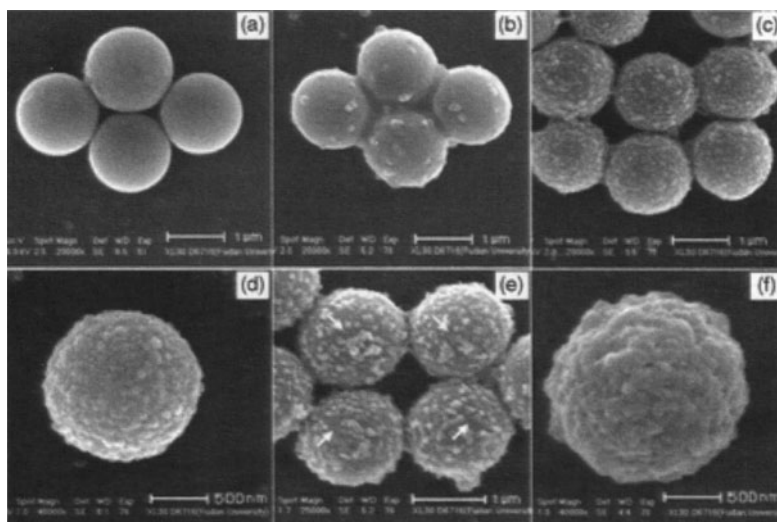
FIGURE 9.15. SEM micrographs showing (a) original PS spheres; silver-latex composites obtained at (b) pH 2.5; (c) pH 4.5; (d) high magnification of (c); (e) pH 6.0, arrows indicate some non-coated parts on PS spheres; and (f) pH 4.5 with PS spheres coated with four layers of silver nanocrystals. (Reprinted with permission from Ref. 79, © 2002 Royal Society of Chemistry).

The LBL assembly process based on electrostatic interactions is versatile in the sense that it can be extended to the assembly of charged biomacromolecules such as proteins/enzymes and DNA. In particular, the immobilization of enzymes in the form of thin films is important in biotechnological applications to increase the shelf life, dynamic range and reusability characteristics of the enzymes. Protein (enzyme)/polymer hybrid

films may easily be deposited by the electrostatic LBL method both on planar surfaces[68,80] and on polymer microspheres.[81]

9.3.4. NANOCOMPOSITES BY ELECTROSTATIC ENTRAPMENT IN THERMALLY EVAPORATED LIPID FILMS

A lipid-based protocol for the formation of nanocomposites has been developed in the author's group and has progressed chronologically from electrostatic entrapment of inorganic ions[82-84] to surface-modified inorganic nanoparticles such as silver,[85,86] gold[87-88] and CdS[89] to charged biomacromolecules such as proteins/enzymes[90-93] and DNA/peptide nucleic acids (PNA).[94,95] This simple beaker-based immersion method is illustrated in Figure 9.16 for the electrostatically controlled formation of nanoparticle-lipid hybrid films. The first step in this protocol consists of deposition of a suitable ionizable fatty lipid film on a solid substrate.
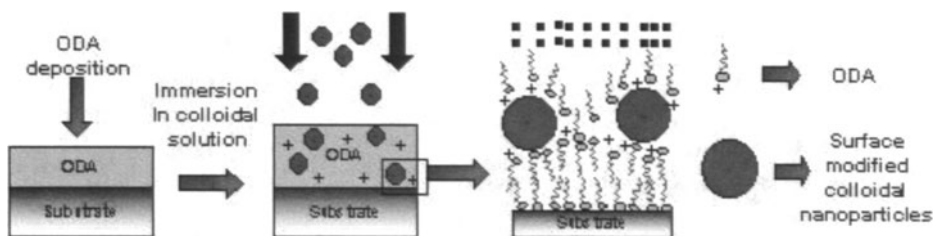
FIGURE 9.16. Diagram showing the various steps involved in the electrostatic entrapment of charged nanoparticles in thermally evaporated ionizable fatty lipid thin films.

This may be accomplished by resistive heating of the lipid powder in a conventional vacuum coating unit. In Figure 9.16, an octadecylamine (ODA) film has been shown, which during immersion in acidic solution, becomes positively charged. This film is then immersed in the colloidal solution consisting of negatively charged nanoparticles, the charging of the nanoparticles arising from ionization of carboxylic acid groups from 3-D self-assembled monolayers on the nanoparticle surface. During immersion, it is observed that the nanoparticles diffuse into the lipid film and in the case of gold, silver and CdS nanoparticles, this diffusion process is easily followed by the change in color that occurs in the films as they are populated by a progressively increasing number of nanoparticles.

An important challenge in nanoscale assembly concerns the growth of two-dimensional hetero-nanoparticle structures that are spatially separated. The formation of patterned hetero-colloidal particle composite thin films on

solid supports using the diffusion technique has been shown recently.[96] The process is extremely simple and consists of masking a thermally evaporated ODA film and immersing it sequentially in carboxylic acid derivatized silver (70 Å), gold (130 Å) and CdS (45 Å) nanoparticle solutions after exposing progressively larger areas of the film surface each time. In this manner, the silver nanoparticle region would be exposed to both the gold and CdS solutions while the gold region would experience an immersion in the CdS solution. However, little intermixing of the colloidal nanoparticles within any region was observed indicating that the trajectory of the nanoparticles in the film as they diffuse into the lipid matrix is essentially ballistic over large time scales.[96]

Development of protocols for the assembly of nanoparticles both in solution and in the form of thin films is an important aspect of nanotechnology that directly impacts commercialization of nanoparticle-based products. I have attempted to cover this fascinating area concentrating on one type of interaction, viz. electrostatic interactions, for enabling nanoparticle assembly. There are a number of advantages to using electrostatic interactions, some of the more important ones being that disassembly of superstructures can often be achieved and most of the protocols, be it assembly on planar surfaces or nanoscale curved surfaces, can be extended to charged biomacromolecules such as proteins and DNA. This is a vast area and it is very likely that I have missed citing important references. Such oversights are purely unintentional.

ACKNOWLEDGEMENTS

REFERENCES

1. Fendler, J.H. *Membrane Mimetic Chemistry Approach to Advanced Materials*; Springer-Verlag : Berlin, 1992.
2. Henglein. A. *Top. Curr. Chem.* **143**, 113 (1988).
3. El-Sayed, M.A. *Acc.Chem.Res.* **2001**, *34*, 257.
4. Alivisatos, A.P. *Science* **1996**, *271*, 933.
5. Ahmadi, T.; Wang, Z.L.; Green, T.C.; Henglein, A.; El-Sayed, M.A. *Science* **1996**, *272*, 1924.
6. Hamilton, J.F.; Baetzold, R.C. *Science* **1979**, *205*, 1213.

7. Weller, H. *Angew.Chem.Int.Ed.Engl.* **1998**, *37*, 1658.
8. Wang, Y. *Acc.Chem.Res.* **1991**, *24*, 133.
9. Mansur, H.S.; Grieser, F.; Marychurch, M.S.; Biggs, S.; Urquhart, R.S.; Furlong, D.N. *J.Chem.Soc., Faraday Trans.* **1995**, *91*, 665.
10. Shi, J.; Gider, S.; Babcock, K.; Awschalom, D.D. *Science* **1996**, *271*, 937.
11. Symonds, J.L. *Phys.Today* **1995**, *48*, 26.
12. Bulte, J.W.M.; Douglas, T.; Mann, S.; Frankel, R.B.; Moskovitz, B.M.; Brooks, R.A.; Baumgarner, C.D.; Vymazal, J.; Frank, J.A. *Invest.Radiol.* **1994**, *29*, 5214.
13. Shull, R.D.; McMichael, R.D.; Ritter, J.J. *Nanostruct. Mat.* **1993**, *2*, 205.
14. Fendler, J.H.; Meldrum, F. *Adv.Mater.* **1995**, *5*, 607.
15. Ledentsov, N.N.; Grundmann, M.; Kirstaedter, N.; Schmidt, O.; Heitz, R.; Bohrer, J.; Bimberg, D.; Ustinov, V.M.; Shchukin, V.A.; Yu Egorov, A.; Zhukov, A.E.; Zaitsev, S.; Kop'ev, P.S.; Alferov, Zh.I.; Ruvimov, S.S.; Kosogov, A.O.; Werner, P.; Gosele, U.; Heydenrich, J. *Solid State Electron.* **1996**, *40*, 785.
16. See the recent Feb.28, 200 issue of Chem.Eng.News and articles by R. Dagani therein for coverage of the new applications envisaged for nanomaterials.
17. Taton, T.A.; Mirkin, C.A.; Letsinger, R.L. *Science* **2000**, *289*, 1757.
18. Cao, Y.C.; Jin, R.; Mirkin, C.A. *Science* **2002**, *297*, 1536.
19. Chan, W.C.W.; Nie, S. *Science* **1998**, *281*, 2016.
20. Chan, W.C.; Maxwell, D.J.; Gao, X.; Bailey, R.E.; Han, M.; Nie, S. *Curr.Opinion Biotech.* **2002**, *13*, 40.
21. Sandhu, K.K.; McIntosh, C.M.; Simard, J.M.; Smith, S.W.; Rotello, V.M. *Bioconj.Chem.* **2002**, *13*, 3.
22. Collier, C.P.; Saykally, R.J.; Shiang, J.J.; Henrichs, S.E.; Heath, J.R. *Science* **1997**, *277*, 1978.
23. Maier, S.A.; Brongersma, M.L.; Kik, P.G.; Meltzer, S.; Requicha, A.A.G.; Atwater, H.A. *Adv.Mater.* **2001**, *13*, 1501.
24. Honig, B.; Nicholls, A. *Science* **1995**, *268*, 1144.
25. Weisbecker, C.S.; Merritt, M.V.; Whitesides, G.M. *Langmuir* **1996**, *12*, 3763.
26. Sastry, M.; Bandyopadhyay, K.; Mayya, K.S. *Colloids Surf.A.* **1997**, *127*, 221.
27. Mayya, K.S.; Patil, V.; Sastry, M. *Langmuir* **1997**, *13*, 3944.
28. Shipway, A.N.; Katz, E.; Willner, I. *ChemPhysChem* **2000**, *1*, 19.
29. Mandal, S.; Gole, A.; Lala, N.; Gonnade, R.; Ganvir, V.; Sastry, M. *Langmuir* **2001**, *17*, 6262.
30. Templeton, A.C.; Zamborini, F.P.; Wuelfing, W.P.; Murray, R.W. *Langmuir.* **2000**, 16, 6682.
31. Galow, T.H.; Boal, A.K.; Rotello, V.M. *Adv.Mater.***2000**, *12*, 576.
32. Kolny, J.; Kornowski, A.; Weller, H. *Nano Lett.***2002**, *2*, 361.
33. Ulman, A. *An Introduction to Ultrathin Organic Films : From Langmuir-Blodgett to Self-Assembly*, Academic Press, San Diego, 1991.
34. Auer, F.; Scotti, M.; Ulman, A.; Jordan, R.; Sellergren, B.; Garno, J.; Liu, G.-Y. *Langmuir* **2000**, *16*, 7554.
35. Gole, A.; Sainkar, S.R.; Sastry, M. *Chem.Mater.***2000**, *12*, 1234.
36. Chan, E.W.L.; Yu, L. *Langmuir* **2002**, *18*, 311.
37. He, H.X.; Zhang, H.; Li, Q.C.; Zhu, T.; Li, S.F.Y.; Liu, Z.F. *Langmuir* **2000**, *16*, 3846.
38. Hutter, E.; Fendler, J.H.; Roy, D. *J.Phys.Chem.B.* **2001**, *105*, 11159.
39 Xia, Y.; Rogers, J.A.; Paul, K.E.; Whitesides, G.M. *Chem.Rev.* **1999**, *99*, 1823.
40. Clemente-Leon, M.; Coronado, E.; Delhaes, P.; Gomez-Garcia, C.J.; Mignotaud, C. *Adv.Mater.* **2001**, *13*, 574.
41. Ganguly, P.; Paranjape, D.V.; Sastry, M. *J.Am.Chem.Soc.* **1993**, *115*, 793.
42. Riccio, A.; Lanzi, M.; Antolini, F.; De Nitti, C.; Tavani, C.; Nicolini, C. *Langmuir* **1996**, *12*, 1545.
43. Ebara, Y.; Mizutani, K.; Okahata, Y. *Langmuir* **2000**, *16*, 2416.
44. Sastry, M.; Ramakrishnan, V.; Pattarkine, M.; Gole, A.; Ganesh, K.N. *Langmuir* **2000**, *16*, 9142.
45. Sastry, M. *Current Sci.* **2000**, *78*, 1089.
46. Damle, C.; Gole, A.; Sastry, M. *J.Mater.Chem.* **2000**, *10*, 1389.
47. Kurth, D.G.; Lehmann, P.; Lesser, C. *Chem.Commun.* **2000**, 949.
48. Chen, X.Y.; Li, J.R.; Jiang, L. *Nanotechnology* **2000**, *11*, 189.
49. Tian, Y.; Wu, C.; Fendler, J.H. *J.Phys.Chem.* **1995**, *98*, 4913.
50. Patil, V.; Mayya, K.S.; Pradhan, S.D.; Sastry, M. *J.Am.Chem.Soc.*, **1997**, *119*, 9281.

51. Sastry, M.; Mayya, K.S.; Patil, V.; Paranjape, D.V.; Hegde, S.G. *J.Phys.Chem.B.*, **1997**, *101*, 4954.
52. Mayya, K.S.; Sastry, M. *J.Phys.Chem.B.*, **1997**, *101*, 9790.
53. Mayya, K.S.; Sastry, M. *Langmuir*, **1998**, *14*, 74.
54. Sastry, M.; Mayya, K.S.; Patil, V. *Langmuir*, **1998**, *14*, 5291.
55. Sastry, M.; Mayya, K.S. *J.Nano.Res.*, **2000**, *2*, 183.
56. Tran, Y.; Bernard, S.; Peretti, P. *Eur.Phys.J.Appl.Phys.*, **2000**, *12*, 201.
57. Sastry, M.; Rao, M.; Ganesh, K.N. *Acc.Chem.Res.*, **2002**, *35*, 847.
58. Mayya, K.S.; Patil, V.; Sastry, M. *Langmuir*, **1997**, *13*, 2575.
59. Mayya, K.S.; Patil, V.; Sastry, M. *J.Chem.Soc.Faraday Trans.*, **1997**, *93*, 3377.
60. Mayya, K.S.; Patil, V.; Kumar, P.M.; Sastry, M. *Thin Solid Films*, **1998**, *312*, 300.
61. Zhavnerko, G.K.; Agabekov, V.E.; Gallyamov, M.O.; Yaminsky, I.V.; Rogach, A.L. *Coll.Surf.A.*, **2002**, *202*, 233.
62. Muramatsu,K.; Takahashi, M.; Tajima, K.; Kobayashi, K. *J.Colloid Interface Sci.*, **2001**, *242*, 127.
63. Lee, D.K.; Kang, Y.S.; Lee, C.S.; Stroeve, P. *J.Phys.Chem.B.*, **2002**, *106*, 7267.
64. Kang, Y.S.; Lee, D.K.; Lee, C.S.; Stroeve, P. *J.Phys.Chem.B.* **2002**; *106*, 9341.
65. Du, H.; Bai, Y.B.; Hui, Z.; Li, L.S.; Chen, Y.M. Tang, X.Y.; Li, T.J. *Langmuir*, **1997**, *13*, 2538.
66. Iler, R.K. *J.Colloid Interface Sci.* **1966**, *21*, 569.
67. Decher, G. *Science* **1997**, *277*, 1232 and references therein.
68. Caruso, F.; Niikura, K.; Furlong, D.N.; Okahata, Y. *Langmuir* **1997**, *13*, 3427.
69. Mamedov, A.; Ostrander, J.; Aliev, F.; Kotov, N.A. *Langmuir* **2000**, *16*, 3941.
70. Hao, E.; Yang, B.; Ren, H.; Qian, X.; Xie, R.; Shen, J.; Li, D. *Mater.Sci.Engg.C.* **1999**, *10*, 119.
71. Lvov, Y.; Ariga, K.; Onda, M.; Ichinose, I.; Kunitake, T. *Langmuir* **1997**, *13*, 6195.
72. Maya, L.; Muralidharan, G.; Thundat, T.G.; Kenik, E.A. *Langmuir* **2000**, *16*, 9151.
73. Feldheim, D.L.; Grabar, K.C.; Natan, M.J.; Mallouk, T.E.; *J.Am.Chem.Soc.* **1996**, *118*, 7640.
74. He, J.-A.; Valluzzi, R.; Yang, K.; Dolukhanyan, T.; Sung, C.; Kumar, J.; Tripathy, S.K.; Samuelson, L.; Balogh, L.; Tomalia, D.A. *Chem.Mater.* **1999**, *11*, 3268.
75. Kumar, A.; Mandale, A.B.; Sastry, M. *Langmuir* **2000**, *16*, 6921.
76. Cassagneau, T.; Mallouk, T.E.; Fendler, J.H. *J.Am.Chem.Soc.* **1998**, *120*, 7848.
77. Kumar, A.; Mukherjee, P.; Guha, A.; Adyantaya, S.D.; Mandale, A.B.; Kumar, R.; Sastry, M. *Langmuir* **2000**, *16*, 9775.
78. Caruso, F.; Lichtenfeld, H.; Giersig, M.; Mohwald, H. *J.Am.Chem.Soc.* **1998**, *120*, 8523.
79. Dong, A.G.; Wang, Y.J.; Tang, Y.; Ren, N.; Yang, W.L.; Gao, Z. *Chem.Commun.* **2002**, 350.
80. Lvov, Y.; Ariga, K.; Ichinose, I.; Kunitake, T. *J.Am.Chem.Soc.* **1995**, *117*, 6117.
81. Caruso, F.; Mohwald, H. *J.Am.Chem.Soc.* **1999**, *121*, 6039.
82. Ganguly, P.; Sastry, M.; Pal, S.; Shashikala, M.N. *Langmuir* **1995**, *11*, 1079.
83. Mandal, S.; Sainkar, S.R.; Sastry, M. *Nanotechnology* **2001**, *12*, 358.
84. Damle, C.; Kumar, A.; Sastry, M. *J.Phys.Chem.B.* **2002**, *106*, 297.
85. Sastry, M.; Patil, V.; Sainkar, S.R. *J.Phys.Chem.B.* **1998**, *102*, 1404.
86. Patil, V.; Sastry, M. *Langmuir* **1998**, *14*, 2707.
87. Sastry, M.; Patil, V.; Mayya, K.S. *Langmuir* **1997**, *13*, 4490.
88. Patil, V.; Malvankar, R.B.; Sastry, M. *Langmuir* **1999**, *15*, 8197.
89. Patil, V.; Sastry, M. *J.Chem.Soc.Faraday Trans.* **1997**, *93*, 4347.
90. Gole, A.; Dash, C.; Rao, M.; Sastry, M. *Chem.Commun.* **2000**, 297.
91. Gole, A.; Dash, C.; Mandale, A.B.; Rao, M.; Sastry, M. *Anal.Chem.* **2000**, *72*, 1401.

92. Gole, A.; Sastry, M. *Biotech.Bioeng.* **2001**, *74*, 172.

93. Gole, A.; Chaudhari, P.; Kaur, J.; Sastry, M. *Langmuir* **2001**, *17*, 5646.

94. Sastry, M.; Ramakrishnan, V.; Pattarkine, M.; Ganesh, K.N. *J.Phys.Chem.B.* **2001**, *105*, 4409.

95. Ramakrishnan, V.; Sable, M.; D'Costa, M.; Ganesh, K.N.; Sastry, M. *Chem.Commun.* **2001**, 2622.

96. Sastry, M.; Gole, A.; Sainkar, S.R. *Langmuir* **2000**, *16*, 3553.

10

Biological and Biomimetic Applications of Nanoparticles

Lucia Pasquato,[†] Paolo Pengo,[‡] and Paolo Scrimin[‡]

[†]*Dipartimento di Scienze Chimiche, Università di Trieste, via L. Giorgieri 1, I-34127 Trieste, Italy and* [‡]*Dipartimento di Chimica Organica, and ITM-CNR, Sezione di Padova, Università di Padova, via Marzolo 1, I-35131 Padova, Italy.*

10.1. INTRODUCTION

Over the last few decades, nanometer sized particles have been extensively exploited in conjunction with macromolecular species in the development of analytical tools for biological purposes; this trend did not stop through the years. Actually the growing interest and knowledge on nanoscale materials has positively increased the tools available in cell biology, analytical biochemistry, cytohistochemistry and immunocytochemistry. Historically, the major role was played by bioconjugate latex nanospheres[1] and gold colloids,[2,3] while more recently low and high nuclearity gold clusters have been exploited. An emerging literature concerns group II-VI and III-V semiconductor nanocrystals bioconjugates, having unique and appealing optical properties. In this overview latex bioconjugates will not be discussed; gold colloids, gold clusters and semiconductor bioconjugates will be described in some detail, with particular attention to gold colloids and clusters.

10.2. COLLOIDAL GOLD BIOCONJUGATES

Colloidal gold can be easily prepared from diluted $HAuCl_4$ aqueous solution by action of a wide variety of reducing agents,[4] the changing the experimental conditions allows one to obtain gold colloids of different size and size distributions. Several procedures are well-established and 3 nm to few hundreds nm colloids are easily available in a reproducible way. Gold colloids show an absorption band due to the excitation of the surface plasmons in the UV-Vis region of electromagnetic spectrum.[5] To that band is due the ruby-red color of colloidal gold and to its shift to longer wavelength upon aggregation[6] is due the application of such colloids in aggregation assays (see below). Macromolecules are known to stabilize gold colloids through absorption on the particles. It is widely accepted that absorption occurs by an ensemble of electrostatic and weak interactions, although the formation of real chemical bonds cannot be ruled out. Stabilization by biomolecules was recognized at the early beginning of colloidal gold history but an accurate analysis of this phenomenon was possible only in more recent years.[7] It was possible to highlight that electrolyte-induced colloids flocculation is inhibited if a sufficient amount of macromolecule is added to the sol. The stabilization increases with macromolecule concentration, until the addition of a further amount is no longer effective. This analysis, applied to many biomolecules of different size, allowed to conclude that the stabilization process consists, at the molecular level, in the formation of a monolayer of macromolecules on the gold surface or, in other words, a 3D self-assembled monolayer formed by weak interactions. When proteins are taken into account, absorption is better achieved when the pH of the colloidal solution is brought near or slightly above the isoelectric point[8] of the macromolecule, while other experimental conditions give less stable conjugates. The important point to be stressed is that proteins absorbed on gold colloids retain their native structure without denaturation, while denaturation occurs upon absorption on flat gold surfaces.[9] Nevertheless Rotello[10] and co-workers reported an example of negatively charged monolayer protected clusters (MPC), not a naked colloid, that inhibit chymotrypsin (K_i^{app} = 10.4±1.3 nM) with enzyme denaturation, while little or no inhibition was observed with elastase, β-galactosidase, or cellular retinoic acid binding protein. The scope of proteins absorbed onto gold colloids is extremely large, ranging from antibodies to lectins to enzymes and lipoproteins. In all cases their activity was comparable to that of free proteins. The conjugates between colloids and proteins were extremely appealing in histochemical analysis, due to their particulate nature and their high electron density, making them easily localized by optic and electron microscopy. The most important feature of such systems was the

specificity imparted by the particular protein chosen. This allowed the preparation of very specific and sensitive probes in ultrastructural analysis. The first routinely used gold conjugate was gold-protein A,[11] a immunoreactive protein from staphylococci, then the more efficient protein G (from streptococci) gold conjugate was introduced. The interesting properties of proteins A and G is their binding affinity towards immunoglobulines occurring in the Fc region which is not involved in antigen binding. Within this approach, it is possible to detect the formation of an antigen-antibody complex by gold protein A(G) labels which stick only where the antibody is present. This is an indirect method, since the gold conjugate is used to detect the presence of an antigen antibody complex and not to detect the antigen itself, Figure 10.1a. The success of this method depends on the quality of the antibody (usually called primary antibody) used. This technique led to the ultrastructural localization of antigens in cells and tissues, and various type of antigens have been successfully revealed,[3] but the accuracy of such localization has an upper limit due to the dimension of gold-protein A(G)-antibody complex. To circumvent this problem gold-antibody conjugates have been developed. This is a direct method, but requires the availability of different conjugates for each different antigen to be detected, Figure 10.1b.
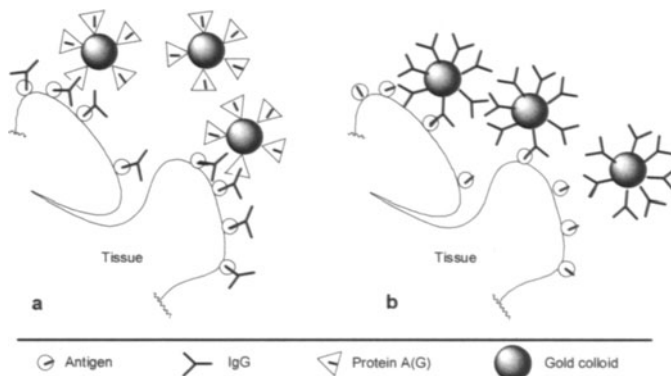
FIGURE 10.1. Indirect (a) and direct (b) method for gold colloids labeling with antibodies.

Another important class of gold conjugates is the one derived from lectins, that are carbohydrates binding proteins. Keeping in mind that cell recognition and cells adhesion are carbohydrates mediated processes (see a subsequent section),[12] it is easy to understand the important role played by lectins conjugated gold colloids in the analysis of cells surface topology. Here again, optimal absorption of lectins to colloids, occurs at pH near the lectins isoelectric point. In the same way for gold antibody technique, gold lectins technique may be a direct or indirect one. In the direct one, lectin is

directly absorbed onto colloids, and this multivalent particle interact with the target sugar moiety, in the indirect one, lectins interact with the sugar moiety, and a gold tagged molecule with affinity for lectin is added. This approach suffers the same limitation of the gold-protein A(G)-antibody approach. Enzyme-conjugated colloids are useful as markers to understand metabolic pathways through *in-situ* localization of substrate molecules, enabling the topological detection of binding events in fixed cells. The first enzymes conjugated on gold colloids were RNase and DNase for nucleic acids localization by electron and optical microscopy in cells and tissue.[13] After that, various examples of enzyme-conjugates appeared. Albumin from bovine serum, (BSA) was conjugated to gold colloids, this complex was used in understanding the albumin transport in capillary endothelial cells. Streptavidin and avidin were conjugated to gold, taking advantage from the strong affinity of these proteins for biotin ($K_d = 10^{-15}$ M)[14] and others biotinylated molecules such as antibodies, DNA strands etc. This makes streptavidin-gold conjugates a useful, potentially "universal", tag in the development of new aggregation assays. In fact, the gold-biotin-avidin system is continuously refined. A previously developed empirical "flocculation parameter"[15] was used to quantify the avidin induced flocculation of biotinylated gold colloids.[16] Lipoproteins were conjugated to gold, but in this case the development was not as straightforward as in other cases, due to the colloidal nature of lipoproteins. VLDL, LDL, HDL were conjugated to gold, allowing to get an insight on receptor binding and internalization in a variety of cell types. Still in recent year many examples of enzyme and protein conjugated to gold colloids have been reported[17,18] and new methods of functionalization are emerging.[19] An alternative approach for the functionalization of colloidal gold has been described by Sastry and co-workers,[19] they used a non covalent self-assembling approach for the functionalization of octadecanethiol protected colloids (35±7 nm diameter) with an alkylbiotin moiety. The self-assembling of this biotinylated compounds gave an interdigitated bilayer. These functional colloids proved to be stable and were aggregated by addition of avidin. Control experiments conducted by addition of BSA, hemoglobin, cytochrome C to the biotinylated colloids did not show any aggregation. Sastry and co-workers reported that a novel gold colloid endoglucanase conjugate[20] increased the half life of the enzyme with respect to that of the free enzyme in solution, envisioning potential industrial applications for such systems. Rosenzweig[21] and co-workers reported a new aggregation test to quantify the level of anti-protein A in serum samples based on protein A-conjugated gold colloids (10 nm in diameter). The authors reported a detection limit of 1 μg/ml. The aggregation process was followed at 620 nm by spectrophotometric technique. Mirkin and co-workers[22,23,24] reported a

similar approach aimed to the development of DNA hybridization assays that will be discussed in detail in a following section. Englebienne[25] reported that the surface plasmon resonance peak of colloidal gold conjugated with monoclonal antibodies is red-shifted upon complexation with their antigen targets. The shift occurs even in absence of aggregation or flocculation processes. Moreover the author claim that this method can be applied in the measurement of the apparent antibody-ligand affinity constant. A new approach to the colorimetric detection of human lung carcinoma cells (LCC) based on gold colloids conjugates was reported recently,[26] in this study 10 nm gold colloids conjugated to ALT-04 monoclonal antibody specific to surface antigen of human lung carcinoma cells were used to detect successfully such kind of cells. Nitrocellulose strip was spotted with a solution of ALT-04, then BSA was added to block non-specific absorption and eventually a suspension of LCC was added and the strip, stained with ALT-04 functionalized gold colloids. After size enlargement with HAuCl$_4$/ hydroxylamine, a lower detection limit of 100 cells/ml was obtained, allowing naked eye diagnosis. The colloidal gold technique was undoubtedly very successful in immunocytochemical analysis but it suffers of many disadvantages mainly due to the large size of the colloids with respect to the domains to be labeled; an important problem concerned the quantitative data obtained in colloidal gold technique. It is not generally possible to obtain a one-to-one correlation between density of labeling and density of target in the tissue, because of the multivalent nature of conjugated gold particles and to the obvious steric effect. An accurate study showed that the efficiency of this method is below 20%.[27,28] The second major problem is related to the low capability of such systems to interact with target molecules placed in depth in the sample, so that only exposed epitopes are easily labeled. It was than realized that efficiency in quantitative analysis is strongly dependant on the size of colloidal gold. The smaller the colloids, the larger is the efficiency of the labeling process. This observation was corroborated by many studies conducted under different labeling conditions. It was argued that small particles having higher labeling efficiency may be suitable for semi quantitative analysis and this led to the development of low and high nuclearity metal clusters compounds as markers in immunocytochemistry. Nowadays these compounds are the most used ones for those purposes.

10.3. LOW AND HIGH NUCLEARITY METAL CLUSTERS CONJUGATES

Many heavy metal clusters such as Hg_4, W_{11}, Ir_4, Au_{11},[29] that can be attached to side groups of biomolecules as thiols, amine, carboxylates have been exploited as markers in electron microscopy analysis of tissue sections.[30,31] These compounds are significantly smaller than gold colloids. This allows them to penetrate deeply in the sample to be labeled. Among these metal clusters compounds, triphenilphospane stabilized undecagold clusters are very promising, since they are not naked colloids but passivated nanoparticles, Figure 10.2a. Such system proved to be one of the best probe in electron, optic and confocal microscopy.[30] Undecagold clusters are quite stable; they are functionalizable (by a real covalent bond) in such a way that they may be covalently tagged to macromolecules.
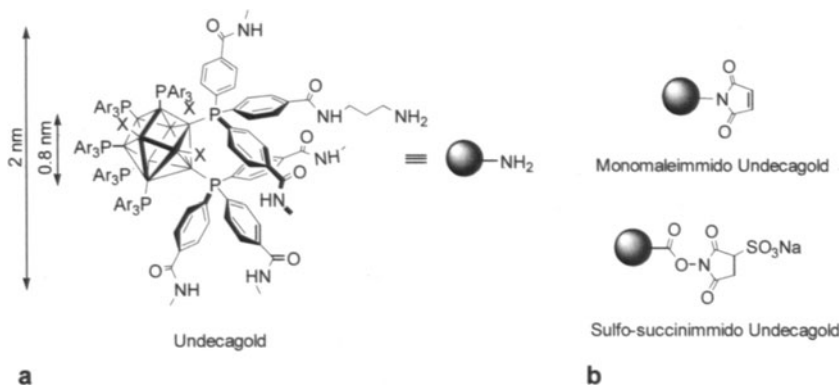
FIGURE 10.2. Schematic representations of commercially available gold clusters.

Undecagold clusters bind only one molecule; they are monovalent species, although there are no conceptual limits in building up multivalent analogs. The dimension of the undecagold core is ca. 0.8 nm. Larger gold clusters with diameter of about 1.4 nm and counting ca. 67 gold atoms have been prepared as well.[32] These gold cluster probes are commercially available and are known as Undecagol[®] and Nanogold[®] (NG), respectively. Monomaleimmido undecagold, sulfo-succinimmido undecagold clusters are commercially available as well. They have on their outer surface a maleimmido group reactive towards thiols or a sulfo-N-hydroxysuccinimide ester reactive towards free amine, Figure 10.2b. The functionalization reactions are carried out under very mild conditions and the reaction product can be recovered free of unbound reagent by simple gel chromatography protocols. A great variety of biologically interesting molecules (macromolecular species or not), ranging from proteins, Fab' antibody

fragment[33] and peptides,[34,35] to ATP, nucleic acids,[36] lipids, phospholipids, carbohydrates,[37] and Ni(II) chelator,[38] have been conjugated to Au_{11} or NG clusters. These molecules generally retain their biological activity after grafting to gold clusters. However, it is worth noting that many of these molecules, especially the smaller ones, can not be conjugated to gold colloids because they do not form stable compounds.[39] Gregori et al reported an interesting example of peptide tagged with nanogold clusters,[35] by labeling the β-amyloid peptide (a 40 residue peptide involved in the development of the Alzheimer disease) with NG clusters. They were able to detect the binding site of the β-amyloid peptide in the proteosome. Shipley[40] reported the use of monomaleimmido Nanogold® in the localization of the N-terminal domain of the LDL receptors, reconstructed into egg yolk phosphstidylcholine vesicles double layer. This receptor has its binding site in the N-terminal domain, where modular cysteine-rich repeats are found. After reduction of the disulfide bond, the reconstructed receptor was labeled with monomaleimmido Nanogold® and imaged by cryoelectron microscopy. In the receptor images, the cysteine-rich domain was found at the distal end of the extravesicle domain. On the basis of their data, the authors proposed two models for the arrangement of the seven cysteine-rich repeats of the ligand binding domain of the LDL receptor. In this case gold labeling technique showed to be a useful tool to obtain structural information when RX data are not available. The functionalization of gold clusters with the Fab' fragment of immunoglobulins G, which is the antigen reactive moiety of IgG, allowed the introduction of these compounds in immunocytochemistry as substitutes for gold colloids. These Fab' conjugates are similar in action to the IgG conjugates gold colloids but their small size allows a better localization of antigens and a better understanding of cell surface topology and to obtain more reliable semiquantitative data of antigen density. The conjugation occurs by interaction of maleimmido undecagold (nanogold) with a free –SH moiety in the hinge region of the Fab' fragment under protein friendly conditions. A further improvement in gold clusters immunocytochemical techniques was the introduction of fluorophore tagged gold clusters conjugates. Because this probe may be used as dual probe in correlative microscopy, these compounds are known as FluoroNanogold® or FluoroUndecagold®. Fluorophore conjugated colloidal gold has proven to be of limited applicability due to the extensive fluorescence quenching by the gold colloid. When a fluorophore is bound to a Fab' fragment or streptavidin conjugated NG, the distance between the gold cluster and the fluorophore, makes the fluorescence quenching less pronounced. Fluorescein[41,42] and Cy3 were used as fluorophore. FluoroNanogold has been successfully used in visualization of antigens in the same cell by light and electron microscopy.[42,43,44] There is a major disadvantage in the undecagold technique

related to the small size of the clusters: thus a further process of size enlargement by metal silver deposition on the gold clusters is required in order to make them visible by microscopy techniques. This process, called silver enhancement, is routinely used and well established.[45]

10.4. BIOLOGICAL APPLICATIONS OF SEMICONDUCTORS QUANTUM DOTS

Highly fluorescent nanoparticles like the ones derived from group II-VI and III-V semiconductors, usually called quantum dots (QDs)[46,47] are very appealing for application as labels in cell biology[48,49,50,51,52,53,54,55] and bioassays development, providing advantages over lanthanides and organic dye probes. The most used semiconductors are CdS, CdTe, ZnSe and CdSe-core/ZnS-shell and ZnSe nanocrystals capped with small organic molecules; the sizes of these nanocrystals, ranging from 1 to 10 nm, may be tuned during their synthesis[56,57] and their size dispersion is usually moderate. Interesting features of such nanosized semiconductors are their broad absorption and their narrow, symmetrical, photoluminescence spectra (typical full width at half maximum about 20 nm). The photoluminescence maximum position, usually occurring in the Vis-near IR, is strongly size dependant, and their fluorescence quantum yield ranges from 10% to 40-50% depending on preparation. The conjugation with biologically interesting molecules is generally achieved adopting a covalent[50,51,52,55] or self-assembling approach.[54] A bifunctional molecule (like mercaptoacetic acid or dihydrolipoic acid) used as nanoparticle cap may be covalently linked to the desired macromolecule,[53] or may interact with it by electrostatic interactions.[54] Having broad absorption spectra many different nanocrystals may be simultaneously excited at a single wavelength, but the small overlap in the fluorescence spectra allows one to detect the presence of each type of semiconductor nanocrystals without interference by the others. These properties have been exploited in the simultaneous detection of many substances and multiplexed applications are envisioned.[55] An interesting example was reported by Goldman and co-workers.[58] They synthesized CdSe-core/ZnS shell nanocrystals quantum dots capped with dihydrolipoic acid, and used these negatively charged nanoparticles as scaffold to self-assemble avidin and a maltose binding protein genetically fused with a positively charged leucine zipper domain (MBP-zp). Both avidin and MBP-zp are positively charged molecules that strongly self-assemble onto the negatively charged quantum dots. Avidin is a well known tetrameric biotin binding protein that binds commercially available biotinylated antibodies with high affinity constants as well, Figure 10.3.
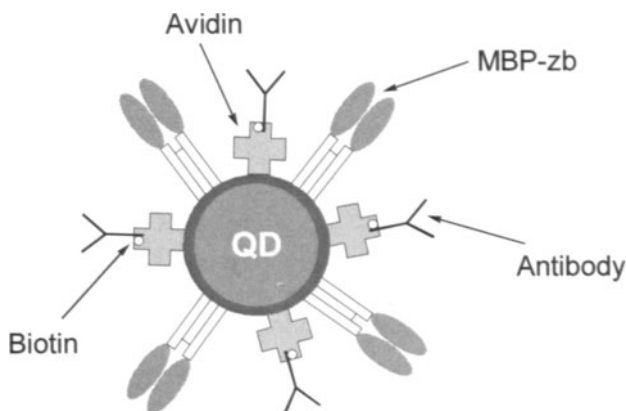
FIGURE 10.3. Cartoon representation of avidin-MBP-zb quantum dot assembly.

MBP-zp was introduced only to improve the purification process. Two different sample of avidin modified QDs emitting at 520 nm and 590 nm, were incubated with biotinylated antibodies against staphylococcal entherotoxin B (SEB) and cholera toxin respectively. The prepared QDs conjugates were tested in the simultaneous detection of SEB and cholera toxin. When the samples were imaged using a 535 nm filter, only the anti cholera toxin was detected, while using a 595 nm filter only the anti SEB conjugated QDs were detected, allowing separate detection of two protein toxins in the same sample. The authors claim that improved instrumentation will allow QD-antibodies to be used in multianalyte assays. Moreover their high quantum yield makes them a good tag for macromolecules when confocal microscopy is used as the analytical technique.[59,60] QDs have been incorporated in nanobeads.[55] For instance a system developed by Nie and co-workers consists in CdSe QDs with different emission maxima and intensities incorporated into 1.2 μm polystyrene beads, for optical encoding. If a 6 colors, 10 emission intensities array is used, this system can theoretically encode one million protein or nucleic acids sequences. Further examples will be discussed in the section devoted to DNA recognition. Semiconductor nanocrystals have been used to prepare QDs tagged multiple layered shell microsphere by stepwise self-assembly.[61] In this last example, due to Caruso and co-workers, composite microsphere based on a polystyrene (PS) core and a multilayer shell containing CdTe QDs were used in agglutination assay. The multilayer deposition was achieved by a self-assembling approach based on electrostatic interactions. The PS core was coated with a triple polyelectrolyte layer (PE$_3$) made of poly (allylamine hydrochloride) (PAH), poly (sodium styrenesulfonate) (PSS) and again poly

(allylamine hydrochloride) (PAH), then negatively charged thioglycolic capped CdTe QDs were added. The process was repeated up to three times, before eventually capping the microsphere with a $(PAH/PSS)_2$ layer followed by an Anti IgG layer to impart biospecificity to the composite particle. The effectiveness of this system was tested in an agglutination assay for mouse IgG. Different amounts of mouse IgG were added to anti-mouse IgG coated beads, leading to aggregation of the particles as proven by light scattering measurements and fluorescence microscopy experiments. Bioconjugated semiconductor nanoparticles have been used in immunoassay. ZnS capped CdSe semiconductor nanoparticles reported by Dubertret and co-workers[62] were encapsulated in phospholipid block-copolymer micelle, Figure 10.4, and used as probes for *in vivo* and *in vitro* imaging.
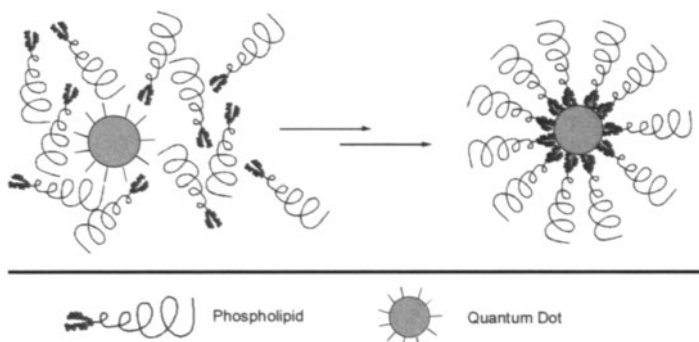
FIGURE 10.4. Polymeric phospholipids encapsulated quantum dots.

The same system, subsequently functionalized with DNA, was used to hybridize to specific, complementary sequences in vitro. When injected in Xenopus embryos these nanoparticles showed to be nontoxic and stable towards photobleaching. Their long time photostability allows one to use them for the real time monitoring of cellular processes.

10.5. DNA AND NANOPARTICLES

DNA stores the genetic information for the living matter. The properties that allow it to act so well for this purpose have started to be exploited for the obtainment of nanostructures.[63] Thus it is not surprising that DNA has been attracting, since the mid eighties, a large number of scientists for the construction of nanoparticle network materials. Mirkin[64] and Alivisatos[65] published in 1996 two important contributions on the use of DNA-derivatized gold colloids for the realization of self-assembled nanoparticles.

The basic idea behind their work is that particles, functionalized with oligonucleotides, may interact if hybridization with a complementary polynucleotide occurs (Figure 10.5).
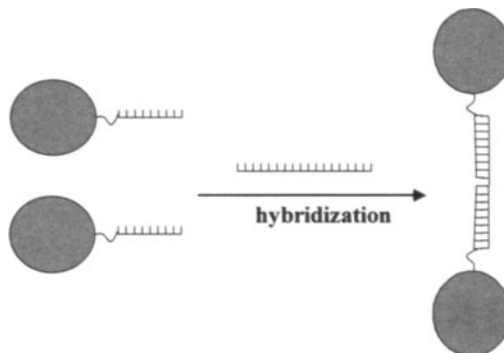
FIGURE 10.5. Oligonucleotide-functionalized nanoparticles interact via hybridization with a complementary polynucleotide

This may lead to the generation of precisely designed arrangements of these particles (either composed of a metal or a semiconductor) for the obtainment of new materials with potential application in electronics (laser technology, for instance). This topic was already reviewed in 1999[66] and its application to DNA detection will be discussed in a subsequent section. The most recent paper on hybridization and enzymatic extension of gold nanoparticles-bound oligonucleotides has been published by Keating and Fedoroff.[67] They have found that, although steric factors are important for hybridization to particle-bound primers, the efficiency of the process can be greatly improved by decreasing primer surface coverage. They have also demonstrated the possibility to extend the nanoparticle-bound primers by DNA polymerase. As said above the "communication" between the particles is possible because of their functionalization with oligonucleotides and the presence of a complementary linker oligonucleotide in the solution. By using nanoparticles of different size quite elaborate patterns of interconnected materials can be obtained (Figure 10.6).[68, 69]

An obvious prerequisite for the generation of assemblies of this sort is the appropriate functionalization of the Au-nanoparticle with a protecting monolayer. Thus Mirkin's group used citrate for this purpose while Alivisatos's one used the dipotassium salt of bis(p-sulphonatophenyl)phenylphosphane. Both protecting shells allow the penetration of the thiol-functionalized oligonucleotides thus leading to their incorporation into the nanoparticle. The problem is more complex in the case of metal particles different from gold and quantum dots assemblies (CdSe, for instance). However, Mirkin et al. were able to solve the problem in both

cases. With Ag this was done very elegantly by covering the silver core with a gold layer.[70] In the case of QDs by using trioctylphosphine- and trioctylphosphine-covered CdSe/ZnS QDs and subjecting them to exchange with an excess of 3-mercaptopropionic acid. These nanoparticles, in their anionic form, were readily soluble in water and could be functionalized with thiol-terminated oligonucleotides.[71]

Niemeyer's group used a different strategy for the obtainment of the nanostructures. While they used also single stranded DNA as the templating unit, the communication with the nanoparticles was mediated by the interaction streptavidin/biotin.[72] An analogous strategy was also used by Mirkin and Letsinger.[73] They were able to prove, for the first time, the reversibility of the assembly process which is controlled by the temperature of the mixing of the functionalized nanoparticles.
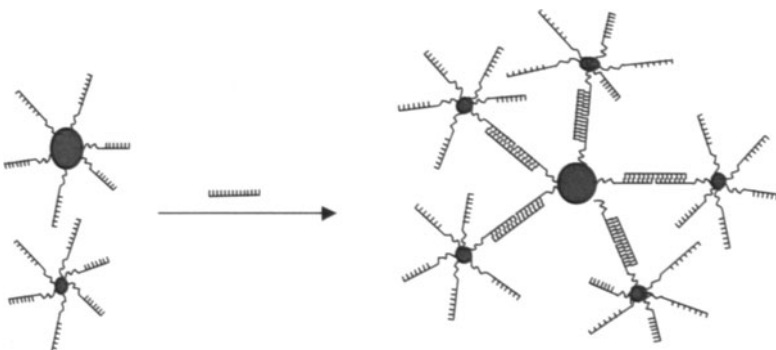
FIGURE 10.6. The interaction between particles of different size may give rise to elaborate patterns of interconnected materials.

Interactions based on less sophisticated principles but, nevertheless leading to interesting structures, are those that lead to parallel linear wires of DNA, covered by lysine-capped Au colloids.[74] Thus double stranded DNA acts as a polyanionic template for the cationic nanoparticles which are sandwiched in between double helices in a continuous array (Figure 10.7). Polycationic polymers may also interact with silver nanoclusters made anionic via functionalization with citrate. This supercluster eventually interacts with plasmid DNA.[75] In this case, too, the driving force is an electrostatic interaction rather than hydrogen bonding like in the examples reported above.

An exciting extension of the nanoparticles communication mediated by DNA is that reported by Mirkin et al. In this case they have targeted a gold surface previously modified with oligonucleotides by using Dip-Pen nanolithography (DPN). In their experiment they have patterned a gold surface with 16-mercaptohexadecanoic acid by using DPN and covered the surrounding area with 1-octanethiol to fully passivate the gold. The surface is subsequently reacted with alkylamine-functionalized DNA via the

formation of an amide bond. The process of DPN is then repeated with a different pattern and a different oligonucleotide sequence. The authors could demonstrate that oligonucleotide-functionalized nanoparticles interacted with a specific pattern on the surface according to the complementarity of their DNA sequences and no cross-reactivity was observed.[76] The immobilization of nanoparticles on solid supports by using analogous procedures was recently achieved also in other laboratories.[77] It was also shown that the particle-surface interaction can be achieved using the biotin-streptavidin interaction and that the scanning electrochemical microscopy can be an excellent tool to imagine the patterned surface.[78] Silver particle deposition greatly enhances the sensitivity.
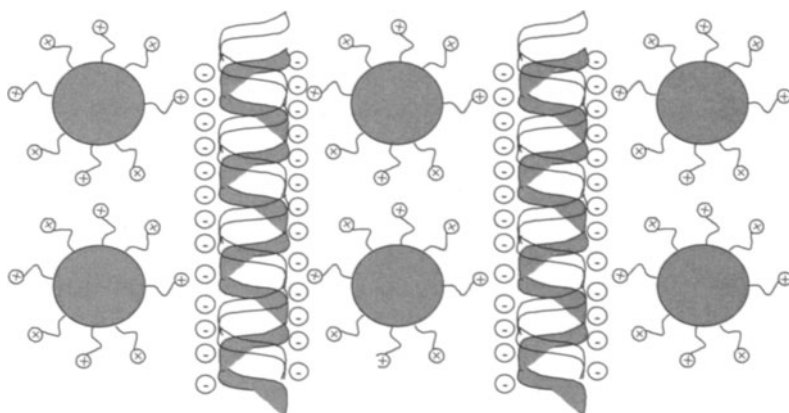
FIGURE 10.7. Nanoparticles functionalized with cationic ammonium groups interact with anionic DNA forming continuous intercalating arrays.

10.6. DNA RECOGNITION

By conjugating the ability of mercaptoalkyloligonucleotide-modified gold nanoparticles to interact in the presence of an appropriate polynucleotide sequence with the change of color of the solution due to the formation of aggregates, Letsinger and Mirkin[22] were able to obtain a selective colorimetric detection system for polynucleotides.

They have chosen ~13 nm in diameter gold particles that show a sharp plasmon absorption band with wavelength maximum at 520 nm (their solution is red) for the functionalization with a thiol-terminated oligonucleotide. The procedure is very similar to the one described in the previous section for the obtainment of nanostructures. The important point in this case is that when the interparticle distance of the aggregates, formed in the presence of a complementary polynucleotide, is less than the average particle diameter, the plasmon absorption band shifts to a longer wavelength

and the color of the solution becomes blue. Thus, without using radioactive groups or organic substituents, the Au nanoparticles become the reporter groups. The extended network of nanoparticles formed upon hybridization (Figure 10.8) is at the basis of the sensing system! Two interesting aspects are connected to the aggregation process: i) hybridization is greatly accelerated by heating or freezing the solution and ii) the color changes are significantly enhanced and easily visualized if the hybridized sample is "developed" on a solid support. The system is very sensitive and the early experiments indicated that as low as 10 femtomoles of polynucleotide could be detected with this methodology. Even more interesting is the selectivity related to the exceptionally sharp "melting transitions" of the aggregates. This allows one to distinguish target sequences that contain one base end mismatches, deletions, or an insertion from the fully complementary target.[79] It was shown that the change of color is associated with the increase of the extension of the polymeric aggregate rather than to a change of the interparticle distance.[23, 80] Although very attractive, the above system has limitations. Perhaps the most important is related to the sedimentation properties of the nanoparticle networks which precludes the possibility of obtaining acceptable endpoints when the system is used in quantitative determination. In an attempt to find nanoparticles devoid of this problem it was discovered that 50 nm diameter Au clusters are the best choice. However a price has to be paid because the formation of the aggregates can no longer be followed with the naked eye. In fact the aggregation rather than to a color change is associated with a fading of the color. Thus a spectrophotometer allows one to follow the process taking also advantage of the very high extinction coefficient of the surface plasmon band of these relatively big nanoparticles.[81] A powerful technique for the detection of the aggregates formed in the presence of the target ploynucleotide is angle-dependent light scattering and fractal dimension analysis.[82]
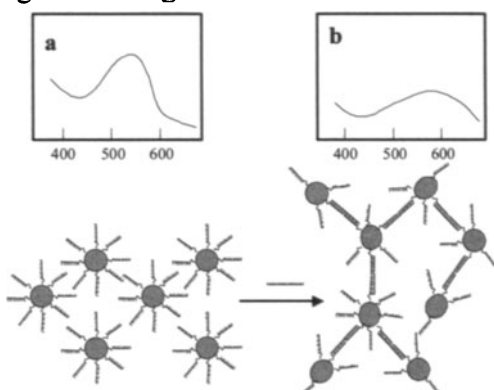
FIGURE 10.8. Au-nanoparticle aggregation is associated with a change of the absorption wavelength of the surface plasmon band which is centered at ~520 nm before aggregation (a) and moves close to ~600 nm after aggregation (b).

In a previous section we have already mentioned the use of 1.4-nm gold clusters conjugated to polyclonal antibodies for the simultaneous detection of a pre-mRNA splicing factor by light and electron microscopy taking advantage of the less pronounced quenching of the fluorescence of these small aggregates.[42] The problem of fluorescence quenching by gold aggregates can be easily solved just by using different nanoparticles. For instance Nie et al.[83] used 20-nm latex nanobeads to probe specific sequences on single DNA molecules. They have covalently linked to DNA EcoRI, a site specific endonuclease that functions as a dimer and recognizes the hexanucleotide sequence GAATTC through 12 hydrogen bonds in the major groove of a duplex DNA molecule. The resulting nanoconjugates display DNA binding and cleavage activities analogous to those of the native enzyme. In the absence of Mg(II), a required cofactor for the enzyme, the conjugates bind to specific sequences without hydrolyzing the polymer. In the case of single DNA molecules stretched and immobilized on a solid surface, binding occurs again very specifically and can be directly visualized by florescence microscopy. The relevance of this approach has been recently enhanced by the observation that DNA-Au nanomaterials conjugation does not disrupt the activity of the native proteins.[84]

The automated detection of DNA or polynucleotides in general is a quite hot topic for its relevance in genomic. The groups of Letsinger and Mirkin have recently reported a scanometric DNA array detection system using gold nanoparticles whose signal was amplified by reduction of Ag(I).[85] They have used their oligonucleotide-modified gold nanoparticles (instead of a florescent probe) and targeted oligonucleotides immobilized on the surface of float glass microscope slides. In the presence of a polynucleotide target the nanoparticles interact with the surface when hybridization occurs (thus only with complementary sequences). Since the labeling of the nucleotide targets with nanoparticles substantially alters the melting profile of the targets (see above), the difference permits the discrimination of an oligonucleotide sequence from targets with single-nucleotide mismatches. The selectivity is three times that observed with fluorophore-labeled targets. More important, the sensitivity can be amplified by two orders of magnitude via nanoparticle-promoted reduction of Ag(I) on the Au aggregate. The sorting of fluorescent nanocrystals (CdSe/ZnS) with DNA has been also reported by the groups of Alivisatos and Gerion.[86] These biocompounds retain the properties of both nanocrystals and DNA. In the particular case described by the authors four different sequences of DNA are linked to four nanocrystals samples having different colors of emission. When the conjugates are mixed together it is possible to sort each type of nanoparticle by using hybridization on a defined micrometer-size surface containing the complementary oligonucleotide. Since the above nanoparticles are about 7 to

14 nm in diameter it may be possible to control their positioning to within a few tens of nanometers. This suggests exciting applications in genetics.

The DNA-nanoparticle conjugates have been used in conjunction with other techniques for the detection of target DNA. The principle is basically always the same: two oligonucleotides are hybridized in the presence of a complementary, target substrate. Several groups have functionalized the surface of a quartz crystal microbalance with a oligonucleotide and altered its vibration frequency by interaction with oligonucleotide-Au nanoparticles conjugates.[87, 88, 89] The detection sensitivity was increased to as low as 10^{-14} M with 50-nm gold nanoparticles.[89b] Further amplification of the sensitivity could be provided by formation of a dendritic cluster by connecting several nanoparticles[88] or by enlarging the nanoparticles in situ by treatment with a Au(III) salt and reduction with NH_2OH (Figure 10.9).[90]
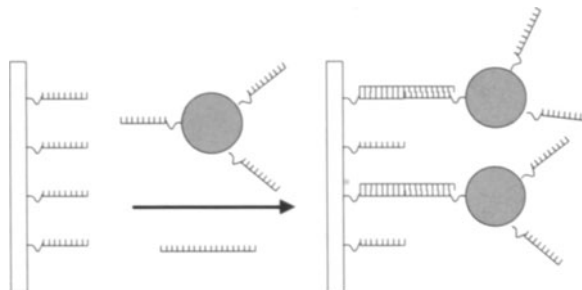
FIGURE 10.9. The oscillation frequency of a quartz crystal microbalance changes when its surface, functionalized with a oligonucleotide, interacts with oligonucleotide-decorated nanoparticles via hybridization.

A nanoparticle-based electrical detection of DNA hybridization based on electrochemical stripping detection of the colloidal gold tag has been also reported.[91] The system is rather complex and comprises the following components: i) streptavidin-coated magnetic beads; ii) biotinylated oligonucleotide probe; iii) biotinylated oligomer target; iv) streptavidin gold particles. In brief, the hybridization of a target oligonucleotide to magnetic bead-linked oligonucleotide probes is followed by binding of the streptavidin-coated metal nanoparticles to the captured DNA. Eventually the dissolution of the nanometer-sized gold tag is followed by potentiometric stripping measurements of the dissolved metal tag at single-use thick-film carbon electrodes. Thus the system combines the inherent signal amplification of stripping metal analysis with the effective discrimination against nonhybridized DNA. However one of the most striking achievements in electrical DNA detection has been reported by Mirkin and his group.[92] They have functionalized the surface of an electrode gap with oligonucleotides and exposed it to oligonucleotide functionalized gold nanoparticles. In the presence of a polynucleotide target, hybridization occurs with binding of the nanoparticles to the electrode gap. Silver

deposition facilitated by these nanoparticles bridges the gap and leads to readily measurable conductivity changes. With this method target DNA was detected at concentrations as low as 500 femtomolar and with a point mutation selectivity factor of ~100,000:1 (Figure 10.10).
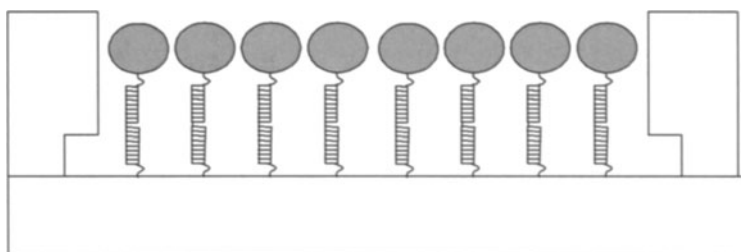
FIGURE 10.10. The assembling of nanoparticles over an electrode gap via hybridization gives an electric signal.

Magnetic nanosensors for the detection of oligonucleotide sequences have been also developed.[93] The starting material for the obtainment of these sensors consisted of monodisperse, fluid-phase nanoparticles containing a core of superparamagnetic, crystalline Fe_2O_3/Fe_3O_4 (3 nm) covered by epichlorohydrin cross-linked dextran and functionalized with amine groups. The amine groups were then coupled to thiolated oligonucleotides with an average of three nucleotide per particle. If particles with oligonucleotides complementary to a target sequence are mixed they hybridize in a few hours giving rise, subsequently, to a brown precipitate that moves on the sides of the tube when a magnet is applied. Although the unassembled nanoparticles are enhancers of the spin-spin and spin-lattice relaxation processes the first was significantly magnified after the hybridization, i.e. with the formation of the assembly. Thus they are potential "magnetic nanosensors". The system has been also applied for the detection of DNA cleaving and methylating enzymes.[93b]

10.7. DNA-NANOPARTICLE-BASED DEVICES

We have grouped under this section examples of the use of nanoparticles and DNA aimed at the obtainment of supramolecular devices thus not just structure organization like in a previous section. The first example has to deal with the following question: can nanoparticles assembled by DNA still conduct electricity or will the DNA interconnects act as insulating shells? The groups of Mirkin and Kannewurf have tried to answer to this question.[94] Their conclusion, in studying oligonucleotide interconnected nanoparticles is that the conductivities of the dried assemblies are virtually independent of the length of the linker. The aggregates with DNA-protected nanoparticles

behave as semiconductors, while films formed from citrate-stabilized particles exhibit irreversible particle fusion and metallic behavior. They suggest that these experiments point to the possible use of these materials in DNA diagnostic applications where sequence-specific binding events may close a circuit and lead to a dramatic increase in conductivity. A completely opposite approach was used by Ford's group.[95] They have used DNA as a template to grow nanoparticles and transform the resulting system into nanowires by electroless gold plating solution. The Pt(0) particles were formed along the DNA double strand by reduction of a Pt(II) complex with an intercalating agent. The size of this particles is very small (~1 nm) and quite interestingly their formation does not affect the solubility properties of the DNA. Wessels et al.[96] have used tris(hydroxymethyl)phosphine-capped gold particles (1-2 nm diameter) and have observed that they bind densely to DNA in spite of the fact that both species are negatively charged. The solvent influences the efficiency of the interaction between particles and between particles and DNA. Via subsequent electroless gold plating they have obtained wires with conductivities of the order of 1/1000 than that of bulk gold.

Nanoparticles have been used for the efficient delivery of DNA thus proving to be nonviral transfection agents.[97,98] This is based on the efficient recognition of DNA and on the ability of functional nanoparticles to act as multivalent receptors. This aspect has been nicely addressed by Rotello's group.[99] They have shown as gold clusters protected by a monolayer terminating with cationic ammonium groups can interact with the DNA backbone via charge complementarity. This aspect will be discussed in the following section.

Nanoparticle-based probes were recently reported.[100] They have been shown to be able to recognize and detect not only specific DNA sequences but they can be applied for the recognition and detection of a wide range of analytes such as small organic molecules and divalent cations: For this reason they are included in this section. These biosensors are based on 2.5-nm gold nanoparticles that function as both nano-scaffolds and nano-quenchers. Attached to the gold cluster, via a thiol group, are oligonucleotides labeled at the end with a fluorophore. The fluorophore tends to stick at the particle surface with quenching of its fluorescence. However the binding of any target substrate changes this conformation resulting in an increase of the fluorescence and, hence, to the possibility to quantify the recognition event. The extension of the principle of polynucleotide recognition to proteins is one of the latest advances in this area (Figure 10.11).[101] The approach takes advantage of protein recognition elements functionalized with oligonucleotide strands. Each of these can be encoded with a different oligonucleotide sequence with discrete and tailorable hybridization/dehybridization properties. A specific spectroscopic

signature for each hybrid completes the recognition process. This method allows one to detect multiple proteins in one solution, a non trivial process, that often requires time-consuming and expensive assay protocols.

Remote electronic control over the hybridization behavior of DNA molecules has been achieved by inductive coupling of radio-frequency magnetic field to a metal nanocrystal covalently linked to DNA.[102] The increase of the local temperature of the bound DNA by inductive coupling to the nanocrystal induces denaturation while leaving surrounding molecules relatively unaffected. The process appears to be totally reversible and it should be possible to extend it from the control of the hybridization to a broad range of other biological functions.
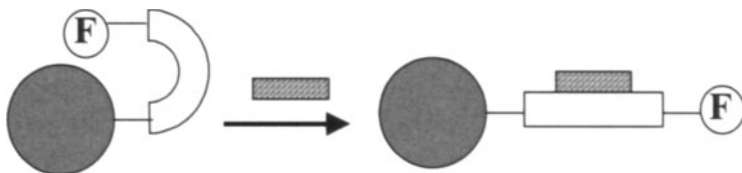
FIGURE 10.11. Fluorophore-functionalized gold nanoparticles with an appropriate spacer able to interact with a suitable target may increase their fluorescence upon binding.

10.8. BIOMIMETIC APPLICATIONS: MIMICRY OF CARBOHYDRATE-PROTEIN AND CARBOHYDRATE-CARBOHYDRATE INTERACTIONS

The binding between gold nanoparticles and biomolecules can be easily extended to other species by self-assembling thiolated molecules onto the nanoparticle surface.[103] A single thiol can present on the surface of the nanoparticle the desired functional group. This simple and versatile approach has been used by several research groups to generate nanoparticles that have been used to mimic natural systems. In the previous sections we have mostly focused on the merging of biomolecules and nanoparticles to generate new materials and organized networks of nanoparticles.[104] Here we will review selected examples of the many applications appeared recently in the literature were gold nanoparticles are used for molecular recognition, as catalysts to mimic enzymes, to perform biological assays, as gene transfer agents and as promising delivery vehicles.

The linking of carbohydrates to gold nanoparticles is a method for tailoring highly polyvalent water/soluble carbohydrate surfaces with globular shapes. This approach opens the way to the preparation of

glyconanoparticles with a variety of carbohydrate ligands and with different ligand density, providing a controlled model for investigating the influence of carbohydrate clustering and orientation effects on their interactions with specific receptors. In particular, the carbohydrate-protein or carbohydrate-carbohydrate interactions are generally characterized by very low affinity between each other. However, in nature, the low affinity can be compensated by the presentation of multiple ligands to individual receptors. The polyvalent interactions between multi-ligands and their receptor can be collectively much stronger than the corresponding monovalent interactions. Recently, several carbohydrate ligands have been assembled on linear[105] and branched[106] polymers, dendrimers,[107] two-dimensional gold surface,[108] liposomes[109] to enhance receptor-ligand interactions.

The synthesis of water-soluble gold glyconanoparticles has been reported for the first time in 2001 by Penadés.[110] The strategy used was to self-assembly the target thiol- (or disulfide-) derivatized neoglycoconjugates in the formation of the gold nanoparticles using the procedure reported by Brust.[103] Two biologically significant oligosaccharides, the disaccharide lactose (Galβ(1→4)Glcβ1-OR) and the trisaccharide Le^X (Galβ(1→4)[Fucα(1→3)]GlcNAcβ1-OR), have been prepared to functionalize gold nanoparticles (Figure 10.12). Clusters of 1.8 nm gold core diameter were obtained containing 63 (lacto-1), 70 (lacto-2) and 97 (Le^X-3) molecules per 201 gold atoms.

1: X = O
2: X = CH$_2$
3: X = CH$_2$
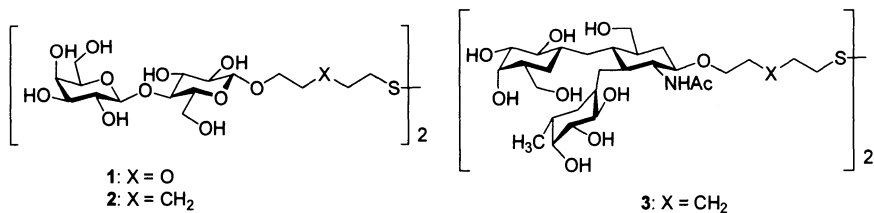
FIGURE 10.12. Structure of carbohydrate ligands used to protect the gold nanoparticles

The glyconanoparticles have been used as 3D models to mimic GSL clustering at the cell surface and to investigate the existence of carbohydrate-carbohydrate interactions in solution. Divalent cations seem to be essential in this process. The Le^X-Au nanoparticles exposed to a calcium solution (10 mM) show 3D aggregates at all concentrations (0.1÷0.9 mg mL^{-1}) while the lacto-Au nanoparticles remain dispersed as in the absence of ions. Studies of the aggregation process in the presence of calcium ions indicate that only specific binding events between Ca^{2+} ions and the Le^X molecules dictate the self-aggregation process and confirm their key role as homophilic adhesion molecules. This selective ability was also confirmed by an atomic force microscopy (AFM) study of adhesion forces between individual Le^X antigen molecules by using well-defined 2D-SAM surfaces.[111] The adhesion of gold-

glyconanoparticles to 2D-SAM functionalized with the ligands **2** and **3** in the presence of Ca^{2+} could be quantified by using the surface plasmon resonance as the analytical method. The results indicate that the affinity of the Le^X antigen for self-recognition is in the µM range, whereas the lactose self-interaction and the heterotopic Le^X/*lacto* interaction show affinity constants in the mM range. The selectivity of Le^X nanoparticles for the Le^X monolayer is about 200 times higher ($\Delta\Delta G \sim 3$ kcal mol^{-1}) than for the *lacto* monolayer and 30 times times higher ($\Delta\Delta G \sim 2$ kcal mol^{-1}) than that of the nanoparticles for its self-assembled monolayers. The binding affinity for Le^X self-recognition ($\Delta G \sim 8$ kcal mol^{-1}) equals the affinity determined for the heterotopic binding of polymeric Gg3 to GM3 monolayers,[112] which is a model system mimicking the Gg3-GM3 interaction between lymphoma and melanoma cells.[113] However, the selectivity found for the Ca^{2+} mediated Le^X-Le^X interaction related to the Le^X-*lacto* in the above mentioned model system is about 3 kcal mol^{-1} higher than that found between Gg3-GM3 and Gg3-lacto interactions ($\Delta G < 1$ kcal mol^{-1}) in the monolayer-polymer system.[10] In addition, the cooperative character of the Le^X self-recognition (that is Ca^{2+} dependent) has[114] a β value of 10^4 ($\beta = K_{mono}/K_{poly}$).

The architecture of the template used is influencing the mechanism of the receptor-ligand binding as demonstrated very recently by Kiessiling.[105] Thus, the activity of carbohydrate-conjugated nanoparticles should be compared to that of similarly functionalized globular polymers or to globular proteins. This comparison may give indication on how good are functional gold nanoparticles to model these specific carbohydrate-containing natural systems.

Gold glyco-nanoparticles have been obtained by Kataoka and coworkers using a different approach.[115] Gold nanoparticles with an average core diameter of 8.9 nm were prepared by reduction of the metal salt with $NaBH_4$ in the presence of acetal-PEG-SH (average molecular weight 3090) at a $HAuCl_4$:acetal-PEG-SH molar ratio of 6:1). These nanoparticles are stable in aqueous solutions with elevated ionic strength (0.3 M phosphate buffer) and also in a serum-containing medium. The conversion of the acetal group into an aldehyde was conducted by immersing the PEGylated gold nanoparticles into an aqueous medium adjusted to pH 2 using hydrochloric acid for 5 h. Lactose (Lac) and mannose (Man) groups were successfully reacted with the distal PEG-chain ends on the gold particles through reductive amination reaction (Figure 10.13). Terminal Lac content could be regulated by varying the molar ratio of *p*-aminophenyl-Lac with *p*-aminophenyl-Man in the reaction mixture. Lac-conjugated gold nanoparticles exhibited selective aggregation when exposed to *Recinus communis* agglutinin (RCA_{120}), a bivalent galactose-binding lectin. The solution color gradually changes from red to purple and correspondingly the

SP band in the UV-Vis spectrum becomes broad and shifts from 523 to longer wavelength. This was attributed to distance-dependent changes in the optical properties of aggregated gold nanoparticles cross-linked by RCA_{120} lectin which recognizes lactose residues on the PEGylated gold surface. Aggregation of the Lac-functionalized gold nanoparticles by the RCA_{120} lectin was reversible, recovering the original dispersed phase and color by addition of excess galactose. The degree of aggregation was proportional to lectin concentration, allowing the system to be utilized to quantify lectin concentration with nearly the same sensitivity as ELISA.
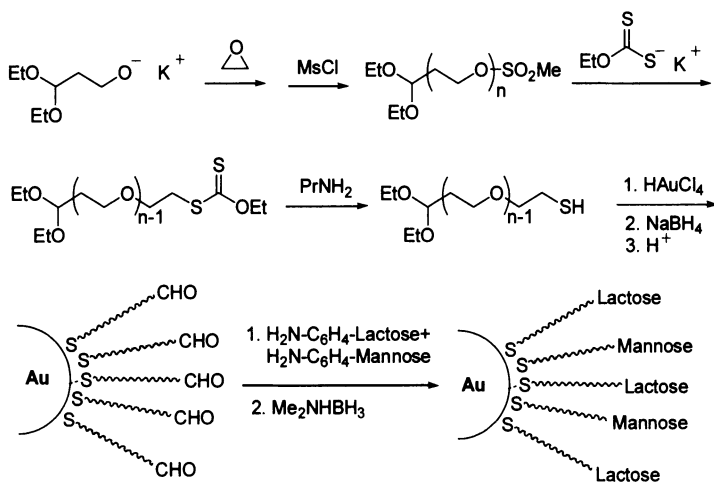
FIGURE 10.13. Preparation of Functionalized Gold Nanoparticles covered with HS-PEG-Lactose and HS-PEG-Mannose

Monolayers protected gold clusters having on the external surface mannose groups (dubbed by the authors m-AuNP) have been reported to bind specifically to FimH adhesion of bacterial type 1 pili in *Escherichia coli* as observed by TEM.[116] Type 1 pili are filamentous proteinaceous appendages that extend from the surface of many gram-negative organisms and are composed of FimA, FimF, FimG, and FimH proteins. FimA accounts for more than 98% of the pilus protein, and FinH is uniquely responsible for the binding to D-mannose. Two E. coli strains ORN178 and ORN208 were used in experiments to confirm the specific binding of m-AuNP to FimH. The TEM results showed that m-AuNP selectively binds the pili of the ORN178 strain but not those of the ORN208 strain, demonstrating specific binding of m-AuNPto FimH. The nanoparticles were localized at the lateral ends and distributed at intervals along the shaft of the pili (on the average of 100-150 nm interval) in ORN178 strain, consistent with the localization pattern of FimH protein along type 1 pili viewed by immunoelectron microscopy. Several experiments with free mannose

suggest that m-AuNP binds FimH better than free mannose does. The strong and selective binding of m-AuNP to bacterial type 1 pili presents a novel method of labeling specific protein on the cell surface using carbohydrate-conjugated nanoparticles. Moreover, in comparison with the conventional sandwich immunoassay, the biomolecule-conjugated nanoparticles can provide a relatively easy and direct method to visualize the target receptors on the cell surface under an electron microscope.

10.9. MIMICRY OF POLYVALENCY AND COOPERATIVITY

What are the properties of a synthetic system in order to mimic natural enzymes or proteins? Are these features present in functional nanoparticles thus to perform (possibly with the same efficiency) the same processes that occur in nature? One property mentioned above is polyvalency. We have recently disclosed a compelling example of multivalent recognition based on functional gold nanoparticles where the single contribution of each binding event could be dissected.[117] *N*-methylimidazole functionalized gold nanoparticles have been used to bind mono-, bis- and tris-Zn-porphyrins (Figure 10.14). As the number of porphyrins increases, the relative gain in binding constant (β) and effective molarity (EM) for intracomplex binding become lower. By extrapolation of this trend, one may speculate that upon increasing the number of porphyrins in the array the binding constant will reach a limiting value with no further improvement. This might be explained by the poor fitting of the porphyrin array to the curved surface of the MPCs or to the accumulation of adverse interactions with the surface (steric interactions between porphyrins and monolayer). Nevertheless, it must be pointed out that the values of β and EM observed for tris-porphyrin are slightly higher than those reported previously using a tripodal methylimidazole derivative whose structure was complementary to that of the tris-Zn-porphyrin used.[118] This indicates that the cooperative binding of the methylimidazoles on the nanoparticles to the tris-porphyrin is as good as (or better than) that of the tripodal ligand. This positive comparison implies that, due to the flexibility of the terminal part of the chain on the MPC surface, the mobility of the methylimidazole thiolates compensates for the lack of complementarity without paying a significant entropic price.

4: m = n = 1; MPC-C12-MI 1:1
5: m =4; n = 1; MPC-C12-MI 4:1
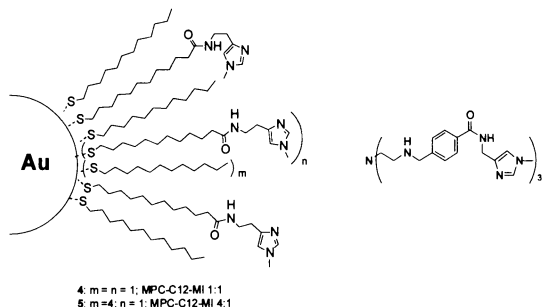
FIGURE 10.14. Gold nanoparticles and tripodal ligand used for binding mono-, bis- and tris-Zn-porphyrins.

The control of the organization of specific functional groups is a prerequisite essential to the activity of enzymes. Rotello and coworkers showed, for example, that the recognition of flavin by functional thiols present in the monolayer of MPCs (for hydrogen bonding and aromatic stacking) is subjected to a strong radial dependence (Figure 10.15).[119] When the recognition site was brought closer to the gold surface, the recognition was enhanced ~3-fold due to increased preorganization. The effect of preorganization is reversed upon reduction of flavin, were the functional thiolates with longer side chains bind the flavin guest ~7-fold stronger than the short chain counterpart due to unfavorable dipolar interactions between the electron-rich aromatic stacking units of the host and the anionic flavin guest.
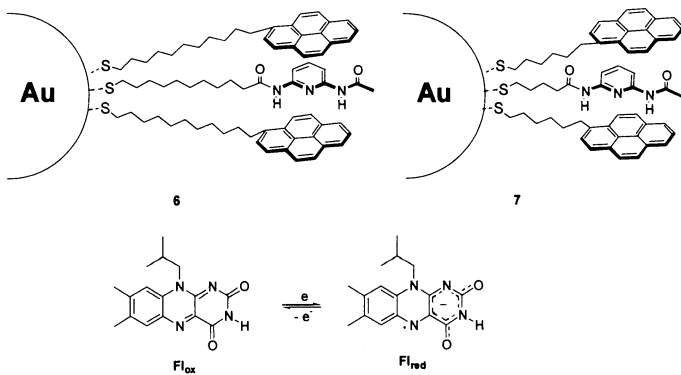
FIGURE 10.15. Functional MPCs used by Rotello for flavin recognition and flavin Fl.

An interesting feature that enzymes exhibit in their activity is cooperativity of functional groups at the active site. Recently, it has been shown that this property can be displayed also by functional groups present

on the surface of the protective monolayer of gold nanoparticles. This has been demonstrated for the first time with functional gold nanoclusters **4** catalytically active in the cleavage of an activated ester.[120] These systems present analogies with micellar aggregates although they exist under solvent conditions where the micelles do not survive. Furthermore, the cooperative effects of the functional moieties may be exploited at very low concentration of the catalyst because the nanocluster does not require the critical aggregate concentration necessary for the formation of micelles. As for these properties Au-MPCs resemble dendrimers, although the synthetic effort required for their obtainment is much less demanding.

With the goal to obtain new and selective catalysts we decided to exploit a self-assembling strategy for the preparation of a putative "artificial protein" by assembling short histidine-based peptides on gold nanoparticles.[121] The peptide, shown in Figure 10.16, comprising six C_α-tetrasubstituted aminoacids and a histidine residue has been chosen as the monomeric unit for the preparation of the functional nanoparticles. Short peptides (7-8 residues), rich in C_α-tetrasubstituted amino acids are usually rather structured, preferentially adopting a 3_{10}-helical conformation.[122] Such peptides provide a conformationally robust element to be assembled on a proper template. The thiol shown in Figure 10.16 was then used for the preparation of peptide-functionalized gold nanoparticles (MPCs) through place exchange[123] with 2 nm size dodecanethiol-functionalized MPCs (MPC-C12).[124] The IR spectrum of this new material matched that of the parent, unbound peptide suggesting that the folded conformation of the peptide is maintained when it is bound to the MPCs. These peptide-functionalized gold nanoclusters show a very peculiar solubility behavior. So, although they could be solubilized in the solvent used for their purification they became almost insoluble once brought to dryness. This problem is now going to be solved by using water soluble nanoparticles.
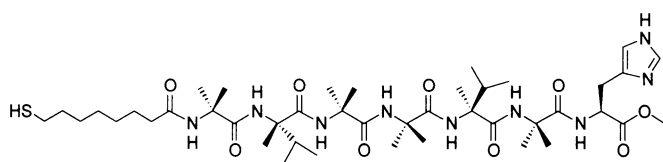
FIGURE 10.16. Peptide containing thiol with helical conformation used for the functionalization of gold nanoparticles.

Colloidal gold particles are considered to be relatively inert, and can be readily conjugated to proteins and other molecular species without altering the biological activity of the conjugated species. Gold particles also can be

visualized by electron microscopy and quantitated in bulk samples by neutron activation analysis.[125]

10.10. NANOMATERIALS AS DELIVERY SYSTEMS

The paracellular mechanism of colloidal gold uptake has been qualitatively and quantitatively studied.[126] Quantitative studies show that colloidal gold uptake is dependent on particle size: smaller particles (4-10 nm) cross the gastrointestinal tract more readily than larger colloids and no aggregation seems to take place. The observation suggests that particles are able to enter the body without being subject to organized intracellular processes such as lysosomal enzymatic degradation that may be deleterious to conjugated proteins or molecular species. This mechanism of uptake, and other physical and chemical properties of colloidal gold, call for studies relative to the use of colloidal gold as a carrier for drugs, vaccines, and/or other molecular species that may not normally be absorbed in their biologically active form when administered orally.

The interaction of nanoparticles with cells depends on the functional groups present on the monolayer surface and these specific interactions may be used for synthetic transfection. It has been demonstrated that MPCs functionalized with tetraalkylammonium ligands interact with the DNA backbone via charge complementarity with the negatively charged DNA phosphate groups giving rise to charge-neutralized, non-aggregated assemblies.[99] Effective demonstration of functional recognition was established by exploring the effects of the positively charged MPCs-DNA interaction on T7 RNA polymerase transcription. In vitro assay indicates that the binding affinity is large enough that the MPC is able to inhibit T7 RNA polymerase from producing RNA oligomers. In addition, it has been reported that gold nanoparticles presenting in the monolayer surface quaternary ammonium ions efficiently transfect a mammalian cells culture.[98] The efficiency of the transfection process is determined by several parameters, including the ratio MPC:DNA used in initial complexation, the surface coverage of quaternary ammonium salts and the length of the uncharged thiol chain. These results open the route to the use of these particles as transfection vectors and the creation of efficient gene regulation systems.
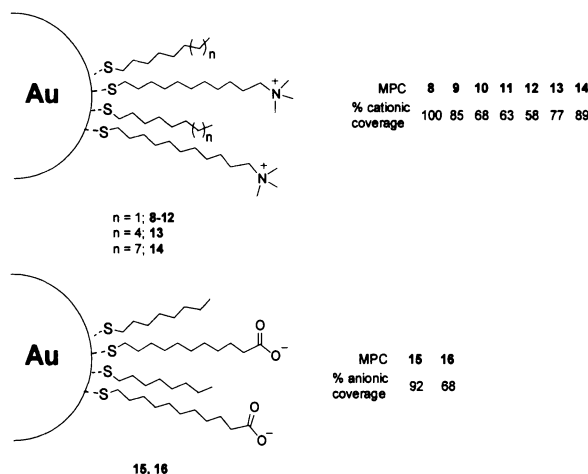
FIGURE 10.17. MPCs presenting on the surface positively charged quaternary ammonium groups or negatively charged carboxyl groups.

10.11. CONCLUSION

We hope we have provided a concise but stimulating overview of the rather successful conjugation of nanoparticles with biomolecules. The chemical literature is recording a soaring number of contributions in this field demonstrating its increasing relevance. The modeling of biological functions is still at its infancy but we can easily forecast its fast development in the near future. With the availability of several techniques for the selective functionalization of nanoparticles, the knowledge of the parameters that keep them in solution and control their reciprocal interactions scientists have in their hands powerful systems to modify them at their wills. As Nobel physicist Richard Feynman[127] pointed out more than 40 years ago "there is plenty of room at the bottom" and we are just starting to take advantage of it.

REFERENCES

1   Bangs, L. B. *Pure Appl. Chem.* **1996**, *68*, 1873-1879.
2   Faulk, W. P.; Taylor, G. M. *Immunochemistry* **1971**, *8*, 1081-1086.
3   Hayat, M. A. Colloidal gold, principle, methods and applications. Academic Press San Diego CA **1989**.
4   Handley, D. A. in Colloidal gold, principle, methods and applications. Vol 1. Academic Press San Diego CA **1989**.
5   Bohren, C. F.; Huffman, D. R. Absorption and Scattering of Light by Small Particles Wiley, **1998**
6   Kreibig, U.; Genzel, L. *Surf. Sci.* **1985**, *156*, 678-700.

7   Baudhuin, P.; van der Smissen, P.; Beauvois, S.; Courtoy, P. J. in Colloidal gold, principle, methods and applications. Vol 2. Academic Press San Diego CA **1989**.

8   Shenton, W.; Davies, S.; Mann, S. *Adv. Mater.* **1999**, *11*, 449-452.

9   Crumbliss, A.; Perine, L.; Stonehuerer, J.; Tuberger, K. R.; Zhao, J.; O'Daly, J. P. *Biotech. Bioeng.* **1992**, *40*, 483-488.

10   Fischer, N. O.; McIntosh, C. M.; Simard, J. M.; Rotello, V. M. *Proc. Nat Acad. Sci. USA* **2002**, *99*, 5018-5023.

11   Romano, E. L.; Romano, M. *Immunochemistry*, **1977**, *14*, 711-718.

12   (a) Varki, A. *Glycobiology* **1993**, *3*, 97-130. (b) Dwek, R. A. *Chem. Rev.* **1996**, *96*, 683-720.

13   Bendayan, M. *J. Histochem. Cytochem.* **1981**, *29*, 531-541.

14   Deonge, R.; Huang, T. *J. Biol. Chem.* **1971**, *246*, 698-703.

15   Weisbecker, C. S.; Merritt, M. V.; Whitesides, G. M. *Langmuir* **1996**, *12*, 3763-3772.

16   Sastry, M.; Lala, N.; Patil, V.; Chavan, S. P.; Chittiboyina, A. G. *Langmuir*, **1998**, *14*, 4138-4142.

17   Gole, A.; Dash, C.; Ramakrishnan, V.; Sainkar, S. R.; Mandale, A. B.; Rao, M.; Sastry, M. *Langmuir* **2001**, *17*, 1674-1679.

18   Gole, A.; Dash, C.; Soman, C.; Sainkar, S. R.; Rao, M.; Sastry, M. *Bioconjug. Chem.* **2001**, *12*, 684-690.

19   Lala, N.; Chittiboyina, A. C.; Chavan, S. P.; Sastry, M. *Col. Surf. A* **2002**, *205*, 15-20.

20   Gole, A.; Vyas, S.; Phadtere, S.; Lachke, A.; Sastry, M. *Col. Surf. B* **2002**, *25*, 129-138.

21   Thant, N. T. K.; Rosenzweig, Z. *Anal. Chem.* **2002**, *74*, 1624-1628.

22   Elganian, R.; Storhoff, J.J.; Mucic, R. C.; Letsinger, R. L.; Mirkin, C. A. *Science* **1997**, *277*, 1078-1081.

23   Storhoff, J. J.; Elghanian, R.; Mucic, R. C.; Mirkin, C. A.; Letsinger, R. L. *J. Am. Chem. Soc.* **1998**, *120*, 1959-1964.

24   Reynolds, R. A.; Mirkin, C. A.; Letsinger, R. L. *Pure appl. Chem.* **2000**, *72*, 229-235.

25   Englebienne, P. *Analyst*, **1998**, *123*, 1599-1603.

26   Ma, Z.; Liang, R.; Jiang, W.; Zhou, T.; Chen, Z.; Duan, M.; Tang, J.; Sui, S-F. *Chem. Lett.* **2002**, 570-571.

27   Dulhunty, A. F.; Junankar, P. A.; Stanhope, C. *J. Histochem. Cytochem.* **1993**, *41*, 1459-1466.

28   Howell, K. E.; Reuter-Carlson, U.; Devaney, E.; Luzio, J. P.; Fuller, S. D. *Eur. J. Cell. Biol.* **1987**, *44*, 318.

29   Bartlett, P. A., Bauer, B.; Singer, S. J. *J. Am. Chem. Soc.* **1978**, *100*, 5085-5089.

30   Hainfeld, J. F. *Ultramicroscopy* **1992**, *46*, 135-144.

31   Hainfeld, J. F.; Powell, R. D. *J. Histochem. Cytochem.* **2000**, *48*, 471-480.

32   Hainfeld, J. F.; Furuia, F. R. *J. Histochem. Cytochem.* **1992**, *40*, 177-184.

33   Hainfeld, J, F. *Science* **1987**, *236*, 450-453.

34   Segon von Banchet, G.; Heppelman, B. *J. Histochem. Cytochem.* **1995**, *43*, 821-827.

35   Gregori, L.; Hainfeld, J. F.; Simon, M. N.; Goldgaber, D. *J. Biol. Chem.* **1997**, *272*, 58-62.

36   Skripkin, E.; Yusupova, G.; Yusupov, M.; Kessler, P.; Ehresman, C.; Ehresman, B. *Bioconj. Chem.* **1993**, *4*, 549-553.

37   Lipka, J. J.; Hainfeld, J. F.; Wall, J. S. *J. Ultrastruct. Res.* **1983**, *84*, 120-126.

38   Hainfeld, J. F.; Liu, W.; Halsey, C. M. R.; Freimuth, P.; Powell, R. D. *J. Struct. Biol.* **1999**, *127*, 120-134.

39   Hainfeld, J. F.; Powell, R. D. *J. Histochem. Cytochem.* **2000**, *48*, 471-480.

40   Jeon, H.; Shipley, G. G. *J. Biol. Chem.* **2000**, *297*, 30465-30470.

41   Robinson, J: M.;Vandre, D. D. *J. Histochem. Cytochem.* **1997**, *45*, 631-642.

42   Powell, R. D.; Halsey, C. M.; Spector, D. C.; Kaurin, S.; L.; McCann, J.; Hainfeld, J. F. *J. Histochem. Cytochem.* **1997**, *45*, 947-956.

43   Powell, R. D.; Halsey, C. M.; Hainfeld, J. F. *Microsc. Res. Tech.* **1998**, *42*, 2-12.

44   Takizawa, T.; Suzuki, K.; Robinson, J. M. *J. Histochem. Cytochem.* **1998**, *46*, 1097-1102.

45   Lackie, P. M. *Histochem Cell. Biol.* **1996**, *106*, 9-17.

46   Henglein, A. *Chem. Rev.* **1989**, *89*, 1861-1873.

47   Nirmal, M.; Brus, L. E. *Acc. Chem. Res.* **1999**, *32*, 407-414.

48   Klarreich, E. *Nature*, **2001**, *413*, 450-452.

49   Gerion, D. Pinaud, F. Williams, S. C.; Parak, W. J.; Zanchet, D.; Weiss, S.; Alivisatos, A. P. *J. Phys. Chem. B* **2001**, *105*, 8861-8871.

50   Parak, W. J.; Gerion, D.; Zanche, D.; Woerz, A. S.; Pellegrino, T.; Micheel, C.; Williams, S. C.; Seitz, M.; Bruehl, R. E.; Bryant, Z.; Bustamente, C.; Bertozzi, C. R.; Alivisatos, A. P. *Chem. Mater.* **2002**, *14*, 2113-2119.

51   Mamedova, N. M.; Kotov, N. A.; Rogach, A. L.; Studer, J. *Nano Lett.* **2001**, *1*, 281-286.

52   Sondi, I.; Siiman, O.; Koester, S.; Matijevic, E. *Langmuir* **2000**, *16*, 3107-3118.

53   Chan, W. C. W.; Nie, S. *Science*, **1998**, *281*, 2016-2018.

54   Matoussi, H.; Mauro, J. M.; Goldman, E. R.; Anderson, G. P.; Sundar, V. C.; Mikulec, F. V.; Bawendi, M. G. *J. Am. Chem. Soc.* **2000**, *122*, 12142-12150.

55   Han, M. Y.; Gao, X.; Su, J. Z.; Nie, S. *Nat. Biotechnol.* **2001**, *19*, 631-635.

56   Alivisatos, A. P. *Science*, **1996**, *271*, 933-937.

57   Weller, H. *Adv. Mater.* **1993**, *5*, 88-93.

58   Goldman, E. R.; Balighian, E. O.; Matoussi, H.; Kuno, M. K.; Mauro, J. M.; Tran, P. T.; Anderson, G. P. *J. Am Chem. Soc.* **2002**, *124*, 6378-6382.

59   Kuno, M.; Fromm, D. P.; Hamann, H. F.; Gallagher, A.; Nesbitt, D. J. *J. Chem. Phys.* **2000**, *112*, 3117-3120.

60   Lacoste, T. D.; Michaelet, X.; Pinaud, F.; Chemla, D. S.; Alivisatos, A. P.; Weiss, S. *Proc. Natl. Acad. Sci. USA* **2000**, *97*, 9461-9466.

61   Wang, D.; Rogach, A. L.; Caruso, F. *Nano Lett.* **2002**, *2*, 857-861.

62   Dubertret, B.; Skourides, P.; Norris, D. J.; Noireaux, V.; Brivanlou, A. H.; Libchaber, A. *Science*, **2002**, *298*, 1759-1762.

63   (a) Seeman, N. C. *Angew. Chem. Int. Ed.* **1998**, *37*, 3220-3228; (b) Seeman, N. C.; Belcher, A. M. *Proc. Natl. Acad. Sci. USA* **2002**, *99*, 6451-6455; (c) Carbone, A.; Seeman, N. C. *Proc. Natl. Acad. Sci. USA* **2002**, *99*, 12577-12582.

64   Mirkin, C. A.; Letsinger, R. L.; Mucic, R. C.; Storhoff, J. J. *Nature*, **1996**, *382*, 607-609.

65   Alivisatos, A. P.; Johnsson, K. P.; Peng, X.; Wilson, T. E.; Loweth, C. J.; Bruchez, M. P. Jr.; Schultz, P. G. *Nature*, **1996**, *382*, 609-611.

66   Storhoff, J. J.; Mirkin, C. A. *Chem. Rev.* **1999**, *99*, 1849-1862.

67   Nicewarner Peña, S. R.; Raina, S.; Goodrich, G. P.; Fedoroff, N. V.; Keating, C. D. *J. Am. Chem. Soc.* **2002**, *124*, 7314-7323.

68   Mucic, R. C.; Storhoff, J. J.; Mirkin, C. A.; Letsinger, R. L. *J. Am. Chem. Soc.* **1998**, *120*, 12674-12675.

69   Loweth, C. J.; Caldwell, W. B.; Paeng, X.; Alivisatos, A. P.; Schultz, P. G. *Angew. Chem. Int. Ed.* **1999**, *38*, 1808-1812.

70   Cao, Y. W.; Jin, R.; Mirkin, C. A. *J. Am. Chem. Soc.* **2001**, *123*, 7961.

71   Mitchell, G. P.; Mirkin, C. A.; Letsinger, R. L. *J. Am. Chem. Soc.* **1999**, *121*, 8122-8123.

72   Niemeyer, C. M.; Bürger, W.; Peplies, J. *Angew. Chem. Int. Ed.* **1998**, *37*, 2265-2268.

73   Park, S.-J.; Lazarides, A. A.; Mirkin, C. A.; Letsinger, R. L. *Angew. Chem. Int. Ed.* **2001**, *40*, 2909-2912.

74   Kumar, A.; Pattarkine, M.; Bhadhade, M.; Mandale, A. B.; Ganesh, K. N.; Datar, S. S.; Dharmadhikari, C. V.; Sastry, M. *Adv. Mater.* **2001**, *13*, 341-344.

75   Sanchez-Cortes, S.; Berenguel, R. M.; Madejon, A.; Perez-Mendez, M. *Biomacromolecules* **2002**, *3*, 655-660.

76   Demers, L. M.; Park, S.-J.; Taton, T. A.; Li, Z.; Mirkin, C. A. *Angew. Chem. Int. Ed.* **2001**, *40*, 3071-3073.

77   (a) Peschel, S.; Ceyhan, B.; Niemeyer, C. M.; Gao, S.; Chi, L.; Simon, U. *Mater. Sci Eng. C* **2002**, *19*, 47-59; (b) Sauthier, M. L. ; Carroll, R. L.; Gorman, C. B.; Franzen, S. *Langmuir* **2002**, *18*, 1825-1830.

78   Wang, J.; Song, F.; Zhou, F. *Langmuir* **2002**, *18*, 6653-6658.

79   Storhoff, J. J.; Elghanian, R.; Mucic, R. C.; Mirkin, C. A.; Letsinger, R. L. *J. Am. Chem. Soc.* **1998**, *120*, 1959-1964.

80   Lazarides, A. A.; Schatz, G. C. *J. Phys. Chem. B* **2000**, *104*, 460-467.

81   Reynolds III, R. A.; Mirkin, C. A.; Letsinger, R. L. *J. Am. Chem. Soc.* **2000**, *122*, 3795-3796.

82   Souza, G. R.; Miller, J. H. *J. Am. Chem. Soc.* **2001**, *123*, 6734-6735.

83   Taylor, J. R.; Fang, M. M.; Nie, S. M. *Anal. Chem.* **2000**, *72*, 1979-1986.

84   Yun, C. S.; Khitrov, G. A. ; Vergona, D. E.; Reich, N. O.; Strouse, G. F. *J. Am. Chem. Soc.* **2002**, *124*, 7644-7645.

85   Taton, T. A.; Mirkin, C. A.; Letsinger, R. L. *Science* **2000**, *289*, 1757-1760.

86   Gerion, D.; Parak, W. J.; Williams, S. C.; Zanchet, D.; Micheel, C. M.; Alivisatos, A. P. *J. Am. Chem. Soc.* **2002**, *124*, 7070-7074.

87   (a) Zhou, X. C.; O'Shea, S. J.; Li, S. F. Y. *Chem. Commun.* **2000**, 953-954; (b) Han, S.; Lin, J.; Satjapipat, M.; Baca, A. J.; Zhou, F. *Chem. Commun.* **2001**, 609-610.

88   Patolsky, F.; Ranjit, K.; Lichtenstein, A.; Willner, I. *Chem. Commun.* **2000**, 1025-1026.

89   (a) Lin, L.; Zhao, H. Q.; Li, J. R.; Tang, J. A.; Duan, M. X.; Jiang, L. *Biochem. Biphys. Res. Commun.* **2000**, *274*, 817-820; (b) Zhao, H. Q.; Lin, L.; Li, J. R.; Tang, J. A.; Duan, M. X.; Jiang, L. *J. Nanopart.Res.* **2001**, *3*, 321-323; (c) Liu, T.; Tang, J.; Zhao, H. Q.; Deng, Y. P.; Jiang, L. *Langmuir* **2002**, *18*, 5624-5626.

90   Ma, Z. F.; Li, J. R.; Jiang, L.; Yang, M. S.; Sui, S. F. *Chem. Lett.* **2002**, 328-329.

91   Wang, J.; Xu, D. K.; Kawde, A. N.; Polsky, R. *Anal. Chem.* **2001**, *73*, 5576-5581.

92   Park, S. J.; Taton, T. A.; Mirkin, C. A. *Science* **2002**, *295*, 1503-1506.

93   (a) Josephson, L.; Perez, J. M.; Weisslender, R. *Angew. Chem. Int. Ed.* **2001**, *40*, 3204-3206: (b) Perez, J. M.; O'Laughin, T.; Simeone, F. J.; Weissleder, R.; Josephson, L. *J. Am. Chem. Soc.* **2002**, *124*, 2856-2857.

94   Park, S.-J.; Lazarides, A. A.; Mirkin, C. A.; Brazis, P. W.; Kannewurf, C. R.; Letsinger, R. L. *Angew. Chem. Int. Ed.* **2000**, *39*, 3845-3848.

95   Ford, W. E.; Harnack, O.; Yasuda, A.; Wessels, J. M. *Adv. Mater.* **2001**, *13*, 1793-1796.

96   Harnack, O.; Ford, W. E.; Yasuda, A.; Wessels, J. M. *Nano Lett.* **2002**, *2*, 919-923.

97   (a) Bertling, W. M.; Gareis, M.; Paspaleeva, V.; Zimmer, A.; Kreuter, J.; Nurnberg, E.; Harrer, P. *Biotech. App. Biochem.***1991**, *13*, 390-405; (b) Maruyama, A.; Ishihara, T.; Kim, J. S.; Kim, S. W.; Akaike, T. *Coll. Surf. A* **1999**, *153*, 439-443; (c) Kneuer,

C.; Sameti, M.; Bakowsky, U.; Schiestel, T.; Schirra, H.; Schmidt, H.; Lehr, C. M. *Bioconj. Chem.* **2000**, *11*, 926-932; (d) Kneuer, C.; Sameti, M.; Haltner, E. G.; Schiestel, T.; Schirra, H.; Schmidt, H.; Lehr, C. M. *Internat. J. Pharm.* **2000**, *196*, 257-261; (e) Mao, H. Q.; Roy, K.; Troung-Le, V. L.; Janes, K. A.; Lin, K. Y.; Wang, Y.; August, J. T.; Leong, K. W. *J. Controll.Rel.* **2001**, *70*, 399-421; (f) Olbrich, C.; Bakowsky, U.; Lehr, C. M.; Muller, R. H.; Kneuer, C. *J. Controll.Rel.* **2001**, *77*, 345-355; (g) Prabha, S.; Zhou, W. Z.; Panyam, J.; Labhasetwar, V. *Internat. J. Pharm.* **2002**, *244*, 105-115.

98   Sandhu, K. K.; McIntosh, C. M.; Simard, J. M.; Smith, S. W.; Rotello, V. M. *Bioconj. Chem.* **2002**, *13*, 3-6.

99   McIntosh, C. M.; Esposito III, E. A.; Boal, A. K.; Simard, J. M.; Martin, C. T.; Rotello, V. M. *J. Am. Chem. Soc.* **2001**, *123*, 7626-7629.

100   Maxwell, D. J.; Taylor, J. R.; Nie, S. M. *J. Am. Chem. Soc.* **2002**, *124*, 9606-9612.

101   Nam, J. M.; Park, S. J.; Mirkin, C. A. *J. Am. Chem. Soc.* **2002**, *124*, 3820-3821.

102   Hamad-Schifferly, K.; Schwartz, J. J.; Santos, A. T.; Zhang, S.; Jacobson, J. M. *Nature*, **2002**, *415*, 152-155.

103   Brust, M.; Walker, M; Betthell, D.; Schiffrin, D. J.; Whyman, R. *J. Chem. Soc., Chem. Commun.* **1994**, 801-802.

104   Niemeyer, C. M. *Angew. Chem. Int. Ed.* **2001**, *40*, 4128-4158.

105   Gestwicki, J. E.; Kiessling, L. L. *Nature* **2002**, *415*, 81-84.

106   Gestwicki, J. E.; Cairo, C. W.; Strong, L. E.; Oetjen, K. A.; Kiessling, L. L. *J. Am. Chem. Soc.* **2002**, *124*, 14922-14933.

107   For example: Backinowsky, L. V.; Abronina, P. I.; Shashkov, A. S.; Grachev, A. A.; Kochetkov, N. K.; Nepogodiev, S. A.; Stoddart, J. F. *Chem. Eur. J.* **2002**, *8*, 4412-4423 and references cited therein.

108   (a) Liang, M. N.; Smith, S. P., Metallo, S. J.; Choi, I. S.; Prentiss, M.; Whitesides, G. M. *Proc. Natl. Acad. Sci. U.S.A.* **2000**, *97*, 13092-13096; (b) Mann, D. A.; Kanai, M.; Maly, D. J.; Kiessling, L. L. *J. Am. Chem. Soc.* **1998**, *120*, 10575-10582.

109   Kingerly-Wood, J. E.; Williams, K. W.; Sigal, G. B.; Whitesides, G. M. *J. Am. Chem. Soc.* **1992**, *114*, 7303-7305.

110   De la Fuente, J.; Barrientos, A. G.; Rojas, T. C.; Rojo, J.; Cañada, J.; Fernández, A.; Penadés, S. *Angew. Chem. Int. Ed.* **2001**, *40*, 2257-2261.

111   Tromas, C.; Rojo, J.; De la Fuente, J. M.; Barrientos, A. G.; García, R.; Penadés, S. *Angew. Chem. Int. Ed.* **2001**, *40*, 3052-3055.

112   Matsuura, K.; Kitakouji, H.; Sawada, N.; Ishida, H.; Kiso, M.; Kitajima, K.; Kobajashi, K. *J. Am. Chem. Soc.* **2000**, *122*, 7406-7407.

113   Iwabuchi, K.; Yamamura, S.; Prinetti, A.; Hanada, K.; Hakomori, S.-I. *J. Biol. Chem.* **1998**, *273*, 9130-9138.

114   Mammen, M.; Choi, S.-K.; Whitesides, G. M. *Angew. Chem. Int. Ed.* **1998**, *37*, 2754-2794.

115   Otsuka, H.; Akiyama, Y.; Nagasaki, Y.; Kataoka, K. *J. Am. Chem. Soc.* **2001**, *123*, 8226-8230.

116   Lin, C.-C.; Yeh, Y.-C.; Yang, C.-Y.; Chen, C.-L.; Chen, G.-F.; Chen, C.-C.; Wu, Y.-C. *J. Am. Chem. Soc.* **2002**, *124*, 3508-3509.

117   Fantuzzi, G.; Pengo, P.; Gomila, R.; Ballester, P.; Hunter, C. A.; Pasquato, L.; Scrimin, P. submitted for publication.

118   Felluga, P. Tecilla, L. Hillier, C. A. Hunter, G. Licini, P. Scrimin, *Chem. Commun.* **2000**, 1087-1088.

119   Boal, A. K.; Rotello, V. M. *J. Am. Chem. Soc.* **2002**, *124*, 5019-5024.

120   Pasquato, L.; Rancan, F.; Scrimin, P.; Mancin, F.; Frigeri, C. *Chem. Commun.* **2000**, 2253-2254.

121   Pengo, P.; Broxterman, Q. B.; Kaptein, B.; Pasquato, L.; Scrimin, P. *Langmuir* **2003**, *19*, 0000.

122   Polese, A.; Formaggio, F.; Crisma, M.; Valle, G.; Toniolo, C.; Bonora, G. M.; Broxterman, Q. B.; Kamphuis, J. *Chem. Eur. J.* **1996**, *2*, 1104-1111.

123   Hostetler, M. J.; Green, S. J.; Stokes, J. J.; Murray, R. W. *J. Am. Chem. Soc.* **1996**, *118*, 4212-4213.

124   Ingram, R. S.; Hostetler, M. J.; Murray, R. W. *J. Am. Chem. Soc.* **1997**, *119*, 9175-9178.

125   (a) Hillyer, J. F.; Albrecht, R. M. *Microsc. Microanal.* (Suppl. 2: proceedings) **1998**, 4, 998-999; (b) Hillyer, J. F.; Albrecht, R. M. *Microsc. Microanal.* **1998**, 4, 481-490.

126   Hillyer, J. F.; Albrecht, R. M. *J. Pharm. Sciences* **2001**, *90*, 1927-1936.

127   Feynman, R. P. in *Miniaturization*, Gilbert, H. D. ed., Reinhold, New York, **1961**, pp. 282-296.

Index